

# The Competing Roles of Microstructure and Flaw Size on the Fatigue Limit of Metals

by

Timothy Edward McGreevy

B.S., Bradley University, 1991

M.S., Bradley University, 1994

## THESIS

Submitted in partial fulfillment of the requirements  
for the degree of Doctor of Philosophy in Mechanical Engineering  
in the Graduate College of the  
University of Illinois at Urbana-Champaign, 1998

Urbana, Illinois

© Copyright by Timothy Edward McGreevy, 1998

UNIVERSITY OF ILLINOIS AT URBANA-CHAMPAIGN  
THE GRADUATE COLLEGE

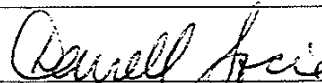
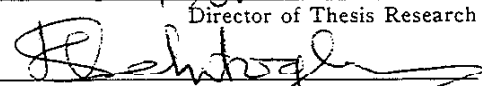
APRIL 10, 1998

(date)


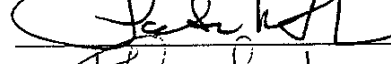
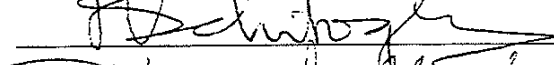

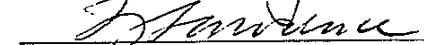
WE HEREBY RECOMMEND THAT THE THESIS BY  
TIMOTHY EDWARD MCGREEVY

THE COMPETING ROLES OF MICROSTRUCTURE  
ENTITLED  
AND FLAW SIZE ON THE FATIGUE LIMIT OF METALS

BE ACCEPTED IN PARTIAL FULFILLMENT OF THE REQUIREMENTS FOR  
THE DEGREE OF DOCTOR OF PHILOSOPHY

  
Director of Thesis Research  
  
Head of Department

Committee on Final Examination†

  
  
Chairperson  
  
  


† Required for doctor's degree but not for master's.

## ABSTRACT

Slip band and crack formation, propagation, and arrest are the active mechanisms in the fatigue process as was first observed in 1903. However, engineers relied on macroscopic properties such as hardness and tensile strength to predict fatigue limits since analytical tools to model the process did not exist. Many empirical modifications to the fatigue limit have since been made to account for variables such as surface roughness, state of stress, inclusion content, environmental effects, etc. A method is proposed to qualitatively and quantitatively predict the effects of several of these parameters on the fatigue limit of metals, specifically steels.

Research includes the development and verification of an analytical model that addresses the fatigue process, namely the threshold condition of non-propagating cracks. Two parameters are identified to govern the fatigue resistance: non-propagating crack size and crack barrier strength. The concept of three defect types associated with three different flaw dominated fatigue regimes is introduced. Furthermore, application of the model to fatigue mechanisms in high strength steels, synergistic effects of surface finish and intergranular cracks, competition between surface and subsurface fatigue nucleation, and unexplained observations and scatter in fatigue behavior is demonstrated. Overall, the model is proven as a simple and robust tool for qualifying and statistically quantifying material behavior. In addition, the model can be implemented in material screening, selection, and processing as well as a guide for future material research and design.

## ACKNOWLEDGEMENTS

Financial support of this work was provided by Caterpillar Inc. through the Fracture Control Program, College of Engineering, University of Illinois. Special thanks to Egon Wolf of Caterpillar for providing the opportunity to further my education and conduct this work.

The author is indebted to his advisor, Professor Darrell Socie, for stimulating discussions, emphasizing the power of simple but fundamental solutions, his friendship, and especially the opportunity and freedom to pursue various aspects related to the work presented herein.

Special thanks is given to Dr. Peter Kurath for his expertise and assistance with technical aspects of fatigue testing equipment and several intriguing discussions related to this investigation.

Mr. Daryl Brower is affably thanked for the countless flaw size measurements that allowed for a statistical approach of the fatigue problem. Ms. Nancy Finnegan is thanked for her patience and diligence in conducting the Auger spectroscopy work. Mr. Ed Rejda, my officemate is thanked for numerous discussions and useful feedback on many aspects of this research. Also, a great thanks is given to the machinists in the TAM machine shop, Bill, Kent, David, and Dan.

## TABLE OF CONTENTS

	Page
LIST OF TABLES .....	viii
LIST OF FIGURES .....	x
NOMENCLATURE .....	xvi
 CHAPTER	
1. INTRODUCTION .....	1
1.1 Literature Review.....	3
1.2 Purpose and Scope .....	22
2. EXPERIMENTAL PROGRAM .....	25
2.1 Testing Equipment and Procedure .....	25
2.2 Materials .....	25
2.2.1 4340 Vacuum Arc-Melted Steel .....	25
2.2.2 Modified 8680 Vacuum-Induction-Melt Steel.....	27
3. RESULTS .....	29
3.1 Literature Data .....	29
3.1.1 Ferritic Steels .....	29
3.1.2 Ferritic-Pearlitic Steels.....	30
3.1.3 Variety of Steel and Iron.....	31
3.1.4 Martensitic and Bainitic Steels .....	31
3.2 Experimental Results .....	32
3.2.1 High Carbon Martensitic Steels .....	32

3.2.2	Tempered High Carbon Martensitic Steels.....	32
3.2.3	Competition of Surface Finish and Inclusions in Hardened 4340 Steel.....	36
4.	FORMULATION OF THE HALL-PETCH-MURAKAMI MODEL (HPM) .....	39
4.1	The Intrinsically Flawed Regime.....	49
4.2	The Inherently Flawed Regime.....	54
4.3	The Processing Flawed Regime.....	55
5.	QUANTITATIVE EVIDENCE.....	61
5.1	Intrinsic Regime.....	61
5.1.1	Single Phase Equiaxed Structures.....	62
5.1.2	Duplex Structures.....	65
5.1.3	Examining a Variety of Industrial Steel and Iron Fatigue Limits .....	74
5.2	Inherent Regime.....	85
5.3	Processing Regime.....	87
6.	FLAW SIZE AND NUCLEATION MECHANISMS .....	92
6.1	Tempering of Medium Carbon Steel - Garwood et al .....	92
6.2	Tempering & Altering the Fatigue Nucleation Mechanism .....	97
6.2.1	150°C Temper Fatigue Behavior .....	100
6.2.2	315°C Tempered Fatigue Behavior .....	106
6.3	Transgranular vs. Intergranular Nucleation Mechanisms .....	116
6.4	Predicting Scatter in High Strength Steels.....	117

7.	COMPETING FLAWS AND SYNERGISTIC FLAW EFFECTS .....	122
7.1	Historical Surface Finish Studies.....	122
7.2	Surface Finish – Equivalent Notch Approach .....	124
7.3	Surface Finish and Intergranular Crack Nucleation.....	126
7.4	A Hypothesis for the Competition of Surface Finish and Inclusion Defects .....	131
7.5	Surface Finish and Inclusion Competition in 4340 Steel.....	140
7.5.1	Flaw Competition Predictions.....	140
7.5.2	Flaw Competition Results.....	150
7.6	Observations of Critical Surface Roughness .....	163
7.7	Transition from the Inherent Regime to the Intrinsic Regime in Smooth Specimens .....	168
8.	CONCLUSIONS AND RECOMMENDATIONS FOR FUTURE WORK.....	172
8.1	Summary and Conclusions .....	172
8.2	Future Work .....	176
	APPENDICES .....	178
	APPENDIX: A METALLURGICAL DETAILS OF HEAT TREATMENT AND STEELS TESTED BY GARWOOD ET AL.....	178
	APPENDIX: B CLASSICAL EXPERIMENTAL SURFACE FINISH STUDIES.....	180
	APPENDIX C: AUGER ELECTRON SPECTROSCOPY .....	183
	LIST OF REFERENCES .....	187
	VITA.....	200



## LIST OF TABLES

	Page
Table 2.1      Composition of Vacuum Arc-Melted 4340 Plate Steel .....	27
Table 2.2      Composition of Modified 8680 Steel.....	28
Table 3.1      Intrinsic Fatigue Limit of Ferritic Steel – I [45] .....	30
Table 3.2      Intrinsic Fatigue Limit of Ferritic Steel – II [15].....	30
Table 3.3      Fatigue Limit of Various Ferritic-Pearlitic Steels [24,25] .....	31
Table 3.4a     Carburized Steel [47] .....	33
Table 3.4b     Carburized Steel [48-49,51-52] .....	34
Table 3.5      Synergistic Effects of Surface Finish and Intergranular Crack Nucleation - I [53] .....	34
Table 3.6      Synergistic Effects of Surface Finish and Intergranular Crack Nucleation – II .....	36
Table 3.7      Grain Size Refinement Effects in 8680 Steel .....	36
Table 5.1      Intrinsic Fatigue Limit Verification – Radhakrishnan et al [45].....	64
Table 5.2      Ideal Intrinsic Fatigue Limit Verification – Taira et al [15] .....	64
Table 5.3a     Duplex Structure Intrinsic Fatigue Limit Verification I .....	69
Table 5.3b     Duplex Structure Intrinsic Fatigue Limit Verification II.....	69
Table 5.4      Duplex Structure Intrinsic Fatigue Limit Verification III.....	74
Table 5.5      Indirect Verification of Inherent Inclusion Predictions [9].....	85
Table 5.6      Intergranular Crack Nucleation in Carburized 4320 [47] .....	90

Table 6.1	Fatigue Limit of Embrittled 8680 Steel .....	104
Table 6.2a	Effect of Tempering on the Fatigue Limit of 8680 Steel.....	115
Table 6.2b	Predicted Effects of Tempering on the Fatigue Limit of 8680 Steel .....	115
Table 6.3	Effect of Nucleation Mechanism on Fatigue Resistance .....	117
Table 7.1	Synergistic Effects of Surface Finish and Intergranular Cracking - I.....	129
Table 7.2	Synergistic Effects of Surface Finish and Intergranular Cracking – II....	130
Table 7.3	Critical Conditions for Transition of Dominating Flaw .....	134
Table 7.4	Measured and Predicted Flaws in Vacuum Arc-Melted 4340 Steel .....	142
Table 7.5	Predicted Peak-Valley to Inclusion Diameter Ratios in 4340 Vacuum Arc-Melted Steel .....	150

## LIST OF FIGURES

	Page
Figure 1.1    Non-propagating Fatigue Cracks Observed at the Fatigue Limit [1] .....	2
Figure 1.2    Observed Relationship Between Rotating Bending Fatigue Limit and Tensile Strength [4].....	5
Figure 1.3    Kitagawa Diagram: Difference in Threshold Behavior for Long and Short Cracks [7].....	6
Figure 1.4    Observed Relationship Between Non-propagating Crack Size and Grain Size.....	9
Figure 1.5    Kitagawa Diagram: Threshold Models Proposed by Smith and El Haddad [10,11,42].....	10
Figure 1.6    Kitagawa Diagram: Threshold Model Proposed by Tanaka et al [12] .....	11
Figure 1.7    Effect of Inherent Flaw Size on Normalized Threshold Behavior vs. Relative Crack Length [12].....	14
Figure 1.8a    Size Dilemma.....	15
Figure 1.8b    Size Solution .....	15
Figure 1.9    Definition of $\sqrt{\text{area}}$ Parameter.....	17
Figure 1.10    Relationship Between Maximum Stress Intensity of an Arbitrarily Shaped Flaw and the $\sqrt{\text{area}}$ Parameter [8] .....	18
Figure 1.11    Short Crack Threshold Stress Intensity for Ferrous and Non-ferrous Metals with Various Flaw Sizes [8].....	20

Figure 1.12	Normalized Threshold Stress Intensity vs. $\sqrt{\text{area}}$ Parameter [8].....	21
Figure 2.1a	4340 Four-Point Bend Fatigue Specimen.....	26
Figure 2.1b	8680 Four-Point Bend Fatigue Specimen.....	26
Figure 3.1	Relationship Between Fatigue Limit and Hardness as Observed by Garwood et al [54] .....	35
Figure 3.2	Four-Point Bending Fatigue Results of Vacuum Arc-Melted 4340 Steel.....	38
Figure 4.1	General Relationship Between the Fatigue Limit and Hardness .....	40
Figure 4.2	Definition of Three Different Flaw Dominated Fatigue Regimes .....	41
Figure 4.3	Short Crack Threshold Stress Intensity as a Function of Strength and Flaw Size [8].....	43
Figure 4.4	Fatigue Process in Intrinsic Flaw Regime .....	44
Figure 4.5	Convolutd Relationship Between Flaw Size and $K_{th,sc}$ .....	45
Figure 4.6	Fatigue Process in Inherent Flaw Regime .....	46
Figure 4.7	Fatigue Process in the Process Flaw Regime.....	48
Figure 4.8	Determining Whether an Inherent Flaw is Damaging Relative to the Intrinsic Flaw .....	50
Figure 4.9	Observed Variation in Fatigue Life and Fatigue Limit of Cold Drawn Wire [58].....	57
Figure 4.10	Relationship Between Fatigue Limit and Hardness as Observed by Garwood et al [54] .....	58
Figure 5.1	Observed and Predicted Non-propagating Crack Size vs. Hardness .....	66
Figure 5.2	Variation in Fatigue Limits of Pearlitic Steel [24] .....	72

Figure 5.3	Effect of Conventional Annealing Process and Constant Proeutectoid Structure Size on the Fatigue Limit of Ferritic-Pearlitic Steel [24].....	73
Figure 5.4	HPM Model Intrinsic Fatigue Limit Prediction vs. Empirical Relationship .....	76
Figure 5.5	Observed Relationship Between Non-propagating Crack Size and Grain Size.....	77
Figure 5.6	HPM Model Predictions with Non-propagating Crack Sizes vs. Empirical Relationship .....	78
Figure 5.7	Effect of Barrier Strength and NPC Size on the Fatigue Limit: HPM Model vs. Empirical Relationship.....	80
Figure 5.8	Importance of Accounting for Primary Phase Grain Size in Determining Non-propagating Crack Size.....	82
Figure 5.9	Comparison of HPM Model Predictions and Empirical Predictions with Observed Fatigue Limits of Various Low and Intermediate Carbon Steels Reported in the Literature .....	83
Figure 5.10	Comparison of Rotating Bending Fatigue Test Data with $\sqrt{\text{area}}$ Parameter Model Combined with the Statistics of Extremes Inclusion Rating Method of Predicting a Lower Bound Fatigue Limit [9] .....	88
Figure 6.1	Relationship Between Fatigue Limit and Hardness as Observed by Garwood et al [54] .....	93
Figure 6.2	Predicted Fatigue Limits for Microstructure of Garwood's Material .....	95
Figure 6.3	Comparison of HPM Predictions with Fatigue Limits Observed by Garwood.....	96

Figure 6.4	HPM Model Predictions for Various Larger Flaws.....	98
Figure 6.5	Comparison of HPM Model Predictions and Observed Fatigue Limits- Effect of Larger Flaws .....	99
Figure 6.6a	Intergranular Crack Nucleation and Growth in 8680 Triple Vacuum Steel .....	101
Figure 6.6b	Intergranular Crack Nucleation and Growth in 8680 Triple Vacuum Steel: 875X.....	102
Figure 6.6c	Intergranular Crack Nucleation in 8680 Triple Vacuum Steel: 1000X ....	103
Figure 6.7	Observed Fatigue Limit of 8680 Vacuum Heat Treated Steel.....	105
Figure 6.8a	Intergranular Crack Nucleation and Transgranular Growth in 8680 Single Vacuum Steel.....	107
Figure 6.8b	Intergranular Crack Nucleation and Transgranular Growth in 8680 Single Vacuum Steel: 500X.....	108
Figure 6.8c	Intergranular Crack Nucleation and Transgranular Growth in 8680 Single Vacuum Steel: 1400X.....	109
Figure 6.9a	Intergranular Nucleation and Transgranular Growth in Tempered 8680 Triple Vacuum Steel .....	110
Figure 6.9b	Intergranular Nucleation and Transgranular Growth in Tempered 8680 Triple Vacuum Steel : 470X .....	111
Figure 6.9c	Intergranular Nucleation in Tempered 8680 Triple Vacuum Steel: 2800X.....	112
Figure 6.10	Comparison of 8680 Steel Fatigue Limits – Before and After Additional Tempering .....	114

Figure 6.11	Suggested Lower Bound Fatigue Strength for High Strength Steels [4] .....	119
Figure 6.12	Observed Fatigue Limit Scatter in Steels [84] .....	120
Figure 6.13	Comparison of Observed Fatigue Limits and HPM Predictions for Numerous High Strength Steels.....	121
Figure 7.1	Observed Relationship Between Surface Finish and Tensile Strength: Noll & Lipson [85].....	123
Figure 7.2	Equivalent Notch Effects for Surface Finish Flaws.....	125
Figure 7.3	Three-dimensional View of a Ground Surface Finish .....	128
Figure 7.4	Four Possible Conditions of Competing Flaws .....	133
Figure 7.5	Map of Dominant Flaw Regions and Transition Points .....	136
Figure 7.6	Equally Damaging Flaws: No Dominant Flaw.....	138
Figure 7.7	Unequal Flaw Sizes: One Dominant Flaw.....	139
Figure 7.8	Inclusion Distribution in 4340 Steel .....	143
Figure 7.9	Milled 600 Surface Flaw Distribution .....	144
Figure 7.10	Milled 300 Surface Flaw Distribution .....	145
Figure 7.11	Ground Surface Flaw Distribution.....	146
Figure 7.12	Comparison of Flaw Distributions.....	147
Figure 7.13	Vickers Hardness Distribution for Quenched and Tempered 4340 .....	148
Figure 7.14	Predicted Fatigue Behavior of Competing Flaws in 4340 Steel .....	149
Figure 7.15	Observed Fatigue Results of Competing Flaws in 4340 Steel.....	151
Figure 7.16	Comparison of Predicted and Observed Fatigue Behavior of Competing Flaws in 4340 Steel.....	153

Figure 7.17	Subsurface Inclusion Origin in 4340 Steel .....	154
Figure 7.18a	Macroscopic View of Surface Finish Nucleated Fatigue Origin in M600 Group .....	156
Figure 7.18b	Surface Finish Nucleated Fatigue Origin in M600 Group .....	157
Figure 7.19	Predicting the Percentages of Failed Specimens Associated with Two Competing Flaws .....	159
Figure 7.20a	Macroscopic View of Surface Finish Nucleated Fatigue Origin in M300 Group .....	161
Figure 7.20b	Surface Finish Nucleated Fatigue Origin in M300 Group .....	162
Figure 7.21	Siebel & Gaier's Observations of $R_o$ in Tempered and Annealed Steels [86] .....	164
Figure 7.22	Relationship Between Rate of Change of Threshold Stress Intensity Range and Flaw Size for Various Strengths of Materials [8] .....	167
Figure 7.23	Transition from Inherent to Intrinsic Flaw Regime in Two Annealed Carbon Steels .....	170
Figure 8.1	Comparison of HPM Model Predictions and Empirical Predictions to Observed Results of Various Low and Intermediate Strength Steels .....	173
Figure 8.2	Comparison of HPM Model Predictions vs. Observed Fatigue Behavior of Numerous High Strength Steels .....	174
Figure C.1	Derivative Peak Heights for Bulk and Grain Boundary Surfaces .....	184
Figure C.2	Carbon Profile for Grain Boundary .....	186



## NOMENCLATURE

<b>a:</b>	<b>crack length</b>
<b><math>a_0</math>:</b>	<b>fictitious crack length</b>
<b><math>a_i</math>:</b>	<b>inherent defect/crack length</b>
<b><math>a_0'</math>:</b>	<b>fictitious crack length plus inherent crack length</b>
<b><math>\sqrt{\text{area}}</math>:</b>	<b>square root area of a defect/flaw</b>
<b><math>\sqrt{\text{area}_0}</math>:</b>	<b>isolated defect size for a notch</b>
<b><math>\sqrt{\text{area}_R}</math>:</b>	<b>effective defect size due to multiple notch effect</b>
<b>BSB:</b>	<b>blocked slip band model, Tanaka et al</b>
<b>d:</b>	<b>grain diameter</b>
<b>D:</b>	<b>inclusion diameter</b>
<b>F:</b>	<b>geometry factor for stress intensity</b>
<b><math>H_v</math>:</b>	<b>Vicker's hardness (<math>\text{kg/mm}^2</math>)</b>
<b>HPM:</b>	<b>Hall-Petch-Murakami model</b>
<b><math>K_t</math>:</b>	<b>theoretical stress concentration factor</b>
<b><math>\Delta K_{th}</math>:</b>	<b>linear elastic fracture mechanics threshold stress intensity range</b>
<b><math>\Delta K_{th,lc}</math>:</b>	<b>long crack threshold stress intensity range</b>
<b><math>\Delta K_{th,sc}</math>:</b>	<b>short crack threshold stress intensity range</b>
<b><math>l_0</math>:</b>	<b>crack length where LEFM threshold prediction and the polished fatigue limit intersect in the Kitagawa diagram</b>

$l_2$ :	<b>minimum crack length where LEFM is applicable as seen in a Kitagawa diagram</b>
<b>LEFM:</b>	<b>linear elastic fracture mechanics</b>
<b>N:</b>	<b>number of specimens for statistical measure of defect size</b>
<b>NPC :</b>	<b>non-propagating crack</b>
<b>PV:</b>	<b>peak-valley measure from profilometer trace</b>
<b>PV/D:</b>	<b>ratio of peak-valley depth to inclusion diameter</b>
$R_o$ :	<b>critical roughness depth</b>
$\sigma_o$ :	<b>fatigue limit of single notched material</b>
$\sigma_R$ :	<b>fatigue limit of multiple notched material</b>
$\sigma_y$ :	<b>monotonic yield strength</b>
$\sigma_u$ :	<b>ultimate tensile strength</b>
$\sigma_w$ :	<b>fully reversed fatigue limit</b>
$\sigma_R / \sigma_o$ :	<b>ratio of multiple notch to single notch fatigue limit</b>
$\Delta\sigma_{w0}$ :	<b>fatigue limit of a polished (smooth) specimen</b>
$\Delta\sigma_{w0}'$ :	<b>polished specimen fatigue limit of inherently flawed material</b>

## CHAPTER 1

### INTRODUCTION

Despite the observations of Ewing and Humfrey [1] in 1903 and Forsyth [2] in 1963, the fatigue limit has historically been considered as the stress at which cracks do not form in a material under repeated loading. They observed that the fatigue limit is actually the stress at which a crack may form and propagate for a finite length but arrest due to the presence of a barrier, hence the term non-propagating crack (NPC). A picture of several non-propagating cracks blocked by grain boundaries as observed by Ewing and Humfrey is presented in figure 1.1. The simplest scenario is a material consisting of a single-phase equiaxed grain structure. Upon cycling, dislocations move due to local shear stresses and pile up at the nearest barriers, grain boundaries. If the stress ahead of the pile-up and the applied stress are just large enough, slip occurs across the barrier and the crack will propagate to failure. However, if the combined driving force is slightly lower than the former condition, the crack will arrest. The modern view of the fatigue limit embraces this concept; in fact, numerous models attempt to predict this physical phenomenon.

Of course, most materials in industry are much more complicated in structure and consist of multiple phases with various shapes, sizes, connectivity, spacing, and distributions of the constituents. Some of these phases are additional barriers to crack propagation, i.e. finely dispersed hard second phases. Others actually facilitate the nucleation and growth of cracks, i.e. intergranular crack nucleation and growth due to



Figure 1.1 Non-propagating Fatigue Cracks Observed at the Fatigue Limit [1]

large carbides at phase/grain boundaries. This makes the application of any model based on the idealized equiaxed single-phase structure too simplistic to predict the material behavior. Consequently, this has forced the development and use of empirically based and often vague models for assessing the influence of surface finish, inclusions, etc. Although necessary at the time of their development, these approaches have and continue to hinder the understanding and modeling of the underlying mechanisms that govern material behavior.

## 1.1 Literature Review

The most common empirically based models for predicting the fully reversed fatigue limit of low and intermediate strength steels are given in equations 1.1 and 1.2 as

$$\sigma_w = 1.6 H_v + / - 0.1 H_v \quad (1.1)$$

$$\begin{aligned} \sigma_w &= 0.5 \sigma_u + / - 0.1 \sigma_u \text{ or equivalently} \\ &\approx 1.55 H_v + / - 0.31 H_v \end{aligned} \quad (1.2)$$

Equation 1.1 was reported by Murakami [3]. Equation 1.2 is given in most text books on fatigue and can be expressed in terms of the ultimate strength or hardness. Murakami's empirical relation has a smaller error band than that of equation 1.2. This is because Murakami's relationship was derived from a small set of carbon steels whereas the relationship in equation 1.2 was fit with data consisting of carbon steels, low-alloy steels, gray cast iron, nodular cast iron, and wrought iron. Application of both models is

restricted to steels with ultimate tensile strengths less than 1400 MPa as illustrated in figure 1.2 [4]. The restriction is due to the sensitivity of the high strength steel to flaws and a change in the active fatigue mechanisms for high strength steels. Other empirically based approaches by Peterson and Neuber [5] are still used in industry to account for notch sensitivity. Similarly, Mitchell [6] developed a more elaborate fatigue notch factor model to account for various flaws sizes and matrix strengths in cast and wrought ferrous metals.

Predicting the fatigue limit with conventional LEFM is further complicated by the fact that the threshold stress intensity range,  $\Delta K_{th}$ , decreases for short cracks as characterized by Kitagawa and Takahashi [7] and illustrated in figure 1.3. The breakdown of LEFM for cracks whose lengths are on the order of several grains arises from the non-continuum (microstructural) effects on crack tip plasticity. In addition, the conventional definition of a crack is that of an idealized one dimensional slender sharp crack; whereas the modern view of a crack includes two and three-dimensional flaws that may not necessarily be crack-like in shape, i.e. inclusions, pores, oxides, grain boundaries, secondary phases, and slip bands [8,9]. Furthermore, different mechanisms often operate during the growth and threshold conditions for short and long cracks. Short cracks have limited or no plasticity in the wake of the crack and any elastic anisotropy can be significant; long cracks may have significant closure while the anisotropy effects are typically averaged out. Inclusions, carbides, and weak interfaces between phases or grain boundaries may activate microcracking ahead of the main long crack. This mechanism may not be as prominent in the case of short cracks because the elevated

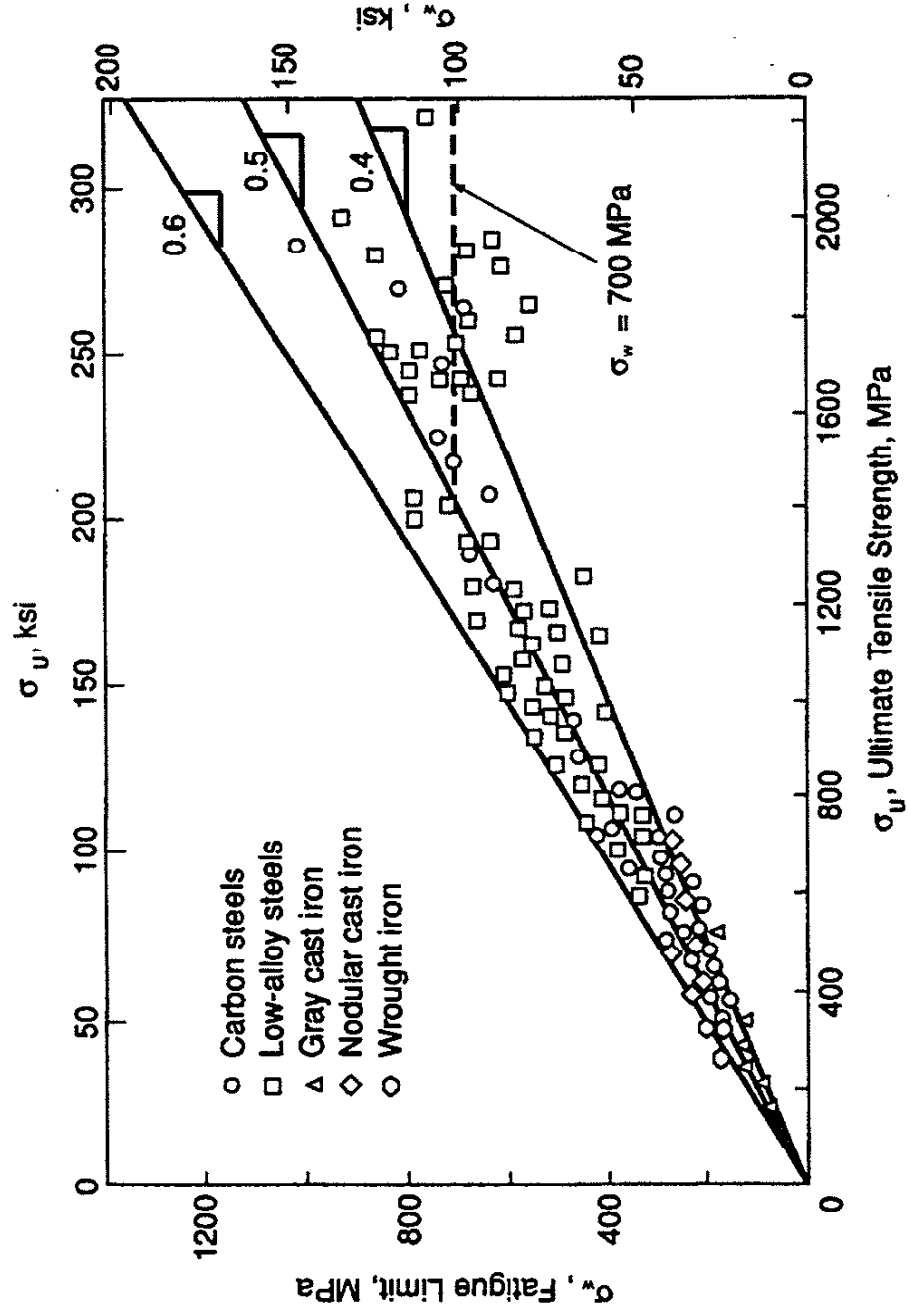


Figure 1.2 Observed Relationship Between Rotating Bending Fatigue Limit and Tensile Strength [4]

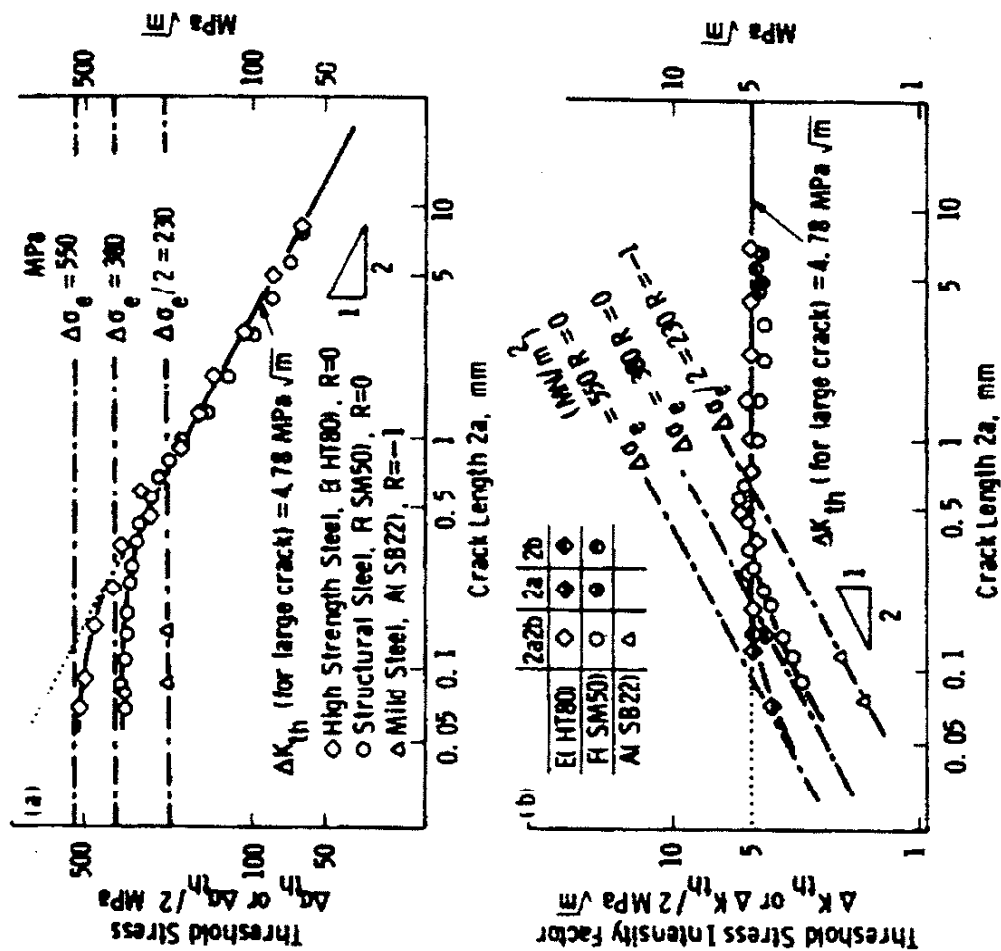


Figure 1.3 Kitagawa Diagram: Difference in Threshold Behavior for Long and Short Cracks [7]



stress field associated with the crack tip is limited to one grain size or one microstructural unit.

Although the long crack threshold,  $\Delta K_{th,lc}$ , is observed to decrease with strength engineers often overlook the fact that the short crack threshold,  $\Delta K_{th,sc}$ , increases with strength as shown in figure 1.3 [8]. Researchers have acknowledged these differences but the complexity of modeling the physics has resulted in the development of simplistic short crack models. Typically,  $\Delta K_{th}$  is assumed to be a constant and equal to  $\Delta K_{th,lc}$  with some corrective means to account for an increase in the allowable stress,  $\Delta \sigma_{th}$ , as the crack size decreases [10-12]. Much work has been conducted in the last twenty to thirty years to address the problems associated with the complexity of short crack behavior. The focus of such studies is on incorporating the mechanisms of crack growth into fatigue models. These concepts include the development of robust micromechanically based nucleation, short crack growth, and short crack threshold models for both uniaxial and multiaxial fatigue [8-23]. In addition, some researchers have begun valuable observations and measurements of the NPC [24-26].

Few studies of the NPC have been conducted. These limited studies have revealed that the NPC is considerably larger than the average grain size, mean second phase spacing, or other measure of metallurgical length scale. Kunio et al [24,25] observed this behavior in ferritic-pearlitic steels containing volume fractions of pearlite from 45-71% where cracks were observed to arrest at pearlite colonies. Tokaji et al [26] also observed NPCs of the same order in a fine and coarse grained low carbon steel

where ferrite grain boundaries served as crack barriers since the volume fraction of pearlite was very small. Figure 1.4 illustrates that the ratio of the NPC to the mean ferrite grain size of the aforementioned investigations varies but is on the order of ten. Although the role of the NPC size in the fatigue limit of materials is crucial, neither a qualitative nor a quantitative understanding of its relationship to microstructure has been proposed.

The models by Smith [10], El Haddad [11], Tanaka [12], and Murakami [8] are some of the most popular fracture mechanics based models used to predicting short crack thresholds in uniaxial fatigue. They vary in their degree of success and ease of use. A brief review of these is provided since an understanding of their strengths and limitations is essential in understanding the importance of physically based models and the unsolved problem, the linking of threshold models to the microstructure and the NPC.

Smith's model, shown in figure 1.5, is the simplest of the models. The allowable stress is predicted based on LEFM and  $\Delta K_{th,lc}$  until the intersection with the fatigue limit of the polished specimen,  $\Delta\sigma_{wo}$ . Fatigue mechanisms are not considered in the model; the method is known to be restricted to high strength materials that contain flaws large enough so that the restrictions regarding LEFM are satisfied.

Lower strength materials deviate from Smith's predictions as illustrated in figures 1.5 and 1.6. A fictitious crack length is implemented in the model proposed by El Haddad [11] so that predictions follow this experimentally observed behavior. They

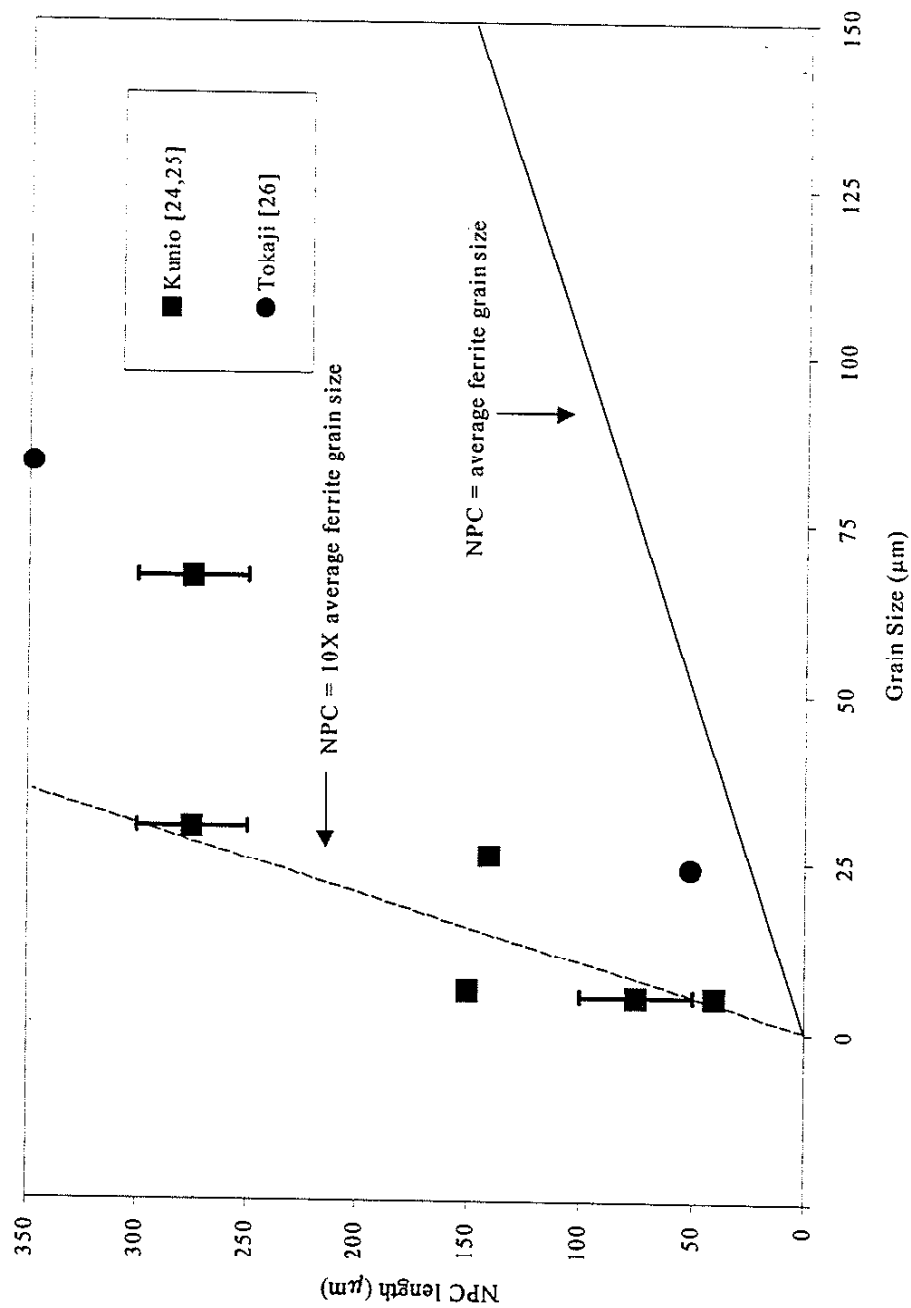


Figure 1.4 Observed Relationship Between Non-propagating Crack Size and Grain Size

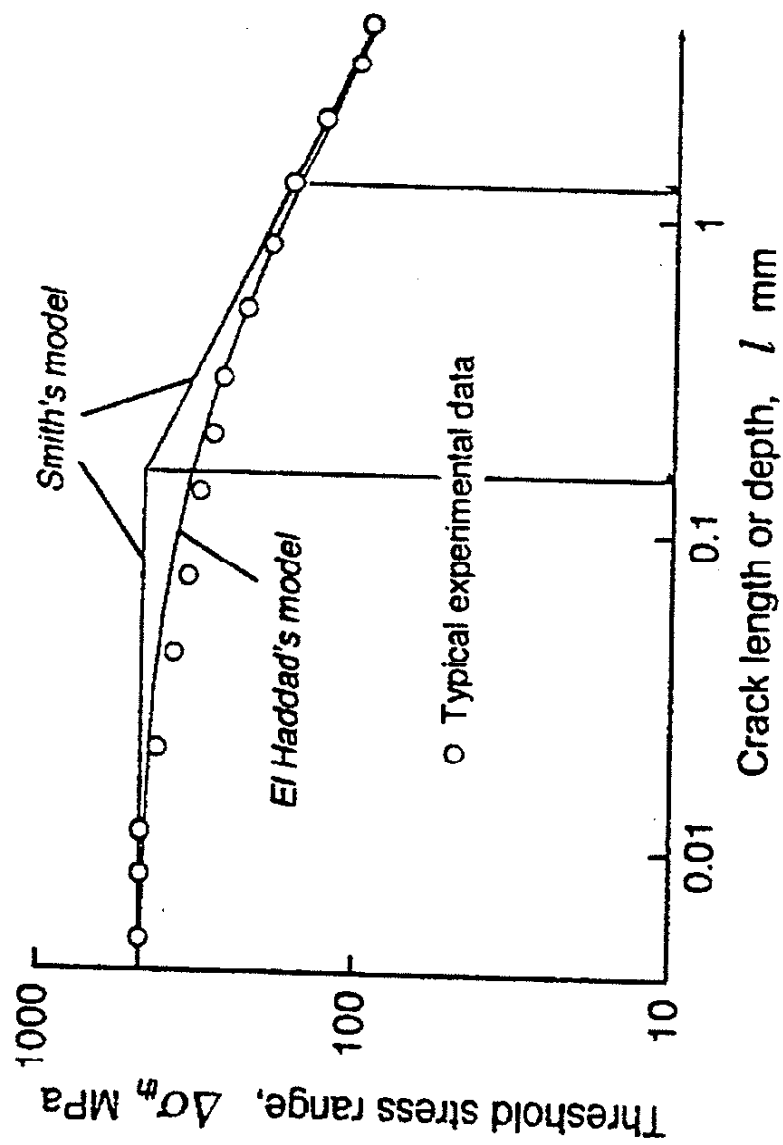


Figure 1.5 Kitagawa Diagram: Threshold Models Proposed by Smith and El Haddad [10,11,42]

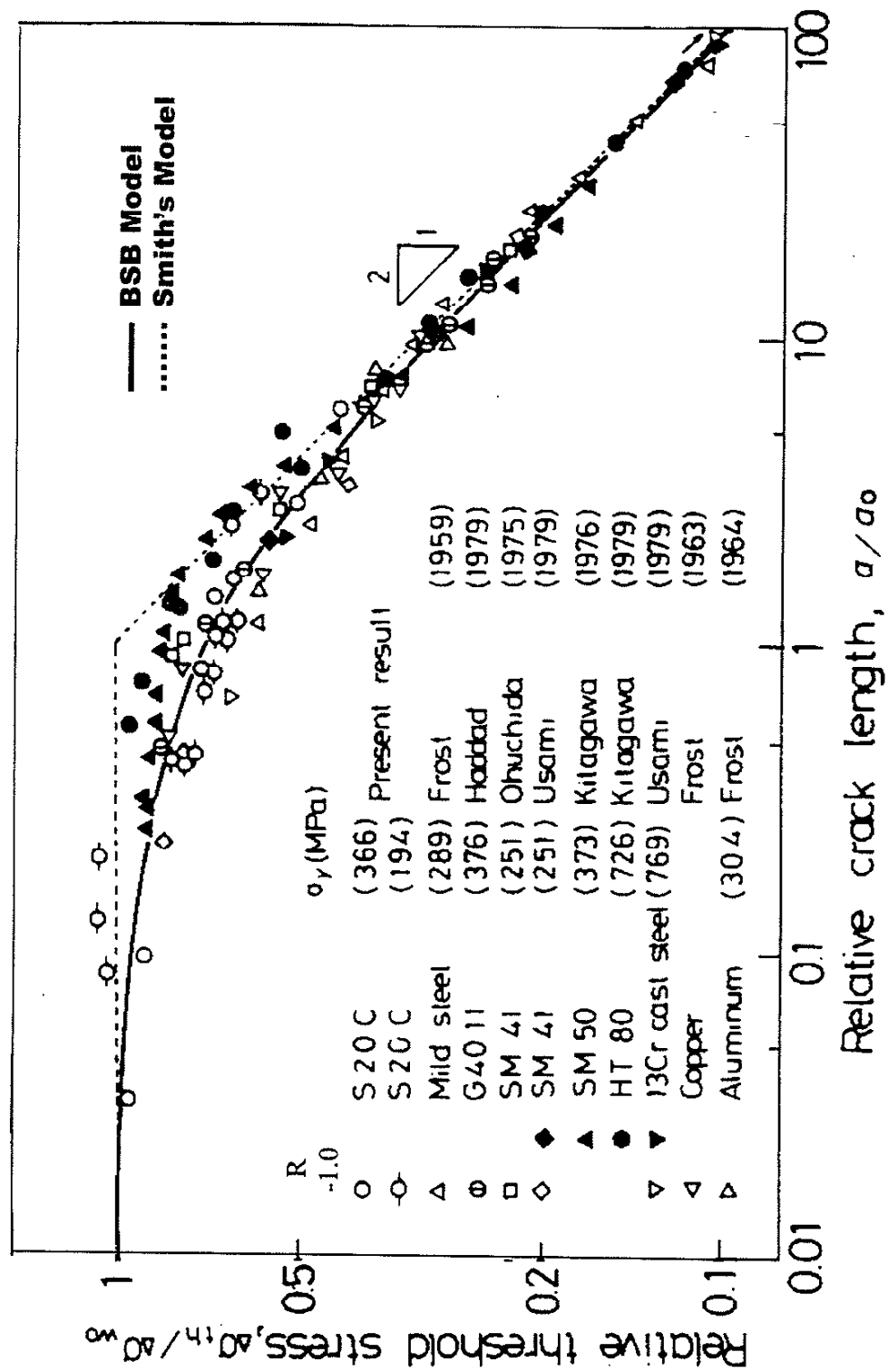


Figure 1.6 Kitagawa Diagram: Threshold Model Proposed by Tanaka et al [12]

assume that the threshold stress intensity range is a constant and equal to  $\Delta K_{th,lc}$ . However, the crack length is modified by the fictitious crack length  $a_o$  given as,

$$a_o = \left( \frac{\Delta K_{th,lc}}{\Delta \sigma_{w0}} \right)^2 \pi \quad (1.3)$$

and the allowable stress range is given as

$$\Delta \sigma_{th} = \Delta \sigma_{w0} [a_o / (a + a_o)]^{1/2} \quad (1.4)$$

Although successful in predicting many experimental observations, the physical meaning of  $a_o$  is vague, and the model does not address crack closure which is now known to contribute (although not entirely responsible) to differences in short and long crack thresholds.

A more robust model proposed by Tanaka et al [12] addresses the mechanisms of short crack growth. The simplest scenario, the situation of a grain boundary blocking a slip band or crack-tip, is modeled. Accordingly, the model is called the blocked slip band (BSB) model. El Haddad's and several critical plastic zone size models are shown to be special cases of the BSB model. Figure 1.6 illustrates the relative threshold stress relationship with the relative crack length for eleven materials. Notice that a log-log scale is used; what may appear to be only a slight difference between behavior of two different materials must be carefully considered because even a large percent difference can appear small on a log-log graph. For instance, the S20C materials generally follow

the gradual decrease in allowable stress with crack length as predicted by El Haddad, cases where materials contain inherent flaws smaller than the intrinsic microstructure size. On the contrary, both the SM50 and HT80 materials exhibit behavior similar to that predicted by Smith, materials with flaws larger than the intrinsic microstructure size. The BSB model can, at least qualitatively, account for these variations in material behavior when the fictitious crack length includes the inherent flaw crack length  $a_i$  as illustrated in figure 1.7. Total crack length is expressed as,

$$a_o' = a_o + a_i . \quad (1.5)$$

Allowable stress is then predicted with the fatigue limit of the polished but flawed material by,

$$\Delta\sigma_{th} = \Delta\sigma_{\infty} \left[ a_o' / (a + a_o) \right]^{1/2} . \quad (1.6)$$

Note, as  $a_i / a_o'$  increases from 0 to 1 the relation shifts from a curve representative of materials with relatively nondetrimental flaws, typically low strength materials, to that of detrimentally flawed materials, typically high strength materials. The BSB model can also incorporate the effect of crack closure.

A more recent mechanics based approach that accounts for small flaws of arbitrary shape and size has been proposed by Murakami [8-9,27-42]. The concept can readily be explained by considering the simple problem of a plate with a central hole as

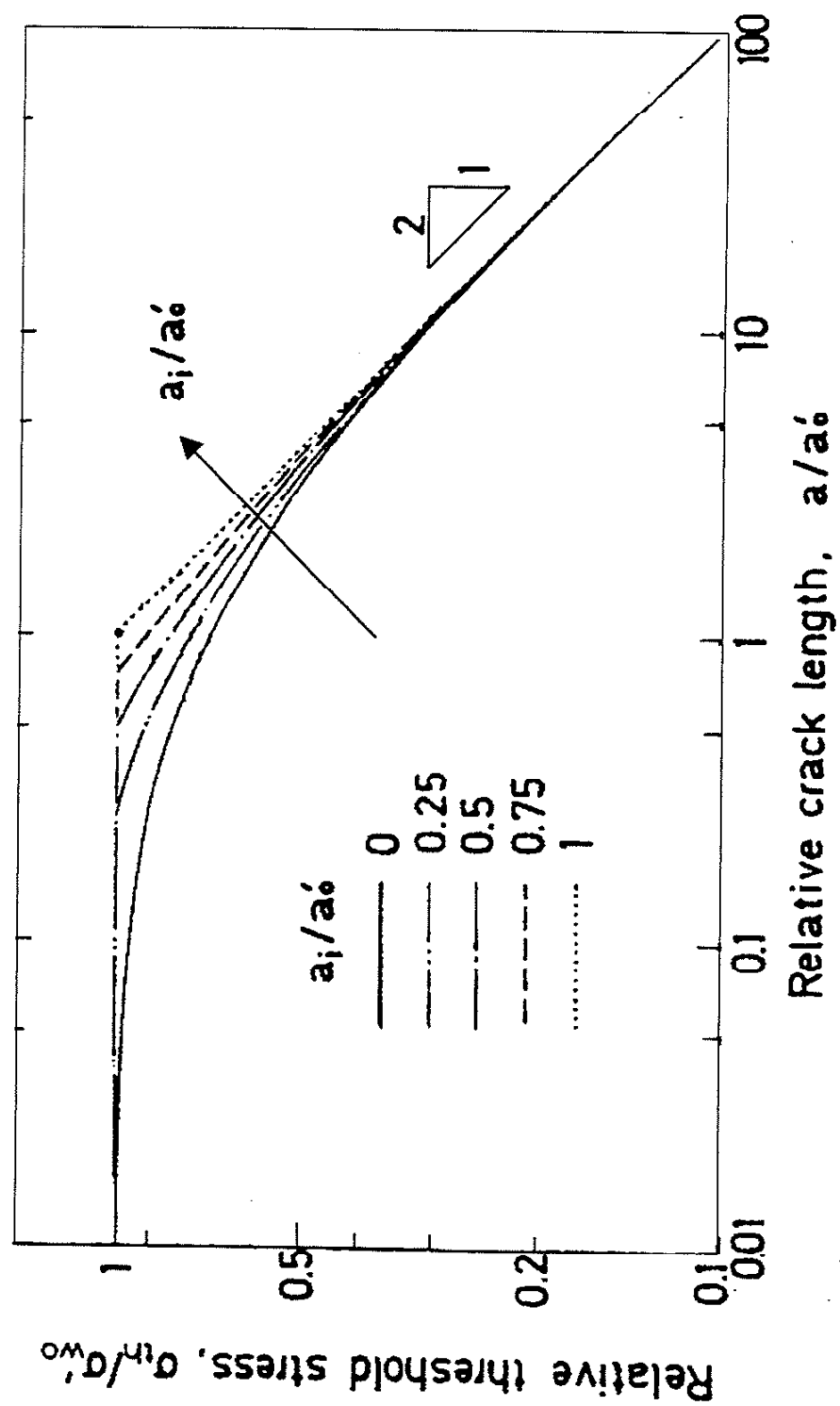


Figure 1.7 Effect of Inherent Flaw Size on Normalized Threshold Behavior vs. Relative Crack Length [12]



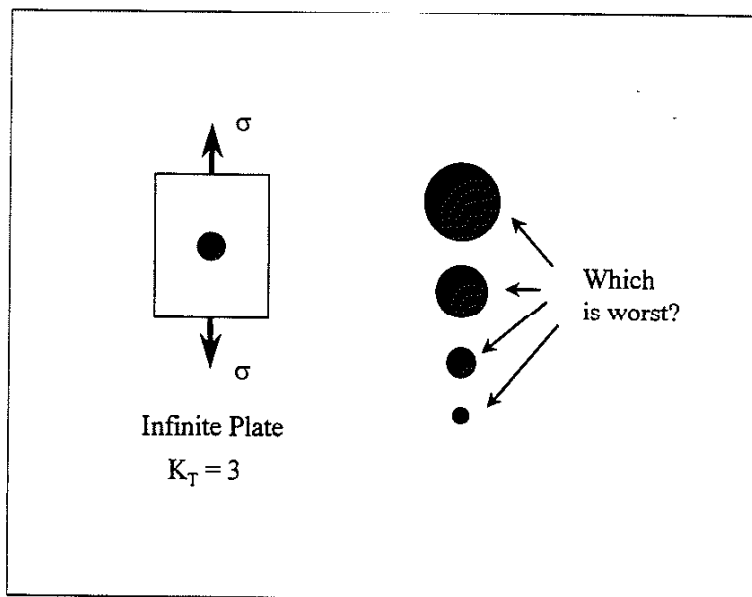


Figure 1.8a Size Dilemma

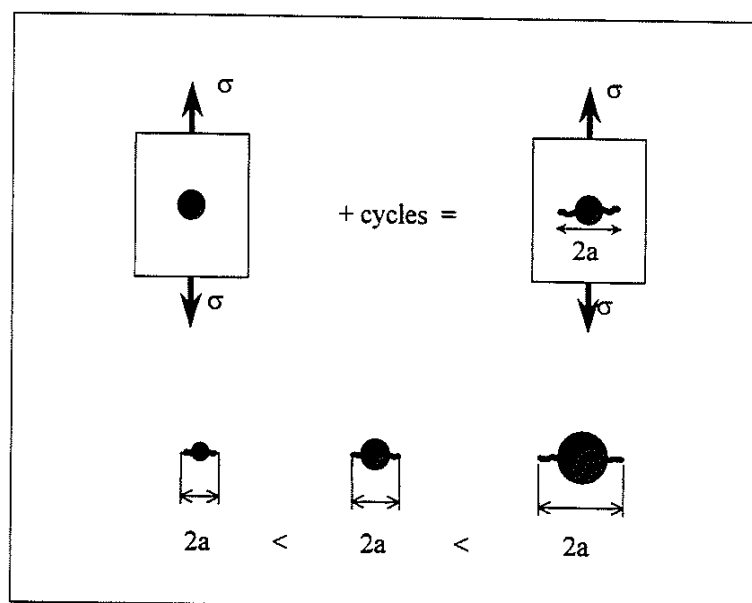


Figure 1.8b Size Solution

seen in figure 1.8a. Which case is the worst, the smallest or largest hole? Size is a dilemma since the theoretical stress concentration factor ( $K_t$ ) is equal for any hole size. As illustrated in figure 1.8b, the answer lies in addressing the real problem where upon cyclic loading cracks nucleate from the stress concentrator. The fatigue limit is governed by whether or not the cracks can propagate, not nucleate. This problem can be solved by considering the effect of the hole diameter and notch radius on the local stress field in the region where the crack nucleates as proposed by Miller et al [43,44]. Simply put, the larger hole is more damaging because the actual crack length includes the notch itself. Thus, size is also the answer.

Murakami investigated whether this concept could be applied to small flaws or holes whose size is on the order of small cracks. Tiny holes, 50-500 $\mu\text{m}$  in diameter, were drilled into the surface of specimens and the allowable stress was determined. The allowable stress was observed to increase with a decrease in hole size until a critical hole size was reached where any further reduction in hole size did not affect the allowable stress. Conventional fracture mechanics could not predict this observation. Consequently, Murakami and colleagues [27-30] employed the body force method and developed a means of quantifying the effects of the size of a flaw of arbitrary shape and size on the maximum stress intensity. Figures 1.9 and 1.10 illustrate that the maximum stress intensity can be predicted within 10% by the  $\sqrt{\text{area}}$  parameter, the square root of the area of the flaw projected onto the plane normal to the maximum tensile stress direction.

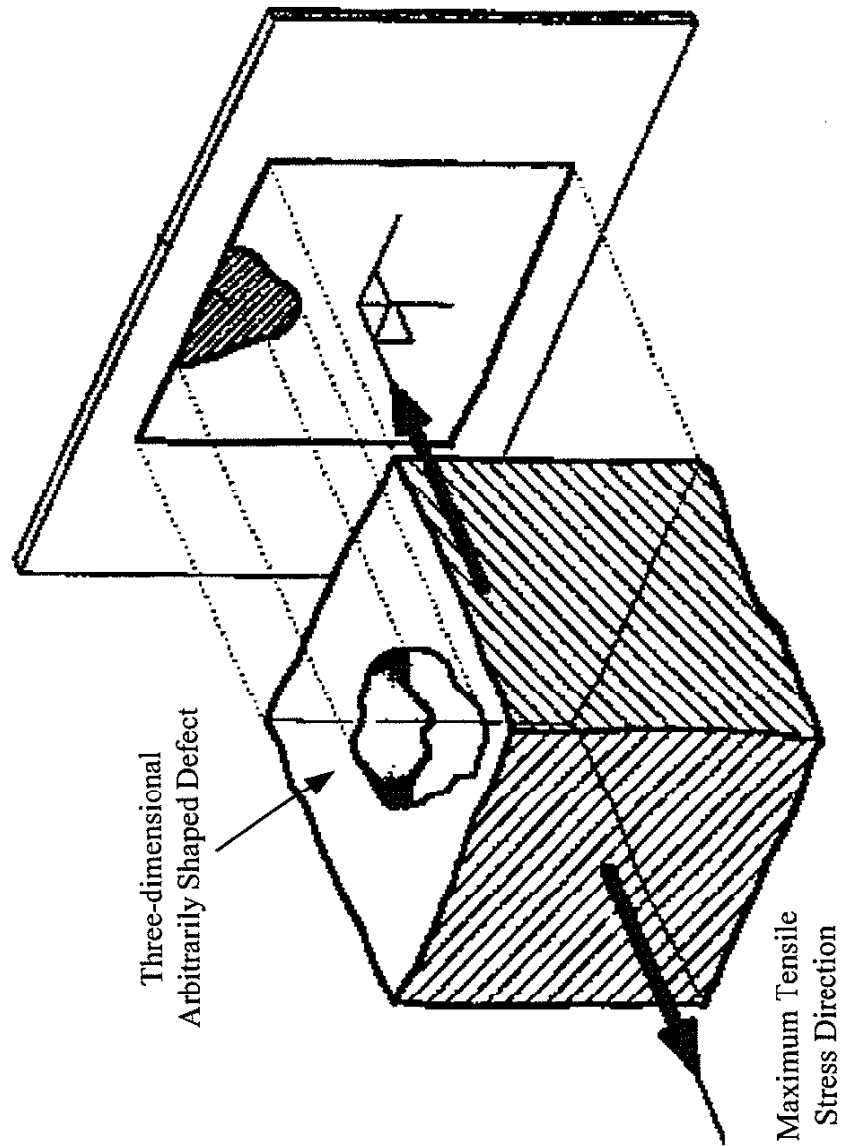


Figure 1.9 Definition of  $\sqrt{\text{area}}$  Parameter

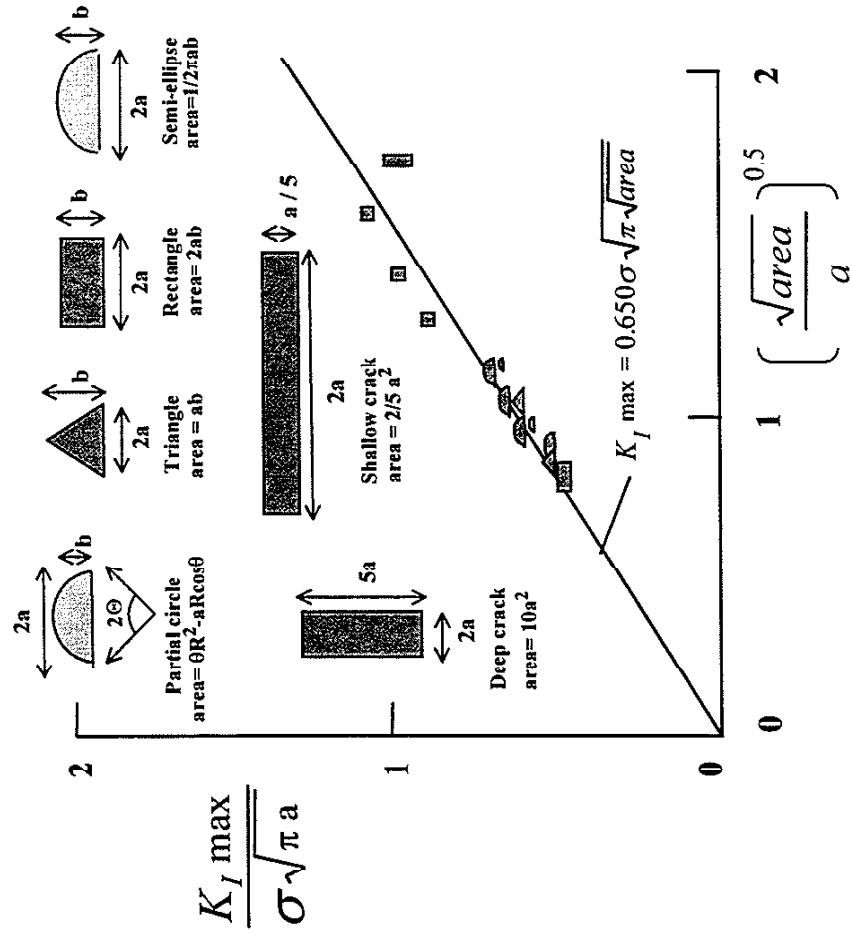


Figure 1.10 Relationship Between Maximum Stress Intensity of an Arbitrarily Shaped Defect and the Area Parameter [8]

The  $\sqrt{area}$  parameter was applied to a series of tests on many ferrous and non-ferrous metals containing both artificial and natural flaws. Materials tested included low, medium, and high carbon steels, aluminum, brass, copper, stainless steel, and maraging steel. Various heat treatment processes were applied including annealed, tempered, as quenched, quenched and tempered, and several aging processes. Results are summarized in figure 1.11. Three important points are immediately observed: (1) a simple relationship exists between  $\Delta K_{th,sc}$  and the  $\sqrt{area}$  parameter, (2) this relationship holds for all the metals tested, and (3) the allowable threshold increases with hardness. The role of barrier strength (hardness) is revealed when the results are normalized with respect to strength as illustrated in figure 1.12.  $\Delta K_{th,sc}$  or equivalently the fatigue limit is predicted without any testing within 10% with only the knowledge of the material hardness and the area of the flaw as given by,

$$\Delta K_{th,sc} = 3.33 \times 10^{-3} (H_v + 120) (\sqrt{area})^{1/3}, \quad (1.7)$$

or in terms of applied stress,

$$\Delta \sigma = \frac{1.43 (H_v + 120)}{\sqrt{area}^{1/6}}. \quad (1.8)$$

A means of accounting for mean stress effects is given as,

$$\Delta \sigma = \frac{1.43 (H_v + 120)}{\sqrt{area}^{1/6}} \left( \frac{1 - R}{2} \right)^{0.226 + H_v \times 10^{-4}}, \quad (1.9)$$

with units,  
 $\Delta K_{th,sc}$  (MPa - m<sup>1/2</sup>),  $\Delta \sigma$  (MPa),  $\sqrt{area}$  ( $\mu\text{m}$ ),  $H_v$  (kg/mm<sup>2</sup>),

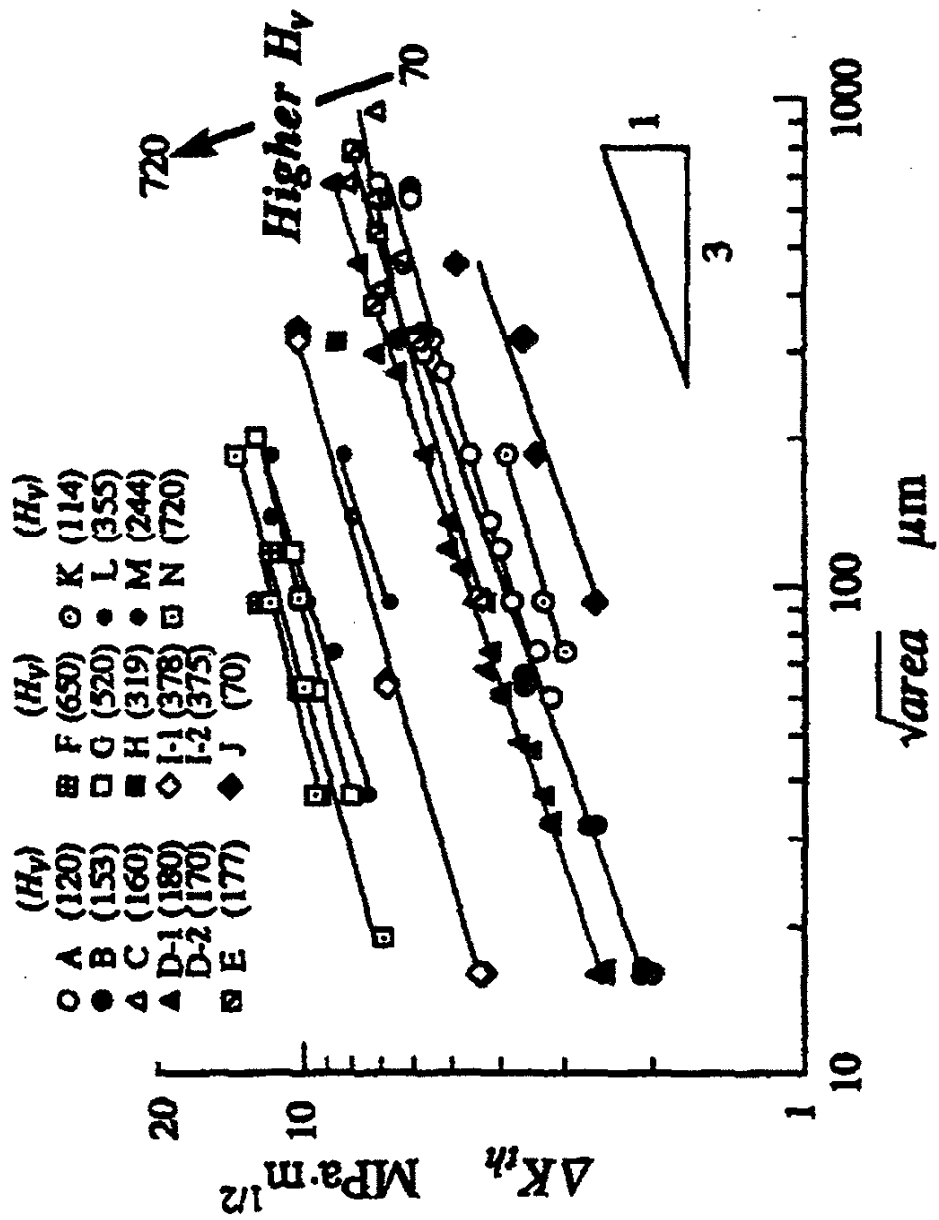
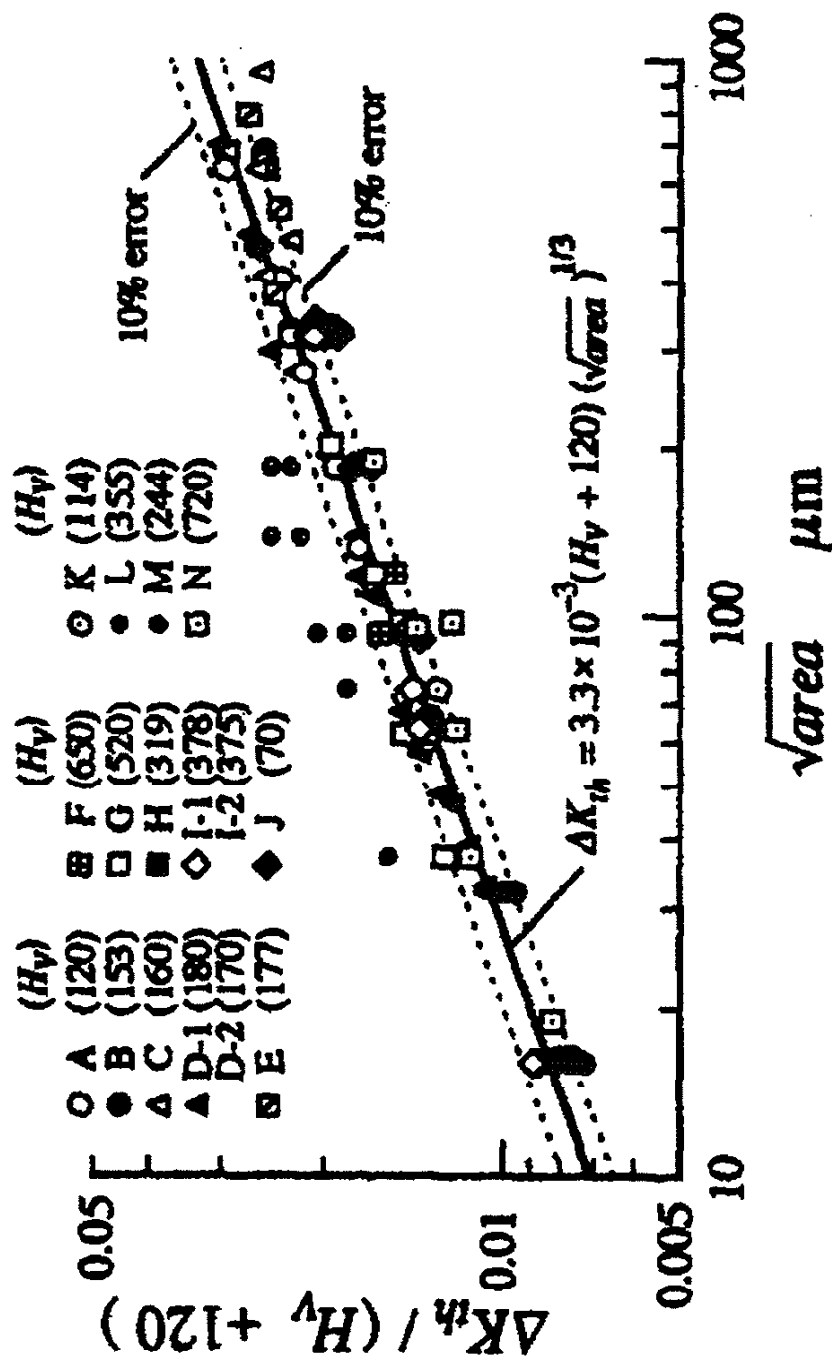


Figure 1.11 Short Crack Threshold Stress Intensity for Ferrous and Non-ferrous Metals with Various Flaw Sizes [8]

Figure 1.12 Normalized Threshold Stress Intensity vs.  $\sqrt{area}$  Parameter [8]

and has proven to be successful in many industrial applications, especially when applied with a statistical means of quantifying the maximum size flaw likely to be found in the material [31-41]. Thus, the  $\sqrt{\text{area}}$  approach is analogous to that of Miller's approach in that the effect of the flaw or notch on the local stress field and crack tip stress intensity is quantified in a simple and useful manner for engineering applications.

## 1.2 Purpose and Scope

What remains to be solved is a means of linking the allowable stress or threshold stress intensity to the basic microstructural unit, the objective of this study. The solution would provide industry with a tool to qualitatively and quantitatively predict the effects of crack nucleation mechanisms (transgranular vs. intergranular), surface finish, inclusions, heat treating processes, steel making processes, residual stresses, and any combination of these factors on the fatigue strength of metals. In addition, the true upper limit of the fatigue strength of a material would be defined and better understood. This would allow designers to optimize the cost and performance of engineering components by proper design, selection, and processing of materials. The strength of the proposed model lies in the fact that it is simple, does not rely upon empirically based models, lends itself to applications involving design reliability, and most importantly defines and outlines the competing roles of the size of flaws and microstructure. This is achieved by a simple combination of the Hall-Petch relationship, Murakami's  $\sqrt{\text{area}}$  parameter model, and the classic punch problem, hereafter referred to as the HPM model.



This thesis has been organized with the intent to emphasize the simplistic and robust nature of the proposed modeling concept. Chapter 2 reports the experimental program and testing procedures including details regarding the materials tested and the manufacturing of specimens. Results are presented in two sections in chapter 3, one for results that were found in the literature and analyzed with the proposed model and another for the tests conducted in this thesis. The data set as a whole includes fatigue limits for over 55 materials, more than 40 were taken from the literature while 15 were obtained in this study. Materials have been classified into subsets according to microstructure, e.g. ferritic steels, ferritic-pearlitic steels, martensitic steels, and martensitic-bainitic steels. Formulation of the proposed model is addressed in Chapter 4 where observed fatigue behavior is divided into three regimes, and each regime is shown to be associated with a different flaw type. Qualitative and quantitative evidence to support the concept is presented in Chapter 5. Chapters 6 and 7 expand upon implementation of the HPM model to industrial problems and the direction of material research and design. In chapter 6 certain types of flaws, defined as processing flaws in this paper, are ascertained to be prominent in high strength steels thus limiting their fatigue strength. These processing flaws are typically associated with different nucleation mechanisms than in lower strength materials. Tempering is proven as a means of limiting their effects and reestablishing the material's fatigue resistance by altering the fatigue threshold mechanism. Three important concepts are addressed in chapter 7: competition between two flaws that have distinctly different shapes and variable size,

synergistic effects of interacting flaws, and the role of inclusions and naturally occurring non-propagating cracks in the transition from one flaw regime to another.

Certain details associated with the microstructure of materials are critical in obtaining a complete understanding of the problem at hand. However, these details can often detract from the overall methodology and value of the proposed model. Therefore, additional information has occasionally been placed in the appendixes. Although these details are important and relevant to understanding the observed material behavior, it is suggested that they be read after the main text.

## **CHAPTER 2**

### **EXPERIMENTAL PROGRAM**

#### **2.1 Testing Equipment and Procedure**

All tests in this study were conducted with the following testing conditions. Four point bending fatigue tests were performed with a load ratio of 0.1 in three different hydraulic testing machines. Test frequencies used were 10 and 50 Hz. Errors associated with the test frequencies were examined. A test specimen was gauged and loaded to the maximum stress range used in this study at 1, 10, 50, and 100 Hz. The measured errors relative to the 1 Hz measurements were less than 1% at 10 Hz and 50 Hz. At 100 Hz the error was greater than 1%; thus, test frequencies were limited to 50 Hz. Run-out was defined as  $2 \times 10^6$  cycles based on preliminary tests and observations.

#### **2.2 Materials**

##### **2.2.1 4340 Vacuum Arc-Melted Steel**

Material was provided in plate form with dimensions of  $305 \times 305 \times 19 \text{ mm}^3$ . The chemistry is provided in table 2.1. Rectangular beam specimens were cut out of the plate with the longitudinal axis in the direction of rolling; material was fully annealed prior to the machining. Specimen dimensions are illustrated in figure 2.1a. Polished specimens

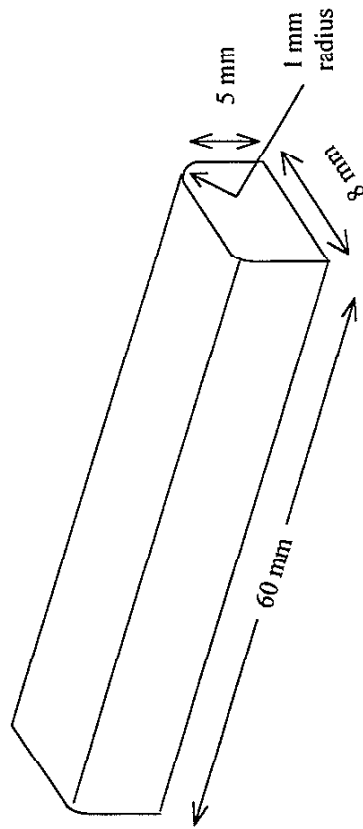


Figure 2.1a 4340 Four-Point Bend Fatigue Specimen

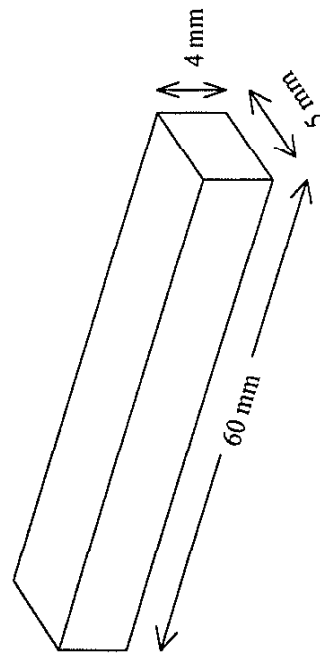


Figure 2.1b 8680 Four-Point Bend Fatigue Specimen

were made by grinding with 240, 320, and 600 grit paper followed by polishing with 6  $\mu\text{m}$  and 0.05  $\mu\text{m}$  diamond particles. Milled surface finishes were generated over a previously ground surface with an indexable carbide face milling cutter in a vertical mill. A 75mm diameter cutter was used which left a finish with large sweeping arc grooves, closely representing the parallel grooves left in surface ground finishes. Cuts were made with several spindle speeds and feed rates to determine the parameters required to generate the desired surfaces. Depth of cut was approximately 50  $\mu\text{m}$ . Two different spindle speeds were used, nominally 600 and 300 RPM for the M600 and M300 groups respectively. Feed rates were 50 mm/min for the M600 and 100 mm/min for the M300. The rough ground surface was achieved by gouging a coarse grinding wheel and using a high feed rate. Heat treating consisted of austenitizing at 850°C for 1 hour, quenching in agitated oil, and tempering for one hour at 150°C.

Table 2.1 Composition of Vacuum Arc-Melted 4340 Plate Steel

4340 Steel <sup>†</sup>	C	Mn	P	S	Si	Ni	Cr	Mn	Cu	Al	B	Zr	V	O	N
	0.42	0.65	0.011	0.004	0.25	1.76	0.76	0.24	0.13	0.019	0.0007	0.01	0.06	9	107

<sup>†</sup> (wt%. O, N in ppm)

### 2.2.2 Modified 8680 Vacuum-Induction-Melt Steel

This material was an experimental heat that was vacuum-induction-melted and poured into a 50 lb. ingot mold. Hereafter, the heat is referred to as a modified 8680 steel; the steel composition is listed in table 2.2. Ingots were reheated to 1230°C and rolled to a 43x43 mm<sup>2</sup> bar; no annealing was required before machining. Rectangular

beam specimens were wire EDM from the bar stock and ground to dimensions as illustrated in figure 2.1b. Polished specimens were made by grinding with 240, 320, and 600 grit paper followed by polishing with 6  $\mu\text{m}$  and 0.05  $\mu\text{m}$  diamond particles. Ground surfaces were generated by intentionally gouging a standard coarse grinding wheel (36H) on a surface grinding machine. Specimens were austenitized in vacuum at 850°C for one hour, quenched in agitated oil, and tempered for one hour at 150°C. Subsequent heat treating cycles for reheat specimens were identical to the first cycle. Additional tempering for the tempered lot was conducted in air at 315°C for one hour.

Table 2.2 Composition of Modified 8680 Steel

Modified	C	Mn	P	S	Si	Ni	Cr	Mo	Cu	O	N
8680 <sup>†</sup>	0.79	0.38	0.010	0.010	0.003	0.10	<0.002	0.30	0.008	0.046	0.001

<sup>†</sup> (wt%)

## CHAPTER 3

### RESULTS

Seemingly endless amounts of fatigue data can be found in the literature. However, only a few percent of the studies include detailed observations and documentation of material properties and microstructure that are necessary for this study. Fortunately, most of the data necessary to validate the HPM model does lie in the small handful of well-documented studies. Materials investigated include a broad range of steels which can be grouped into the following categories: ferritic steels, ferritic-pearlitic steels, martensitic steels, and martensitic-bainitic steels. Literature data was used extensively in this study whenever possible. However, several sets of experiments were conducted to generate data necessary in illustrating several key concepts for which data was not found in the literature.

### 3.1 Literature Data

#### 3.1.1 Ferritic Steels

Two sets of data on the fatigue limit of ferritic steel were found in the literature. Radhakrishnan and Mutoh [45], conducted tests on a 0.10%C steel with an R-ratio of 0.1. Taira et al [15] conducted fatigue tests on a 0.20%C steel with an R-ratio of  $-1$ . These data were selected for comparison with the HPM model because 1) the steels represented

an ideal equiaxed single-phase ferritic steel microstructure, and 2) a total of six different grain sizes were reported. Results are listed in tables 3.1 and 3.2.

Table 3.1 Intrinsic Fatigue Limit of Ferritic Steel – I [45]

d ( $\mu\text{m}$ )	$\sigma_y$ (MPa)	Observed Fatigue Limit (MPa)
18	240	175
27	210	162
44	190	149

Radihakrishnan & Mutoh, R=0.1

Table 3.2 Intrinsic Fatigue Limit of Ferritic Steel – II [15]

d ( $\mu\text{m}$ )	$\sigma_y$ (MPa)	Observed Fatigue Limit (MPa)
7.8	366	235
20.5	275	178
55	194	163

Taira et al, R=-1

### 3.1.2 Ferritic-Pearlitic Steels

A number of data sets were found in the literature on duplex structured steels, e.g. ferritic-pearlitic steels. They were selected for comparison with the HPM model predictions of materials with complicated microstructures. All of the duplex structured steel data was taken from investigations conducted by Kunio and colleagues [24,25] because of their excellent observations and documentation of critical fatigue phenomenon. Furthermore, a variety of grain sizes and volume fractions of ferrite and pearlite were investigated. Results are shown in table 3.3.



Table 3.3 Fatigue Limit of Various Ferritic-Pearlitic Steels [24,25]

Material Designation	Fatigue Limit (MPa)
0.36%C	194
0.55%C	245
0.84%C	210
S35C-F	194
S55C-G	274
S55C-I	194
S55C-L	216

### 3.1.3 Variety of Steel and Iron

A large set of data from which the empirical relationship between the fatigue strength and ultimate tensile strength given in equation 1.2 was derived was also examined. Data consisted of carbon steels, low-alloy steels, gray cast irons, nodular cast iron, and wrought iron as illustrated in figure 1.2 [4]. These data were selected to explain the physical nature of the fatigue limit and to compare the analytical predictions with observation made during the last one hundred years or more of fatigue research.

### 3.1.4 Martensitic and Bainitic Steels

Numerous sets of martensitic steel data were located in the literature. Most of the data is on carburized steel while most studies were conducted on specimens with polished surfaces [46-53]. Results of those studies are found in tables 3.4a and 3.4b. Effects of surface finish and intergranular crack nucleation were reported in only one data set,

which is listed separately in table 3.5. Data was selected to compare the predictive capabilities of the HPM model with those observations made on high strength steels, materials that have historically exhibited large variations in fatigue strength.

Observations made by Garwood et al [64] on several medium carbon martensitic and martensitic-bainitic automotive steels were also examined. The systematic fatigue behavior associated with various tempering temperatures that were used to produce material with a wide range of hardness was investigated. Garwood's results are plotted in figure 3.1.

## **3.2 Experimental Results**

### **3.2.1 High Carbon Martensitic Steels**

Experiments were conducted on the modified 8680 steel to verify the HPM model's predictions for the synergistic effects of intergranular crack nucleation and surface roughness. Results are listed in table 3.6.

### **3.2.2 Tempered High Carbon Martensitic Steels**

Experiments were performed with the modified 8680 steel to illustrate the effects of additional tempering on the fatigue crack nucleation and propagation mechanisms.

Table 3.4a Carburized Steel [47]

Material	Observed Fatigue Limit <sup>†</sup> (MPa)	Intergranular Nucleation Depth ( $\mu\text{m}$ )	Prior Austenite Grain Size <sup>††</sup> ( $\mu\text{m}$ )
Base Carburized			
Material	518	25	15
As-Carburized <sup>‡</sup>			
0.005 P	506	20	15
0.017 P	484	30	15
0.031P	394	40	15
Single Reheat <sup>‡</sup>			
0.005 P	608	10	5-15
0.017 P	608	10	5-15
0.031 P	574	30	5-15
Triple Reheat <sup>‡</sup>			
0.005 P	641	10	5-9
0.017 P	641	10	5-9
0.031 P	641	10	5-9
Boron & Titanium <sup>‡</sup>			
0.001 Ti	596	40	16
0.015 Ti	617	20	23
0.039 Ti	581	40	23
Si,Cr Free <sup>‡</sup>			
No B&Ti	709	25	15
0.0014 B & 0.038 Ti	644	50	22

<sup>†</sup> Stress amplitude at actual R-ratio.  $R_{\text{applied}}=0.1$   
and  $R_{\text{actual}} : [-0.21, +0.05]$ .

<sup>††</sup> Uniform or surface-core grain size(s).

<sup>‡</sup> Numbers correspond to bulk wt. % phosphorous,  
titanium, and boron.

Table 3.4b Carburized Steel [48-49,51-52]

Material	Observed Fatigue Limit <sup>†</sup> (MPa)	Ref.
In-L	495	[48]
ReIn-L	621	
Carburized Steel	792	[49]
Carburized Steel	792	
Gas DQ	639	[51]
Gas SR	743	
Plasma DQ	473	
Plasma SR	529	
Gas Carburized <sup>††</sup>	868	[52]

<sup>†</sup> Stress amplitude at actual R-ratio.

$R_{\text{applied}}=0.1$  and  $R_{\text{actual}} : [-0.21, +0.05]$ .

<sup>††</sup>  $R_{\text{applied}}=-1$ ,  $R_{\text{actual}}=-2.17$ .

Table 3.5 Synergistic Effects of Surface Finish and Intergranular Crack Nucleation – I [53]

Carburized Steel <sup>‡</sup> Test Condition	Fatigue Limit Observed <sup>†</sup>
4320 Base chemical polish	683
1.3 $\mu\text{m}$ (50 $\mu\text{in}$ )	450
2.6 $\mu\text{m}$ (100 $\mu\text{in}$ )	465
4320M 2.6 $\mu\text{m}$ (100 $\mu\text{in}$ )	465
4320 VC w/ Si, Cr chemical polish	450
4320 VC w/o Si, Cr chemical polish	434
1.3 $\mu\text{m}$ (50 $\mu\text{in}$ )	357

<sup>‡</sup> Kristan [53]. <sup>†</sup> Stress amplitude (MPa). Applied R-ratio=0.1, residual stresses taken into account.

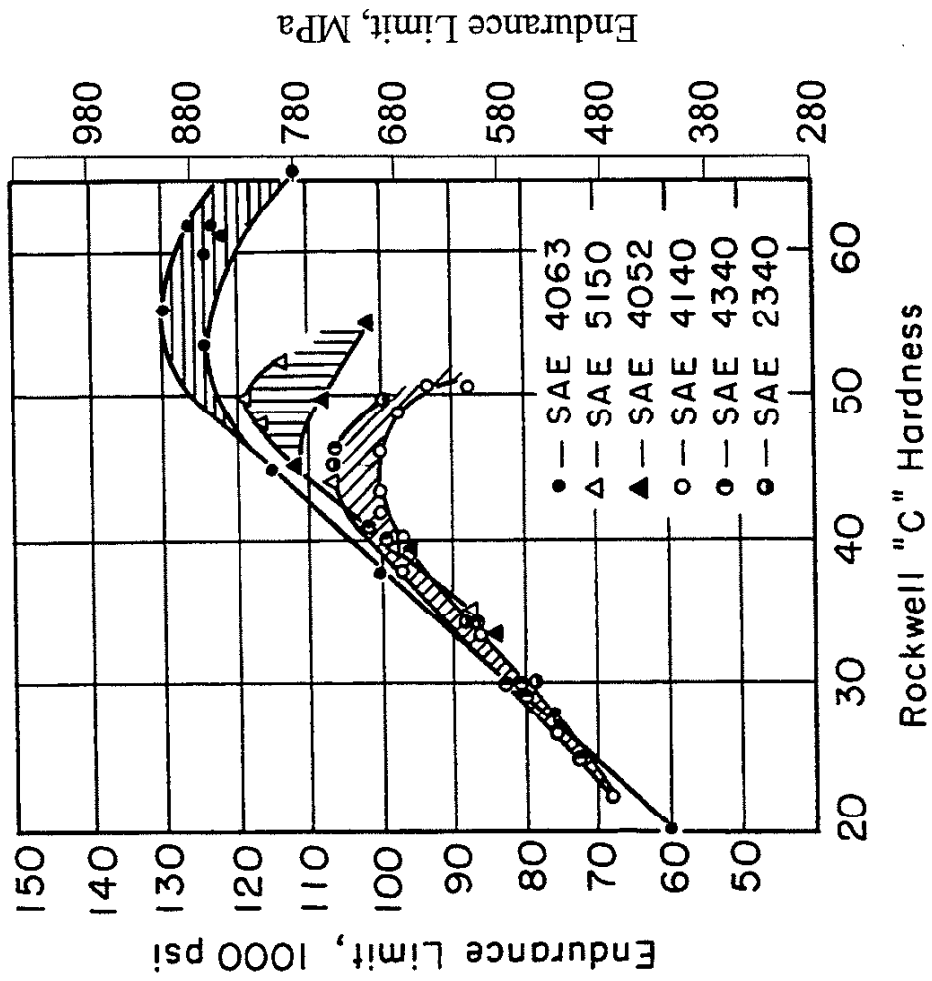


Figure 3.1 Relationship Between Fatigue Limit and Hardness as Observed by Garwood et al [54]

Table 3.6 Synergistic Effects of Surface Finish and Intergranular Crack Nucleation – II

Surface Finish Characterization		Fatigue Limit
$R_a$ ( $\mu\text{m}$ )	Peak-Valley ( $\mu\text{m}$ )	(MPa)
0.05	1	488
1	10	446
2	20	418

<sup>†</sup> Stress amplitude @  $R=0.1$

Intergranular crack nucleation depth  $\approx 20 \mu\text{m}$

Table 3.7 Grain Size Refinement Effects in 8680 Steel

Modified 8680 Steel	Surface Finish	Fatigue Limit (MPa)
Single Vacuum (No reheat)	Polished	180
	$R_a = 3 \mu\text{m}$	180
Triple Vacuum (Double reheat)	Polished	250
	$R_a = 1, 3, 12 \mu\text{m}$	180

Only one additional tempering stage was applied, tempering at 315C for one hour. Several surface finishes and two grain sizes were investigated. Results are listed in table 3.7.

### 3.2.3 Competition of Surface Finish and Inclusions in Hardened 4340 Steel

Experiments were designed and performed to validate the proposed competition for flaw dominance between two different types of flaws, surface roughness and inclusions. Hardened 4340 steel was used in this study. Four groups of specimens were

tested with polished, milled and ground surfaces. Two milled surfaces were investigated, fine and rough, and are designated M600 and M300 respectively. Results are presented in figure 3.2 with increasing surface finish plotted on the abscissa.

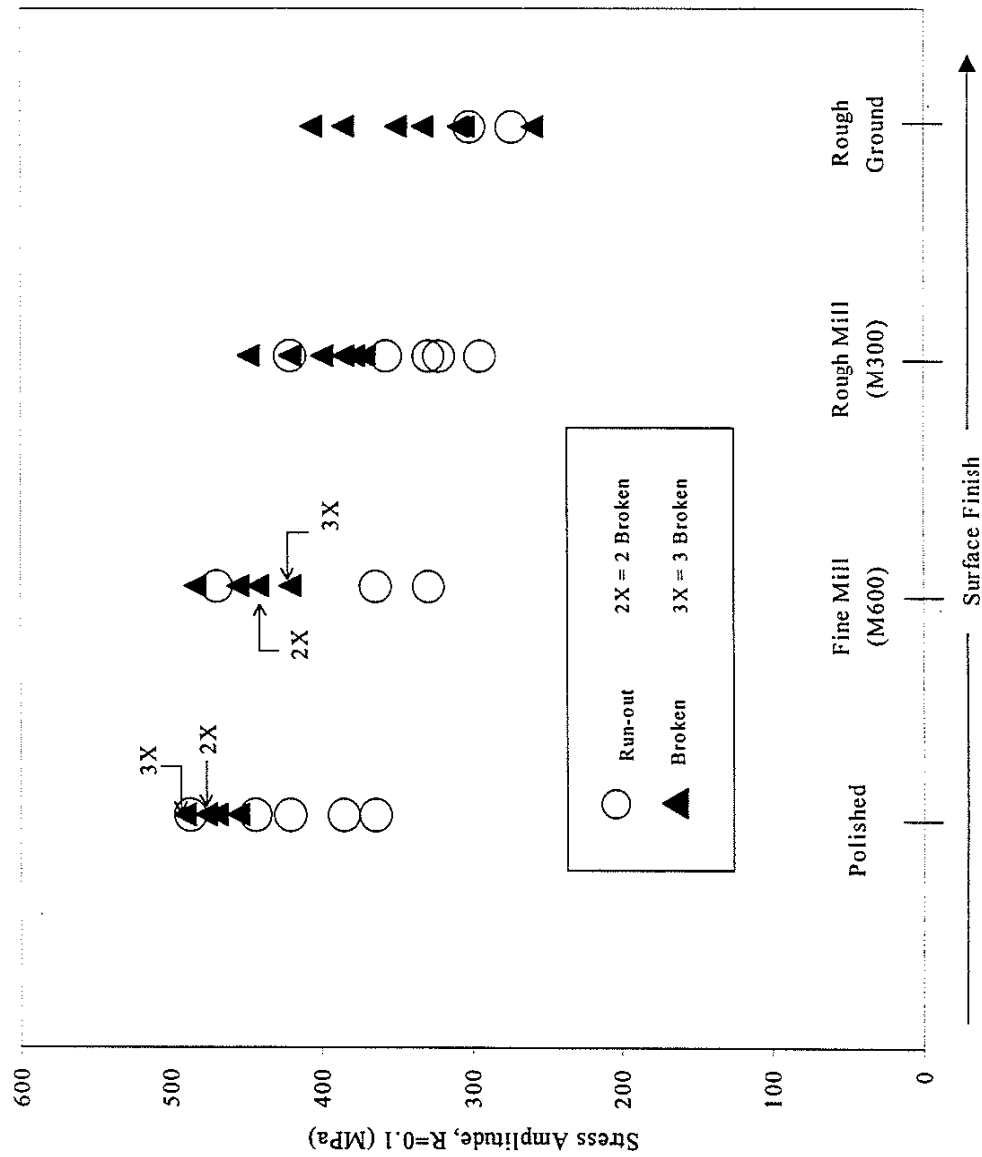


Figure 3.2 Four-Point Bending Fatigue Results of Vacuum Arc-Melted 4340 Steel



## CHAPTER 4

### FORMULATION OF THE HALL-PETCH-MURAKAMI MODEL (HPM)

The general observed relationship between hardness and the fatigue strength of steels is well known and is depicted in figure 4.1. Fatigue strength initially increases in a nearly linearly fashion with hardness. Eventually the rate of increase of the fatigue limit (the slope of the curve) begins to decrease with hardness until a critical hardness is reached. Once this critical hardness is reached, fatigue strength is observed to remain constant and often times actually decrease with hardness. This observation has been recognized for quite some time to be due to the influence of small flaws and nonmetallic inclusions, but the complexities associated with the controlling mechanisms and flaw configurations have prohibited the complete understanding and evaluation of their effects [55-60]. However, the behavior can be explained with a powerful but simple concept, the competition of flaw and microstructure size. Fatigue strength is proposed to be governed by three different interactions between flaws and microstructure. The zones are related to material strength as illustrated in figure 4.2. Each interaction constitutes a distinctly separate fatigue regime. They are the i) intrinsically flawed regime, ii) inherently flawed regime, and iii) processing flawed regime.

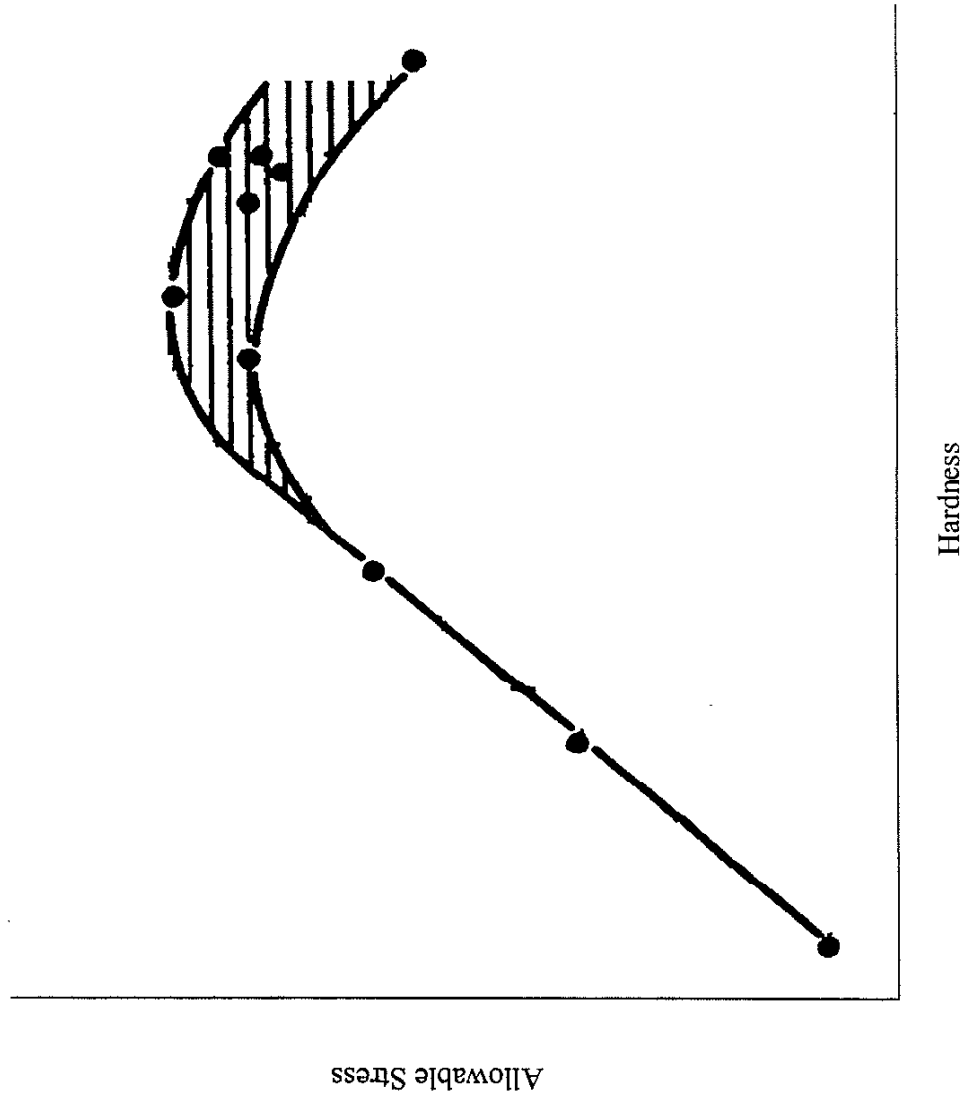


Figure 4.1 General Relationship Between the Fatigue Limit and Hardness

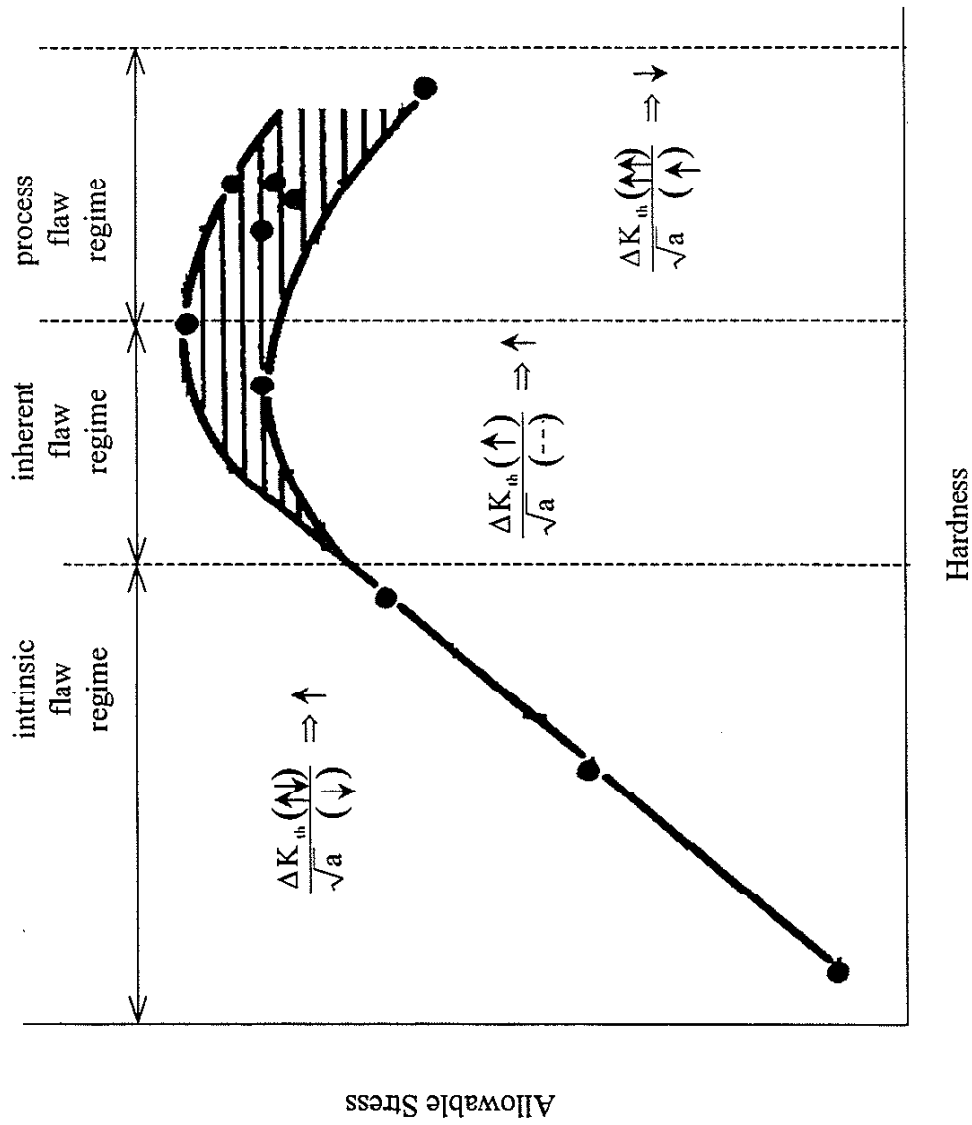


Figure 4.2 Definition of Three Different Flaw Dominated Fatigue Regimes

The three regions are determined as follows. For illustration purposes, let us initially consider a single phase material with equiaxed grains. Allowable stress is related to  $\Delta K_{th,sc}$  and  $\sqrt{a}$  as,

$$\sigma \propto \frac{\Delta K_{th,sc}}{\sqrt{a}} \quad (4.1)$$

In the intrinsic regime cracks nucleate and are blocked by the first grain boundary. As hardness increases,  $\Delta K_{th,sc}$  increases for a given flaw size as seen in figures 4.3. Furthermore, an increase in hardness is typically achieved by microstructure refinement; thus, crack size will also decrease as illustrated in figure 4.4. However, since  $\Delta K_{th,sc}$  is a function of both strength and size,  $\Delta K_{th,sc}$  will also decrease due to the reduction in flaw size as seen in figures 4.3 and 4.5. Although not readily apparent, since

$$\left| \frac{\partial}{\partial a} (\sqrt{a}) \right| > \left| \frac{\partial}{\partial a} \left( \frac{\Delta K_{th,sc}}{H_v + 120} \right) \right|, \quad (4.2)$$

the net effect is that the allowable stress increases as indicated in figures 4.2 and 4.5 where both  $\Delta K_{th,sc}$  and  $\sqrt{a}$  decrease with decreasing flaw size. Intrinsic flaws are discussed further in section 4.1.

Eventually, flaws such as inclusions will become significant in size relative to the grain size as illustrated in figure 4.6. Additional hardening will increase  $\Delta K_{th,sc}$ ,

$$\left. \frac{\partial}{\partial H_v} (\Delta K_{th,sc}) \right|_{a = \text{constant}} > 0, \quad (4.3)$$

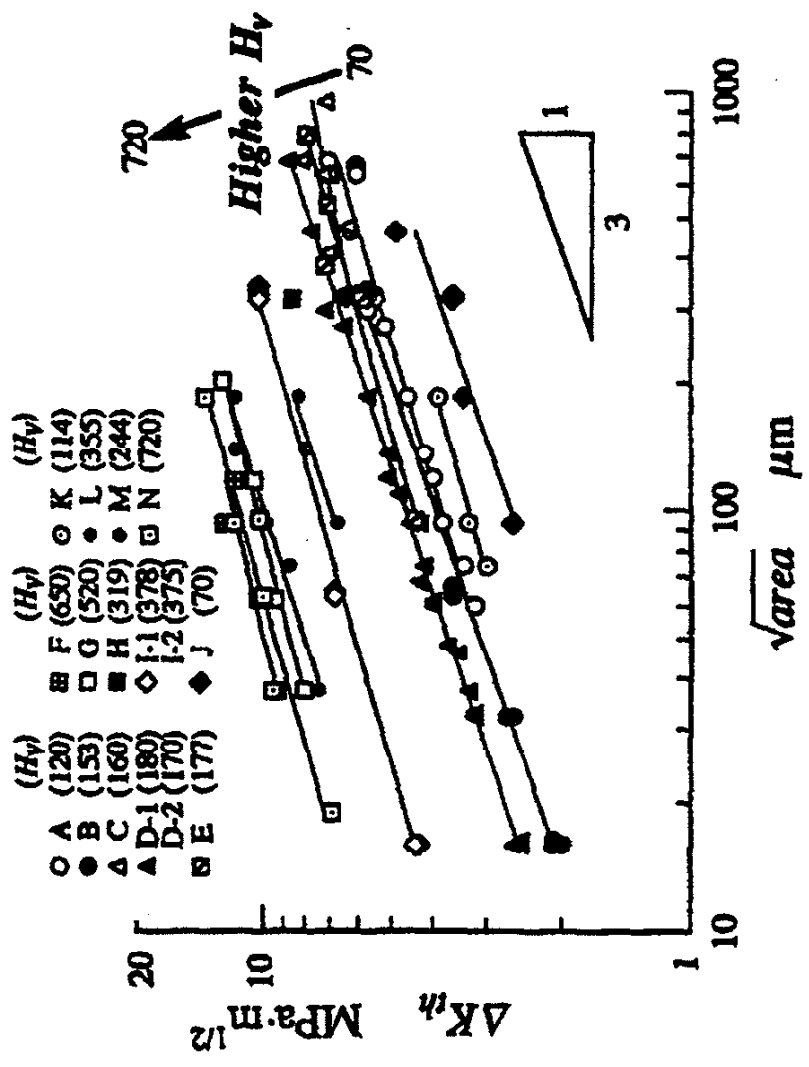


Figure 4.3 Short Crack Threshold Stress Intensity as a Function of Strength and Flaw Size [8]

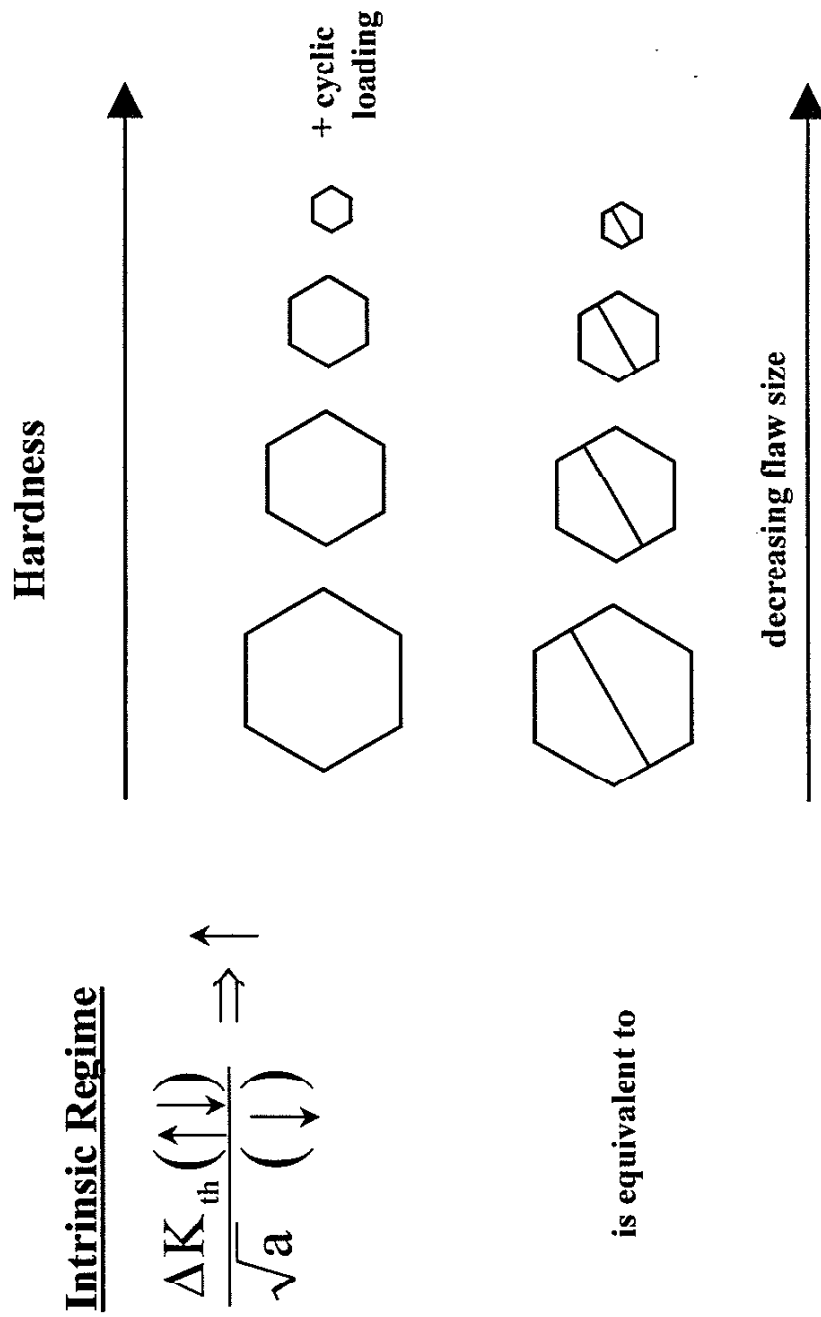


Figure 4.4 Fatigue Process in Intrinsic Flaw Regime

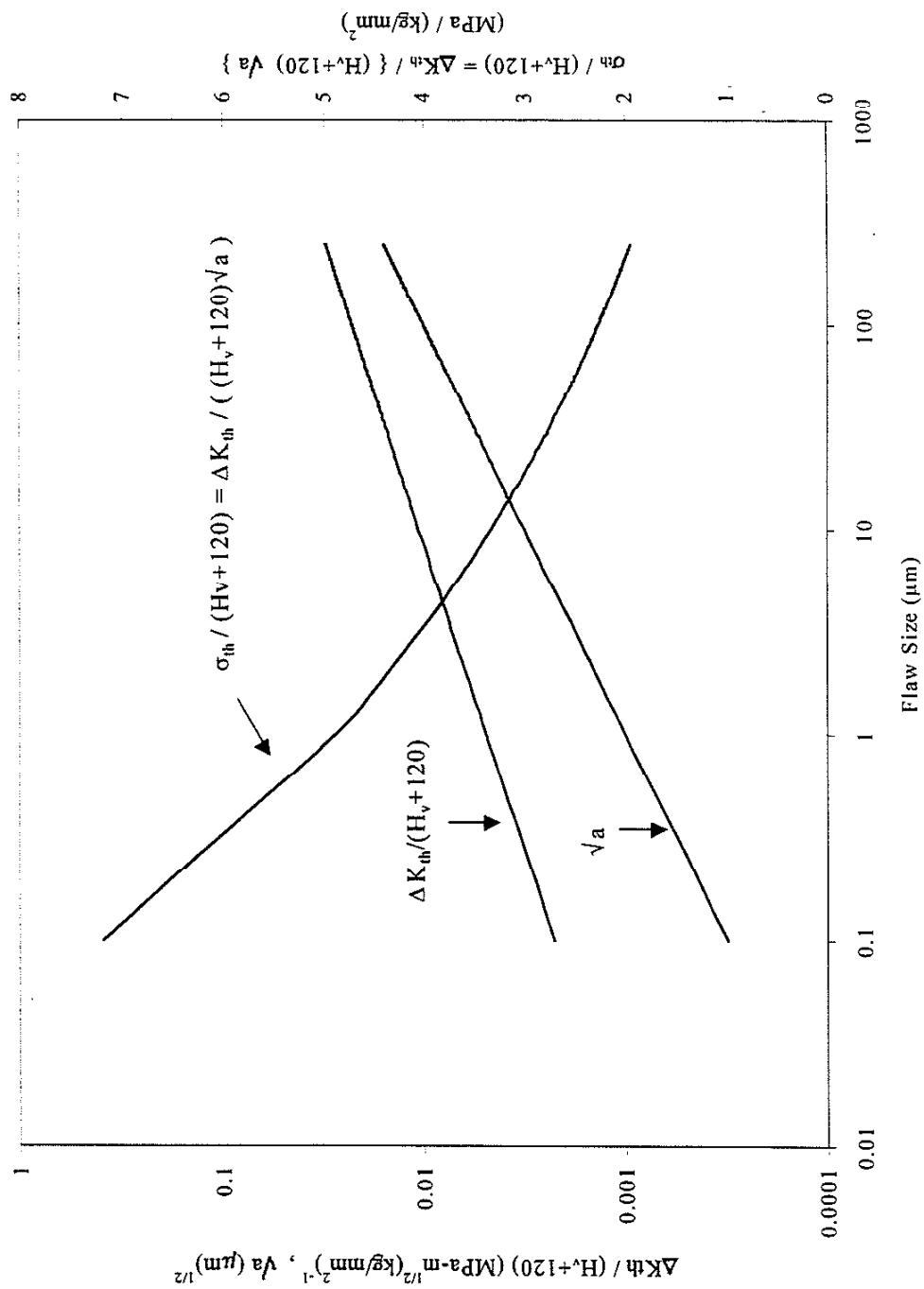
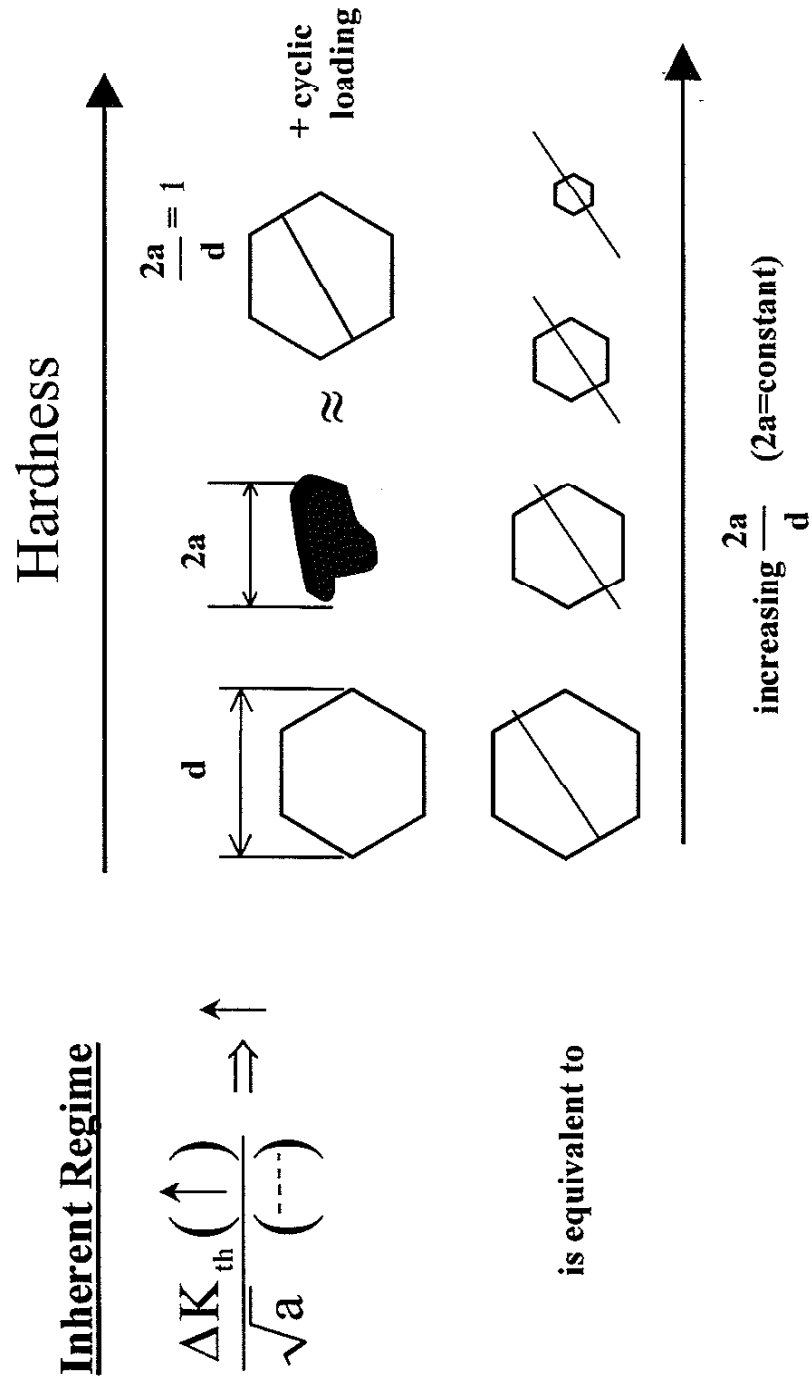


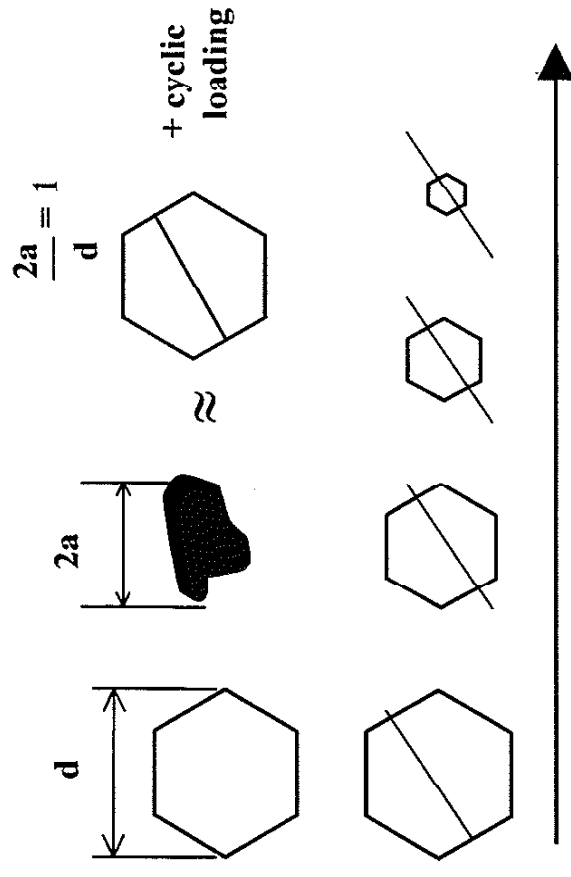
Figure 4.5 Convoluted Relationship Between Flaw Size and  $\Delta K_{th,SC}$



$$\frac{\Delta K_{\text{th}}(\uparrow)}{\sqrt{a}} \frac{(\uparrow)}{(\dots)}$$

**is equivalent to**

# Hardness



$$2a = 1$$

**+ cyclic loading**

22

**2a**  
**increasing**  $\frac{d}{(2a=\text{constant})}$

### Figure 4.6 Fatigue Process in Inherent Flaw Regime



but flaw size will remain essentially constant because the inclusion is larger than the grain size,

$$\left. \frac{\partial}{\partial a} (\sqrt{a}) \right|_{a=\text{constant}} = 0. \quad (4.4)$$

Thus, the allowable stress will continue to increase but at a lower rate than in the intrinsic regime as indicated in figure 4.2. Inherent flaws are addressed in greater detail in section 4.2.

The inherent regime is characterized by cracks that nucleate from the strength controlling microstructure such as grain size, pearlite spacing, etc. On the other hand, inherent flaws are distinguishable by flaws such as inclusions, porosity, carbides, and graphite nodules. However, a third type of flaw becomes active in high strength steels as illustrated in figure 4.7. Again, an increase in hardness results in an initial increase in  $\Delta K_{th,sc}$  as seen in figure 4.3. But, processing flaws such as grinding cracks, severe quench cracks, and intergranular cracking due to grain boundary embrittlement are typically much larger than intrinsic and inherent flaws. Consequently,  $\Delta K_{th,sc}$  will increase further as a result of the increase in flaw size. Due to the nature of processing flaw sizes,

$$\frac{\partial}{\partial a} (\sqrt{a}) > \frac{\partial}{\partial a} \left( \frac{\Delta K_{th,sc}}{H_v + 120} \right). \quad (4.5)$$

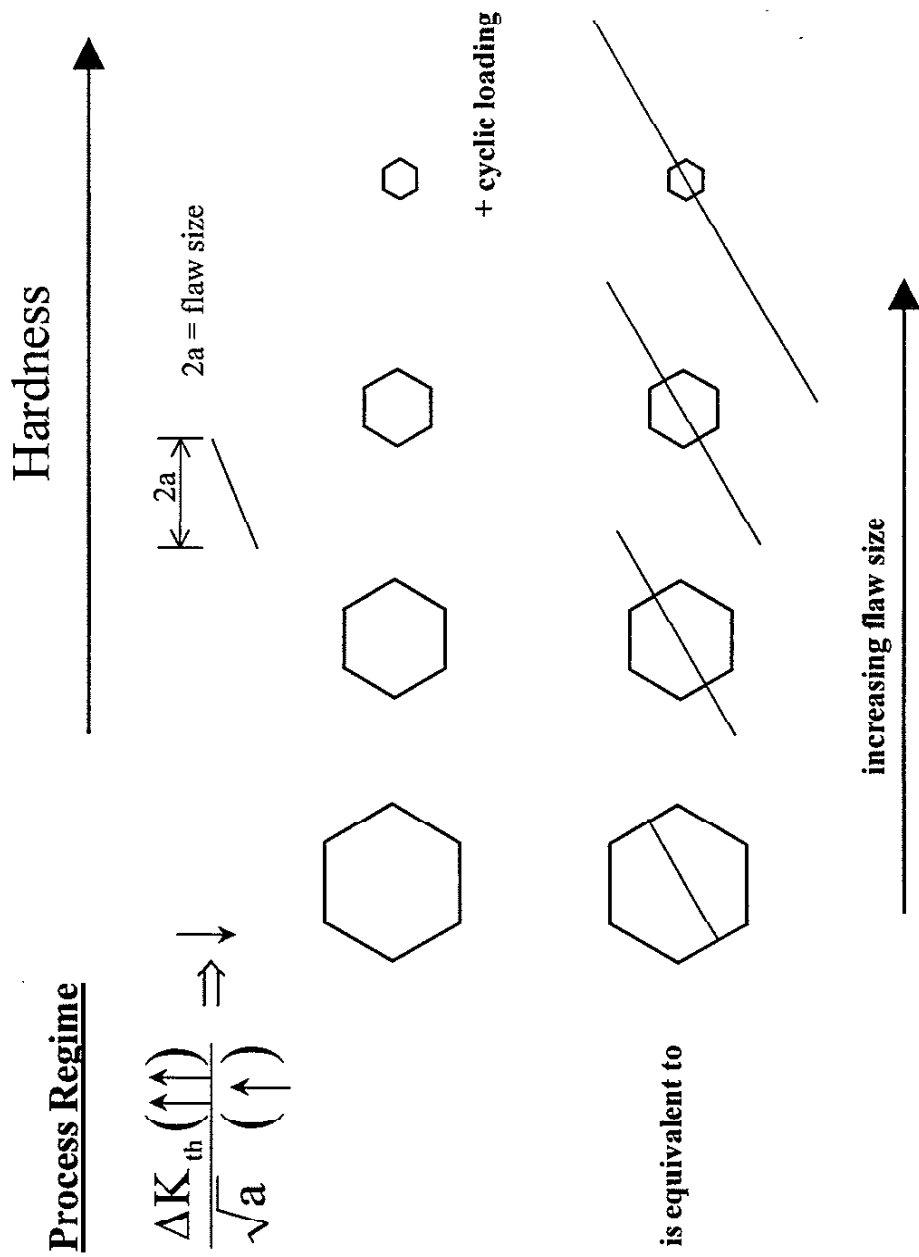


Figure 4.7 Fatigue Process in the Process Flaw Regime

The increase in allowable stress due to an increase in hardness is offset by the increase in flaw size. Hence, the net effect is a reduction in allowable stress as indicated by figures 4.2 and 4.5. Section 4.3 explains these flaws in further detail.

#### **4.1 The Intrinsically Flawed Regime**

In the first regime, the presence of flaws is not disregarded. On the contrary, it is not the presence but the size of the flaw relative to the microstructure that is important. Flaws may be present in this regime; however, their size is smaller than the size of the governing microstructural unit. Hereafter, the governing microstructural unit will be referred to as the grain size since it is easy to visualize. Consider two different equiaxed single-phase materials, one with fine and one with coarse grains. Assume for simplicity that each material has a flaw or inclusion of equal size and that cracks nucleate by transgranular mechanisms as pictured in figure 4.8a. Each flaw is essentially a stress concentrator where upon loading at the fatigue limit dislocations pileup and a slip band or crack originates from the flaw. Slip bands or cracks grow in both materials until they arrest at a local barrier, the grain boundary.

The critical question is then asked: would the elimination of the flaw result in a smaller NPC? In the case of the fine grain material, the answer is yes; however, for coarse grain materials the answer is no. Both scenarios are illustrated in figure 4.8b. If

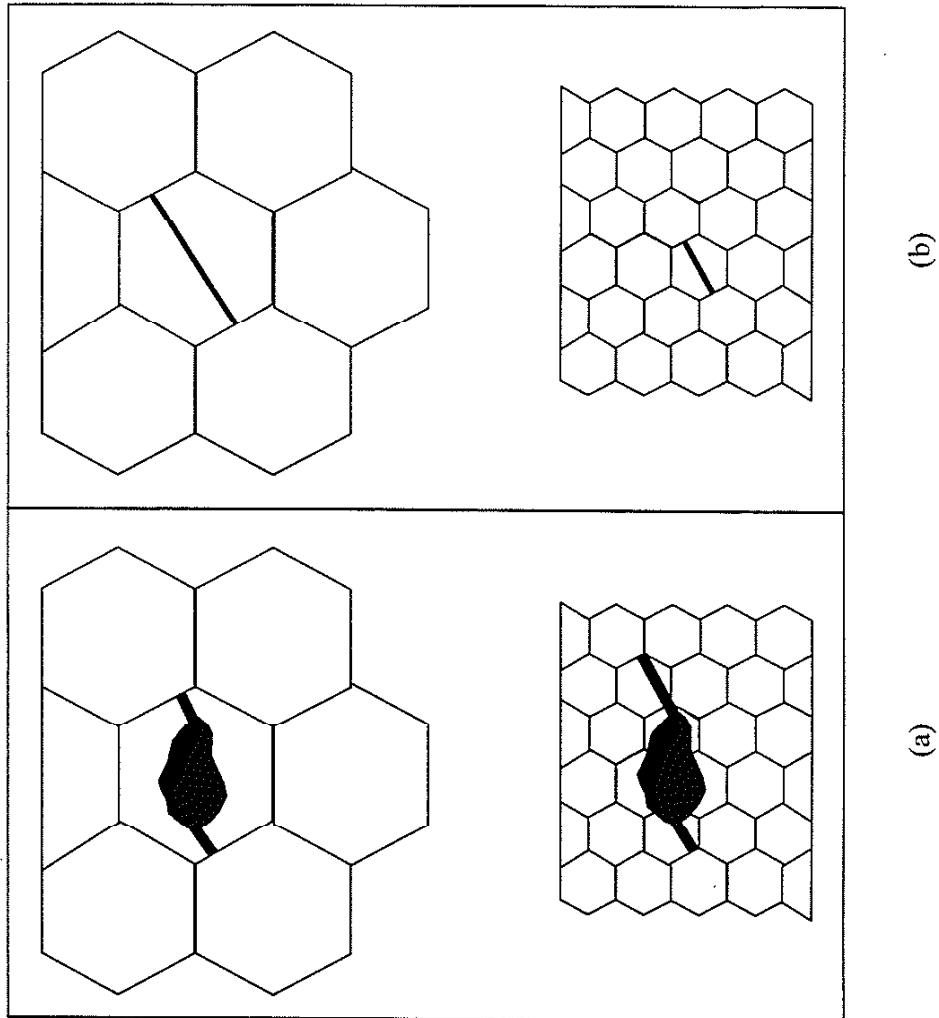


Figure 4.8 Determining Whether an Inherent Flaw is Damaging Relative to the Intrinsic Flaw

the flaw was eliminated from the coarse grain material a slip band or crack would still nucleate, propagate, and arrest at the grain boundary. Since the NPC flaw size would not change, the presence of the flaw is not detrimental with respect to the fatigue limit. The nucleation process may require more cycles to generate a NPC, but the fatigue limit and the size of the NPC would not change. Thus, the term ‘intrinsic’ refers to the intrinsic size of the microstructure.

Quantifying this effect is simple provided the fundamental relationships between flaw size, strength, and threshold conditions for short cracks provided by Murakami are applied correctly. The short crack threshold stress intensity is measured experimentally with the relation,

$$\Delta\sigma = \frac{\Delta K_{th,sc}}{\sqrt{\pi a}} \quad (4.6)$$

Murakami [8,9] has observed that  $\Delta K_{th,sc}$  is related to the Vickers hardness and the  $\sqrt{area}$  of the flaw for a wide variety of metals as,

$$\Delta K_{th,sc} = 3.33 \times 10^{-3} (H_v + 120) (\sqrt{area})^{1/3} \quad (4.7)$$

where the  $\sqrt{area}$  for a semi-elliptical naturally occurring flaw is estimated by,

$$\sqrt{area} \cong a \sqrt{\frac{\pi}{2}} \quad (4.8)$$

Equivalently, an expression for the allowable stress of small flaws is given by:

$$\Delta\sigma = \frac{1.43(H_v + 120)}{\left(a\sqrt{\frac{\pi}{2}}\right)^{1/6}} . \quad (4.9)$$

Recall that  $\Delta K_{th,sc}$  increases with hardness for a constant flaw size as shown in figure 4.3 and that an increase in hardness is typically associated with grain refinement. Equation 4.9 can be rewritten in terms of the grain size alone if a relationship between structure size and hardness exists. This relationship is provided by the solution to the punch problem and the Hall-Petch relationship [61-64].

Slip line theory predicts the relationship between the measured hardness pressure  $P$  and the yield stress  $\sigma_y$  of the material to be:

$$\sigma_y = P / 2.57 , \quad (4.10)$$

but the factor of 3 commonly observed because of work-hardening and constraint effects is used instead:

$$\sigma_y = P / 3 . \quad (4.11)$$

Vickers hardness is related to pressure as,

$$P \text{ (MPa)} = H_v \text{ (kg/mm}^2\text{)} \cdot 9.8 \quad (4.12)$$

and the well-known Hall-Petch relationship,

$$\sigma_y = \sigma_o + \sigma_i / \sqrt{d} , \quad (4.13)$$

is assumed to hold. An intrinsic structure size can be estimated from the Vickers hardness by combining equations 4.11-4.13 as,

$$d = \left( \frac{\sigma_i}{\frac{9.8H_v}{3} - \sigma_o} \right)^2 \quad (4.14)$$

Of course, the constants in the Hall-Petch relationship are material dependent. The Hall-Petch constants reported in the literature for mild steel will be used since steel is the only material discussed in this paper, although the approach should also be applicable for other metals. Finally, the intrinsic fatigue limit can be expressed in terms of the microstructure size alone as,

$$\Delta\sigma = \frac{1.43 \left( \frac{3}{9.8} (\sigma_o + \sigma_i/\sqrt{d}) + 120 \right)}{\left( \frac{d}{2} \sqrt{\frac{\pi}{2}} \right)^{1/6}} \quad (4.15)$$

Since the NPC size,  $a$ , in the intrinsic flaw regime is equal to half the grain size,  $d/2$ , this prediction represents the true upper bound fatigue limit of the material, hence the term ‘intrinsic fatigue limit’.

Equation 4.15 must be used with caution. Thompson [65-66] observed that an increase in the yield strength of nickel via grain size refinement was limited to grain sizes larger than 1  $\mu\text{m}$ . Meyers and Ashworth [67] developed a mechanistic Hall-Petch model based on a few simple micro-deformation processes that agrees well with the results

observed by Thompson. Furthermore, the Hall-Petch constants may vary significantly in some materials due to additional strengthening mechanisms such as solid solution and precipitation hardening. If either of these exceptions occurs, the intrinsic fatigue limit can be expressed in terms of the yield stress,

$$\Delta\sigma = \frac{1.43 \left( \frac{3}{9.8} \sigma_y + 120 \right)}{\left( \frac{d}{2} \sqrt{\frac{\pi}{2}} \right)^{1/6}}, \quad (4.16)$$

or in terms of the measured Vickers hardness,

$$\Delta\sigma = \frac{1.43(H_v + 120)}{\left( \frac{d}{2} \sqrt{\frac{\pi}{2}} \right)^{1/6}}. \quad (4.17)$$

## 4.2 The Inherently Flawed Regime

For the case of simplicity, assume that the size of the inclusion(s) in the material remains constant and is initially small relative to the grain size. Consider what occurs when the hardness of the material is gradually increased by grain refinement. Eventually, the size of the flaws becomes significant relative to the grain size. Crack size is now determined by these inherent flaws or inclusions; however, barrier strength remains a function of the grain size. This marks the transition from the intrinsically flawed regime to the inherently flawed regime. The term ‘intrinsically flawed’ refers to the innate



structure size that determines the strength (hardness) of the material. In contrast, ‘inherently flawed’ refers to the flaws that are associated with the particular steel production route or process, not the fundamental structure size. Thus, the fatigue limit in the second regime is determined by the inherent flaw size and barrier strength. Flaw size at the fatigue limit can no longer be estimated by equation 4.14 but must be measured.

Thus, the intrinsic flaw size,  $d\sqrt{\frac{\pi}{2}}$ , must be replaced by a measure of the inherent flaw size, i.e. the  $\sqrt{\text{area}}$  parameter. Equations 4.16 and 4.17 are then expressed in terms of the  $\sqrt{\text{area}}$  parameter as,

$$\Delta\sigma = \frac{1.43(\frac{3}{9.8}\sigma_y + 120)}{\sqrt{\text{area}}^{1/6}}, \quad (4.18)$$

and

$$\Delta\sigma = \frac{1.43(H_v + 120)}{\sqrt{\text{area}}^{1/6}}, \quad (4.19)$$

respectively.

### 4.3 The Processing Flawed Regime

Scatter in the observed fatigue limit can be explained by the probability of a given fatigue specimen containing a flaw whose size can also be characterized by some statistical distribution function [32-33, 38, 68]. Consequently, each fatigue specimen may have a different fatigue limit. This concept is illustrated by the results of Castilo et

al [58] and is presented in figure 4.9. Twenty-two different lots, each containing 20 or 24 specimens, were sampled from a large population. Each specimen within a given lot was tested at the same stress level. Fatigue lives were observed to vary within each lot. More importantly, the number of tests within each lot that satisfied the run-out criteria differed, ranging from 2 of 24 at a stress range of 315 MPa to 24 of 24 at 280 MPa. However, Garwood et al [54] observed that a large systematic decrease in the fatigue limit occurs when the hardness exceeds some critical level as depicted in figure 4.10. This behavior cannot be attributed to the statistical nature of the fatigue limit. Another fatigue mechanism must be active.

Quenching of high strength steel to obtain hard martensitic structures, generally desired for superior fatigue and wear performance, can introduce microcracking and promote intergranular crack nucleation, both of which have been observed to be detrimental to fatigue properties. Microcracking occurs due to impingement of martensite plates and is believed to assist and increase the amount of intergranular crack nucleation [69]. Grain boundary embrittlement causes intergranular crack nucleation. The cracking mechanism has been attributed to three different types of embrittlement: tempered martensite embrittlement, tempered embrittlement, and quench embrittlement. [46-47,70-73]. In summary, the embrittlement process occurs due to two mechanisms: 1) the precipitation of cementite on prior austenite grain boundaries, and 2) the degradation of the cohesive bond strength of the boundary that results from the presence of impurity atoms such as phosphorous at the boundaries. Neither mechanism is necessary for the other to be active; however, segregation of impurity elements can promote the formation

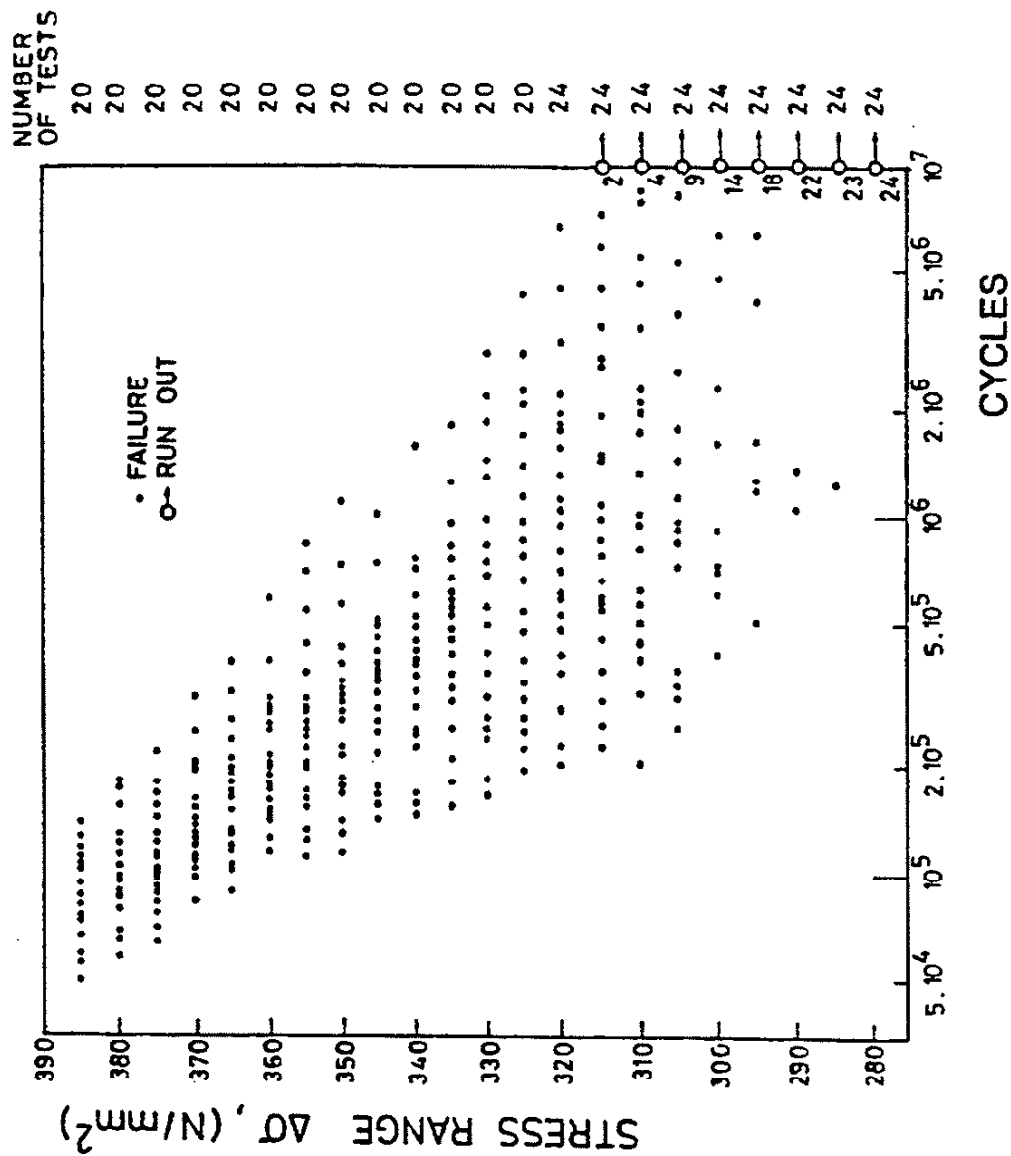


Figure 4.9 Observed Variation in Fatigue Life and Fatigue Limit of Cold Drawn Wire [58]

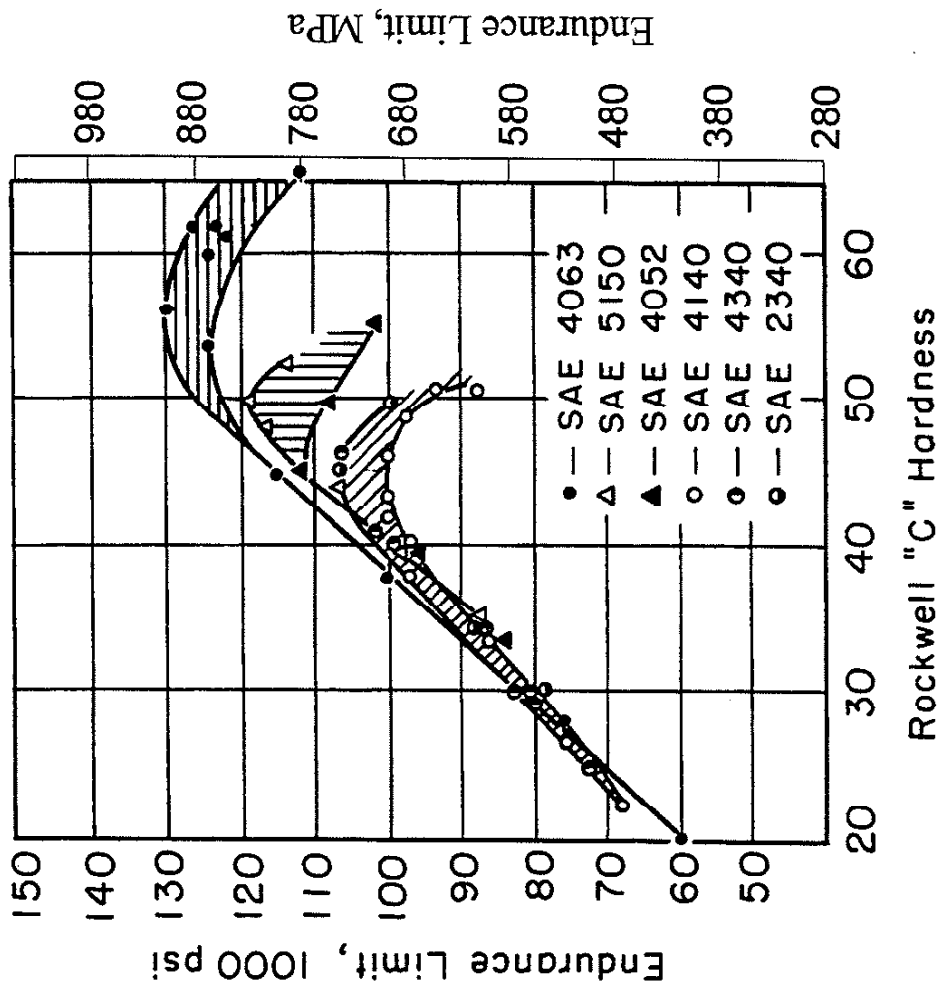


Figure 4.10 Relationship Between Fatigue Limit and Hardness as Observed by Garwood et al [54]

of cementite. Both mechanisms effectively reduce the strength of the interface. Initially, the bulk strength of the grain is weaker than the interface and cracks nucleate transgranularly. However, with increasing hardness eventually the bulk grain strength becomes greater than the strength of the interface and cracks nucleate intergranularly. Krauss reports that the severe implications of cementite formation in austenitic-martensitic steels appears to be restricted to carbon levels greater than 0.5%. Analogous to this mechanism, intergranular fatigue cracking may occur in low carbon martensitic steels where proeutectoid ferrite precipitates at and weakens the prior austenite grain boundaries [74]. Thus, the term 'processing flaw' is adopted since the formation of these flaws occurs during the final heat treating process.

Another simple thought experiment is conducted. Incrementally increase the hardness of a relatively clean high carbon steel. Initially, the fatigue limit will be determined by the intrinsic flaw size and will increase with hardness. Eventually the inherent flaws become significant and the fatigue limit increases with hardness but at a decreasing rate. Finally, a critical hardness is achieved where processing flaws are introduced into the material. A gradual or an abrupt degradation of the fatigue limit may be observed depending on the nature and evolution of the mechanism. Processing flaw size will be a function of the mechanism. For instance, intergranular cracking in high strength carburized steels occurs along prior austenite grain boundaries. Thus, the size of the flaw will be one or more prior austenite grains in size depending on the severity of the embrittlement. Since these grains are generally larger than the inherent inclusion(s) and the martensitic structure, any gain in fatigue strength associated with a small increase in

hardness may easily be outweighed by the increase in flaw size. Unfortunately, predicting the intergranular flaw size in high strength steels requires fatigue testing because an understanding of the embrittling process is currently limited to a qualitative one.

Nucleation mechanisms may differ between the inherent and processing regimes, transgranular and intergranular respectively. However, in order to apply the HPM model in both cases the condition for crack propagation must be transgranular. The HPM model cannot predict thresholds for materials that exhibit intergranular crack propagation because the threshold condition observed by Murakami is governed by transgranular cracking mechanisms only. Thus, quantifying the effect of processing flaws on the fatigue limit may be achieved with equation 4.18 or 4.19 given the flaw size, barrier strength, and a transgranular threshold mechanism.

## CHAPTER 5

### QUANTITATIVE EVIDENCE

#### 5.1 Intrinsic Regime

Consider a single-phase equiaxed material free of inherent flaws. The intrinsic fatigue limit is assumed to be a function of the grain size alone, because the grain size determines both the flaw size and barrier strength. Unfortunately, this simplified concept does not readily apply to most industrial steels because other strengthening mechanisms such as solid solution strengthening and precipitation strengthening may exist. These mechanisms are achieved by various processing parameters such as austenitizing temperature, aging time and temperature, and cooling rates. Such mechanisms will be considered insignificant for our discussion in this section. Application of this concept to a low carbon annealed steel for which the volume fraction of pearlite is small is investigated [15,45]. If the pearlite volume fraction were large enough it may provide another barrier for crack propagation. In such a case, the fatigue limit must be related to the actual NPC length and the strength of the barrier phase, not the grain size. Each case is addressed in turn. Tests were not conducted to illustrate either of these phenomena since adequate data was available in the literature to support them.

### 5.1.1 Single Phase Equiaxed Structures

Two low carbon annealed steels were tested by Radhakrishnan et al [45] and Taira et al [15] containing 0.10% and 0.20% carbon respectively. Since negligible amounts of pearlite were found in the material, the intrinsic form of the HPM model is applied to these two steels. Fatigue limits and yield strengths for three different grains sizes were reported for each investigation. Fatigue limit predictions were made with equations 4.15 and 4.16,

$$\Delta\sigma = \frac{1.43 \left( \frac{3}{9.8} (\sigma_o + \sigma_i/\sqrt{d}) + 120 \right)}{\left( \frac{d}{2} \sqrt{\frac{\pi}{2}} \right)^{1/6}} \quad (4.15)$$

and

$$\Delta\sigma = \frac{1.43 \left( \frac{3}{9.8} \sigma_y + 120 \right)}{\left( \frac{d}{2} \sqrt{\frac{\pi}{2}} \right)^{1/6}}, \quad (4.16)$$

each estimating the fatigue strength via two different approaches. Barrier strength or hardness is estimated by the term in the numerator of equation 4.15,

$$H_v = \frac{3}{9.8} (\sigma_o + \sigma_i/\sqrt{d}), \quad (4.15.1)$$

and is based on the Hall-Petch constants and grain size. In equation 4.16, barrier strength is estimated with the yield strength as,



$$H_v = \frac{3}{9.8} \sigma_y. \quad (4.16.1)$$

The reported grain sizes and Hall-Petch constants measured by Radhakrishnan et al and Taira et al were implemented in the calculations. Results are found in table 5.1 and 5.2. The first and second columns list the grain sizes and yield strengths reported. Estimated Vickers hardness are provided in the third and fourth columns. Hardness estimates based on the reported grain sizes and Hall-Petch constants are in the third column labeled (d), while the hardness estimates based on the yield strengths are provided in the fourth column labeled ( $\sigma_y$ ). Hardness predictions for the two different methods are nearly equal. NPC size for each material was assumed to be equal to the grain size since cracks were reported to nucleate within the grains and arrest at the first grain boundary. Fatigue limits were predicted with equations 4.15 and 4.16. Predictions made with equation 4.15, which implemented the grain size and Hall-Petch constants, are listed in the sixth column labeled (d). Predictions made with equation 4.16 and the reported yield strength are provided in the seventh column labeled ( $\sigma_y$ ). Both fatigue estimates are nearly equal to each other for all six grain sizes. Observed fatigue limits are listed in the last column. Comparisons of the observed fatigue limits with the predicted fatigue limits in columns (d) and ( $\sigma_y$ ) indicate excellent agreement in all cases, approximately within 20% error or less.

Another hardness prediction was made with equation 4.15; however, the Hall-Petch constants initially observed by Petch [54] were implemented rather than those reported by Radhakrishnan or Taira. The estimated Vickers hardness for each material is

Table 5.1 Intrinsic Fatigue Limit Verification – Radhakrishnan et al [45]

Reported d ( $\mu\text{m}$ )	Reported $\sigma_y$ (MPa)	H <sub>v</sub> : Vickers Hardness ( $\text{kg/mm}^2$ ) <sup>†</sup>		Predicted Fatigue Limit (MPa) <sup>†</sup>		Observed Fatigue Limit (MPa)
		(d)	( $\sigma_y$ )	(d)	( $\sigma_y$ )	(Petch)
18	240	83	73	161	153	292
27	210	73	64	143	137	255
44	190	64	58	126	122	220
						175
						162
						149

<sup>†</sup> Estimated with reported grain size (d), measured yield stress ( $\sigma_y$ ), Hall-Petch constants observed by Petch (Petch).

Table 5.2 Ideal Intrinsic Fatigue Limit Verification – Taira et al [15]

Reported d ( $\mu\text{m}$ )	Reported $\sigma_y$ (MPa)	H <sub>v</sub> : Vickers Hardness ( $\text{kg/mm}^2$ ) <sup>†</sup>		Predicted Fatigue Limit (MPa) <sup>†</sup>		Observed Fatigue Limit (MPa)
		(d)	( $\sigma_y$ )	(d)	( $\sigma_y$ )	(Petch)
7.8	366	110	112	253	255	478
20.5	275	80	84	187	191	337
55.0	194	61	59	144	142	248
						235
						178
						163

<sup>†</sup> Estimated with reported grain size (d), measured yield stress ( $\sigma_y$ ), Hall-Petch constants observed by Petch (Petch).

listed in the fifth column labeled (Petch) and the corresponding fatigue limit predicted via equation 4.15 is provided in the eighth column labeled (Petch). One can easily observe that the hardness predictions made with Petch's original constants are much greater those estimated with the Hall-Petch constants reported by Radhakrishnan and Taira. The difference in predicted hardness is because Petch's constants for mild steel differ from those observed by Taira, Radhakrishnan, and many other investigators. Apparent differences in the constants  $\sigma_i$  and  $\sigma_o$  are due to systematic variations in  $\sigma_o$  associated with additional hardening mechanisms resulting from the various heat treatment parameters used by Petch [75]. Hence, the fatigue limit predictions based on Petch's initial constants are very poor relative to the observed fatigue limits, as expected. Thus, caution should be used when implementing the intrinsic form of the HPM model given in equation 4.15.

### 5.1.2 Duplex Structures

When predicting the intrinsic fatigue limit of metals where an equiaxed single-phase microstructure does not exist, i.e. duplex microstructures of ferrite and pearlite, two important concepts must be kept in mind. Barrier strength and NPC remain the critical variables that determine the fatigue limit; however, the NPC length can no longer be determined by the Hall-Petch relationship. Figure 5.1 compares the observed NPC size and predicted intrinsic size over a broad range of hardness. The Hall-Petch prediction is in relatively good agreement with the observed NPC size for very low strength steels.

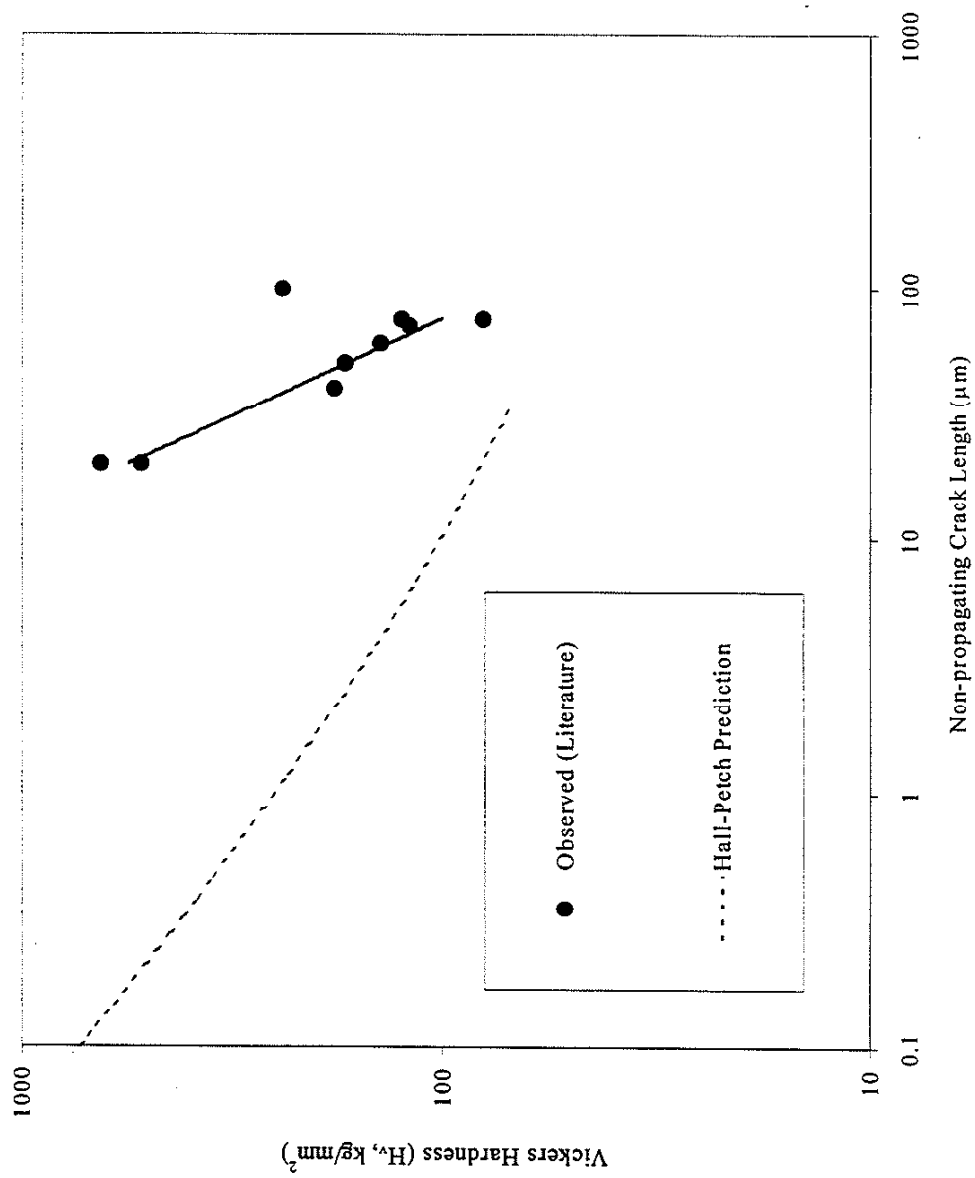


Figure 5.1 Observed and Predicted Non-propagating Crack Size vs. Hardness

This is because typical microstructures of low strength steels consist of equiaxed single-phase grains. With increasing hardness, significantly different flaw sizes are observed than are predicted because of the development of more complicated microstructures including size, strength, distribution, and volume fraction of the constituent phases in the material. (Of course, inherent inclusions can also cause large discrepancies between the observed and predicted NPC size especially for harder materials; but, for simplicity assume that these inherent flaws are small and do not play a role in the NPC size.) Variations in the microstructural parameters will cause changes in the length of the NPC and the barrier strength. In fact, a systematic change in the fatigue limit because of various heat treatment processes may not be observed. To verify this concept, the HPM model is applied to two studies of ferritic-pearlitic steels conducted by Kunio et al [24, 25]. Their work was selected because of the variety of steels tested and their excellent documentation of parameters such as NPC size, strength and volume fraction of individual constituent phases, and the allowable stress.

In one study [25], three ferritic-pearlitic steels with 0.84%C, 0.55%C, and 0.36%C (94%, 71%, and 45% pearlite respectively) were tested and the NPC size and fatigue limits recorded. Micropits, both larger and smaller than the observed NPC, were introduced via electron-discharge-machining into virgin specimens. Similarly, pre-cracked specimens were made whose lengths were equal to the NPC observed at the fatigue limit. All specimens were subsequently annealed to remove residual stresses that may have developed during the introduction of the flaws and afterwards loaded at stresses corresponding to the fatigue limits observed earlier in the virgin specimens.

The maximum size micropit for the 0.84%C and 0.55%C steels that did not cause the specimens to break was found to be of comparable size to the NPC size. However, the largest allowable micropit for the 0.36%C steel was observed to be about half the size of the observed NPC. The difference in the observed NPC size and the largest allowable micropit flaw size in the 0.36%C steel observations was shown to be associated with variations in the microstructure. The volume fraction of pearlite was observed to vary from location to location in the material. Since pearlite was observed as the barrier to crack propagation, the lack of a locally homogenous structure lead to the propagation of the micropit flaw to a size larger than the critical NPC size observed in the virgin specimens. EDM pits equal in size to the observed NPC were placed in locations containing a high volume fraction of pearlite. Specimens were annealed and loaded at the endurance limit of the virgin specimens; none failed.

The HPM model was applied to these materials to examine the role of microstructure in determining the barrier strength, NPC size, and fatigue limit. Tables 5.3a and 5.3b compare the observed results for the three steels with predictions made with the HPM model via equation 4.18,

$$\Delta\sigma = \frac{1.43(H_v + 120)}{\sqrt{area}^{1/6}}, \quad (4.18)$$

where

$$\sqrt{area} \approx \frac{NPC}{2} \sqrt{10} \quad (5.1)$$

Table 5.3a Duplex Structure Intrinsic Fatigue Limit Verification I

%C	% Pearlite	NPC Observed at Fatigue Limit ( $\mu\text{m}$ )		Predicted NPC observed at Fatigue Limit based on $H_v$ <sup>†</sup>		
		Crack	Pit	Ferrite	Pearlite	Bulk <sup>††</sup>
0.36	45	172	140	131	184	155
0.55	71	42	38	3	27	16
0.84	94	80	85	12	91	82

<sup>†</sup> NPC estimated with different barrier strengths.

<sup>††</sup> Bulk strength estimated by rule of mixtures.

Table 5.3b Duplex Structure Intrinsic Fatigue Limit Verification II

%C	% Pearlite	Predicted Fatigue Limit Based on $H_v$ <sup>⊗‡</sup>			Observed Fatigue Limit	% error		
		Ferrite	Pearlite	Bulk		Ferrite	Pearlite	Bulk
0.36	45	131	184	155	194	-32.4	-5.3	-20.2
0.55	71	160	227	208	245	-34.9	-7.2	-15.3
0.84	94	154	214	211	210	-26.9	2.1	0.3

<sup>†</sup> NPC estimated with different barrier strengths. <sup>††</sup> Bulk strength estimated by rule of mixtures.

<sup>‡</sup> Fatigue Limit (MPa). Prediction based on NPC (crack).

<sup>⊗</sup> Barrier strength assumed to be equal to ferrite, pearlite, or bulk respectively.

as suggested by Murakami [8]. NPC sizes were estimated via equation 4.18 by back-calculating flaw size given the observed fatigue limit and a barrier strength. Three different barrier strengths were considered: ferrite, pearlite, and bulk strengths where the bulk strength was estimated by the rule of mixtures. Percent carbon and percent pearlite for each material are reported in the first two columns. Observed NPC sizes and the largest non-detrimental micropit flaw sizes are listed in the third and fourth columns. The pit size for the 0.36%C steel is the size of the pits placed in regions with a high volume fraction of pearlite. Note that the observed NPC size and micropit sizes are approximately equal in all cases. Predicted flaw sizes are given in the three columns to the right of the observed NPC. Each column lists predictions based on different assumed

barrier strengths, i.e. ferrite, pearlite, and bulk. Predictions based on the ferrite barrier strength exhibit large errors in the 0.55%C and 0.84 %C materials with a smaller error in the 0.36%C material. This is attributed to the influence of the microstructure, i.e. since ferrite is the weaker phase only small cracks can be arrested when subjected to the stresses observed at the fatigue limit. Pearlite and bulk strength NPC size predictions are much better than those based on the ferrite barrier strength because both are stronger barriers than the ferrite. However, no readily distinguishable difference exists between the pearlite and bulk NPC estimates.

Fatigue limit predictions based on the three different barrier strengths are reported in table 5.3b along with the observed fatigue limits. Predictions are listed in the third, fourth, and fifth columns followed by the observed fatigue limits in the sixth column. Predictions were made assuming flaws equal in size to the reported NPC sizes. The error for each prediction relative to the corresponding observed fatigue limit is listed in the last three columns. Ferrite is clearly not the true barrier strength due to the large conservative errors for each prediction based on ferrite barrier strength. Errors in the pearlite and bulk barrier predictions are comparable in the 0.84%C steel (94% pearlite) because of the large volume fraction of pearlite. However, as the volume fraction of pearlite decreases the errors in the predicted fatigue limits based on the bulk barrier strength are twice as large as the errors for the pearlite barrier strength predictions. Thus, pearlite is considered as the true barrier strength.



Kunio [24] proposed several important concepts in another study. These concepts are related to the large variations in fatigue strength reported for ferritic-pearlitic steels of a given pearlite volume fraction as shown in figure 5.2. First, he found that the fatigue limit was approximately constant for a given ferrite grain size over a wide range of pearlite volume fractions as illustrated in figure 5.3. Second, systematic increases of the fatigue limit with an increasing fraction of pearlite were only observed in conventionally annealed steels as also illustrated in figure 5.3. This is due to the convoluted effect of NPC length and barrier strength variations that resulted from the different microstructures obtained by the various processing methods; effects of these variations can be quantified with the HPM model.

Table 5.4 lists Kunio's results and the HPM predictions for materials which Kunio reported NPC sizes. Note that three of the four materials have substantially different microstructures as indicated by the different microstructure parameters indicated in the first five rows of the table. For example, ferrite grain sizes are equal to 5, 30, and 67  $\mu\text{m}$ . The S55C-G and S55C-L materials appear to be very similar; however, the morphology of the pearlite differs. Pearlite is distributed in bands in the S55C-G material while it is more randomly distributed in the S55C-L material. Thus, microstructures of all four materials differ. Barrier strength and NPC size were assumed to be equal to the average measured pearlite strength and the maximum observed NPC size for each material and are listed in the table. Fatigue limit predictions were made with equations 4.18 and 5.1 and are provided along with the observed fatigue limits and error in the last

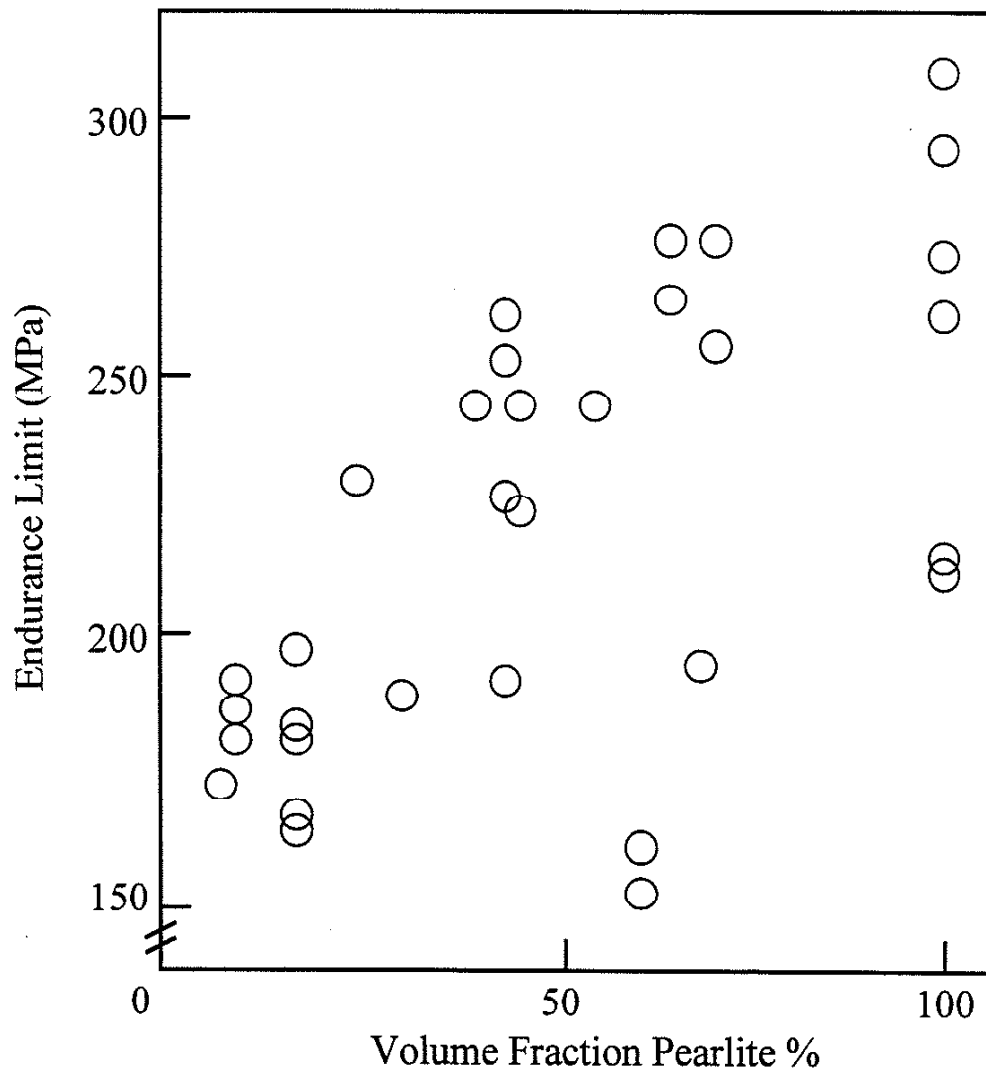


Figure 5.2 Variation in Fatigue Limits of Pearlitic Steel [24]

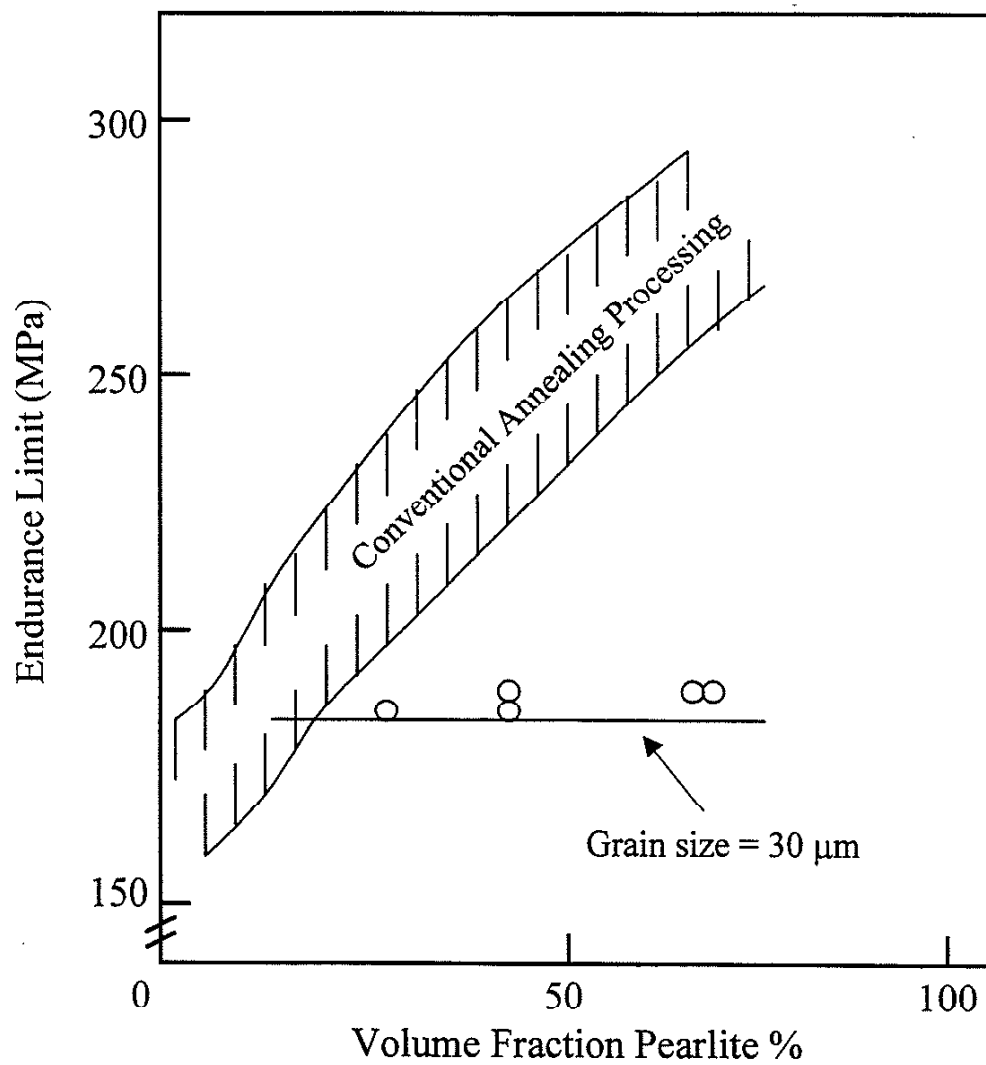


Figure 5.3 Effect of Conventional Annealing Process and Constant Proeutectoid Structure Size on the Fatigue Limit of Ferritic-Pearlitic Steel [24]

three rows of table 5.4. Overall, the predictions are in good agreement with the observed fatigue limits. Errors are conservative and within 20%.

Table 5.4 Duplex Structure Intrinsic Fatigue Limit Verification III

Material	S35C - F	S55C - G	S55C - I	S55C - L
%Pearlite	45	71	71	71
$d_F$ ( $\mu\text{m}$ )	67	5	30	6
$l_P$ ( $\mu\text{m}$ )	48	3	22	1.4
$H_v$ Pearlite	252	239	213	254
$H_v$ Ferrite	121	132	132	158
Max. Observed NPC ( $\mu\text{m}$ )	300	100	300	150
Observed Fatigue Limit (MPa)	194	274	194	216
Predicted Fatigue Limit (MPa)	190	221	171	215
Error (%)	-1.8	-19.4	-12.1	-0.5

$d_F$ : Ferrite grain size.  $l_P$ : Mean second phase spacing.

$H_v$ : Vickers Hardness ( $\text{kg/mm}^2$ )

### 5.1.3 Examining a Variety of Industrial Steel and Iron Fatigue Limits

The intrinsic form of the HPM model has been verified by several detailed data sets taken from the literature for the ideal equiaxed single-phase structured and the more complex duplex structured steels. Next, the model was applied to steel and iron that possess a wide range of strengths and microstructures. Historically the fatigue strength has been related to the bulk strength of materials as given by equations 1.1 and 1.2,

$$\sigma_w = 1.6 H_v + / - 0.1 H_v \quad (1.1)$$

$$\begin{aligned} \sigma_w &= 0.5 \sigma_u + / - 0.1 \sigma_u \text{ or equivalently} \\ &\approx 1.55 H_v + / - 0.31 H_v \end{aligned} \quad (1.2)$$

Assume for the moment that the barrier strength and bulk strength are equal. In figure 5.4, the intrinsic form of the HPM model is plotted along with the empirically observed fatigue relationship given in equation 1.2. Except for the very low strength steels, i.e. ideal single phase structures, the HPM prediction overestimates the observed fatigue limit. This difference is expected since the microstructure of the empirical data is not representative of the ideal equiaxed single-phase structure associated with the prediction. NPC length must be examined rather than the grain size. Consider the ratio of the NPC length to the size of the proeutectoid (ferrite) structure observed by Kunio and Tokaji. Ratios of NPC length to proeutectoid structure size range from 3 to 25 as illustrated in figure 5.5. Thus, the intrinsic flaw size,  $d$ , must be replaced by a typical NPC flaw size. Predictions for non-propagating cracks whose sizes are equal to 1, 3, 10, and 25 times the proeutectoid structure size were made and are plotted in figure 5.6. For example, the prediction for a NPC size equal to  $10d$  is indicated by the line labeled 'intrinsic form: NPC= $10d$ '. Thus, each NPC size is quantified as a multiple of the proeutectoid structure size, i.e. NPC= $d$ , NPC= $3d$ , etc. The empirical relation given in equation 1.2 is also plotted in figure 5.6. Predictions follow the experimental trends well. Furthermore, upper and lower bounds of the empirical results correspond to the HPM model predictions when the NPC flaw sizes are assumed to be equal to the observed lower and upper bound NPC sizes, NPC= $3d$  and NPC= $25d$  respectively. In addition, the prediction based on the intermediate NPC size, NPC= $10d$ , corresponds to the average observed fatigue strength. Agreement is limited to the intermediate and low strength steels because the martensitic and martensitic-bainitic microstructures have drastically

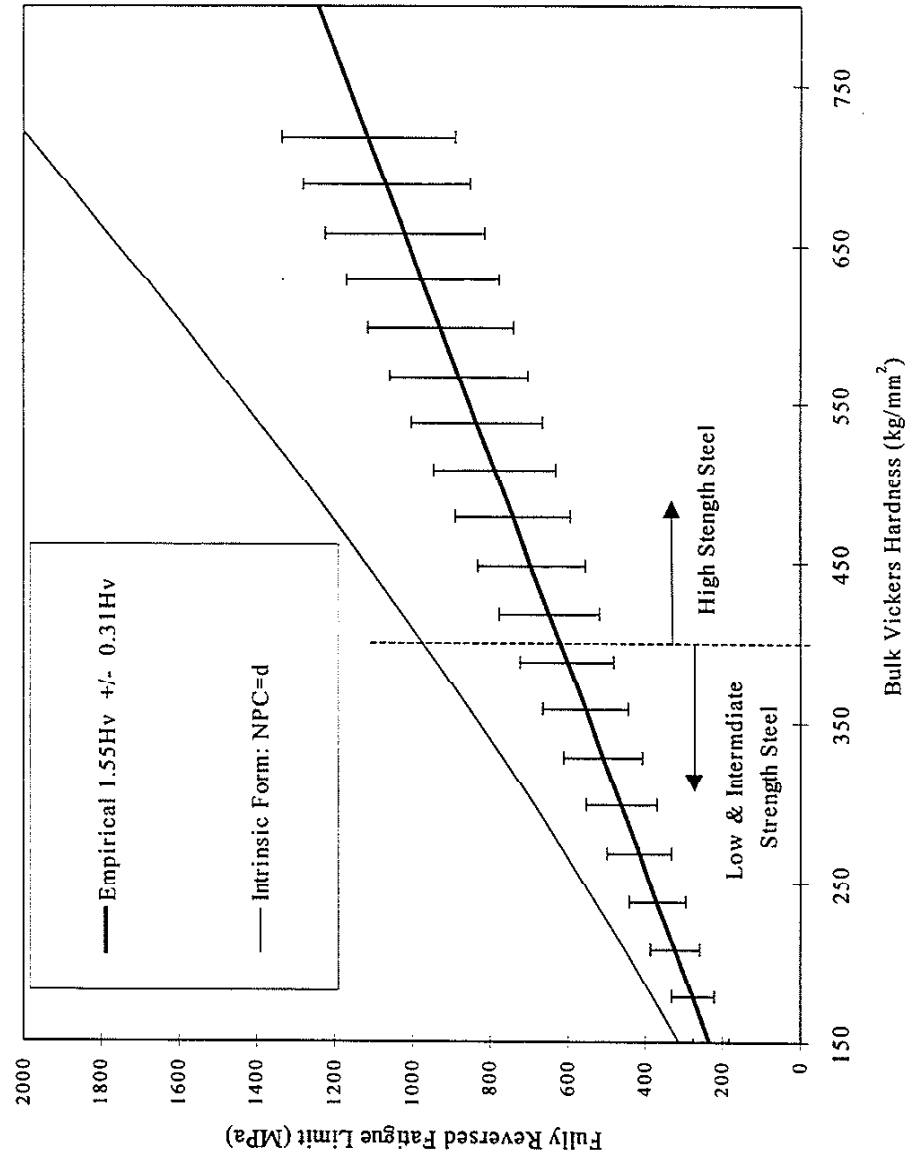


Figure 5.4 HPM Model Intrinsic Fatigue Limit Prediction vs. Empirical Relationship

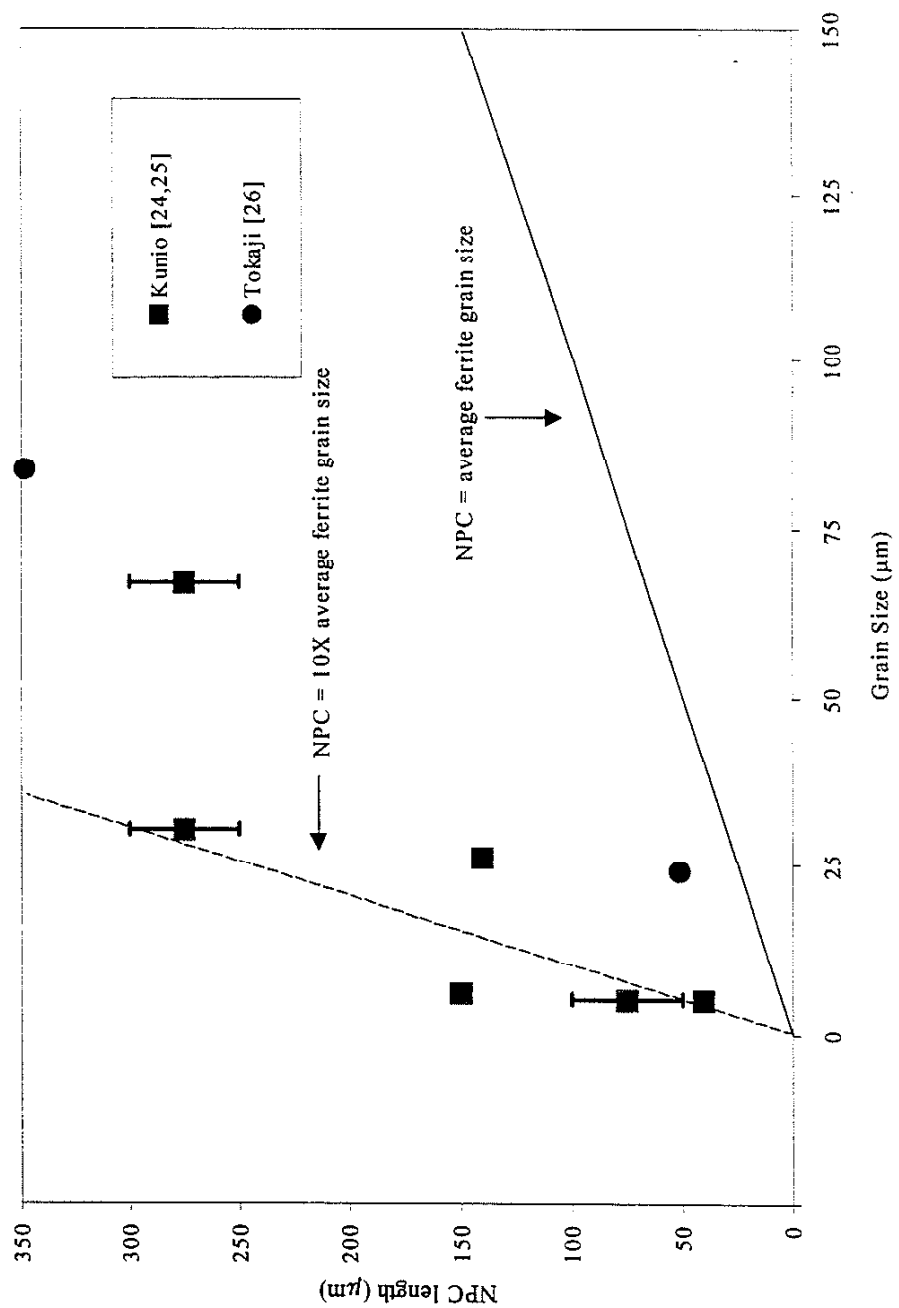


Figure 5.5 Observed Relationship Between Non-propagating Crack Size and Grain Size

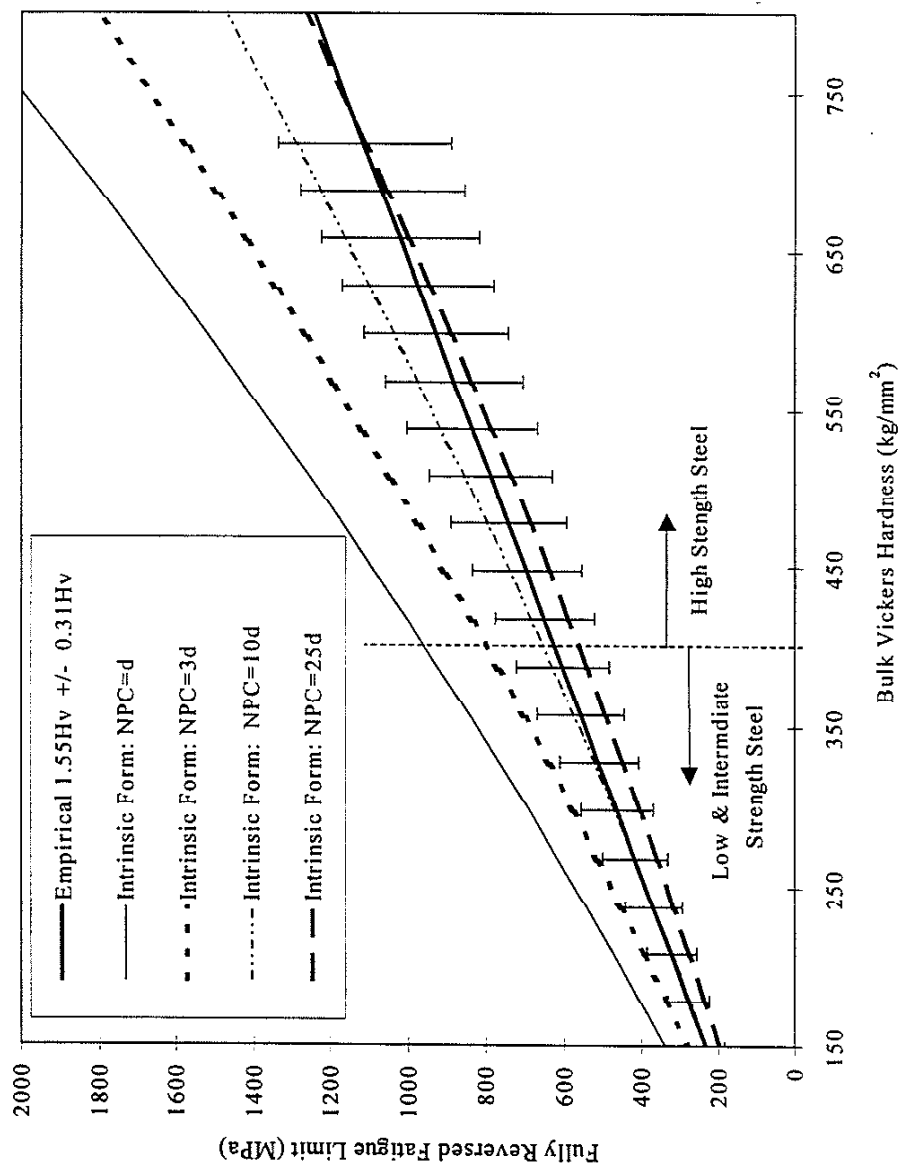


Figure 5.6 HPM Model Predictions with Non-propagating Crack Sizes vs. Empirical Relationship



different structures than ferritic and pearlitic steels. High strength materials are discussed later in section 5.2.

Barrier strength may not be equal to the bulk strength in many materials. In the numerous tests conducted by Kunio et al on ferritic-pearlitic steels, the ratio of the barrier strength to the bulk strength ranged from about 1 to 1.3 where pearlite was observed to be the barrier phase. The intrinsic size of the primary phase or proeutectoid structure cannot be estimated accurately without accounting for the differences between the bulk, pearlite, and proeutectoid hardness. Ratios of the proeutectoid hardness to the bulk hardness observed by Kunio et al ranged from 1 to 0.6 where the ratios 1 and 0.6 correspond to the ratios of barrier hardness to bulk hardness of 1 and 1.3 respectively. In other words, if the ratio of the proeutectoid hardness to bulk hardness is 1, then the corresponding ratio of barrier hardness to bulk hardness is also 1. Similarly, if the ratio of the proeutectoid barrier strength to bulk strength were 0.6, then the corresponding ratio of barrier strength to bulk strength is 1.3. The first set of ratios of  $\{1, 1\}$  are equivalent to the case where the bulk, barrier, and proeutectoid strengths are equal. Predictions for this case have actually already been presented in figure 5.6. The three strengths differ significantly when the ratio of the proeutectoid strength to the bulk strength is 0.6 and the ratio of the barrier strength to bulk strength is 1.3. Figure 5.7 illustrates the HPM model predictions for this case. Virtually no difference exists between the two cases depicted by figures 5.6 and 5.7. One might conclude that the increase in barrier strength assumed in the case depicted in figure 5.7 had no influence on the fatigue strength. However, the conclusion would be wrong since the accompanying decrease in the proeutectoid phase strength, i.e.

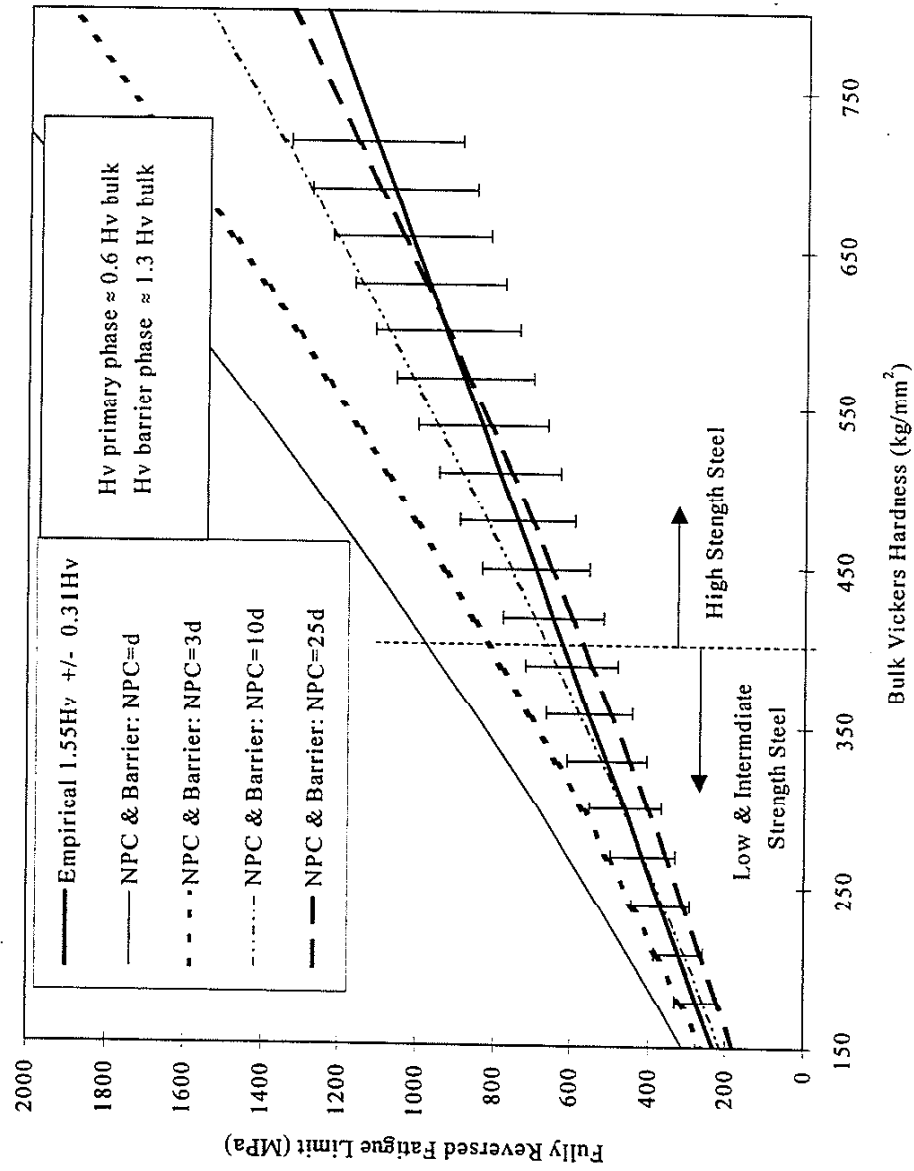


Figure 5.7 Effect of Barrier Strength and NPC Size on the Fatigue Limit: HPM Model vs. Empirical Relationship

larger ferrite grains, results in an increase in the NPC flaw size. Figure 5.8 illustrates the predicted fatigue limits when NPC flaw sizes are equal to  $d$ ,  $3d$ ,  $10d$ , and  $25d$  where the change in  $d$  is not considered. If the change in the flaw size is not considered, then the predicted fatigue limit is observed to increase and fails to agree with the empirical data as shown in figure 5.8. Thus, for the two cases considered here, the benefits of increasing the barrier strength have been equally offset by the increase in the NPC size.

Thus, the HPM model qualitatively and quantitatively predicts the effects of flaw size and barrier strength for many industrial materials. However, one should not interpret that all ferritic and ferritic-pearlitic steels will have fatigue strengths as indicated by the empirical predictions illustrated in figures 5.6-5.8. On the contrary, the behavior observed historically from which the empirical relationship was derived is for conventionally processed steels. Steels that are processed in another manner may behave much differently. This is readily apparent when the results of the literature data examined earlier in this chapter are compared to the empirical and HPM predictions as illustrated in figure 5.9.

The observed fatigue limit is plotted on the abscissa and the predicted fatigue limit on the ordinate. Perfect correlation is designated by the broad solid line with  $\pm 10$ , 20, and 50% errors indicated by the dashed lines. Empirical predictions were made with both forms of equation 1.2, the ultimate tensile strength and hardness forms. Bulk hardness was estimated by employing the rule of mixtures with the hardness of each constituent phase. Hollow circular symbols represent the predictions for the hardness

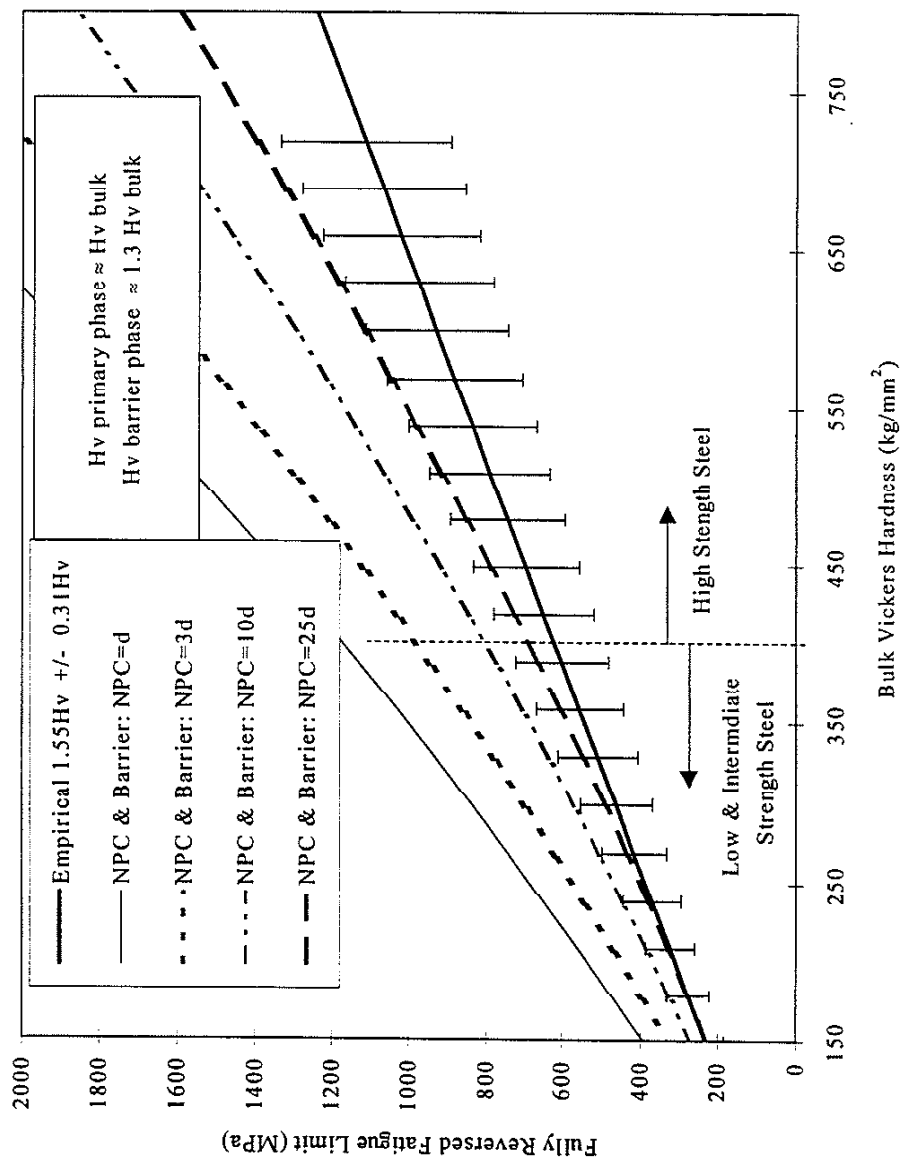


Figure 5.8 Importance of Accounting for Primary Phase Grain Size in Determining Non-propagating Crack Size

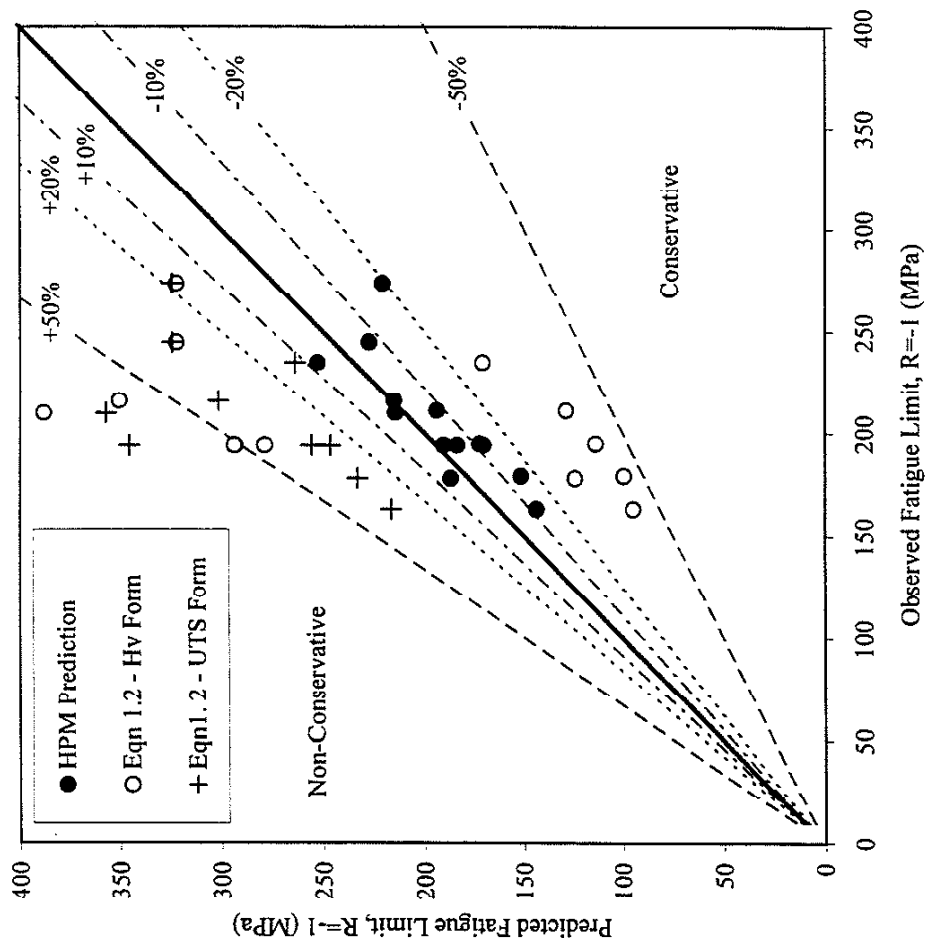


Figure 5.9 Comparison of HPM Model Predictions and Empirical Predictions with Observed Fatigue Limits of Various Low Strength and Intermediate Carbon Steels Reported in the Literature

form of equation 1.2. The predictions are observed to group into two different sets, one set on the conservative side and the other set on the non-conservative side of the perfect correlation line. Examination of each set reveals that the set lying on the conservative side of the solid line consists entirely of the single phase ferritic steels taken from the literature. The other set consists of the duplex steels. Predictions made with the ultimate tensile strength form of equation 1.2 are represented by the plus symbols. Unfortunately, ultimate tensile strengths were not reported for any of the single phase ferritic steel investigations. All of the duplex steel ultimate tensile strength predictions are observed to be non-conservative, by 10% to 50% or more. Thus, use of the empirical relationship to predict fatigue limits can result in conservative or non-conservative predictions with errors ranging from 20% to 50% or more depending on whether the material is a single phase ferritic steel or a duplex phase ferritic-pearlitic steel, at least for the materials examined here. None of the empirical predictions for the materials examined fall within 10% of the observed fatigue limit and only three fall within 20%. On the contrary, all the HPM predictions, which are represented by the solid circular symbols, are observed to fall within 20% of the observed fatigue limits and about two thirds of the data lie within 10%. Thus, the HPM predictions are far superior to the empirical predictions. This is because the HPM model accounts for variations in the microstructure, i.e. flaw size and barrier strength, which cannot be accounted for by bulk properties such as tensile strength and bulk hardness.

## 5.2 Inherent Regime

Not all materials are free of harmful inhomogeneities: inclusions, carbides, porosity, etc. Murakami has shown in detail how to quantify the effects of these inherent flaws with the  $\sqrt{\text{area}}$  parameter model given in equation 4.18. Since the HPM model was derived from the  $\sqrt{\text{area}}$  parameter model to address the intrinsic fatigue strength of a material, the two models are identical in the inherent flaw regime. Validation of the HPM model in this regime has already been conducted by Murakami. However, for completeness, a small subset of validating data reported by Murakami and colleagues is included. The model can be validated via two methods.

Investigation of ‘fish eye’ rotating bending fatigue origins allows one to indirectly verify the model. Murakami and colleagues [35,76-83] have reported a considerable amount of this type of validation. Nominal surface stress is not the true measure of the stress seen by a flaw. The stress that a flaw experiences is a function of the nominal surface stress and the location of the flaw relative to the surface. So, one first calculates the nominal applied stress at the inclusion from which the fatigue crack originated. Then, based on the hardness of the material and the size of the flaw a local fatigue limit prediction is made. The ratio of the nominal stress at the inclusion to the local fatigue limit prediction should be greater than one to validate the model. A sample is provided in table 5.5. Note that the local stress at the fatigue origins are observed to be larger than the predicted fatigue limit, i.e. the ratio is always greater than one. Predicted fatigue limits are made by implementing equation 4.18,

$$\Delta\sigma = \frac{1.43(H_v + 120)}{\sqrt{area}^{1/6}}. \quad (4.18)$$

Table 5.5 Indirect Verification of Inherent Inclusion Predictions [9]

Size and location of inclusions and fatigue limit predicted (Bearing steel ; $H_v = 758$ )							
Nominal stress at surface, $\sigma$ (MPa)	Cycles to failure, $N_f$	Inclusion size, $\sqrt{area}$ ( $\mu m$ )	Distance from surface, $h$ ( $\mu m$ )	Shape of inclusions	Nominal stress at inclusion, $\sigma'$ (MPa)	Fatigue limit predicted $\sigma_w'$ (MPa)	$\frac{\sigma'}{\sigma_w'}$
1030	125.25 $\times 10^4$	24.0	310		954	806	1.18
1030	556.77	15.9	140		995	863	1.15
981	422.95	15.2	28		973	870	1.12
981	898.01	9.9	74		963	934	1.03
981	175.51	12.5	10		978	899	1.09
1030	224.64	18.6	74		1011	841	1.20
1030	30.52	22.2	24		1023	817	1.25
1030	26.48	28.4	110		1003	784	1.28
971	735.45	28.9	350		886	782	1.14

Of course, the size of the flaws varies throughout a material. Similarly, the largest flaw in a given volume of material is a random variable where the nature of the inclusion distribution makes the fatigue limit vary from specimen to specimen as previously discussed. Fortunately, the maximum size flaw that can be expected is predictable if one utilizes the statistics of extremes inclusion rating method proposed by Murakami. The method allows for the prediction of the lower bound fatigue limit and



has been successfully implemented for a large number of applications and materials [9,32-34]. First, one makes numerous measurements of flaw sizes observed in the material. The size and frequency of their occurrence is fit by a double exponential distribution function, a Gumbel function [33]. Then, the maximum flaw size that can be expected in the material for a large number of specimens or components is predicted with the distribution function and a fatigue prediction is made with the predicted extreme flaw size. This prediction is referred to as the lower bound prediction since the largest flaw expected is considered rather than the average or maximum observed flaw. Comparison of rotating bending fatigue test data with the lower bound prediction and the extrapolation of the empirical fatigue prediction provides a means of analyzing scatter in fatigue testing. Figure 5.10 illustrates how some typical fatigue test results correlate with the lower bound fatigue limit prediction and the empirical prediction. Note that the no specimens fail at stresses smaller than the lower bound fatigue limit. Furthermore, some specimens fail at low stresses while others do not fail at even higher stresses. The scatter is due to the probabilistic nature of the size and presence of a flaw in the material.

### 5.3 Processing Regime

Processing flaws are quantified in an identical manner as inherent flaws with the only difference between the two being the manner by which the flaws were introduced

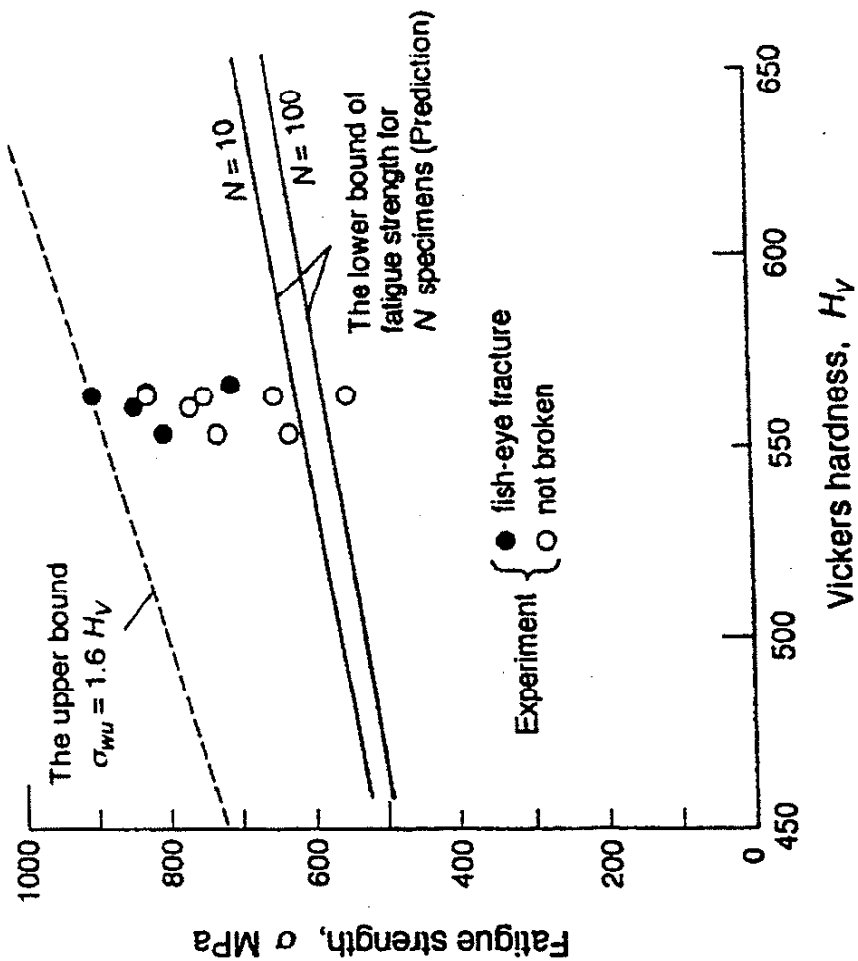


Figure 5.10 Comparison of Rotating Bending Fatigue Test Data with  $\sqrt{\text{area}}$  Parameter Model Combined with the Statistics of Extremes Inclusion Rating Method of Predicting a Lower Bound Fatigue Limit [9]

into the material. Nucleation mechanisms may differ between inherent and processing flaws, transgranular vs. intergranular respectively. However, the condition for crack propagation must be transgranular because the  $\sqrt{area}$  parameter threshold condition is governed by transgranular cracking mechanisms; the HPM model cannot predict the thresholds of materials that exhibit intergranular crack propagation.

Data from both the literature and tests conducted in this study were used to illustrate the adverse effects associated with processing flaws. Most of the literature data was generated with carburized steels; however, this should not imply that the model is limited to carburized or martensitic steels. Some of the literature results are tabulated in tables 5.6. The remaining literature results and results of the tests conducted in this study are addressed later in chapter 6.

Table 5.6 lists the predictions and results of a series of tests conducted by Hyde [47] on fifteen carburized 4320 steels. All applied load ratios were equal to 0.1. However, the presence of residual stresses resulting from the carburizing process alter the actual load ratio the material experiences. Actual load ratios were calculated to account for the effects of residual stresses. The resulting load ratios ranged from  $-0.21$  to  $+0.05$ .

The purpose of the investigation was to determine the effects of alloy content on intergranular crack nucleation, specifically the effects of bulk phosphorous content on the segregation of phosphorous to grain boundaries. Observed and predicted fatigue limits are listed in the second and third columns. Error in the predicted fatigue limit relative to

Table 5.6 Intergranular Crack Nucleation in Carburized 4320 [47]

Material	Observed Fatigue Limit <sup>†</sup> (MPa)	Predicted Fatigue Limit (MPa)	Error (%)	Intergranular Nucleation Depth ( $\mu\text{m}$ )	Prior Austenite Grain Size <sup>††</sup> ( $\mu\text{m}$ )
<b>Base Carburized</b>					
Material	518	523	1	25	15
<b>As-Carburized<sup>‡</sup></b>					
0.005 P	506	541	7	20	15
0.017 P	484	512	6	30	15
0.031 P	394	526	34	40	15
<b>Single Reheat<sup>‡</sup></b>					
0.005 P	608	660	9	10	5-15
0.017 P	608	663	9	10	5-15
0.031 P	574	571	-1	30	5-15
<b>Triple Reheat<sup>‡</sup></b>					
0.005 P	641	659	3	10	5-9
0.017 P	641	667	4	10	5-9
0.031 P	641	671	5	10	5-9
<b>Boron &amp; Titanium<sup>‡</sup></b>					
0.001 Ti	596	540	-9	40	16
0.015 Ti	617	600	-3	20	23
0.039 Ti	581	508	-13	40	23
<b>Si,Cr Free<sup>‡</sup></b>					
No B&Ti	709	613	-14	25	15
0.0014 B & 0.038 Ti	644	522	-19	50	22

<sup>†</sup> Stress amplitude at actual R-ratio.  $R_{\text{applied}}=0.1$  and  $R_{\text{actual}}: [-0.21, +0.05]$ .

<sup>††</sup> Uniform or surface-core grain size(s).

<sup>‡</sup> Numbers correspond to bulk wt. % phosphorous, titanium, and boron.

the observed fatigue limit is provided in the fourth column. Intergranular crack depths and average prior austenitic grain sizes for each material are provided in the last two columns. Flaw depths were estimated with reported flaw sizes and measurements of

actual flaws made from photographs of the fracture surface. The predicted fatigue limits are excellent, within 20% error except for the 0.031 wt%P as-carburized prediction. Note, the intergranular crack sizes are on the order of one or several prior austenite grains. Furthermore, materials with smaller intergranular flaws generally exhibit superior fatigue strengths relative to the materials that contain larger intergranular flaws as expected.

## CHAPTER 6

### FLAW SIZE AND NUCLEATION MECHANISMS

#### 6.1 Tempering of Medium Carbon Steel - Garwood et al

Typically, tempering is a process used to remove residual stresses that exist after martensite formation and to soften the martensite by precipitation of carbon atoms as cementite ( $\text{Fe}_3\text{C}$ ). While the yield strength has been reduced due to a reduction in solid solution hardening of carbon atoms, the cementite particles produce a precipitation hardening effect. This results in a very high strength steel with high toughness. The question arises as to what effects the tempering process has on the intrinsic flaw size and the fatigue strength. A close inspection of the changes that occur in the microstructure during the tempering process is required; for this purpose, the work of Garwood et al [54] will be examined.

Garwood conducted fatigue tests on several series of automotive steels with carbon contents of 0.40%, 0.50%, and 0.60% including the 4000, 5100, 4100, 4300, and 2300 series steels. All specimens were austenitized and quenched in oil followed by tempering at various temperatures to obtain the wide range of hardness levels tested, e.g. HRC 20 to 62. Results are plotted in figure 6.1. As discussed in chapter 4, the fatigue limit initially increases in a near linear fashion with hardness, then the rate of increase decreases until a critical hardness is reached at which point the fatigue limit is observed

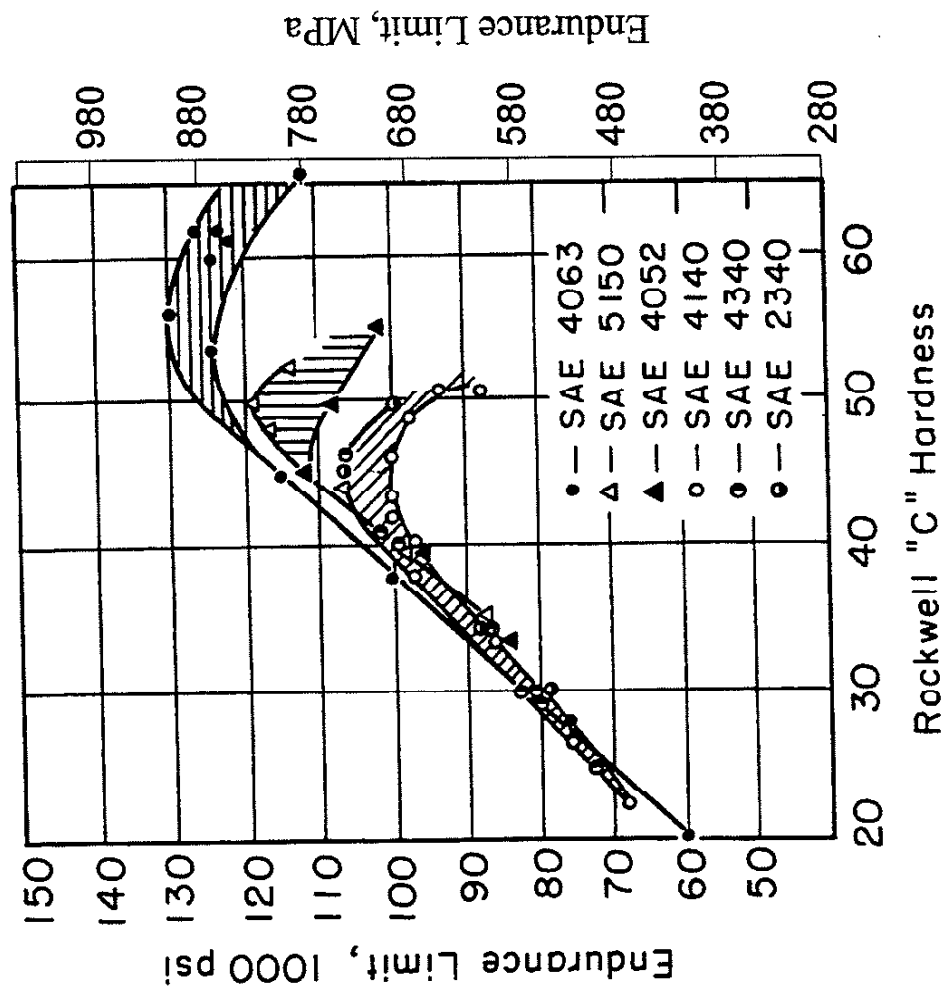


Figure 6.1 Relationship Between Fatigue Limit and Hardness as Observed by Garwood et al [54]

to decrease. Consider the two major effects resulting from the tempering process. The yield strength of the material was lowered although the intrinsic flaw size did not change during tempering; intrinsic flaw size is equal to the structure size of the martensite and/or the bainite present after tempering, approximately 1-3  $\mu\text{m}$ . (The reader should refer to Appendix A for a detailed discussion of the intrinsic flaw size of this material.) However, how do these changes affect the fatigue behavior of the steel? A simple but powerful qualitative and quantitative explanation of the observed behavior is provided by the HPM model.

Allowable stress is predicted with the HPM model over a broad range of hardness levels for a variety of flaw sizes. Figure 6.2 indicates that the predicted fatigue limit initially increases in a nearly linear fashion for flaws of size  $2a=2-3\mu\text{m}$ , the intrinsic structure size of the tempered martensite and bainite. The empirical relationship given in equation 1.2 is also provided. Furthermore, the intrinsic form of the HPM model is also provided for comparison where the intrinsic structure size,  $d$ , was estimated from the measured hardness. Figure 6.3 compares the observed strength with the predictions. The intrinsic HPM model prediction is seen to be very non-conservative. On the contrary, the empirical prediction is conservative until the fatigue limits are observed to decrease with increasing hardness. Garwood's results follow the HPM predictions extremely well until critical hardness levels of about 42, 47, and 52 HRC are reached in the 0.4%, 0.5%, and 0.6% carbon steels respectively. Since the hardness levels were achieved by tempering the intrinsic flaw size should be constant for all hardness levels; inclusion content should be constant as well. Thus, changes in the observed fatigue limits at these transition points



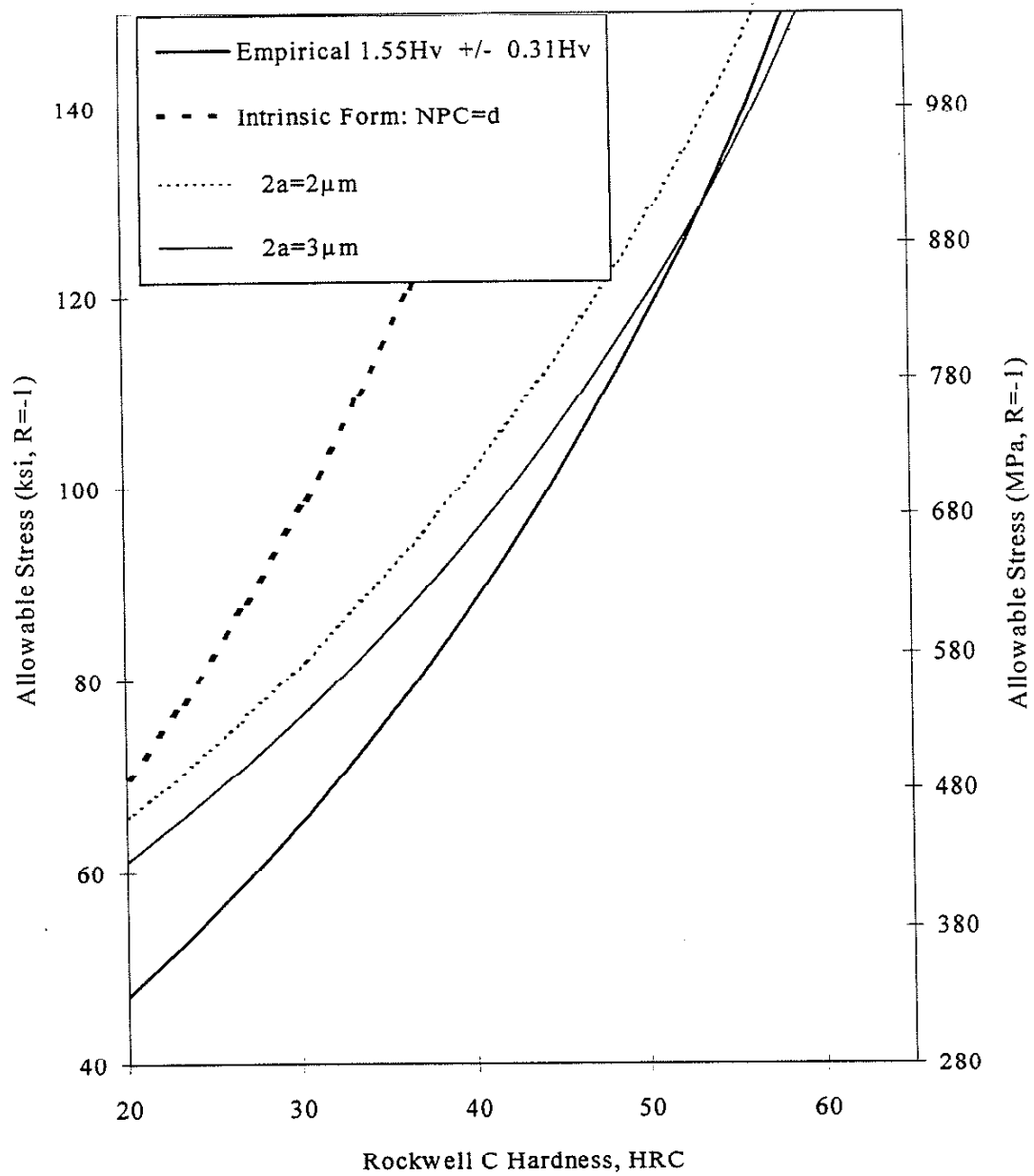


Figure 6.2 Predicted Fatigue Limits for Microstructure of Garwood's Material

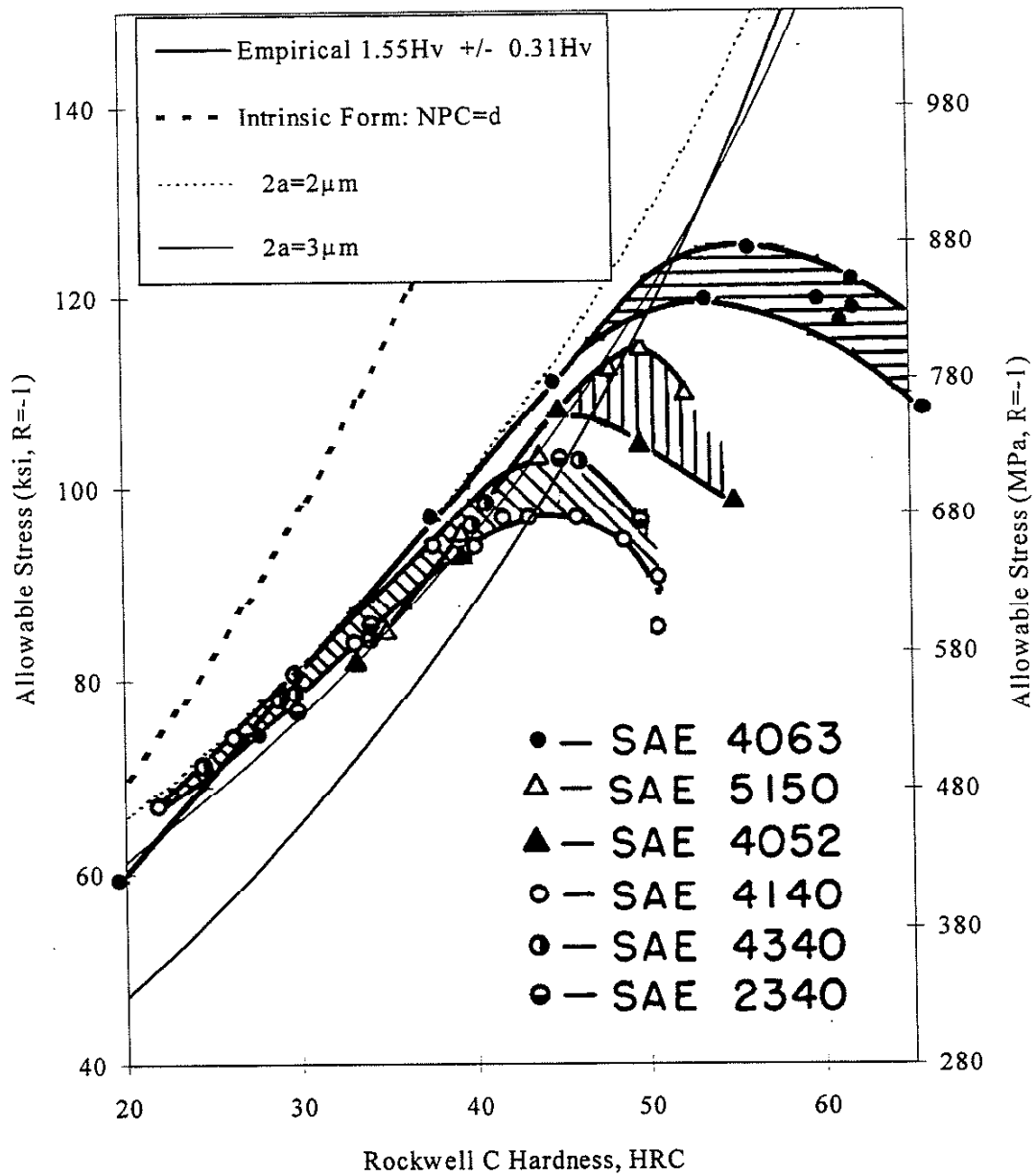


Figure 6.3 Comparison of HPM Predictions with Fatigue Limits Observed by Garwood

must be due to a new active fatigue mechanism. Intergranular cracks are hypothesized to form due to changes in grain boundary and bulk microstructure and properties that resulted from the various tempering treatments. Evidence exists in the literature to support this hypothesis as previously discussed in section 4.3. As seen in figures 6.4 and 6.5, the concept is indirectly verified by the intersection of the HPM model predictions of a given flaw size with the fatigue limits observed by Garwood. For example, flaw sizes corresponding to the fatigue limits for the SAE 4052 and 5150 specimens which are harder than the critical hardness of 50 HRC are approximately  $2a=10\text{ }\mu\text{m}$ , on the order of typical prior austenitic grain sizes. Garwood does not report the mechanisms associated with the observed results. Furthermore, residual stresses and inclusion content more than likely played a role in the observed behavior, but their effects are impossible to predict without quantitative knowledge of their magnitude and size. Thus, several tests were performed to confirm the change in fatigue nucleation mechanisms.

## **6.2 Tempering & Altering the Fatigue Nucleation Mechanism**

Tests were performed to determine if nucleation mechanisms in high strength steel could be altered from an intergranular mode to a transgranular mode solely by tempering. For this study, the experimental modified 8680 heat of steel was selected. Two lots of specimens were manufactured from the same ingot. The first lot was utilized in a surface finish study that is discussed later in chapter 7, while the second was used to investigate the effects of tempering on fatigue nucleation mechanisms. Two prior

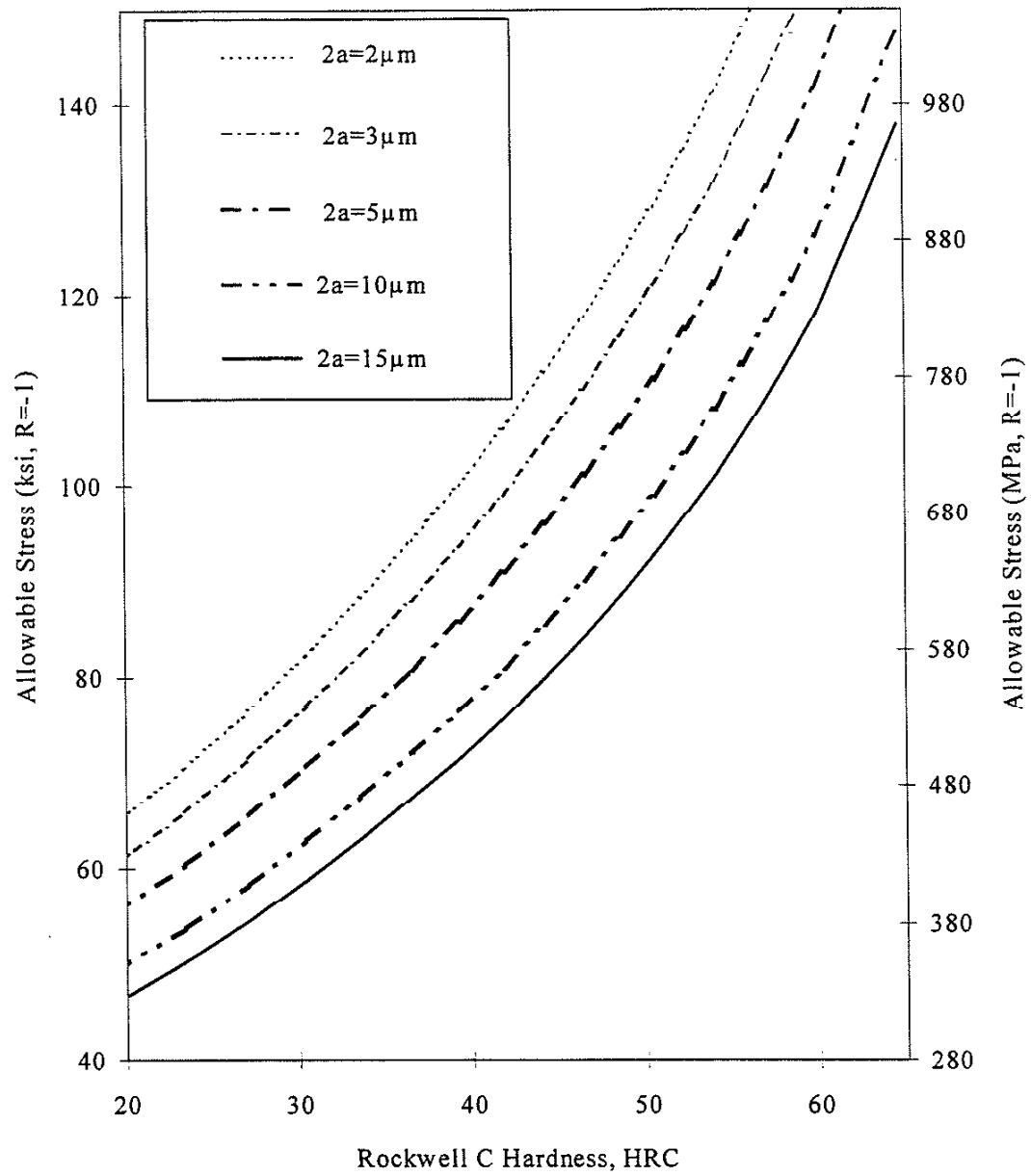


Figure 6.4 HPM Model Predictions for Various Larger Flaws

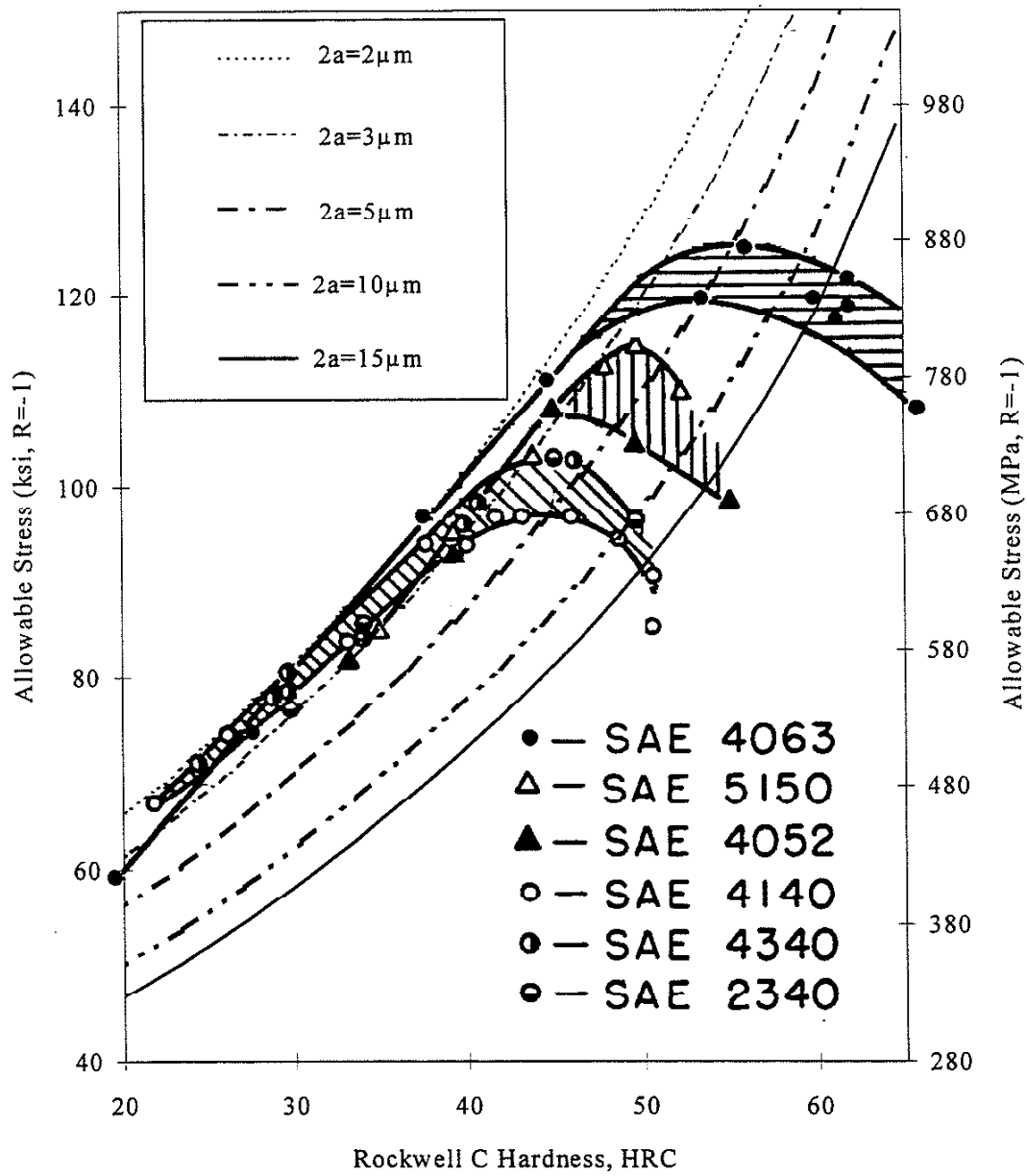


Figure 6.5 Comparison of HPM Model Predictions and Observed Fatigue Limits- Effect of Larger Flaws

austenitic grain sizes were investigated. Measurements of prior austenite grain size could not be achieved due to the difficulty associated in revealing grain boundaries by etching in high strength steels. However, grain sizes based on observations of intergranular facets in broken specimens are estimated to be 10 and 20  $\mu\text{m}$  for the triple vacuum and single vacuum specimens respectively. The single vacuum specimens were heat treated by fully austenitizing in a vacuum and quenching in oil. The finer grained material was achieved by an identical heat treatment as in the single vacuum material, except that the heat treatment process was repeat two times.

### **6.2.1 150°C Temper Fatigue Behavior**

Specimens that received a low temper of 150°C for one hour after quenching in oil are referred to simply as “the second lot” whereas specimens that received additional tempering at 315°C for one hour are referred to as “the tempered lot”. Test results for the tempered lot specimens are presented in section 6.2.2. Regardless of the grain size, intergranular crack nucleation was observed in each specimen within the second lot. Crack nucleation depth could not be discerned because of the subsequent intergranular crack growth. As indicated in figures 6.6a-6.6c, the entire surface of each specimen consisted of intergranular facets. Figure 6.6a indicates the macroscopic features of the fracture surface. A dashed white line outlines the crack origin, which is presented at a higher magnification in figure 6.6b. Intergranular facets are more readily apparent. Further examination of the region outlined by the white rectangle reveals the details of

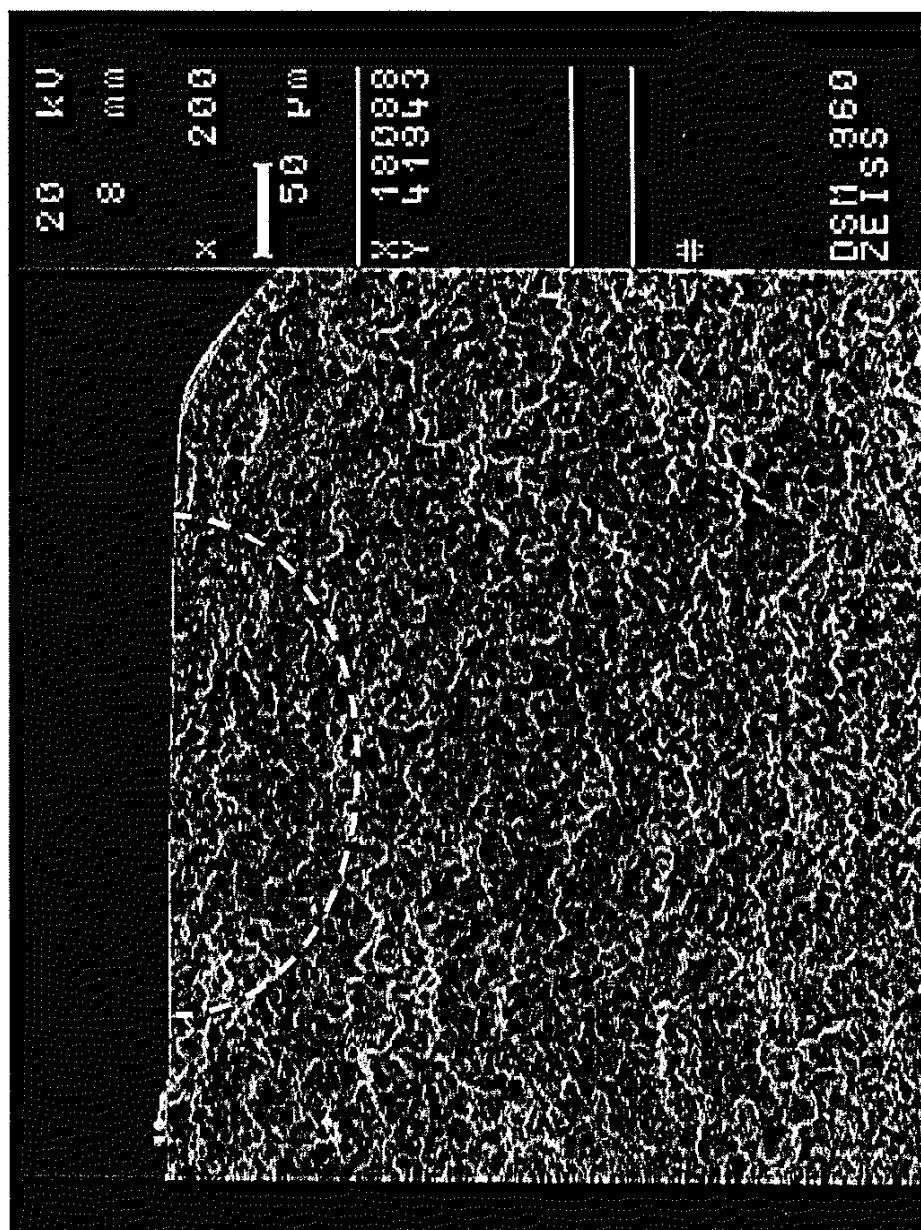


Figure 6.6a Intergranular Crack Nucleation and Growth in 8680 TripleVacuum Steel

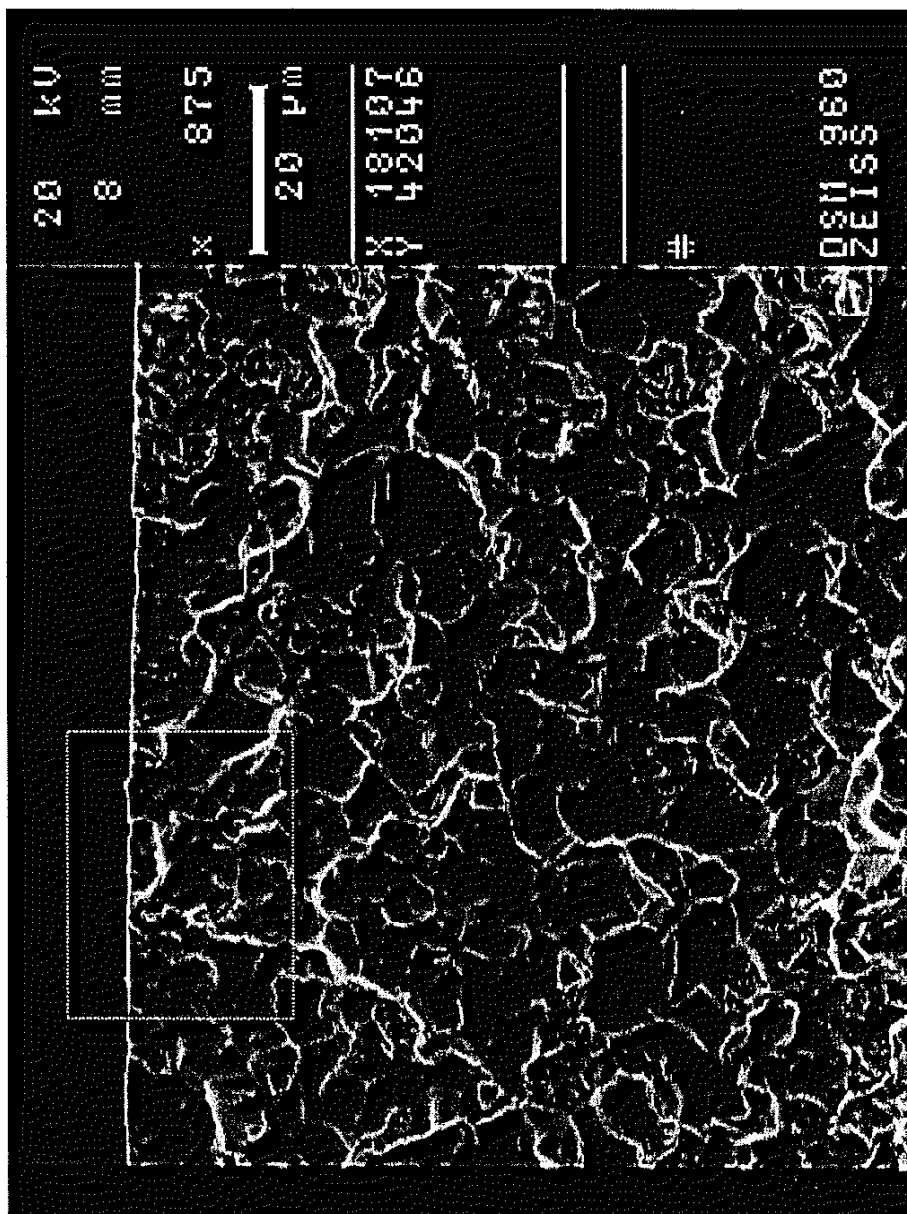


Figure 6.6b Intergranular Crack Nucleation and Growth in 8680 Triple Vacuum Steel: 875X



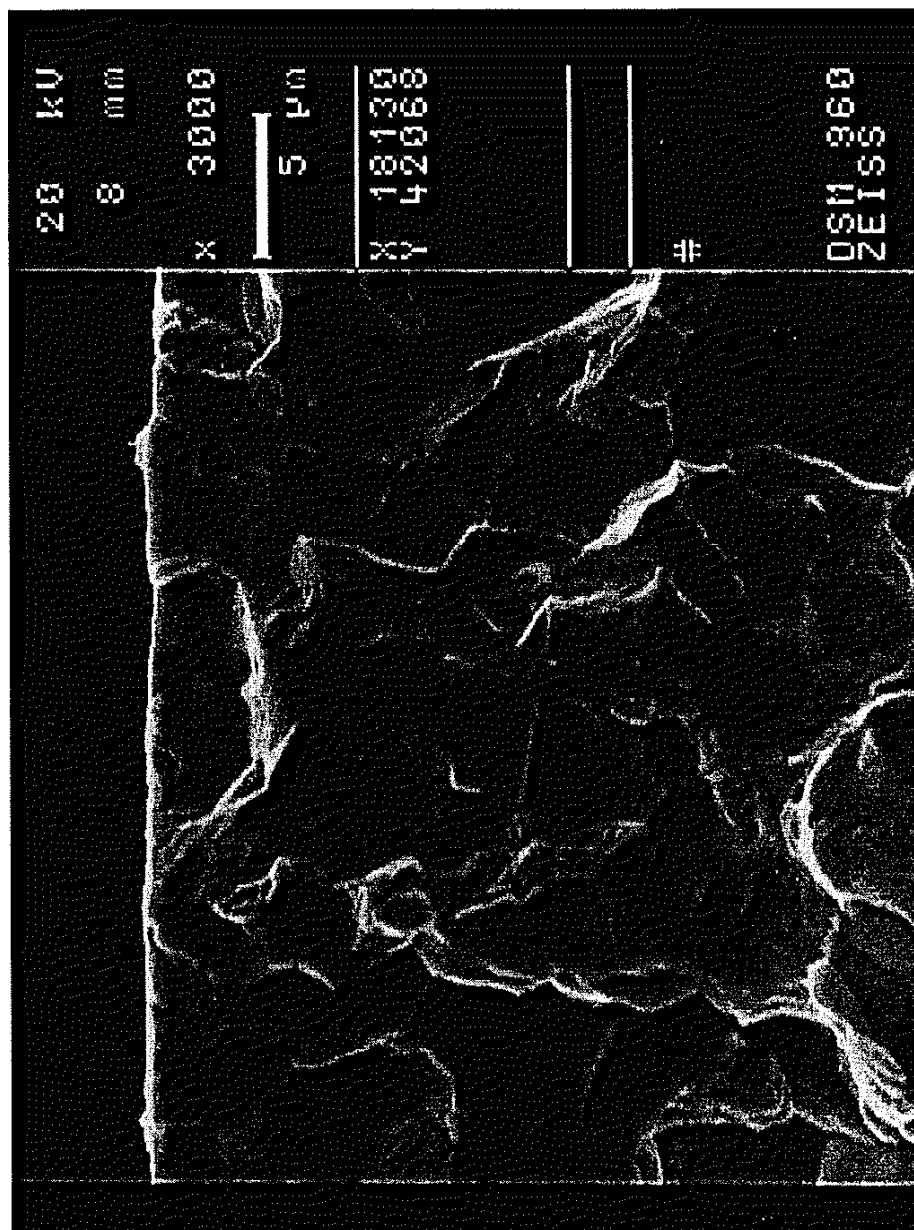


Figure 6.6c Intergranular Crack Nucleation in 8680 TripleVacuum Steel: 1000X

typical intergranular crack nucleation and growth observed in all the second lot specimens, see figure 6.6c. Observed fatigue limits are illustrated in figure 6.7 and listed in table 6.1, note that the triple vacuum specimens do exhibit a significantly higher fatigue resistance than the single vacuum group. This could be attributed to a smaller degree of grain boundary embrittlement associated with the finer grain structure as also observed in carburized steel where reduction of impurity element concentration at the grain boundaries was believed to occur because of the increased interface surface area [47,51]. However, both groups do exhibit considerably lower fatigue limits than commonly reported. This may partially be attributed to the presence of a thin carbide layer at the grain boundaries as indicated by Auger electron spectroscopy results. A carbide layer of approximately 10 nm thick was observed on the grain boundaries of all the modified 8680 specimens regardless of heat treating conditions, see Appendix C for details regarding Auger Electron Spectroscopy. No definite or single metallurgical factor can be identified as being responsible for the weak interface strengths. Results of the second lot, both the single and reheat vacuum 8680 steels, could not be predicted by the HPM model because the threshold condition was determined by the grain boundary strength rather than the bulk strength of the grain.

Table 6.1 Fatigue Limit of Embrittled 8680 Steel

Modified 8680 Steel	Surface Finish	Fatigue Limit (MPa)
Single Vacuum (No reheat)	Polished	180
	Ra = 3 $\mu\text{m}$	180
Triple Vacuum (Double reheat)	Polished	250
	Ra = 1, 3, 12 $\mu\text{m}$	180

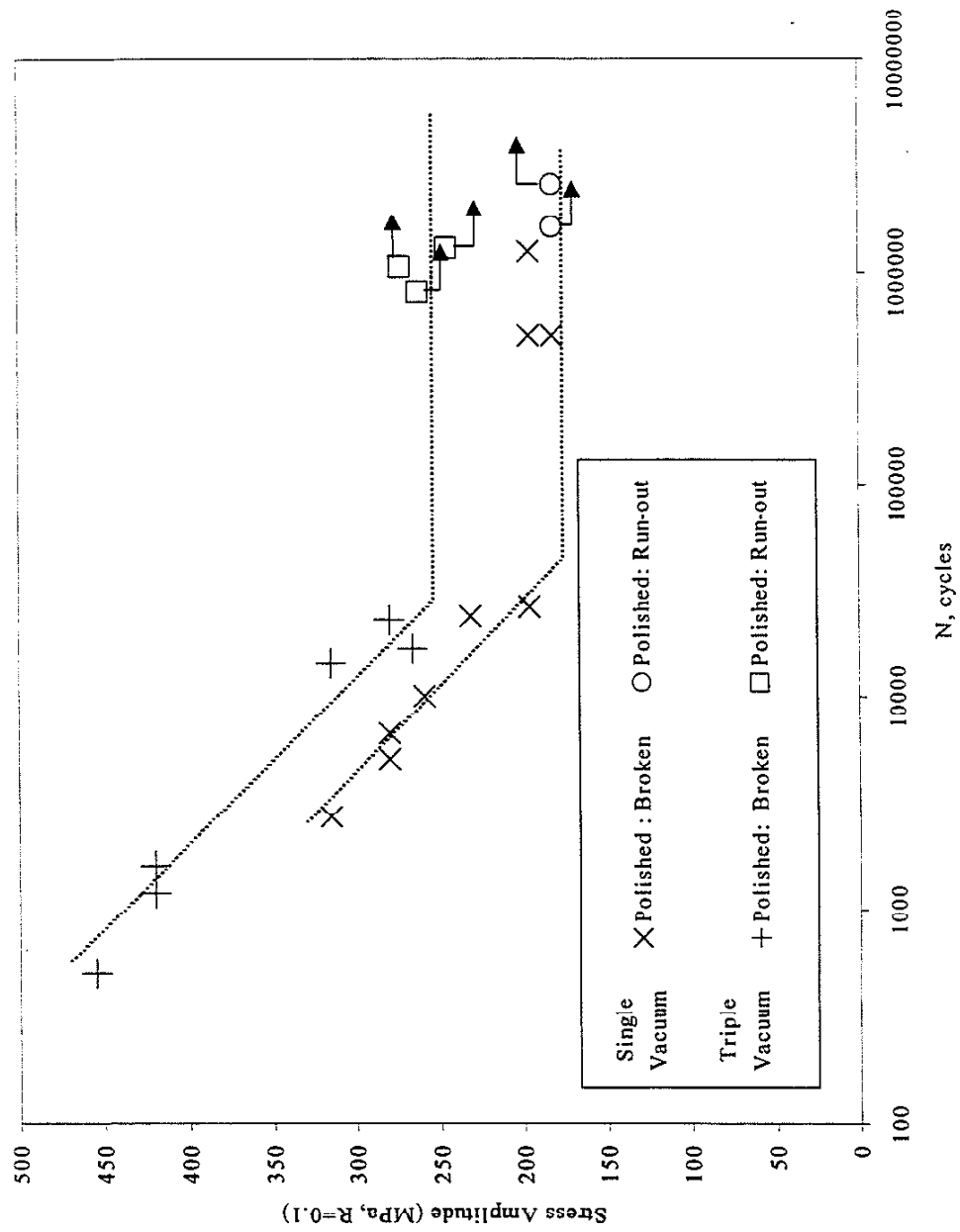


Figure 6.7 Observed Fatigue Limit of 8680 Vacuum Heat Treated Steel

## 6.2.2 315°C Tempered Fatigue Behavior

Several of the untested single and reheat vacuum specimens were tempered for an additional hour at 315°C in an attempt to alter the active fatigue mechanism. Hereafter, the specimens are referred to as the tempered lot. Tempering reduced the average Vickers hardness by about 30% from 660 to 460. Typically, fatigue strength would decrease with the reduction in hardness; however, the fatigue threshold mechanism was altered by the tempering process. Cracks were still observed to nucleate intergranularly in the tempered single vacuum specimens as illustrated in figures 6.8a-6.8c, but the threshold mechanism was observed to be transgranular. Again, macroscopic features are illustrated in figure 6.8a with closer views of the crack origin depicted in figures 6.8b and 6.8c. Intergranular crack nucleation is indicated by the large but smooth facets that have well defined grain boundaries and are labeled with the letter I in figure 6.8c. Transgranular crack growth is revealed by the smaller facets, which have more features than the larger smooth intergranular facets; they are labeled with the letter T.

Cracks were observed to nucleate by even smaller intergranular cracks in the triple vacuum specimens due to the smaller grain size as indicated by figures 6.9a-6.9c. Macroscopic features are illustrated in figure 6.9a and 6.9b whereas the intergranular and transgranular fatigue facets are indicated by the letters I and T respectively in figure 6.9c. All cracks in the triple vacuum tempered lot nucleated at corners of the specimens. In contrast, no cracks nucleated at the corners in the tempered single vacuum specimens. The difference in origin locations may be explained by the fact that specimen corners

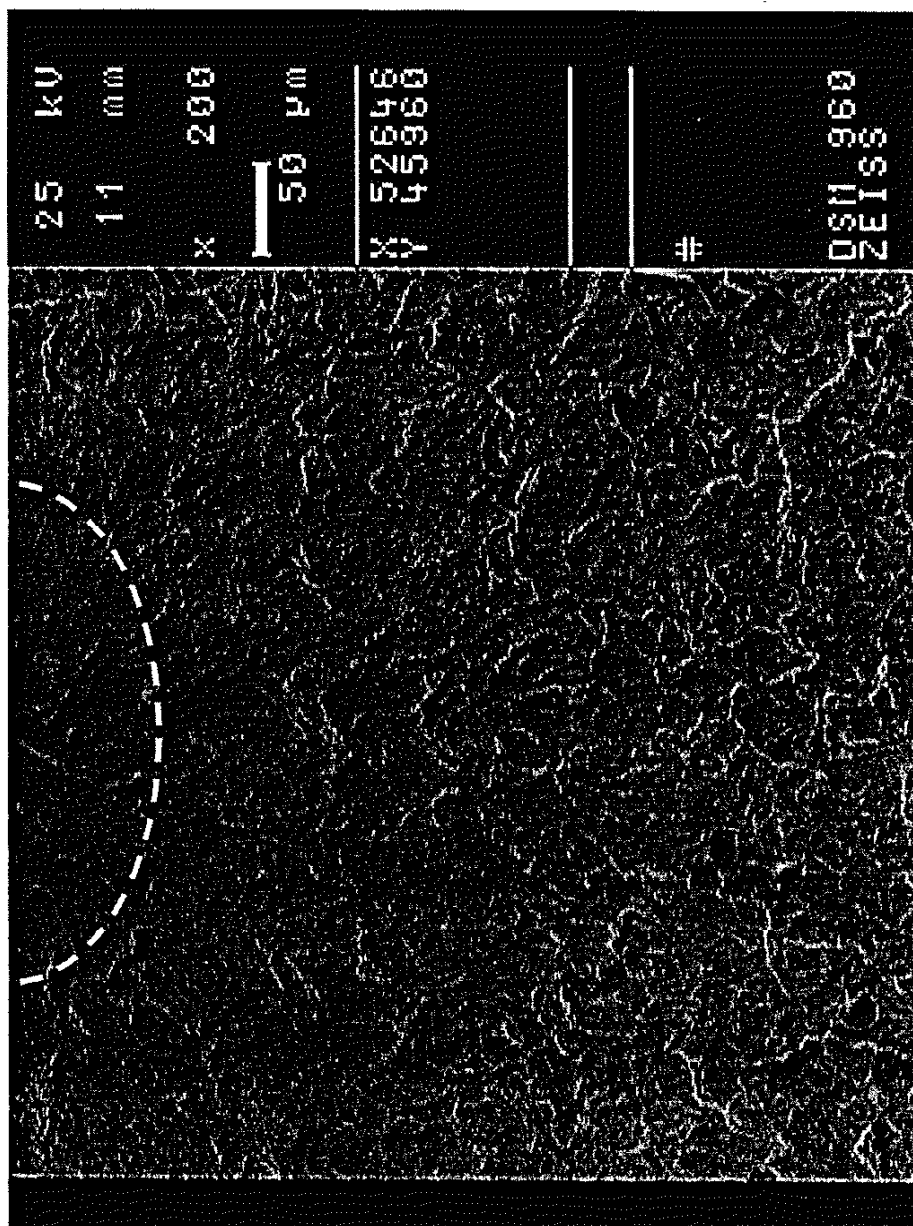


Figure 6.8a Intergranular Crack Nucleation and Transgranular Growth in 8680 Single Vacuum Steel

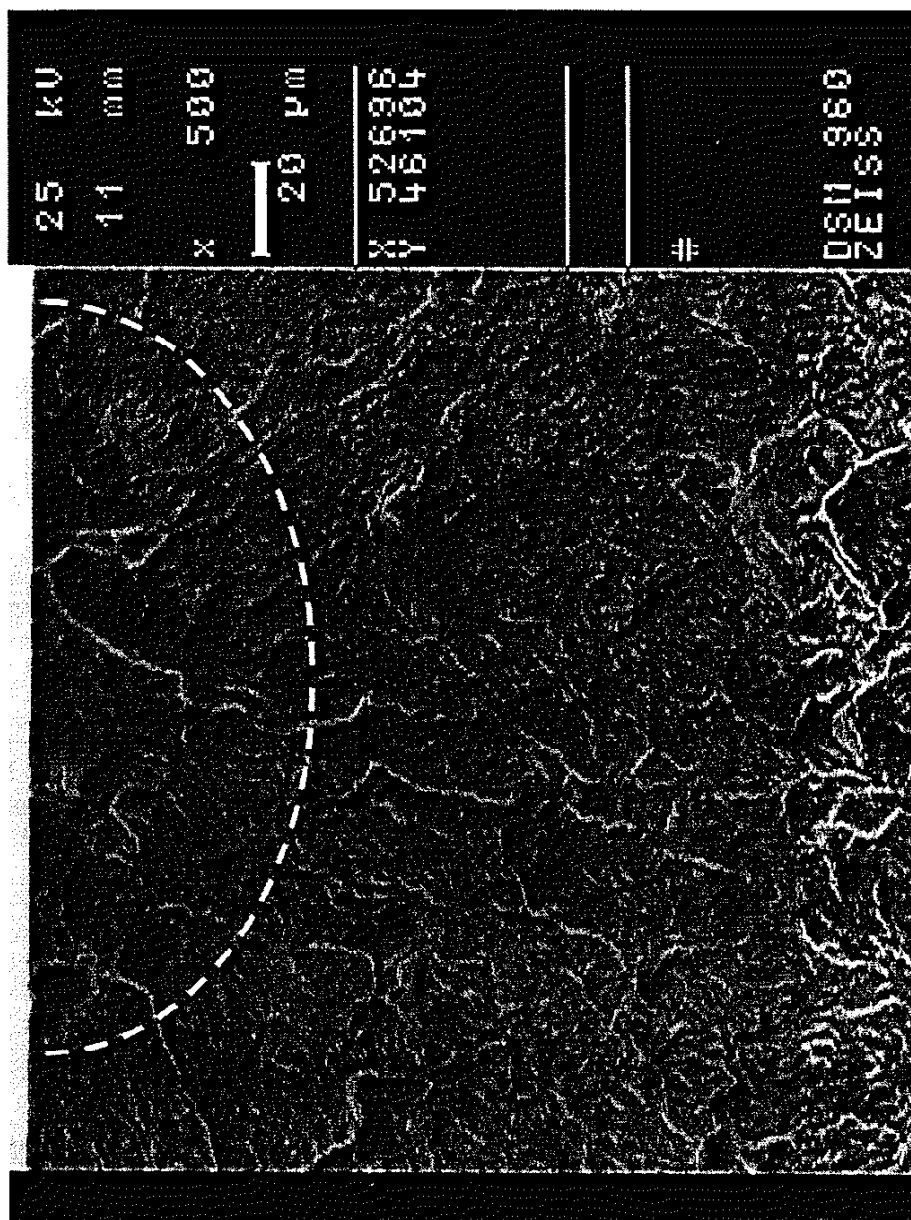


Figure 6.8b Intergranular Crack Nucleation and Transgranular Growth in 8680 Single Vacuum Steel: 500X

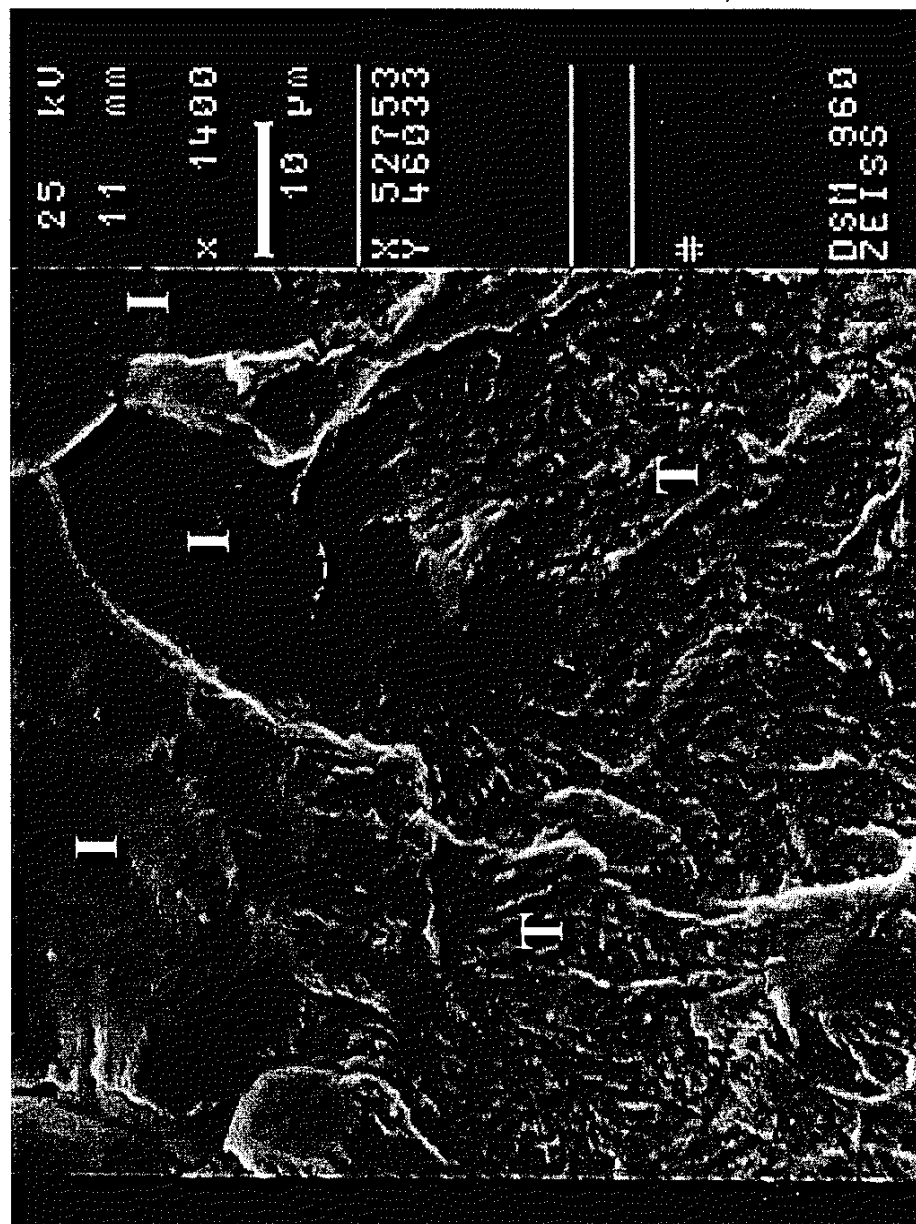


Figure 6.8c Intergranular Crack Nucleation and Transgranular Growth in 8680 Single Vacuum Steel: 1400X

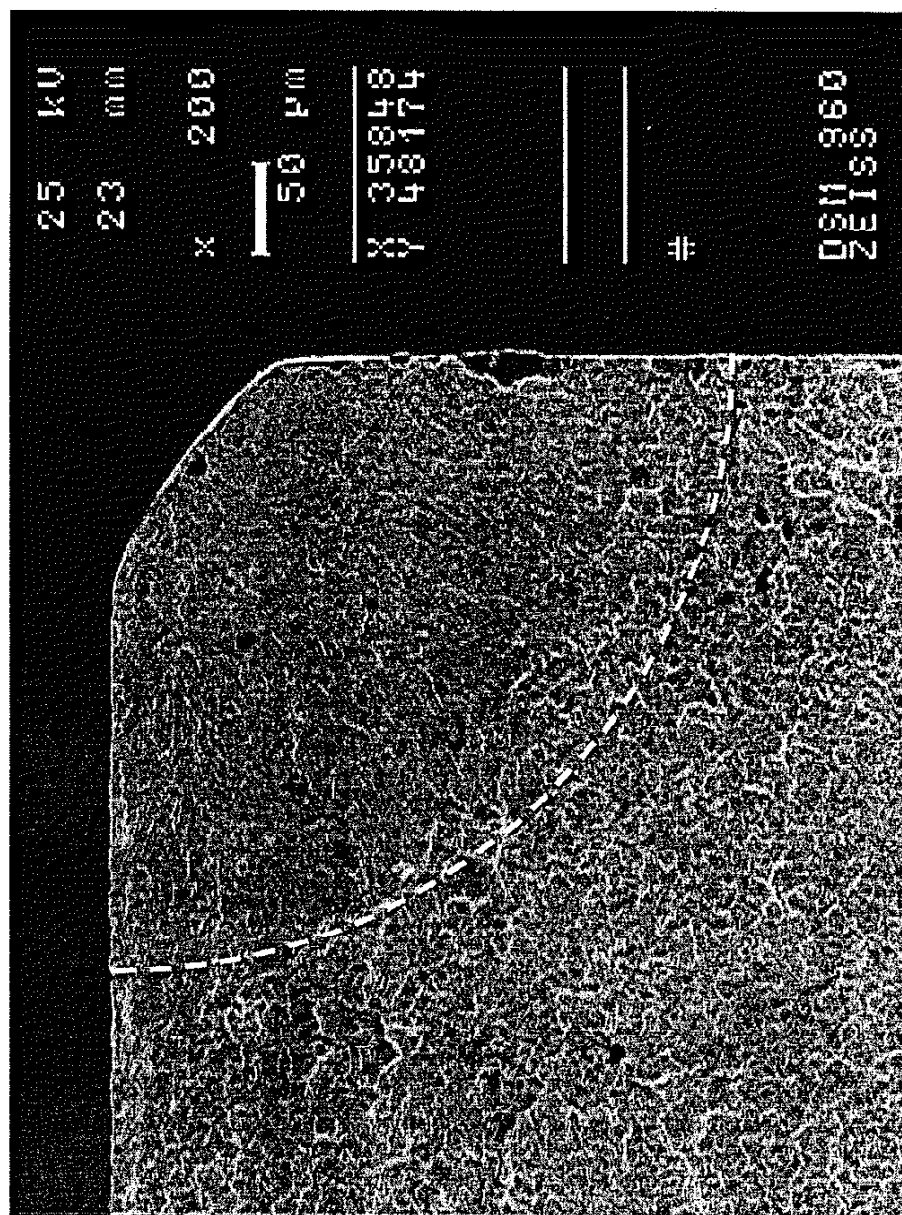


Figure 6.9a Intergranular Nucleation and Transgranular Growth in Tempered 8680 Triple Vacuum Steel



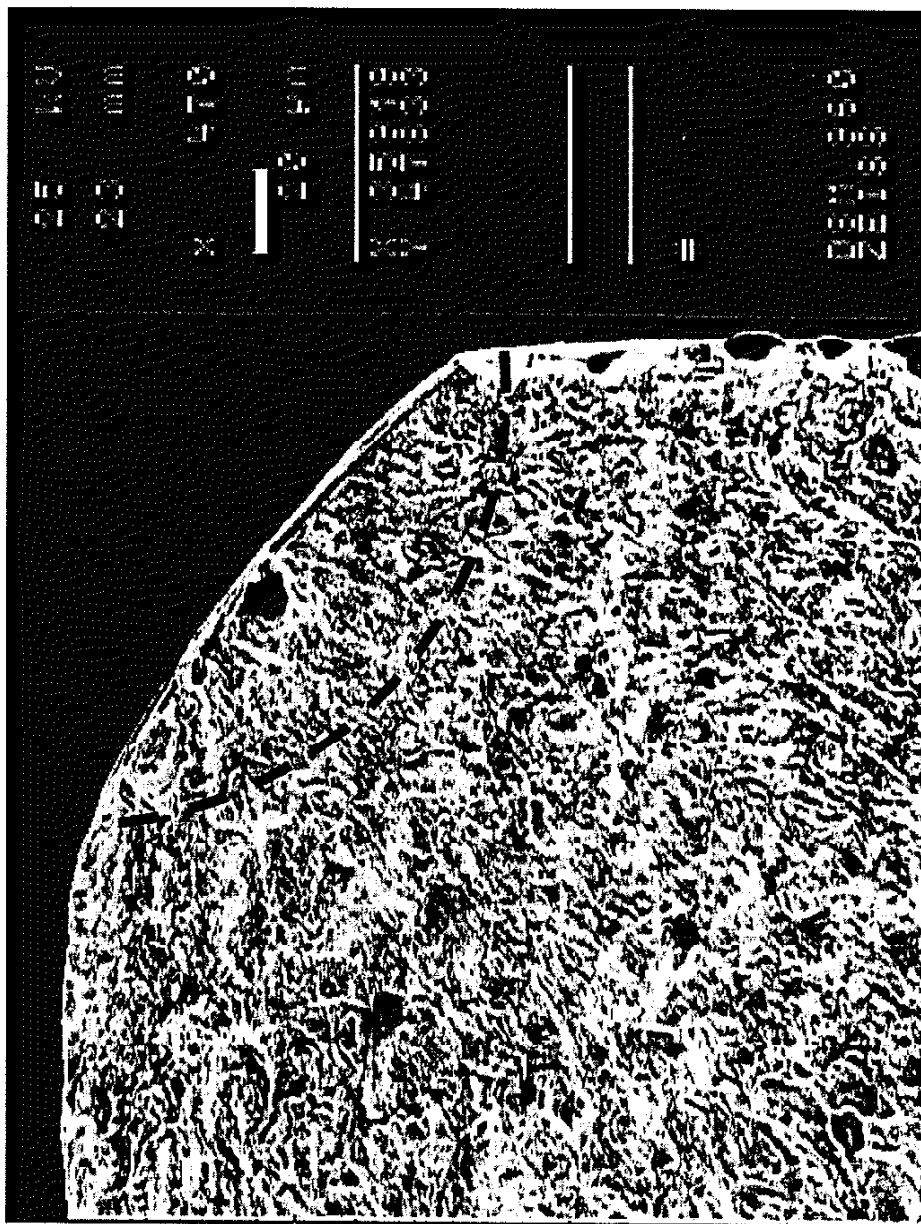


Figure 6.9b Intergranular Nucleation and Transgranular Growth in Tempered 8680 Triple Vacuum Steel : 470X



Figure 6.9c Intergranular Nucleation in Tempered 8680 Triple Vacuum Steel: 2800X

were not rounded but had a slight chamfer applied to them. The chamfer also may have left scratches on the corner surface whereas the top test surface was virtually scratch free. The single vacuum tempered specimens were likely less sensitive to the scratches due to the larger intergranular flaws present in the material whereas the intergranular cracks in the triple vacuum tempered lot were more sensitive. Cracks were always observed to propagate by transgranular mechanisms in the entire tempered lot.

Intergranular crack depths observed in the triple and single vacuum tempered materials were approximately 5-10  $\mu\text{m}$  and 20-40  $\mu\text{m}$  respectively, approximately one to two grains deep. Observed fatigue limits are listed in table 6.2a and depicted in figure 6.10 along with those observed prior to the additional tempering process. Fatigue limits for the second lot prior to additional tempering are listed in the third column. Notice that the fatigue limit of both surface finishes in the single vacuum group are lower than the polished triple vacuum group. In addition, the three different surface finishes tested in the triple vacuum group all exhibit the same fatigue resistance as the single vacuum group. Fatigue limits for the tempered lot are listed in the fourth column and the ratio of the tempered lot to the second lot (the lot with no additional temper) is given in the last column. Fatigue limits for the single and triple vacuum second lot specimens increased 70% by simply changing the propagation mechanism by tempering despite the 30% reduction in bulk hardness. This may seem surprising, but the HPM model suggests that an optimum barrier strength and flaw size exist that will maximize the fatigue limit.

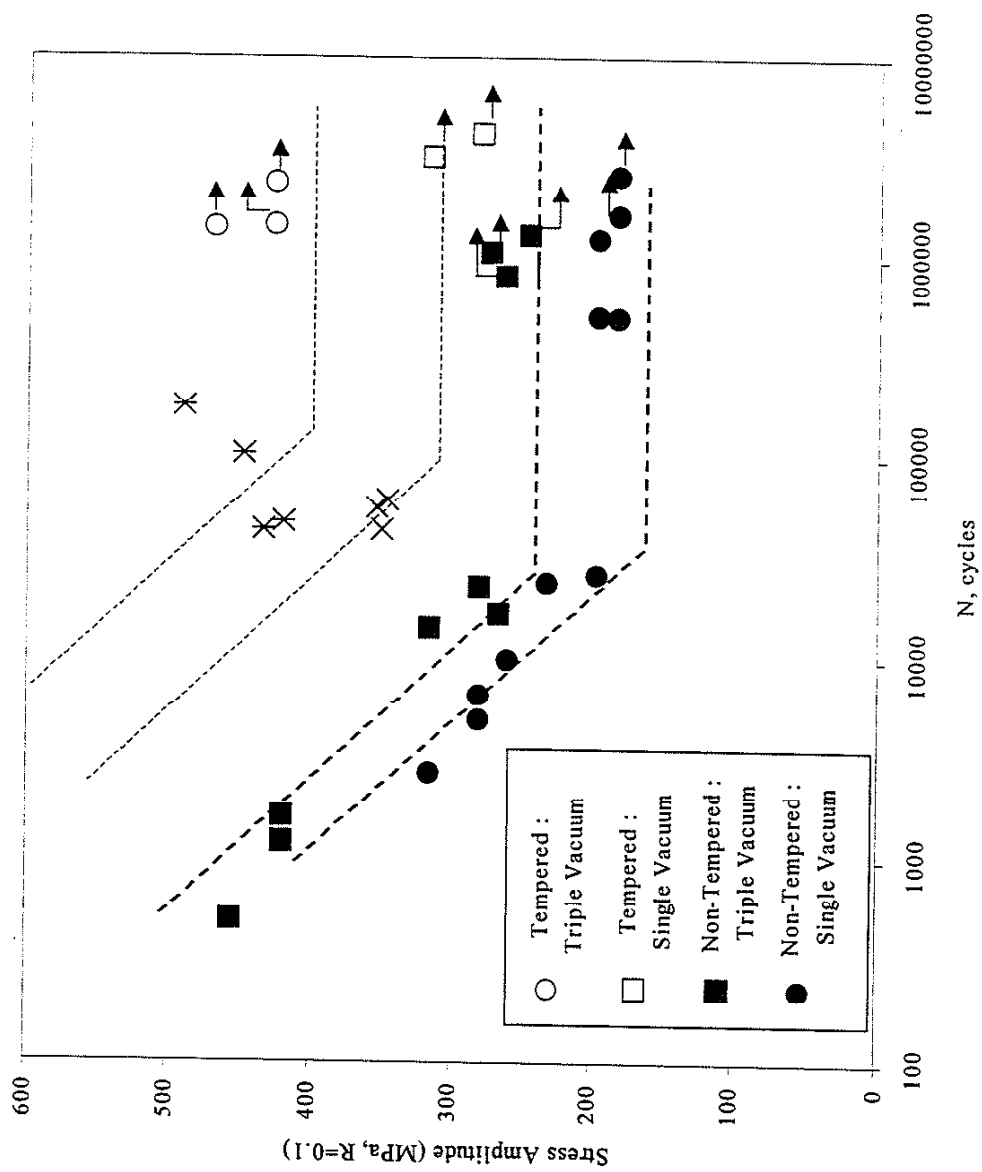


Figure 6.10 Comparison of 8680 Steel Fatigue Limits – Before and After Additional Tempering

Predictions of the tempered lot fatigue limits for polished specimens are provided in table 6.2b along with the observed fatigue limits. Observed flaw sizes of 10 and 40  $\mu\text{m}$  and the average Vickers hardness were implemented in the predictions. Flaws were also assumed to be semi-circular in shape. Triple vacuum specimens exhibit higher fatigue resistance than the single vacuum specimens, which is also predicted by the HPM model. Both predictions are excellent; errors are within 10%.

Table 6.2a Effect of Tempering on the Fatigue Limit of 8680 Steel

Modified 8680 Steel	Surface Finish	Embrittled Fatigue Limit <sup>†</sup>	Tempered Fatigue Limit	F.L. Ratio T/E <sup>††</sup>
Single Vacuum (No reheat)	Polished	180	315	1.75
	Ra = 3 $\mu\text{m}$	180	---	---
Triple Vacuum (Double reheat)	Polished	250	427	1.71
	Ra = 1, 3, 12 $\mu\text{m}$	180	---	---

<sup>†</sup> Fatigue Limit: Stress Amplitude (MPa).

<sup>††</sup> Fatigue Limit Ratio of Tempered to Embrittled Steel.

Table 6.2b Predicted Effects of Tempering on the Fatigue Limit of 8680 Steel

Modified 8680 Steel	Surface Finish	Tempered Fatigue Limit	HPM Predicted Fatigue Limit	% Error
Single Vacuum	Polished	315	347	10.2
Triple Vacuum	Polished	427	437	2.4

<sup>†</sup> Fatigue Limit: Stress Amplitude (MPa).

<sup>††</sup> Fatigue Limit Ratio of Tempered to Embrittled Steel.

Thus, high strength steels are prone to severe grain boundary embrittlement that can result in significant reductions in fatigue strength. Sufficient tempering can recover some of the adverse effects of embrittlement by altering the threshold mechanism from an intergranular mode to a transgranular mode. A complete mechanical and metallurgical understanding of this phenomenon has not been realized at this time. An optimum

tempering scheme is likely to exist where the tempering process reduces or eliminates the grain boundary cracking while the barrier or bulk grain strength is maintained to a certain degree. Effects of various processing parameters on the properties and structure of grain boundary phases would be very beneficial; as such, results in conjunction with the HPM model may facilitate the optimization of high strength steels in industrial applications.

### 6.3 Transgranular vs. Intergranular Nucleation Mechanisms

Data from the literature was analyzed with the HPM model to compare transgranular and intergranular crack nucleation effects on the fatigue limit of high strength steels, specifically carburized steels. Table 6.3 lists the results for nine different carburized steels taken from four different investigations. Observed and predicted fatigue limits are presented in the second and third columns along with the percent error and estimated flaw size in the fourth and fifth columns. Crack nucleation mechanism is identified in the sixth column. Applied R-ratios are 0.1; however, the presence of residual stresses effects the R-ratio that the material actually experiences. The effects of residual stresses have been taken into account by calculating the actual R-ratio. The actual R-ratios ranged from  $-0.21$  to  $+0.05$  with one exception of  $R=-2.17$ . The predictions are all within about 23% error, regardless of nucleation mechanism or flaw size. Unfortunately, flaw size cannot be predicted apriori; flaw sizes were estimated by photographs of actual fracture surfaces provided in the literature for each material. Notice, materials that exhibit intergranular crack nucleation have flaw sizes equal to or

larger than 15 $\mu\text{m}$  while materials observed to nucleate by transgranular mechanisms have flaws equal to or smaller than 20 $\mu\text{m}$ . Furthermore, materials that nucleate transgranularly have superior fatigue resistance mainly due to smaller flaw sizes. Thus, if flaw size can be reduced either by minimizing intergranular crack size or eliminating intergranular cracks in favor of smaller transgranular flaws superior fatigue strengths are expected and observed. Seven of the nine HPM predictions are in excellent agreement with the experimental results while the remaining two error on the conservative side by only 23%.

Table 6.3 Effect of Nucleation Mechanism on Fatigue Resistance

Material	Observed Fatigue Limit <sup>†</sup> (MPa)	Predicted Fatigue Limit <sup>†</sup> (MPa)	Error (%)	Estimated Flaw Size ( $\mu\text{m}$ )	Nucleation Mechanism	Ref.
In-L	495	482	-2.7	15	Inter.	[48]
ReIn-L	621	653	5.1	5	Trans.	
Carburized Steel	792	765	-3.4	5	Trans.	[49]
Carburized Steel	792	607	-23.3	20	Trans.	
Gas DQ	639	651	1.9	20	Trans.	[51]
Gas SR	743	680	-8.4	15	Trans.	
Plasma DQ	473	523	10.7	40	Inter.	
Plasma SR	529	466	-11.8	60	Inter.	
Gas Carburized <sup>††</sup>	868	668	-23.1	20	Inter.	[52]

<sup>†</sup> Stress amplitude at actual R-ratio.  $R_{\text{applied}}=0.1$  and  $R_{\text{actual}} : [-0.21, +0.05]$ .

<sup>††</sup>  $R_{\text{applied}}=-1$ ,  $R_{\text{actual}}=-2.17$ .

#### 6.4 Predicting Scatter in High Strength Steels

Scatter in the fatigue behavior of high strength steels is very common. Consequently, no empirical fatigue relationships have been developed for a wide variety

of high strength steels and heat treatment processes. Typically, a lower bound fatigue limit of 700 MPa (100 ksi) is predicted from experience as indicated in figure 6.11; however, other work indicates that even the so called conservative 700 MPa limit is non-conservative [84]. For example, in figure 6.12 the fatigue limits of steels with an ultimate tensile strength of about 1600 MPa (230 ksi) range from as high as 900 MPa to as low as 560 MPa. In order to ensure superior fatigue performance in high strength steels an understanding of the source of the scatter is essential.

Examination of the mechanisms and fatigue behavior of many high strength steels found in the literature reveals the source of scatter as indicated in figure 6.13 where the observed fatigue limit is compared to the HPM model predictions. Data found in the figure are compiled from the literature data examined and the data generated in this study for which a transgranular threshold mechanism exists. Similar to the general observations depicted in figure 6.12, observed fatigue limits range from about 380 MPa to as high as 870 MPa. However, more importantly the figure indicates that for a majority of the data the HPM predictions are within 20% error relative to the observed fatigue limit.

The advantage of the HPM model approach to the empirical approach is that the two key variables are identified and quantified, flaw size and barrier strength. Since flaw size cannot be identified apriori, mapping of the effects of alloy content and the steel production and heat treating route on intergranular flaw size and barrier strength would prove most valuable. Combining the HPM model with such a mapping scheme would



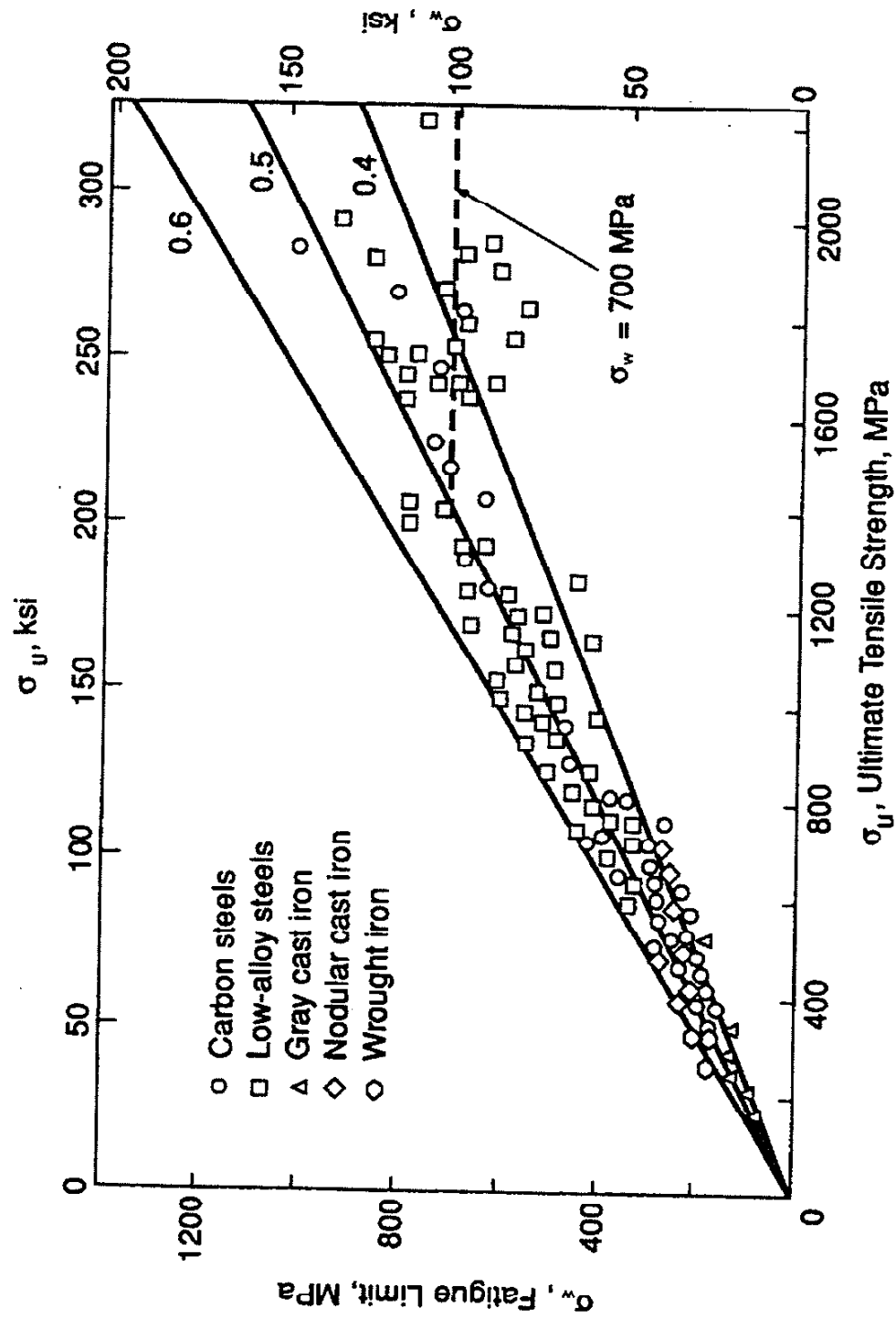


Figure 6.11 Suggested Lower Bound Fatigue Strength for High Strength Steels [4]

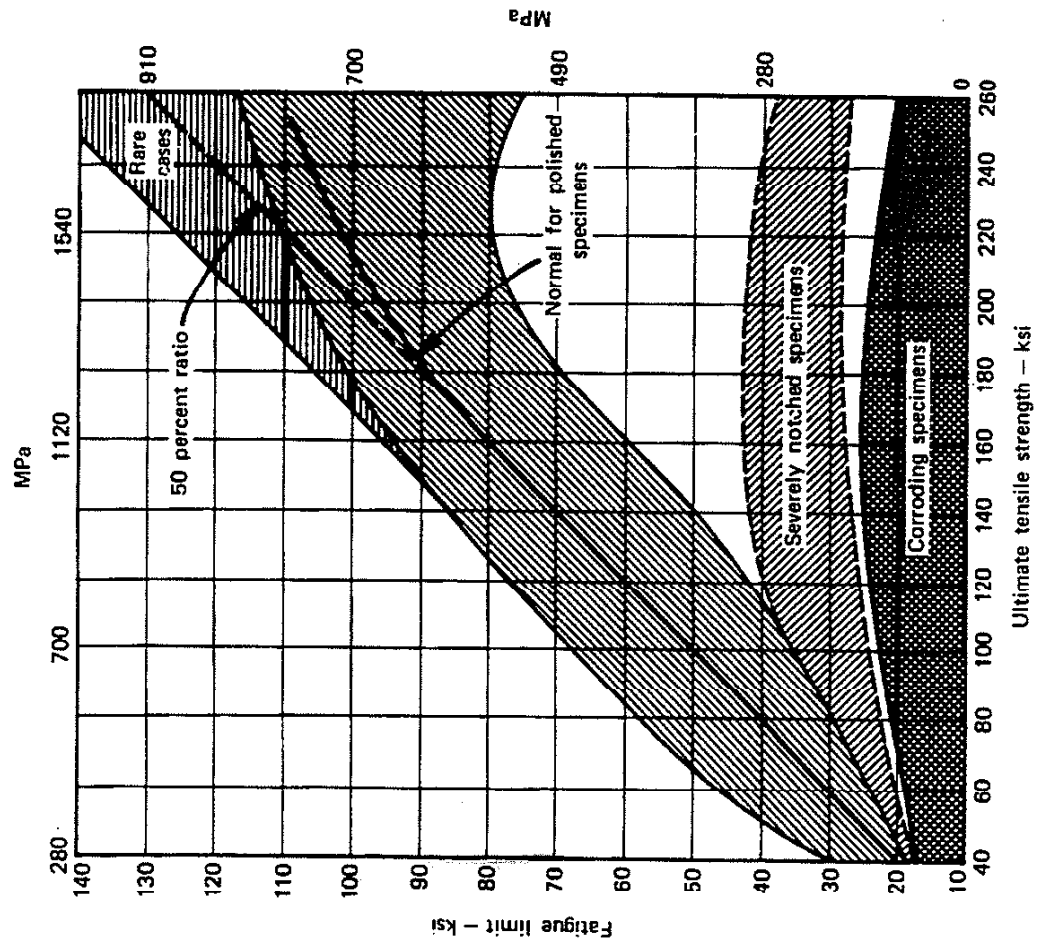


Figure 6.12 Observed Fatigue Limit Scatter in Steels [84]

provide steel manufacturers and product manufacturers with a powerful tool to assist in the design and control of superior fatigue limits in high strength steels.

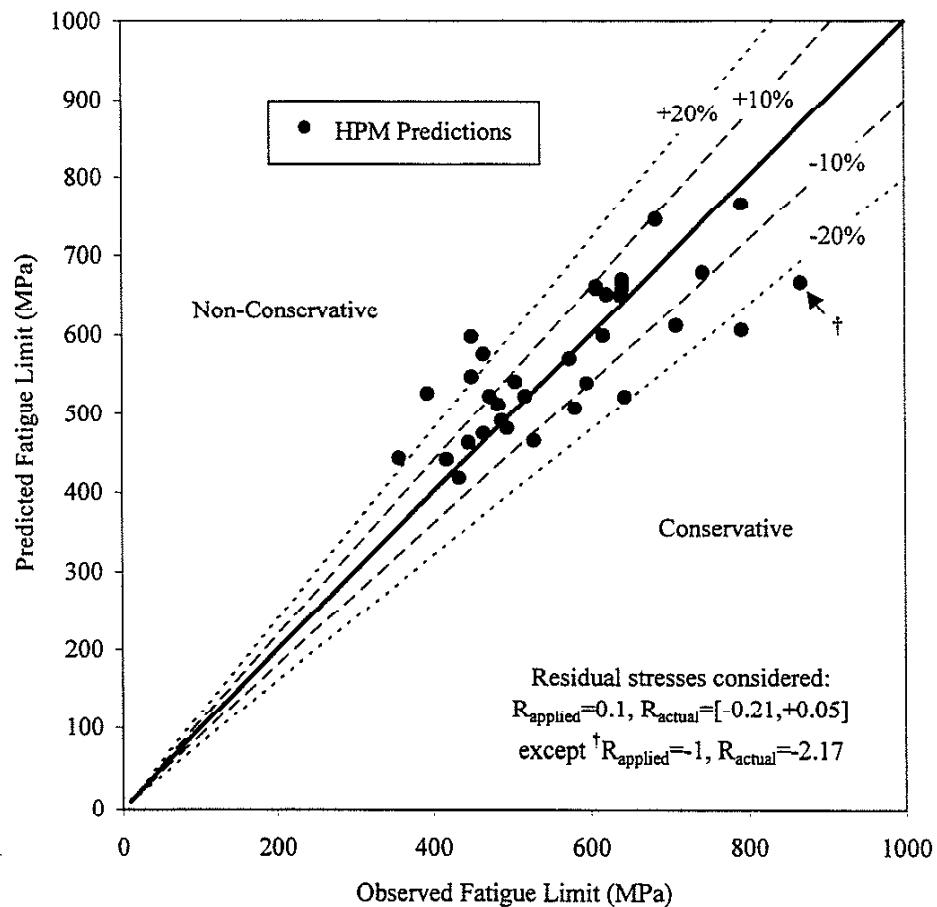


Figure 6.13 Comparison of Observed Fatigue Limits and HPM Predictions for Numerous High Strength Steels

## CHAPTER 7

### COMPETING FLAWS AND SYNERGISTIC FLAW EFFECTS

#### 7.1 Historical Surface Finish Studies

Numerous studies have been conducted on the effects of surface finish on the fatigue limit of steels. The most well known investigation was reported by Noll and Lipson [85]. Their results are plotted in figure 7.1. Notice the limited data, especially for the machined surfaces where extrapolation has been performed for higher strength materials. In addition, broad ranges of surface finishes are grouped under machined and ground surfaces. Industry still uses design tools based on these results or similar studies to account for surface finish effects despite advances in steel cleanliness and manufacturing processes. Most of these empirical studies were conducted in the middle 1900's because fracture mechanics and other sophisticated modeling tools had not been developed at that time. A detailed summary of such work is provided in Appendix B while some of the work is addressed in the following discussion when appropriate. Even after the development of linear elastic fracture mechanics, attempts to account for surface finish flaws have resulted in limited success. That is until recently when Takahashi and Murakami [40] used the  $\sqrt{\text{area}}$  parameter model to quantitatively evaluate the effect of surface roughness on the fatigue strength in a medium carbon steel.

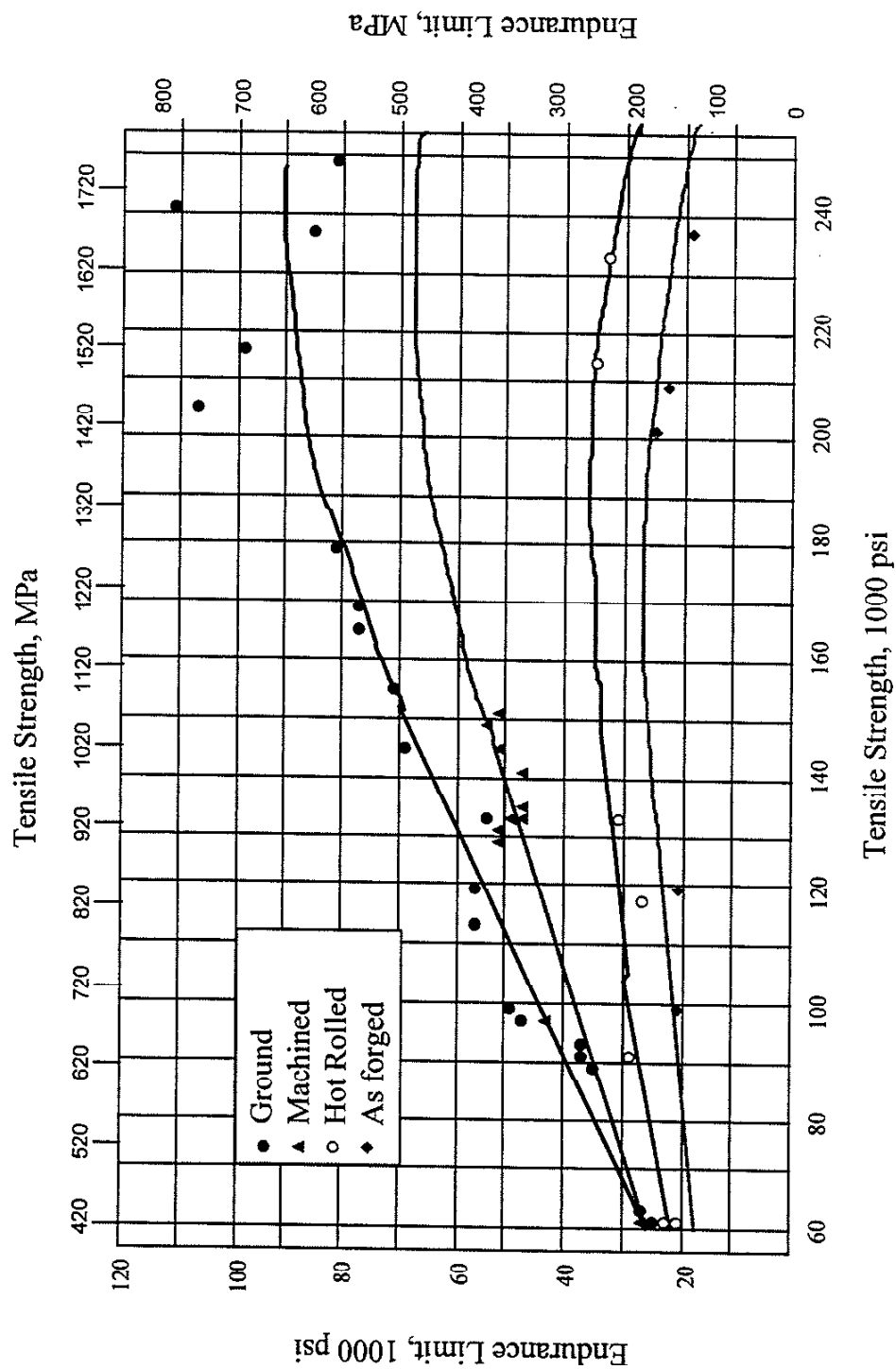


Figure 7.1 Observed Relationship Between Surface Finish and Tensile Strength: Noll & Lipson [85]

## 7.2 Surface Finish – Equivalent Notch Approach

Takahashi and Murakami [40] conducted tests on both annealed and quenched and tempered medium carbon steel. Extremely shallow periodic notches with a constant pitch but irregular depth were machined into the surface to simulate actual surface roughness. They showed that the fatigue limit of a specimen with a surface finish is determined by the threshold condition for a non-propagating crack initiated at the root of the surface groove or notch. Surface roughness was also shown to be equivalent to an array of periodic cracks where the effect was to reduce the maximum stress intensity of the surface flaw. Thus, the fatigue limit of a polished specimen with a single notch was observed to be 30% lower than that of a specimen with periodic notches of the same depth. An equivalent flaw size,  $\sqrt{\text{area}_R}$  was derived to account for the combined effect of flaw depth and periodicity.

Takahashi and Murakami pointed out that the ratio of  $\sqrt{\text{area}_R}$  to  $2b$  quickly saturates as shown in figure 7.2. The statement is true; however, the ratio of the predicted multiple groove to single groove fatigue limit ( $\sigma_R/\sigma_o$ ) is ultimately the most important result to consider. Periodic cracks effectively create a ‘load shedding’ effect by reducing the maximum stress intensity of the crack(s). As the ratio of crack depth to spacing increases the degree of ‘load shedding’ increases as indicated by the decrease in  $F$  shown in figure 7.2. The effect is equivalent to decreasing the original flaw size of  $\sqrt{\text{area}}$  to a measure of  $\sqrt{\text{area}_R}$  as suggested by Takahashi and Murakami. A reduction in the ratio  $\sqrt{\text{area}_R} / \sqrt{\text{area}}$  results in a continuous increase in the predicted fatigue limit

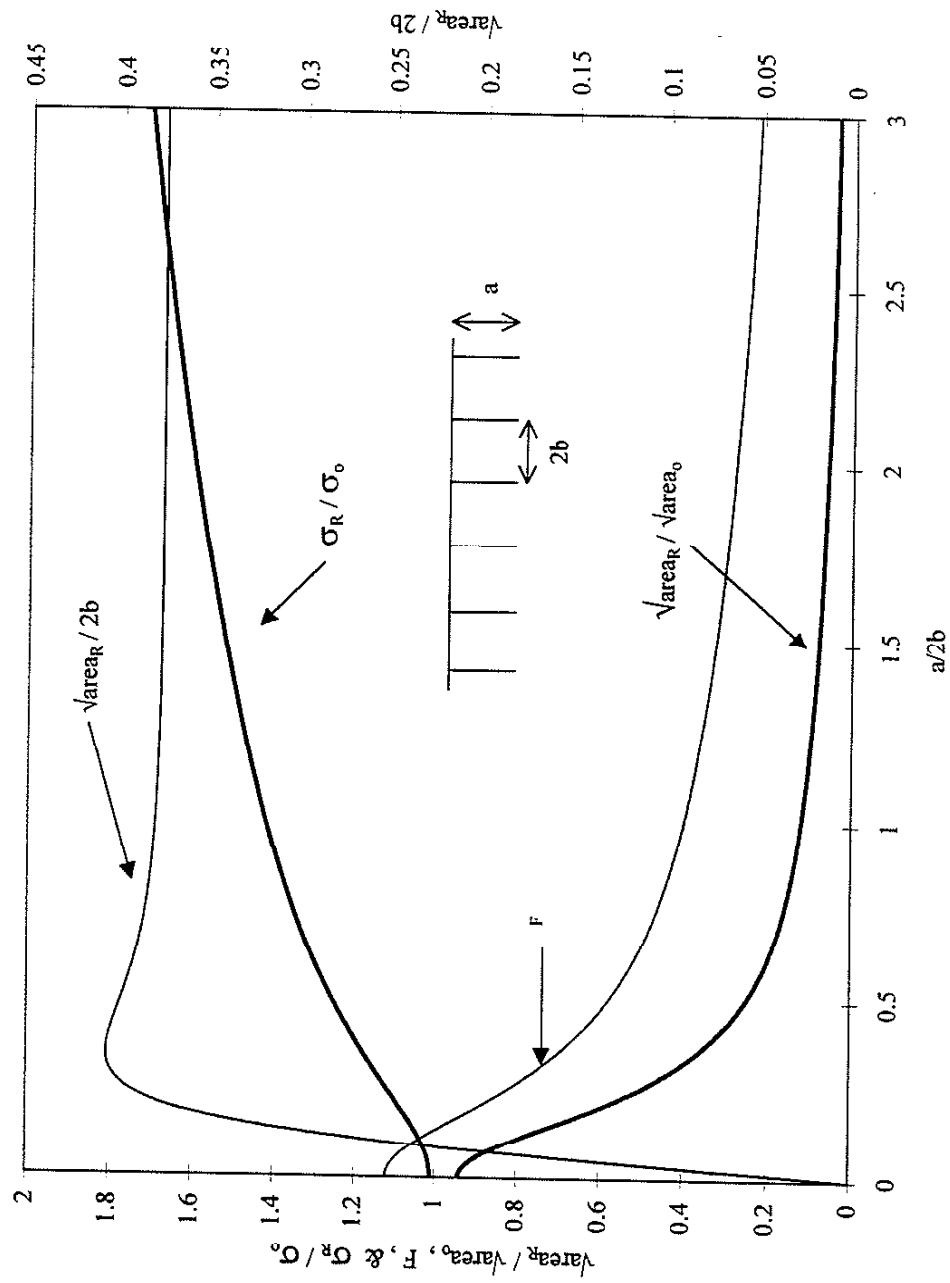


Figure 7.2 Equivalent Notch Effects for Surface Finish Flaws

ratio,  $\sigma_R/\sigma_o$ , as illustrated in figure 7.2. Unfortunately, typical ratios of  $a/2b$  that result from most manufacturing processes are quite low, e.g. less than 0.1, severely limiting the 'load shedding' effect in surface finishes.

### 7.3 Surface Finish and Intergranular Crack Nucleation

With a successful tool to address surface finish flaw effects, the synergistic effect of surface finish and intergranular cracks on the fatigue limit was investigated. Fatigue tests were performed on the modified 8680 steel with several surface finishes. In addition, results of a similar investigation conducted by Kristan [53] on a carburized 4320 steel were analyzed. The problem is analogous to the case of a notch within a notch. An intergranular crack extends into the body of the material, effectively a metallurgical notch. If a surface finish flaw also exists, the effect is to increase the depth of the intergranular notch. Intergranular flaw size in high strength steels is related to the prior austenite grain size, and as such will have depths equal to one or more grains. Since typical surface finish flaws in high strength steels are comparable in size relative to intergranular cracks the two notches are equivalent to one larger notch or flaw. The case of a short crack within a notch need not be considered, and the  $\sqrt{\text{area}}$  parameter model can be applied to the equivalent flaw depth.

First, two types of flaws are defined, type S and type E. Type S flaws have large aspect ratios, e.g. surface finish grooves. Type E flaws are semi-circular or circular in



shape, like cracks that nucleate from the surface and subsurface respectively. The  $\sqrt{\text{area}}$  for type S flaws is estimated by,

$$\sqrt{\text{area}} = PV\sqrt{10}, \quad (7.1)$$

where a shallow crack depth, PV, and a limiting aspect ratio of 5:1 are assumed as suggested by Murakami. PV is assumed to be equal to the peak-valley measurement obtained from a profilometer trace. A typical 3-D profile of a rough ground surface is shown in figure 7.3 and illustrates that fluctuations in a ground surface generate numerous parallel grooves in a material. If the loading axis is perpendicular to the grooves the effective area of the flaw is a rectangle whose area is given by equation 7.1.

Type E flaws, are quantified in a similar manner,

$$\sqrt{\text{area}} = D\sqrt{\pi/2} \quad (7.2)$$

for semi-circular flaws and,

$$\sqrt{\text{area}} = D\sqrt{\pi/4} \quad (7.3)$$

for circular flaws. The synergistic effect of intergranular flaws and surface finish flaws is an increase in the equivalent flaw depth. In other words, the equivalent flaw depth for type S flaws is no longer PV but is equal to PV+I where I is the intergranular flaw depth. Similarly, for type E flaws the equivalent flaw depth is D+I rather than D.

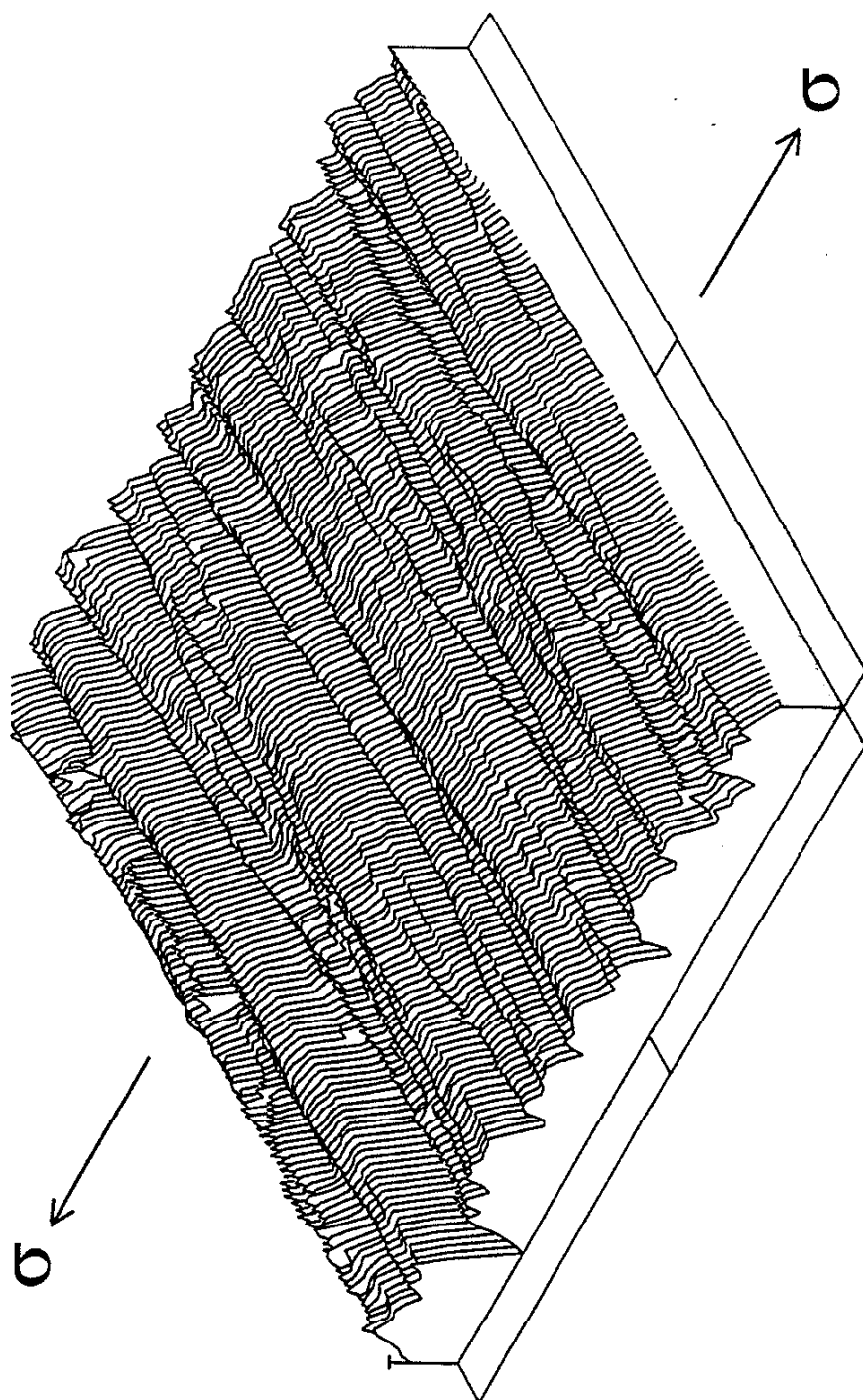


Figure 7.3 Three-dimensional View of a Ground Surface Finish

Intergranular crack depth was observed to be approximately 20  $\mu\text{m}$  in the modified 8680 steel. Since the observed aspect ratio of intergranular cracking tended to be high, i.e. intergranular flaws were rectangular in shape and exhibited a large aspect ratio, the S type flaw was implemented in the predictions. Test results for the 8680 steel are listed in table 7.1 along with the HPM model predictions. For the three surface finishes examined the observed fatigue limits vary by approximately 15%, 488 MPa for the polished specimens and 418 MPa for the specimens with a 20  $\mu\text{m}$  peak-valley surface roughness. The HPM predictions imply the same sensitivity to surface roughness as indicated by the predictions in the third column and the fact that errors for all three predictions are within 6% of the actual fatigue limits.

Table 7.1 Synergistic Effects of Surface Finish and Intergranular Cracking - I

Surface Finish Characterization		Fatigue Limit <sup>†</sup>		Error
$R_a$ ( $\mu\text{m}$ )	Peak-Valley ( $\mu\text{m}$ )	HPM (MPa)	Observed (MPa)	
0.05	1	491	488	0.7
1	10	464	446	3.9
2	20	442	418	5.7

<sup>†</sup> Stress amplitude @  $R=0.1$ . Intergranular crack nucleation depth ( $I$ )  $\approx 20$   $\mu\text{m}$ . S type flaw assumed,  $\sqrt{\text{area}} \approx (PV+I)\sqrt{10}$ .

Results obtained by Kristan [53] are provided in table 7.2 along with the HPM predictions. Crack nucleation depths, listed in the last column, were estimated from sizes reported, either specifically reported or estimated by inspection of SEM photographs of the fatigue origins. Predictions were made assuming E type flaws since photos of the fatigue origins suggested semi-circular shaped flaws. Errors between the predicted and

observed fatigue limits, which are listed in the fourth column, indicate that the correlation of fatigue predictions with Kristan's results is fair, but not as good as the correlation observed in the modified 8680 steel. Errors range from 2% to 33%.

Table 7.2 Synergistic Effects of Surface Finish and Intergranular Cracking - II

Carburized Steel <sup>‡</sup> Test Condition	Fatigue Limit Observed <sup>†</sup>	HPM Prediction <sup>††</sup>	% Error	Crack Depth <sup>‡‡</sup> d (μm)
4320 Base chemical polish	683	745	9	5
50 μin (1.3μm)	450	598	33	10
100 μin (2.6μm)	465	576	24	10
4320M 100 μin (2.6μm)	465	475	2	22
4320 VC w/ Si, Cr chemical polish	450	548	22	45
4320 VC w/o Si, Cr chemical polish	434	419	-4	150
50 μin (1.3μm)	357	444	24	100

<sup>‡</sup> Kristan [53]. <sup>‡‡</sup> Estimated intergranular crack nucleation depth.

<sup>†</sup> Stress amplitude (MPa). Residual stresses were taken into account.

<sup>††</sup> E type flaw assumed,  $\sqrt{\text{area}} \approx \sqrt{(d^2\pi/2)}$

The double notch concept implies that surface finish flaws are detrimental to the fatigue strength of the high strength steels tested. Kristan's results and the results of the modified 8680 steel support this concept; however, the HPM predictions for the carburized 4320 steel are not as accurate as they were in the 8680 material. Discrepancies might be attributed to the variability in the surface finishes applied to the specimens. Kristan tested cantilever beams that were designed with a radius in the test section to simulate a gear tooth. Application of a consistent surface finish was difficult due to the test section geometry. Furthermore, applied surface finishes probably varied

significantly because of the methods of surface finish application: 120 grit sand paper was wrapped around a weld rod and manually worked on the surface of the specimens to generate the 1.3  $\mu\text{m}$  finishes while a steel file was used manually to generate the 2.6  $\mu\text{m}$  surfaces. Surface finish variability is supported by the nonconservative predictions for the 1.3 $\mu\text{m}$  and 2.6 $\mu\text{m}$  surfaces and the excellent fatigue limit predictions for two of the three chemically polished surfaces. In contrast, the 8680 specimens were flat beam specimens with rectangular cross-sections. Surface finishes were consistent because the flat test specimens and gage sections simplified application of the surface finish via surface grinding machine.

#### **7.4 A Hypothesis for the Competition of Surface Finish and Inclusion Flaws**

The presence of two flaws raises additional and important questions for manufacturers. Which is the dominating flaw? Determining which is the dominant flaw is trivial: the dominant flaw is the flaw that has the largest area projected perpendicular to the maximum applied stress direction. But, if the dominating flaw size is reduced, then at what point does the other flaw become the dominating flaw? No studies have addressed this problem. Thus, the competition between inclusion and surface finish flaws was investigated. Predictions were made with a simple extension of the HPM model as discussed below.

Two extremely different types of flaws must be considered due to the nature of the shapes of the surface finish and inclusion flaws in question, type S and type E flaws respectively. As illustrated in figure 7.4, the transition point is determined by examining the four possible cases associated with the simultaneous occurrence of both flaws. The first two conditions are the most common ones. In both cases, flaws are separated by a large distance. Hence, they do not interact with one another and each is treated as an isolated flaw. Flaw interaction does take place in the third and fourth conditions. Two simple approaches are taken to account for the interaction: flaws are equivalent to one larger semi-elliptical flaw, a type E flaw, or one larger shallow rectangular shaped flaw, a type S flaw. Since the equivalent type S flaw is unrealistic, it is disregarded and the transition of the dominating flaw is analyzed in the following manner.

Consider the competition of the two isolated flaws where the flaw areas are depicted in the first and second cases shown in figure 7.4. Start with a polished surface and increase the surface roughness gradually. Initially inclusions will be the dominant flaw. Transition of flaw dominance is assumed to occur when the surface finish flaw  $\sqrt{A_{\text{area}}}$  is greater than the inclusion flaw  $\sqrt{A_{\text{area}}}$ . This condition exists when,

$$PV\sqrt{10} > D\sqrt{\pi/4}, \quad (7.4)$$

or when

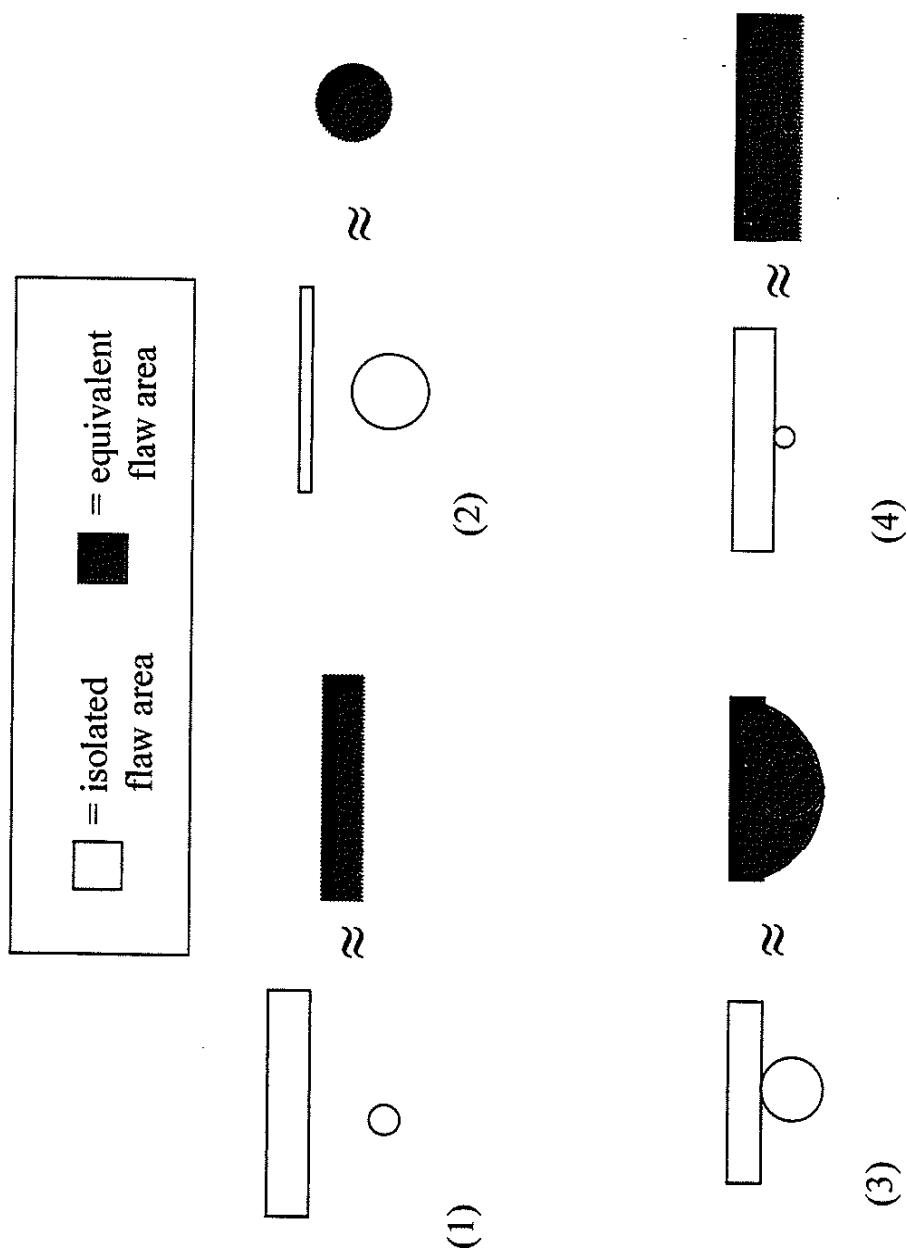


Figure 7.4 Four Possible Conditions of Competing Flaws

$$PV > D\sqrt{\pi/40} \approx 0.28 D, \quad (7.5)$$

and is listed as condition (1) in table 7.3. Interaction of a surface type flaw with an inclusion will always result in a larger equivalent E type flaw as indicated in the third case of figure 7.4; the case is designated as condition (2) in table 7.3. Case (4) in figure 7.4 has already been disregarded, leaving one last interaction of flaws to consider. An equivalent type E flaw, assumed for surface finish and inclusion interaction, is larger than the same isolated surface finish flaw under the conditions,

$$(PV + D)\sqrt{\pi/2} > PV\sqrt{10}, \quad (7.6)$$

or equivalently when

$$D > \frac{(\sqrt{10} - \sqrt{\pi/2})}{\sqrt{\pi/2}} PV \approx 1.53 PV. \quad (7.7)$$

Table 7.3 Critical Conditions for Transition of Dominating Flaw

Critical Condition: Comparing Areas of Defects †			
(1)	$PV_{\text{area}} > D_{\text{area}}$	when	$PV/D > 0.28$
(2)	$(PV+D)_{\text{area}}^S > D_{\text{area}}$	when	ALWAYS.
(3)	$PV_{\text{area}} > (PV+D)_{\text{area}}^E$	when	$PV/D > 0.66$

†  $PV_{\text{area}} =$  Isolated Type S Flaw,  $\sqrt{\text{area}} = PV\sqrt{10}$ ,

$D_{\text{area}} =$  Isolated Type E Flaw,  $\sqrt{\text{area}} = D\sqrt{\pi/4}$ ,

$(PV+D)_{\text{area}}^S$  and  $(PV+D)_{\text{area}}^E$  are equivalent  
flaw sizes for Type S and Type E flaws.



Equation 7.7 can be rewritten to express the transition when an isolated surface flaw is more damaging than the equivalent type E flaw. Demarcation of this event is given by the condition when,

$$PV > \frac{1}{1.53} D \approx 0.66 D, \quad (7.8)$$

which is the third and final condition listed in table 7.3.

An explanation of how to apply the concept follows and is illustrated in figure 7.5. Consider a polished surface and a material that contains inherent inclusions; begin increasing the surface roughness. While the ratio of the measured surface roughness peak-valley to inclusion diameter (PV/D) is less than 0.28, cracks will nucleate from inclusions alone. Interaction of the surface finish with an inclusion is actually a worse condition that may occur as well. However, the occurrence is less likely to due to a higher probability in encountering a subsurface inclusion than an inclusion interacting with the surface. Eventually, surface roughness increases to a point where cracks are most likely to nucleate from them. This occurs when  $PV/D > 0.28$ ; although, inclusion and surface finish interaction remains a worse condition than an isolated surface finish flaw and may still occur when  $0.28 < PV/D < 0.66$ . Finally, cracks will always nucleate from surface finish flaws when the size of the surface finish flaw relative to the inclusion is larger, i.e. when  $PV/D > 0.66$ . Conventionally, the fatigue limit of a specimen with a given surface finish has been related to the smooth or polished specimen fatigue limit by the surface finish fatigue correction factor. Due to the probabilistic nature of the size of

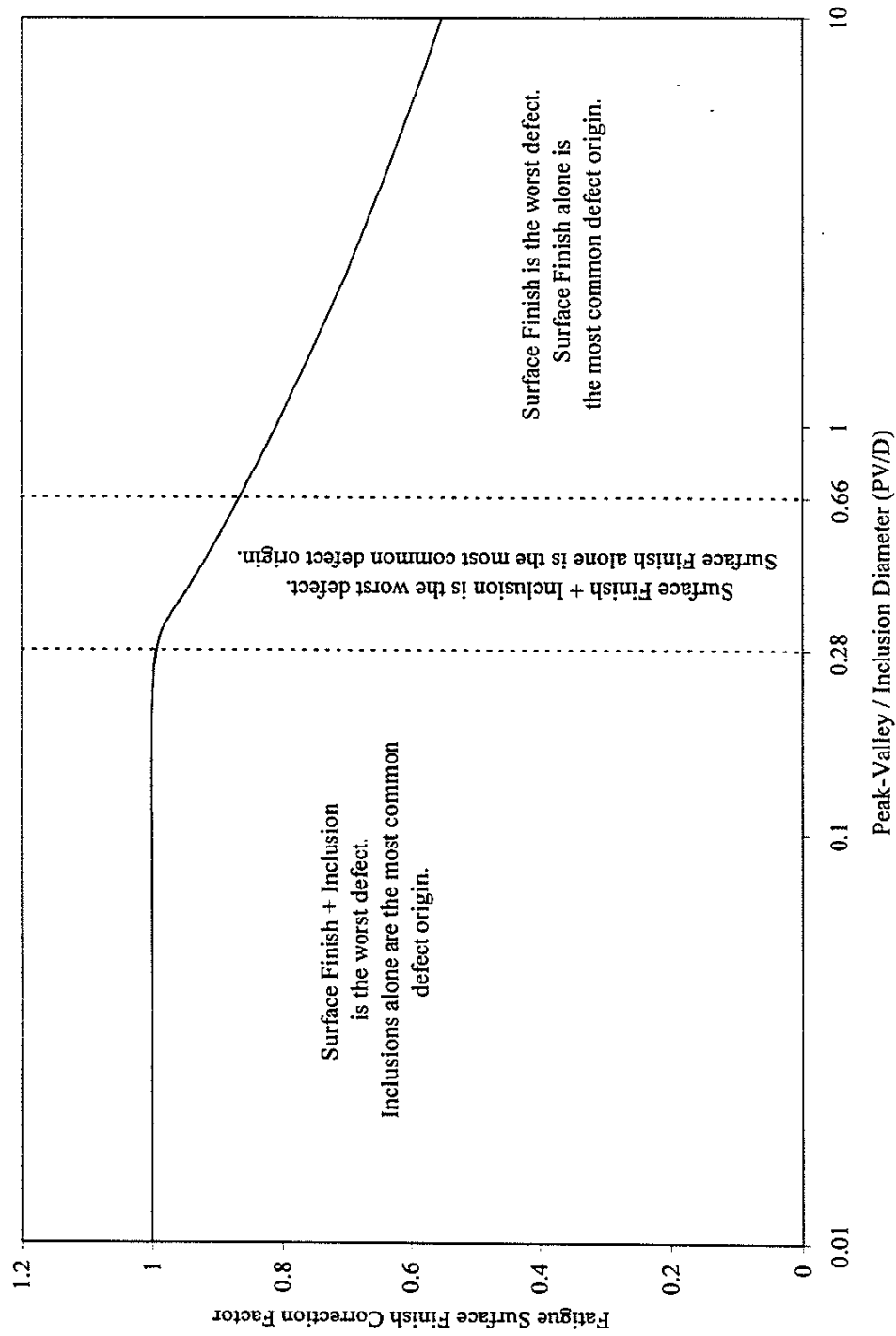


Figure 7.5 Map of Dominant Flaw Regions and Transition Points

flaws found in any given fatigue specimen, an absolute measure of which flaw will dominate is not possible. However, the majority of flaw origins observed in broken specimens should follow the general trend illustrated in figure 7.5:

The PV/D concept can be visualized in another manner by comparing the distribution and size of the two flaw types found in the material as illustrated in figures 7.6 and 7.7. The comparisons made in the figures are for illustration purposes only, but the approach will be applied later to actual surface and inclusion flaws in the 4340 steel investigated. Reduced variate is a measure analogous to the standard deviation of normal distribution. An increase in the reduced variate indicates a larger standard deviation. Variation in flaw size can also be expressed in terms of the cumulative probability of encountering a flaw of a given size as indicated by the cumulative distribution on the secondary vertical axis; in further discussions the variation in flaw size will be discussed in terms of the cumulative distribution. Cumulative distributions functions for each flaw type are determined by numerous measurements of the size and frequencies of flaws present in the material. Then, cumulative distribution functions are fit to the measured data. Maximum flaw size is predictable for each flaw type by calculating their cumulative distribution values which are functions of the number of specimens or components (N) to be tested or manufactured and the critically stressed volume of material [32,33]. Critically stressed volume of material is defined as the volume of material which experiences 90% or more of the maximum stress in the member. The two cumulative distribution values may not necessarily be equal, although they are not restricted to being unequal. Each flaw's corresponding  $\sqrt{\text{area}_{\text{max}}}$  is estimated and if the

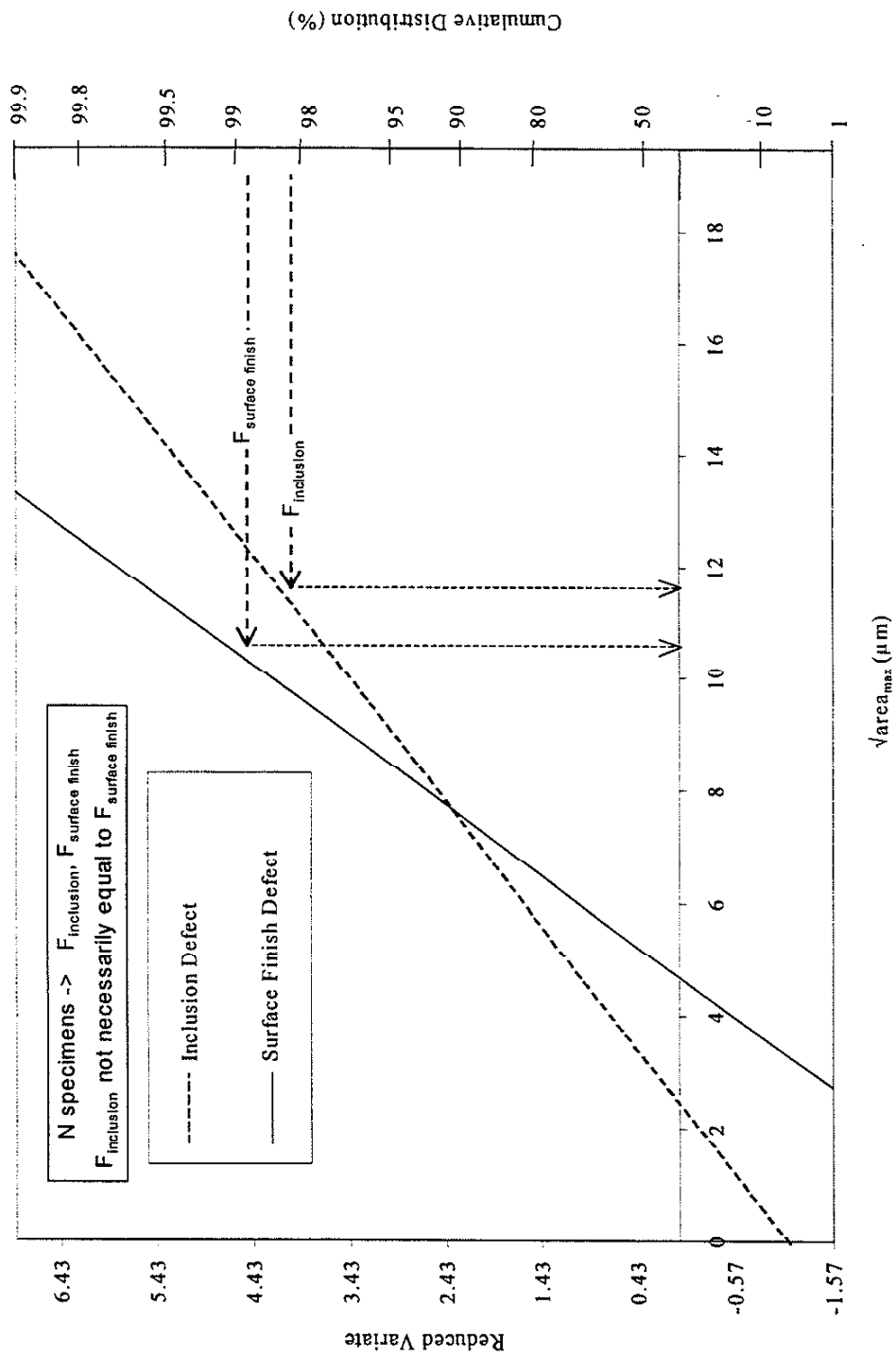


Figure 7.6 Equally Damaging Flaws: No Dominant Flaw

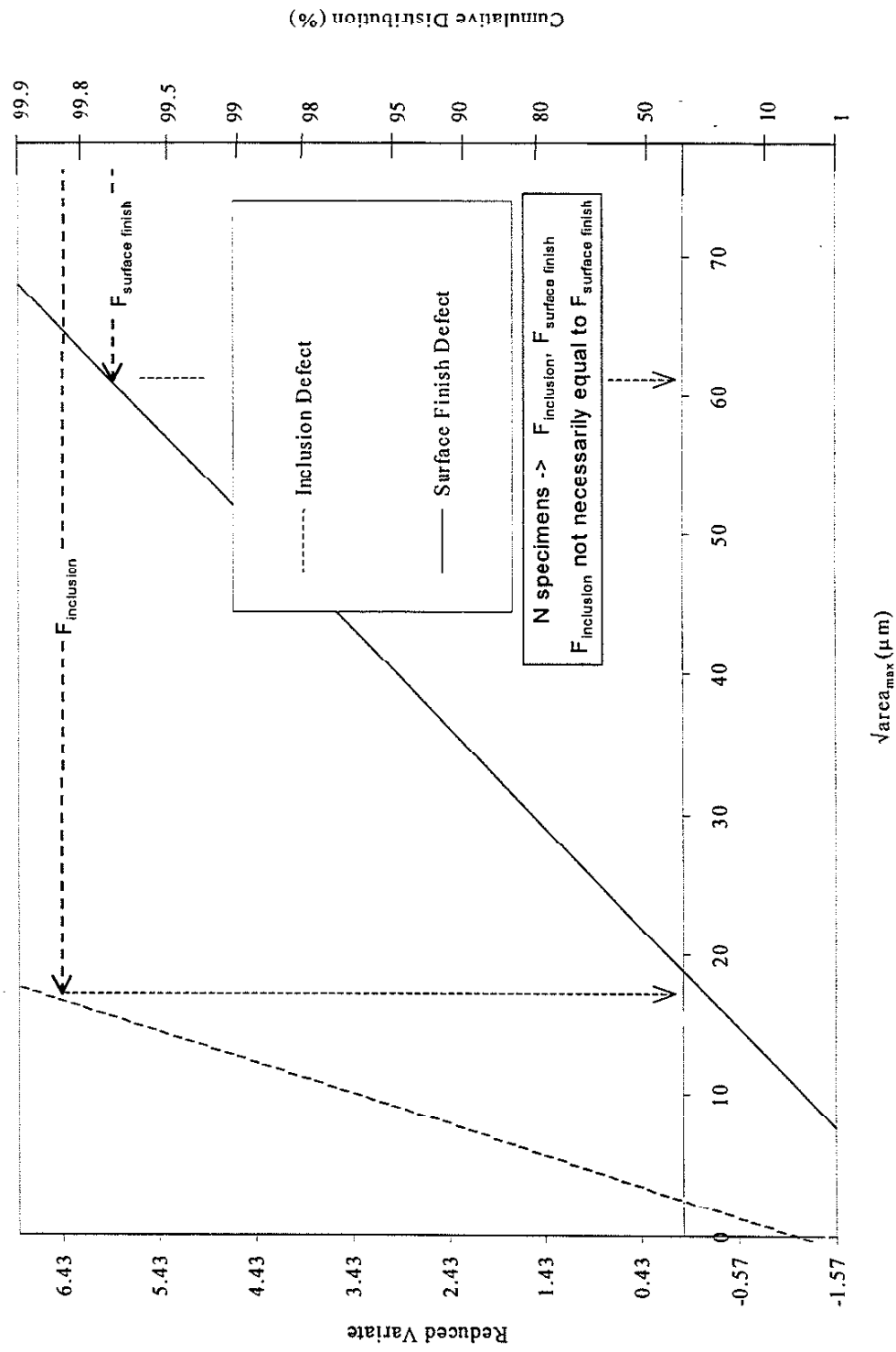


Figure 7.7 Unequal Flaw Sizes: One Dominant Flaw

$\sqrt{\text{area}_{\text{max}}}$  for the two flaw types are nearly equal as seen in figure 7.6, then either flaw types may be observed in fatigue origins of broken specimens. One flaw becomes dominant when its  $\sqrt{\text{area}_{\text{max}}}$  is significantly larger than the other as illustrated in figure 7.7.

## **7.5 Surface Finish and Inclusion Competition in 4340 Steel**

### **7.5.1 Flaw Competition Predictions**

Four different surface finishes were generated on specimens made from a vacuum arc-melted 4340 plate steel. The surfaces investigated, in order of increasing roughness were a polished surface, fine and rough milled surfaces designated as M600 and M300 respectively, and a rough ground surface. Details regarding how surfaces were generated are given in chapter 2. Since fatigue strength varies for each specimen as discussed earlier, predictions were made with four different measures of flaw size to illustrate and provide a sense of the probabilistic nature of the fatigue limit. Numerous measurements were made of the surface finish and inclusion flaw sizes to obtain the following measures: average flaw size observed, maximum flaw size observed, and the flaw size predicted by the statistics of extremes rating method for  $N=1$  and  $N=100$  where  $N$  is equal to the number of specimens or components to be tested or manufactured. For simplicity, fatigue behavior was assumed to be governed solely by an isolated inclusion or surface finish flaw, i.e. interaction of the surface finish and inclusion flaws was assumed to be highly unlikely. However, due to the competition of flaws, two sets of

flaw measures exist for each group of specimens within a given surface finish, one set for inclusion type flaws and another set for surface finish type flaws. Each set includes four measures of flaw size for a given flaw type, although, only one set of measures was derived for the polished surface group since the surface finish type flaw in that case was extremely small relative to the inclusion content. Flaw measures are listed in table 7.4, i.e. the average and maximum observed inclusion diameters are 8.8 and 72.7  $\mu\text{m}$  while the average and maximum observed peak-valley depths for the fine milled (M600) surface were 1.7 and 3.6  $\mu\text{m}$  respectively. Actual flaw sizes and cumulative distributions from which the four measures were derived are provided in figures 7.8-7.12. Figure 7.12 plots the inclusion and surface finish flaw cumulative distributions together for easy comparison. Notice that the inclusion and M600 distributions are similar although not identical indicating somewhat similar flaw content. On the contrary, the M300 and rough ground distributions are located to the right of the inclusion distribution indicating that the surface flaws associated with the two surface finishes are significantly larger than the inclusions.

Hardness was also observed to vary and can be best described by a normal distribution function with an average Vickers hardness of 531 and a standard deviation of 52 as shown in figure 7.13. For practical purposes, all predictions were made using the average hardness although the true threshold condition is determined by the local stress, local hardness, and the size of the flaw under consideration.

Table 7.4 Measured and Predicted Flaws in Vacuum Arc-Melted 4340 Steel

Surface Finish Group	Average Observed PV or D†	Maximum Observed PV or D†	Predicted N=1 PV or D††	Predicted N=100 PV or D††
Polished (D)	8.8	72.7	53.5	80.3
M600 (PV)	1.7	3.6	4.3	6.1
M300 (PV)	7.1	13.1	18.6	29.1
Rough Ground (PV)	41.7	52.5	53.9	70.8

† Value indicates defect size for PV=peak-valley profilometer measurement ( $\mu\text{m}$ ), D=inclusion diameter ( $\mu\text{m}$ ).

†† Predicted by statistics of extremes; N=1,100 specimens.

Figure 7.14 shows the predicted fatigue limits for each of the four groups of surface finishes generated. The applied stress amplitude is plotted on the ordinate axis while the surface finish groups are plotted along the abscissa with increasing surface roughness; note that there is no scale associated with the locations of the surface finish groups. Predictions made with the surface finish measures are labeled SF and predictions made with the inclusion measures are labeled I. Both sets of measures are based on isolated surface finish and inclusion flaws respectively. Predictions for each set of measures are presented in the bar-like form to illustrate the differences and range of fatigue limit predictions for the four measures. Table 7.5 lists the calculated peak-valley to inclusion diameter ratios for the four measures for each surface finish tested. Both table 7.5 and figure 7.14 illustrate the transition from inclusion dominated fatigue to surface finish dominated fatigue. Specimens with a polished surface will be governed by the inclusion content because  $PV/D \approx 0$ . Inclusion and surface finish flaws in the M600 group begin to compete for the dominant flaw role with the increase in roughness, although the ratio remains relatively small, i.e. average  $PV/D \approx 0.19$ . Notice that the



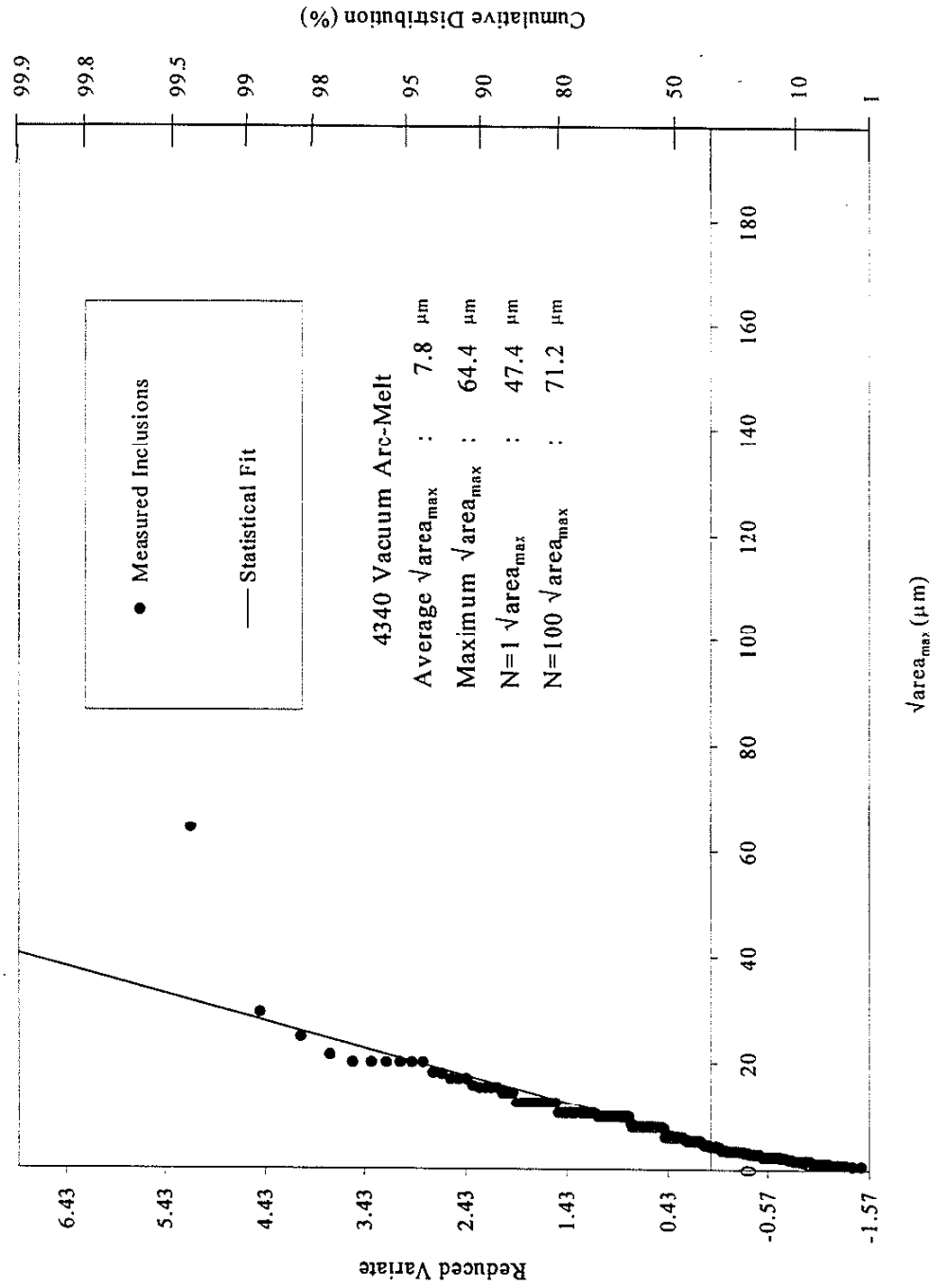


Figure 7.8 Inclusion Distribution in 4340 Steel

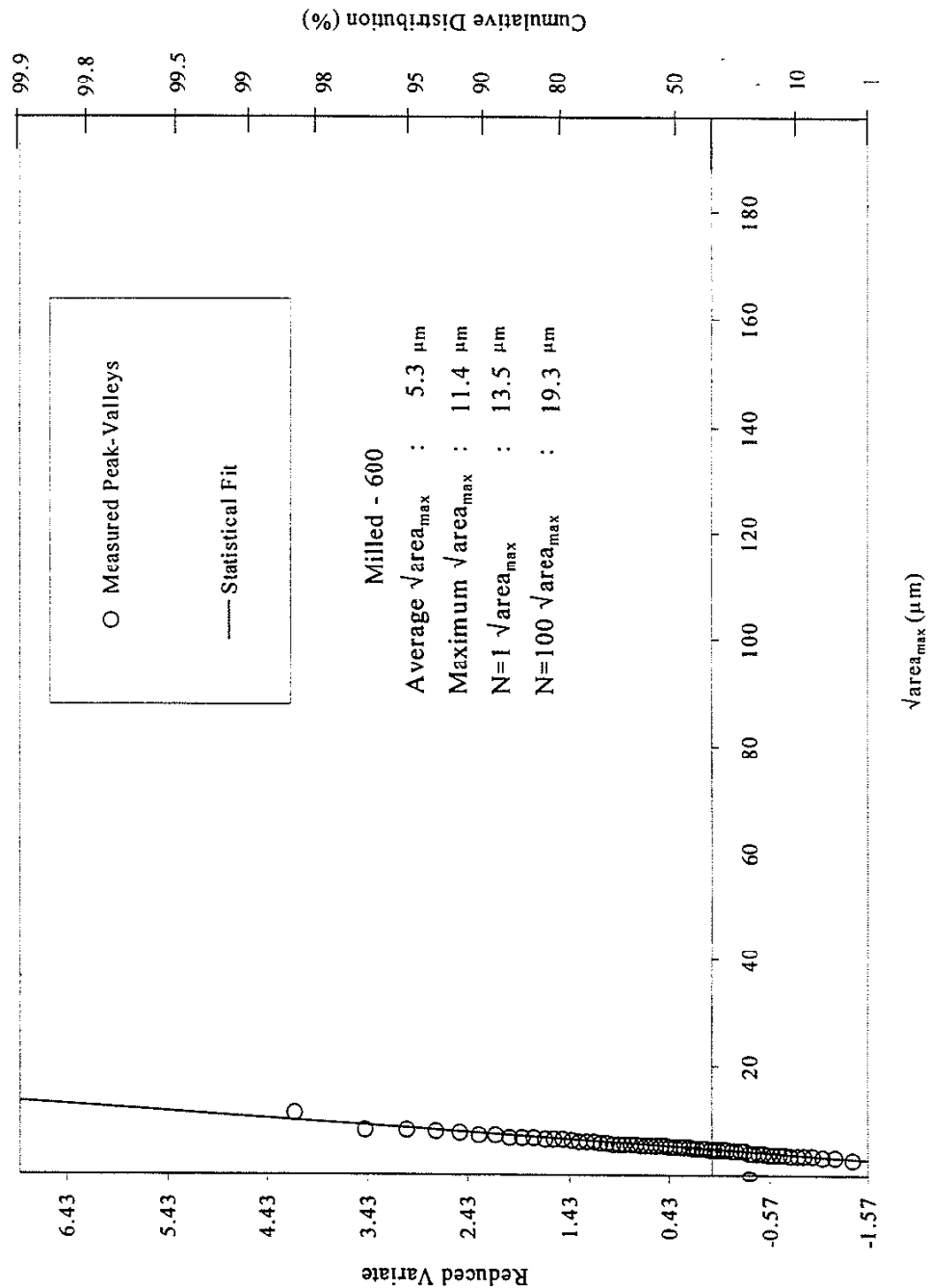


Figure 7.9 Milled 600 Surface Flaw Distribution

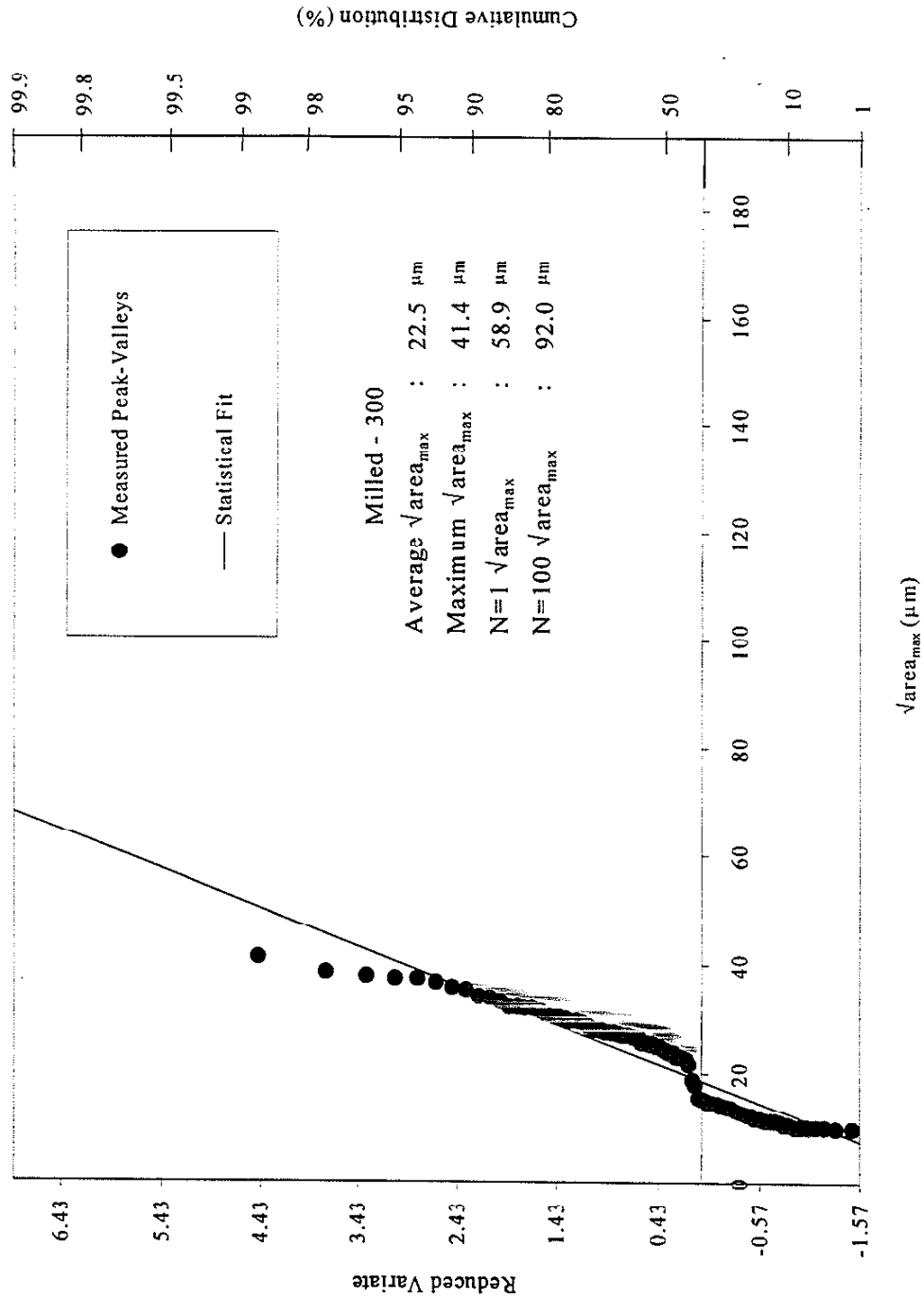


Figure 7.10 Milled 300 Surface Flaw Distribution

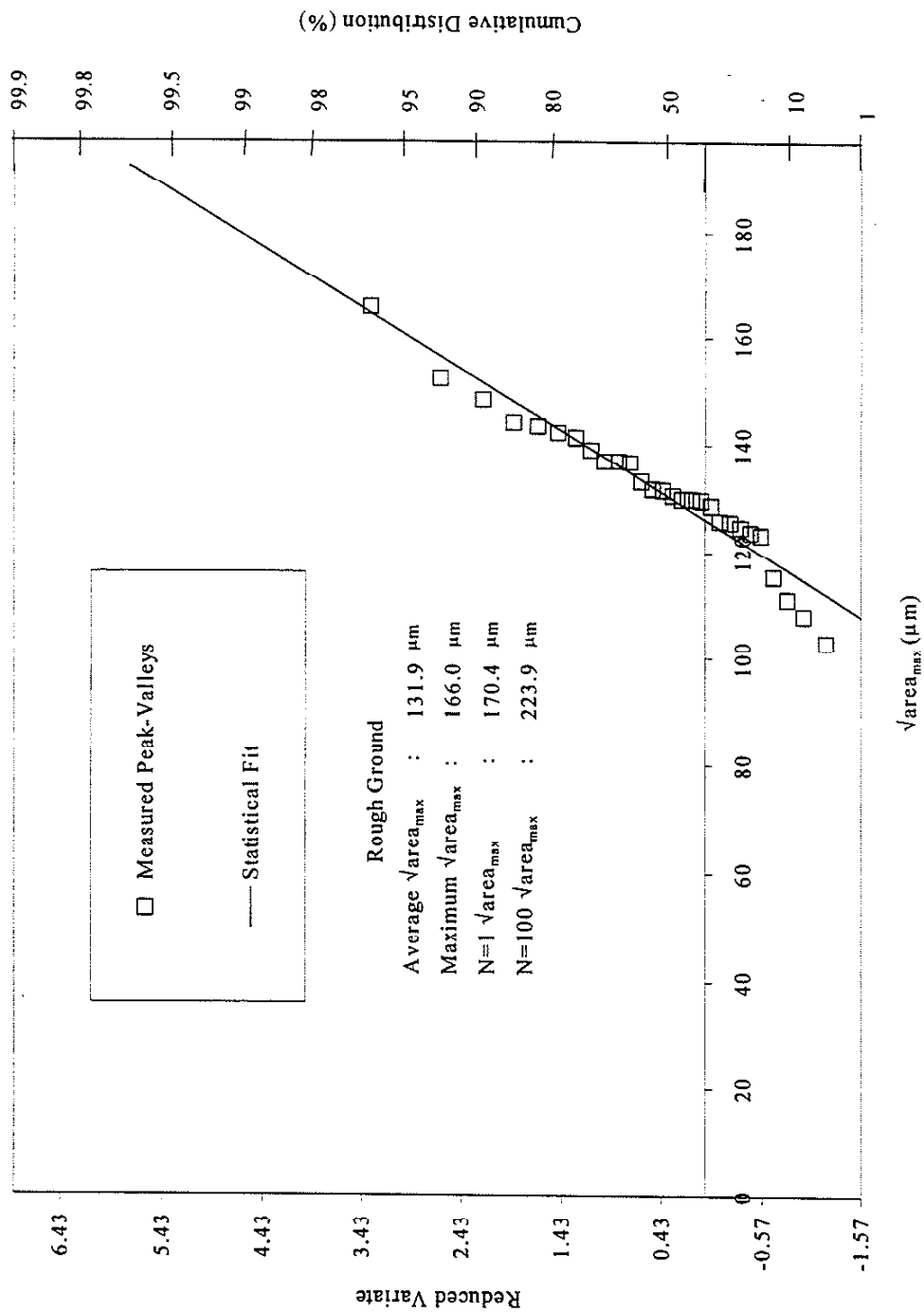


Figure 7.11 Ground Surface Flaw Distribution

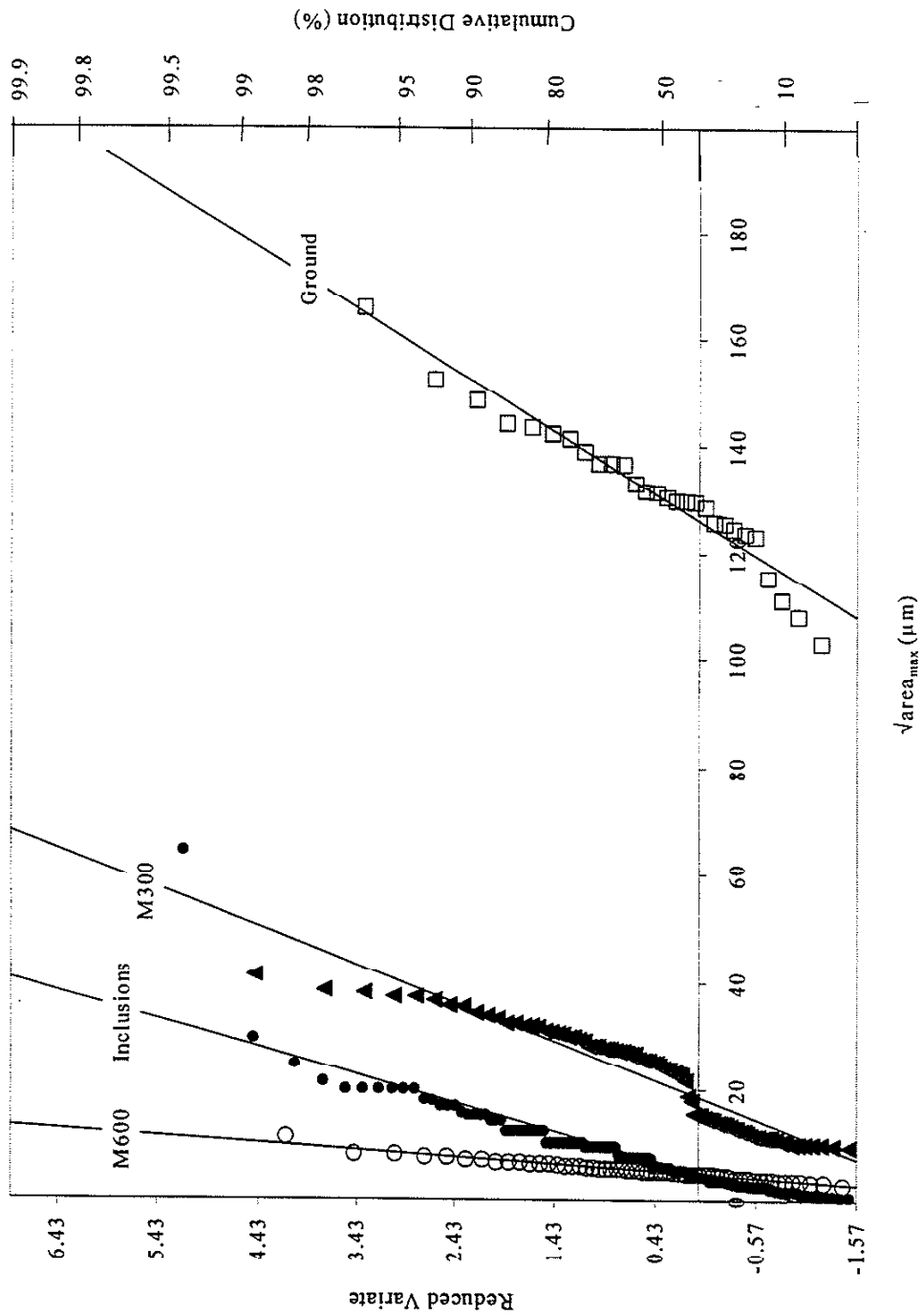


Figure 7.12 Comparison of Flaw Distributions

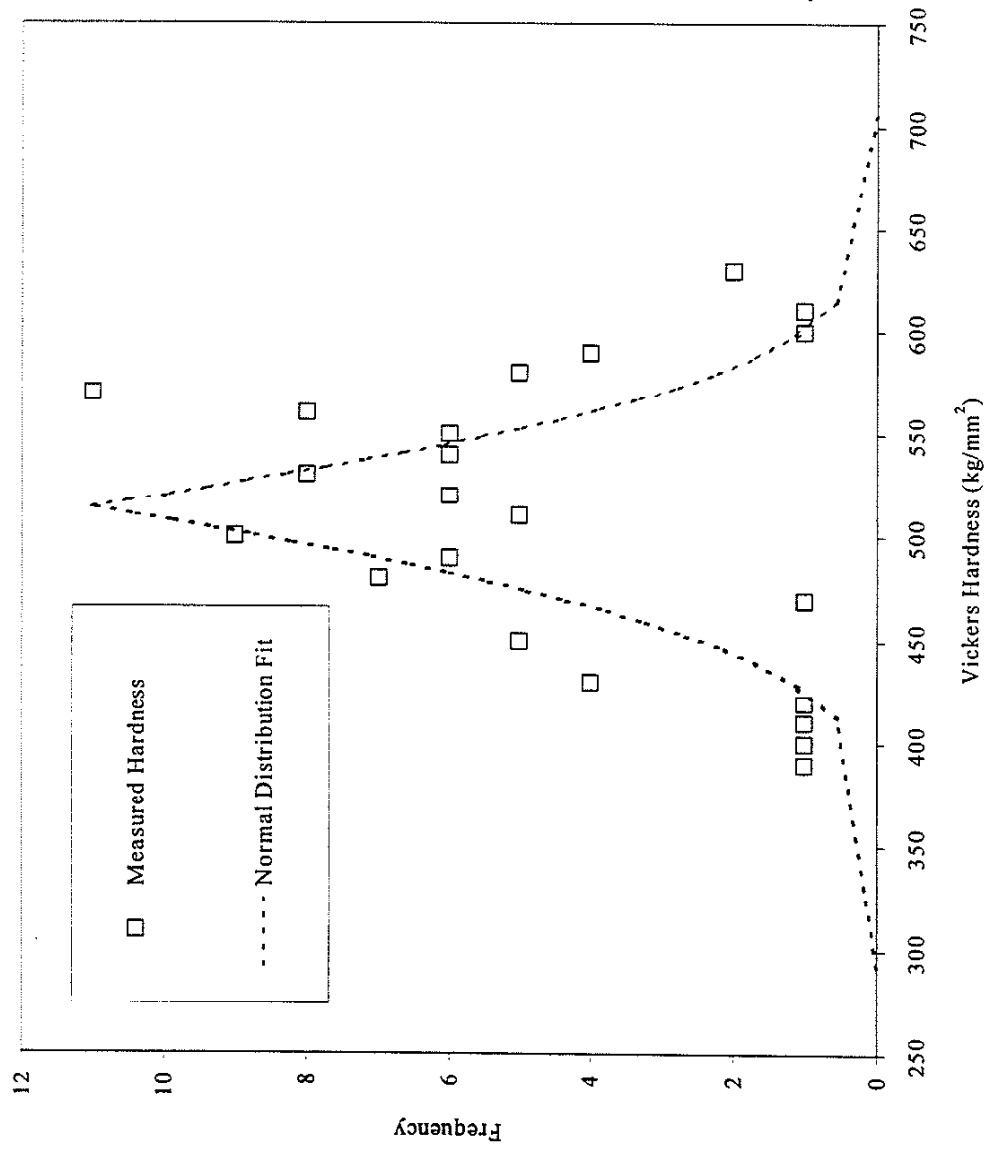


Figure 7.13 Vickers Hardness Distribution for Quenched and Tempered 4340

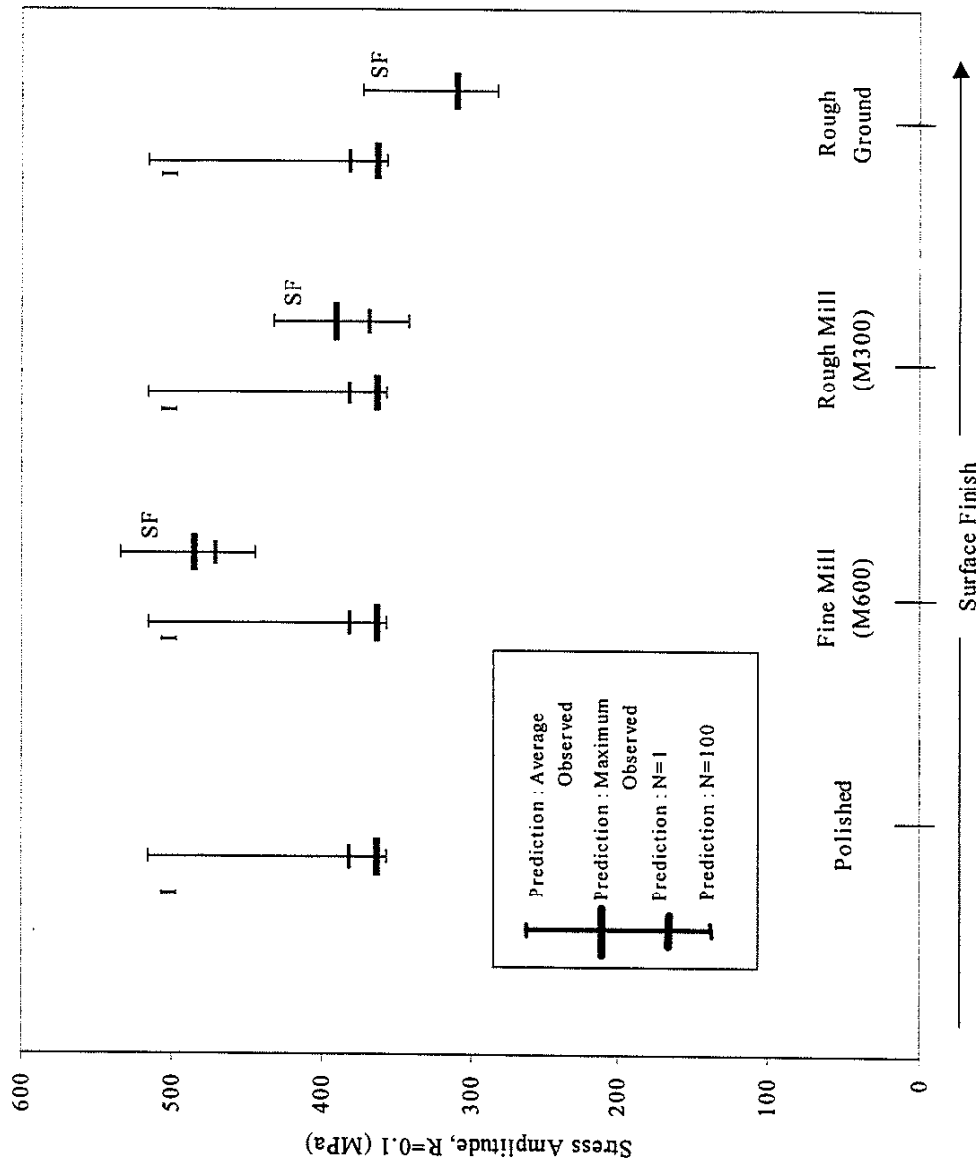


Figure 7.14 Predicted Fatigue Behavior of Competing Flaws in 4340 Steel

predicted fatigue limits begin to overlap for the SF and I measures in the M600 group. Thus, fatigue failures will likely consist of a mixture of inclusion and surface finish origins in the M600 group. In contrast, the  $\sqrt{\text{area}_{\text{max}}}$  for the surface finish flaw in the M300 group is larger than the  $\sqrt{\text{area}_{\text{max}}}$  for the inclusion flaws, e.g. average PV/D  $\approx 0.81$ . All fatigue origins should nucleate from surface finish flaws. Finally, the surface finish flaws in the ground specimens are extremely large relative to inclusion size, average PV/D  $\approx 4.72$ . Fatigue failures will nucleate from surface flaws with no uncertainty.

Table 7.5 Predicted Peak-Valley to Inclusion Diameter Ratios in 4340 Vacuum Arc-Melted Steel

Surface Finish Group	Average Observed PV/D <sup>†</sup>	Maximum Observed PV/D <sup>†</sup>	Predicted N=1 PV/D <sup>††</sup>	Predicted N=100 PV/D <sup>††</sup>
Polished	0	0	0	0
M600	0.19	0.05	0.08	0.08
M300	0.81	0.18	0.35	0.36
Rough Ground	4.72	0.72	1.01	0.88

<sup>†</sup> Ratio of PV=peak-valley measurement to D=inclusion diameter.

<sup>††</sup> Predicted by statistics of extremes. N=1,100 specimens

## 7.5.2 Flaw Competition Results

Test results are indicated in figure 7.15. Broken specimens are indicated by the solid triangle symbols while unbroken specimens are represented by hollow circles. The expected trend in fatigue behavior is discernable, a reduction in allowable stress occurs with increasing surface roughness. Interpreting the results can often be difficult due



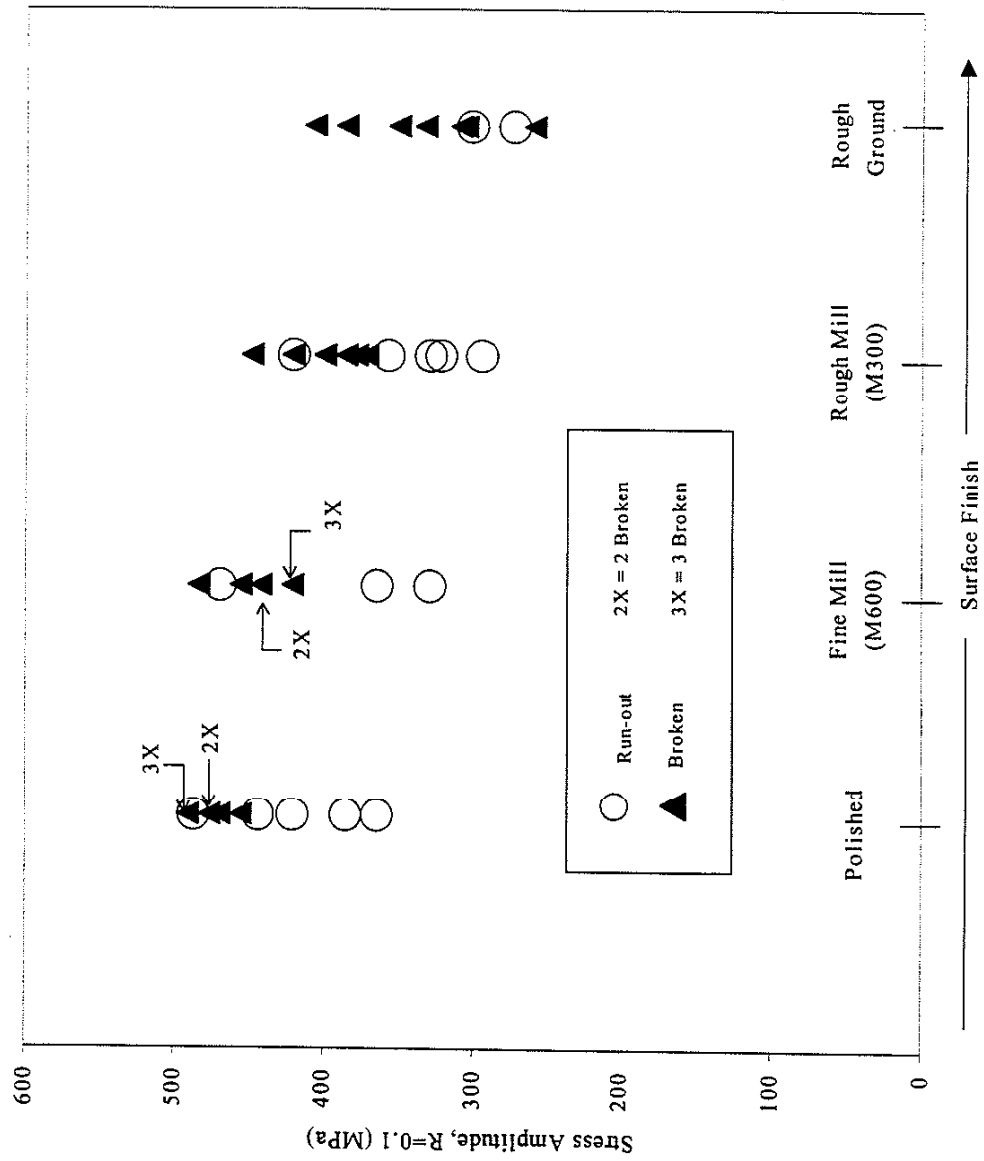


Figure 7.15 Observed Fatigue Results of Competing Flaws in 4340 Steel

to scatter in the data; note the scatter in the present data. However, when the predictions are compared with the data, as illustrated in figure 7.16, the scatter and nature of the fatigue behavior is more easily interpreted. Surface finish has no effect on the fatigue strength in the polished specimens as indicated by the sole inclusion measure prediction and the accompanying data; fatigue failure is solely dependent on the applied stress and the probability of a flaw of sufficient size existing in a given fatigue specimen. Fatigue cracks were predicted to nucleate from surface flaws in the M600 group when the applied stress is greater than the predicted fatigue limit for the SF measure of  $N=100$ , which lies about midway between the predicted fatigue limits for the average and  $N=1$  inclusion measures. In other words, competition for flaw dominance is indicated by the overlapping regions of the SF and I flaw measure predictions. Finally, in both the M300 and rough ground surface finish groups fatigue failure is predicted to occur as a result of surface finish flaws. This is indicated by the lower fatigue limit predictions corresponding to the SF measures than the predictions corresponding to the I measures.

Each fracture surface was examined to determine whether flaws nucleated from inclusions or surface finish flaws. No specimens in the polished group were observed to fail at stresses below the  $N=1$  measure, maximum observed inclusion measure, and  $N=100$  measure. Fatigue failure was observed to occur only when the applied stress was higher than the stress corresponding to about midway between the average and  $N=1$  measure predictions. The fact that no specimens failed below this level is attributed to the statistical nature of the presence and size of an inclusion. Figure 7.17 illustrates a typical subsurface inclusion fatigue origin.

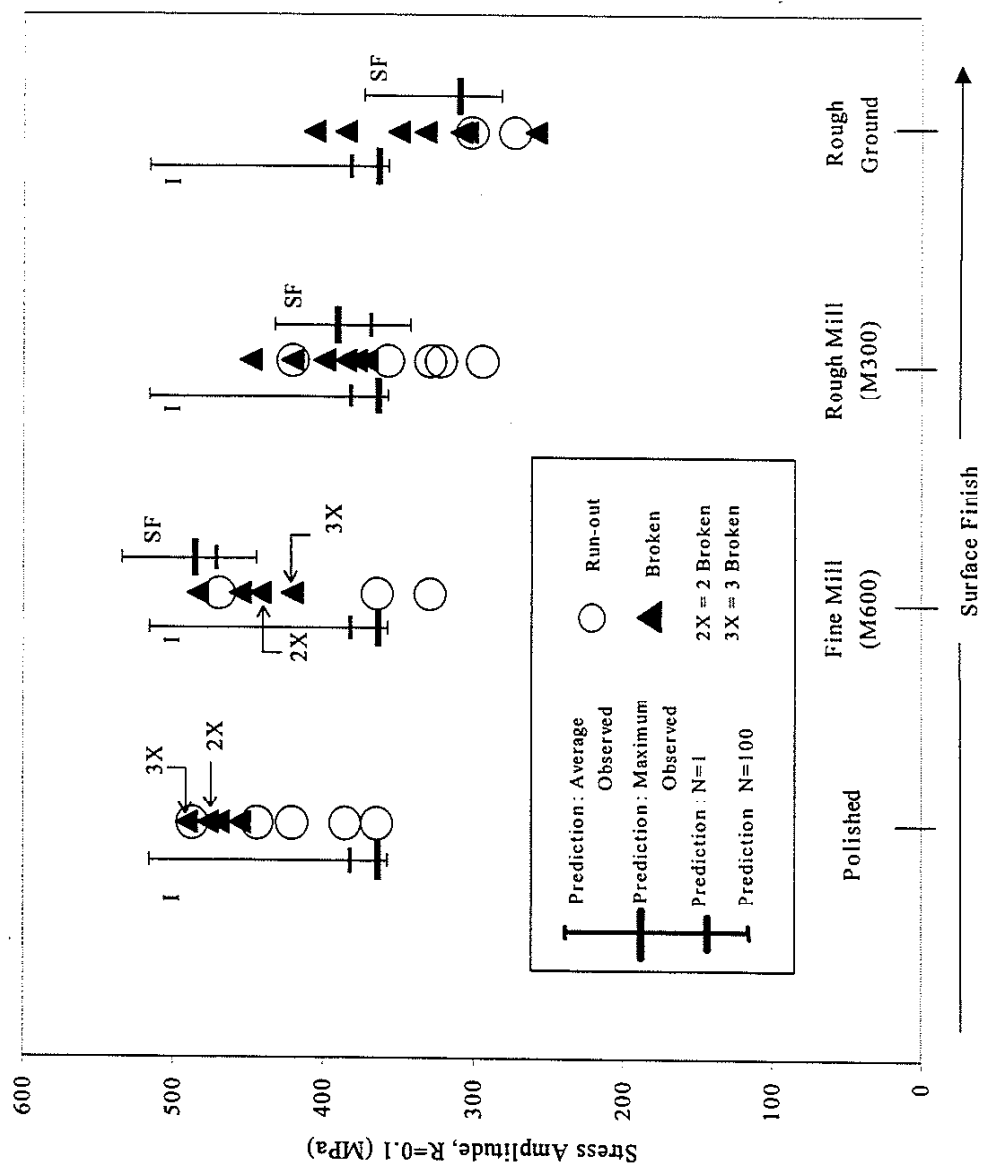


Figure 7.16 Comparison of Predicted and Observed Fatigue Behavior of Competing Flaws in 4340 Steel

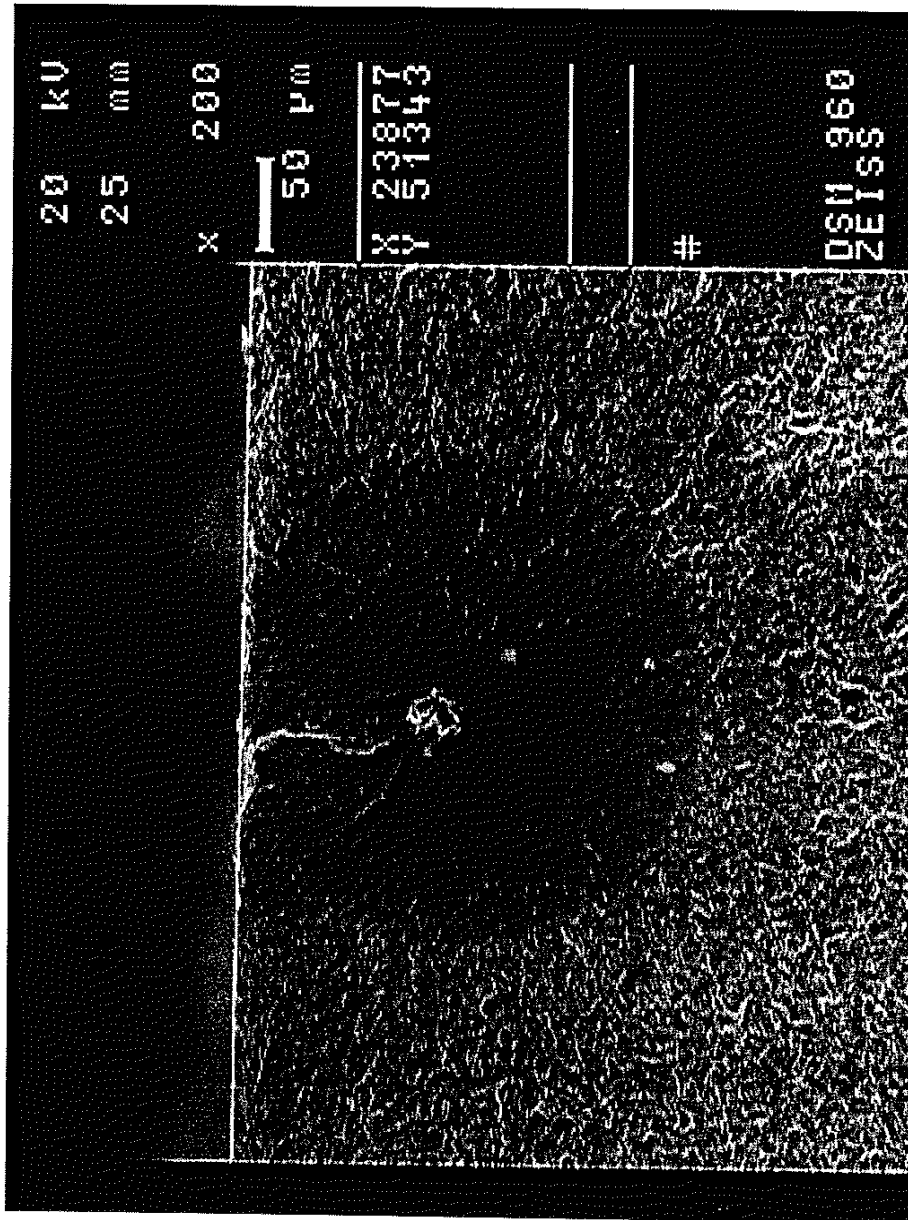


Figure 7.17 Subsurface Inclusion Origin in 4340 Steel

Of the seven broken specimens in the M600 group, three were associated with surface flaw origins while four were associated with inclusion origins. Thus, 42% of the broken specimens had surface flaw nucleated failures. A typical surface finish nucleated fatigue crack observed in the M600 group is shown in figures 7.18a and 7.18b. A dashed white line outlines the crack origin and subsequent growth regions in figure 7.18a. The actual surface flaw is indicated by a set of arrows in figure 7.18b. Note the actual flaw depth is approximately 5  $\mu\text{m}$  compared to the flaw depths predicted by the four measures, which range from 1.7 – 6.1  $\mu\text{m}$ .

If one examines the cumulative distributions of flaw size for the inclusion and M600 surface flaws illustrated in figure 7.12 the two distributions may appear very similar. In fact, they are and they are not, depending on the basis by which the two are compared. For example, one may compare the two flaw types on the basis of average flaw size. In that case, the two are nearly identical as indicated by the intersection of the two distributions at a cumulative distribution of about 45%. However, comparison of the two flaw distributions on the basis of the maximum expected flaw size indicates that the maximum inclusion flaw is significantly larger than the maximum expected surface finish type flaw. For example, assuming a cumulative distribution of 99.9% the  $\sqrt{\text{area}_{\text{max}}}$  for the inclusion flaws is approximately 40  $\mu\text{m}$  whereas the  $\sqrt{\text{area}_{\text{max}}}$  for the M600 surface finish flaw is only about 10  $\mu\text{m}$ . The difference in the basis of comparison is also revealed by the different PV/D ratios found in table 7.5. For instance, predicted PV/D ratios for the observed average and N=100 measures in the M600 group differ considerably, 0.19 and 0.08 respectively.

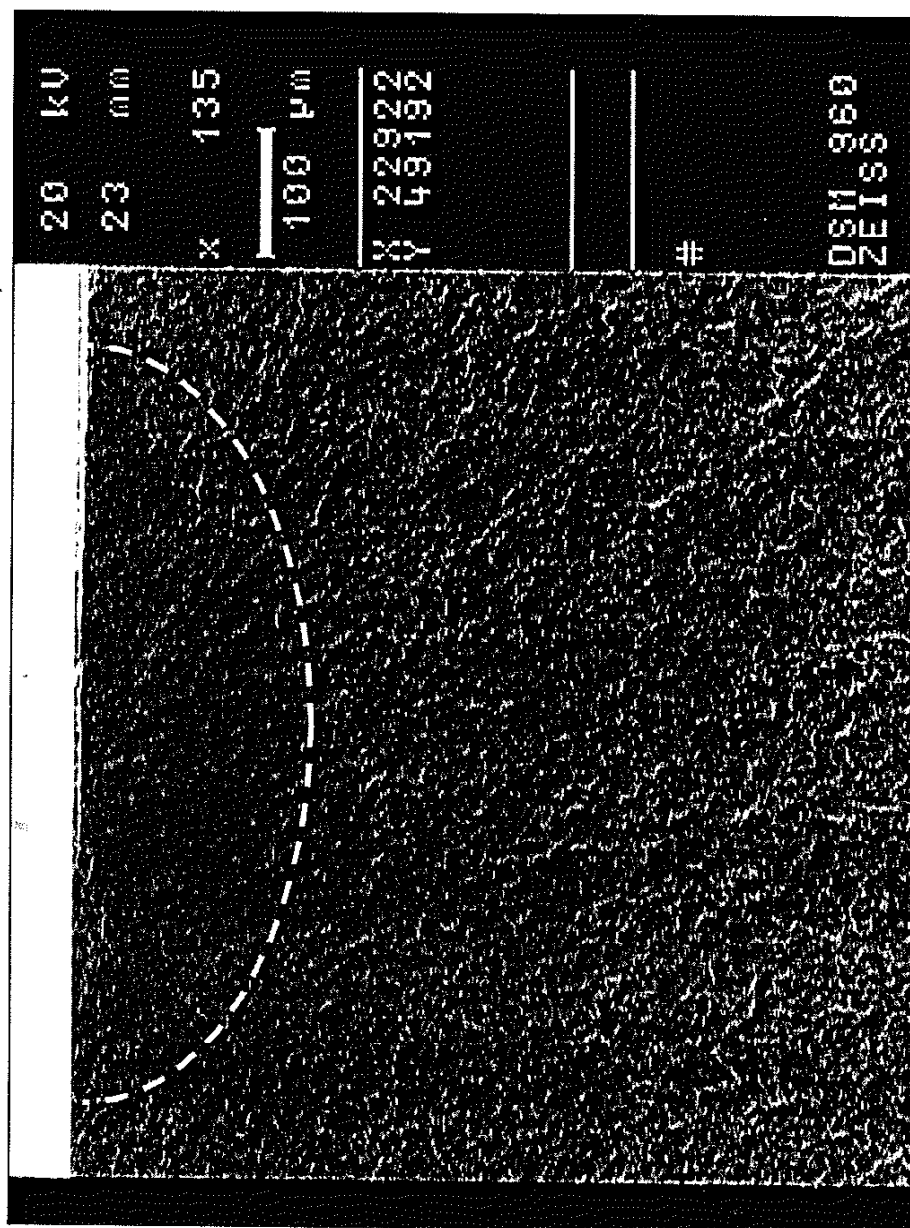


Figure 7.18a Macroscopic View of Surface Finish Nucleated Fatigue Origin in M600 Group

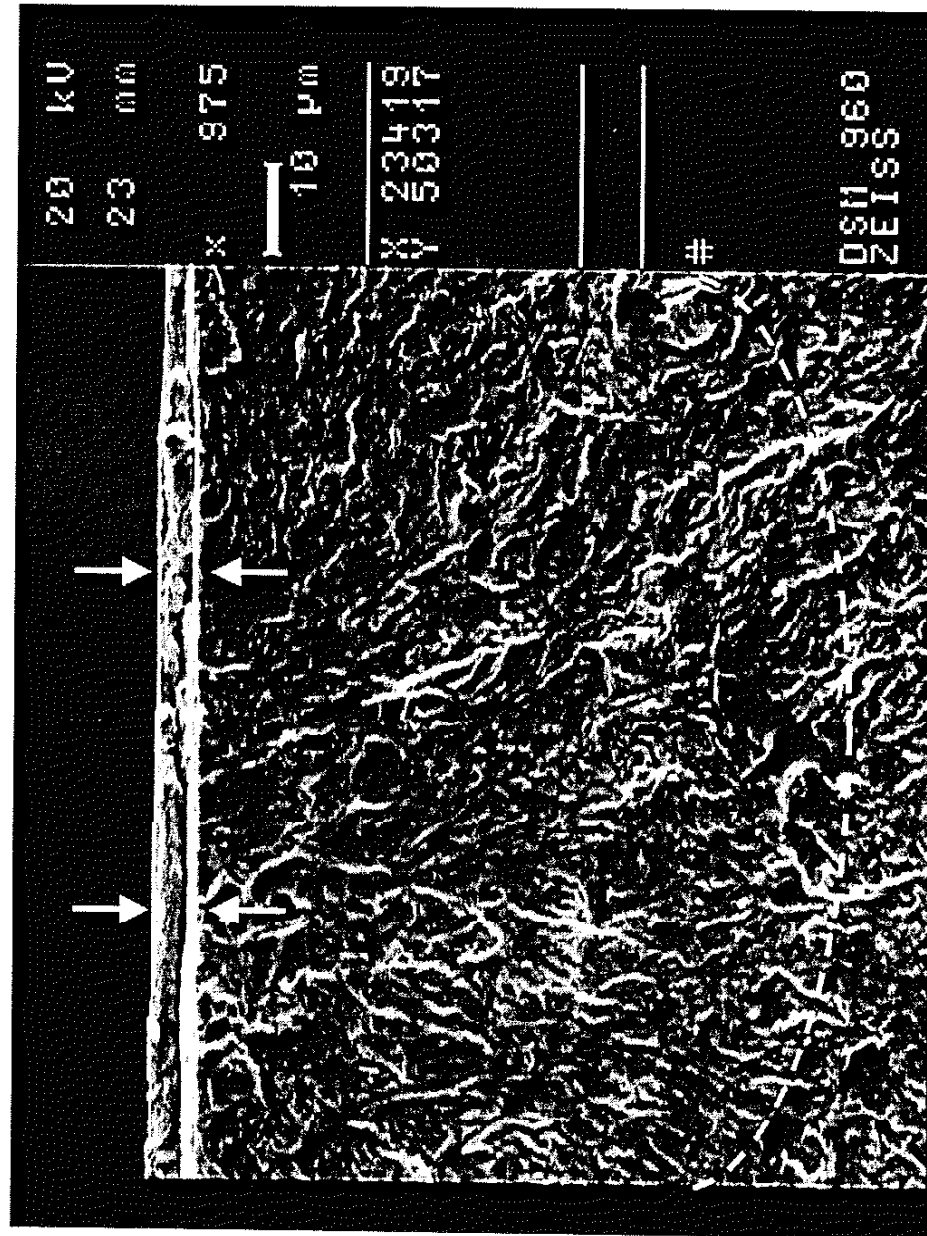


Figure 7.18b Surface Finish Nucleated Fatigue Origin in M600 Group

The fact that about 42% of the fractured specimens failed because of surface finish flaws is not a coincidence. The percentage of fatigue failures associated with a particular flaw type may be approximated as follows. Suppose two different flaw distributions, A and B, intersect as indicated in figure 7.19. One distribution will have a larger estimated flaw size for an extremely low cumulative distribution percentage, i.e.  $a > b$ . Eventually the two distributions intersect at point C. If they never intersect, the case is trivial; i.e. the larger flaw distribution will generally dominate. The cumulative distribution percentage corresponding to the intersection point C, designated X in the figure, is then determined. The percentage of failures predicted to originate from type A flaws may be approximated as equal to X% while (100-X)% will nucleate from type B flaws. Examination of the intersection of the M600 and inclusion flaw distributions indicates that  $X \approx 45\%$ , i.e. 45% of the broken specimens are predicted to fail from surface finish nucleated failures. The prediction is in excellent agreement with the observed 42% despite the small population of specimens tested.

The average predictions are in agreement with the results observed in the laboratory. However, the probability of observing the extreme case where a flaw of extreme size is present in the material is very small in the laboratory. Problems associated with extreme flaws, i.e. the largest 1% flaw size, that are experienced in the service of an engineering structure or component will unlikely be observed in the laboratory. Thus, laboratory testing alone will unlikely reveal the true nature of the problem. In order to address the problem successfully both laboratory testing and an understanding of the statistical nature of flaw size are necessary.



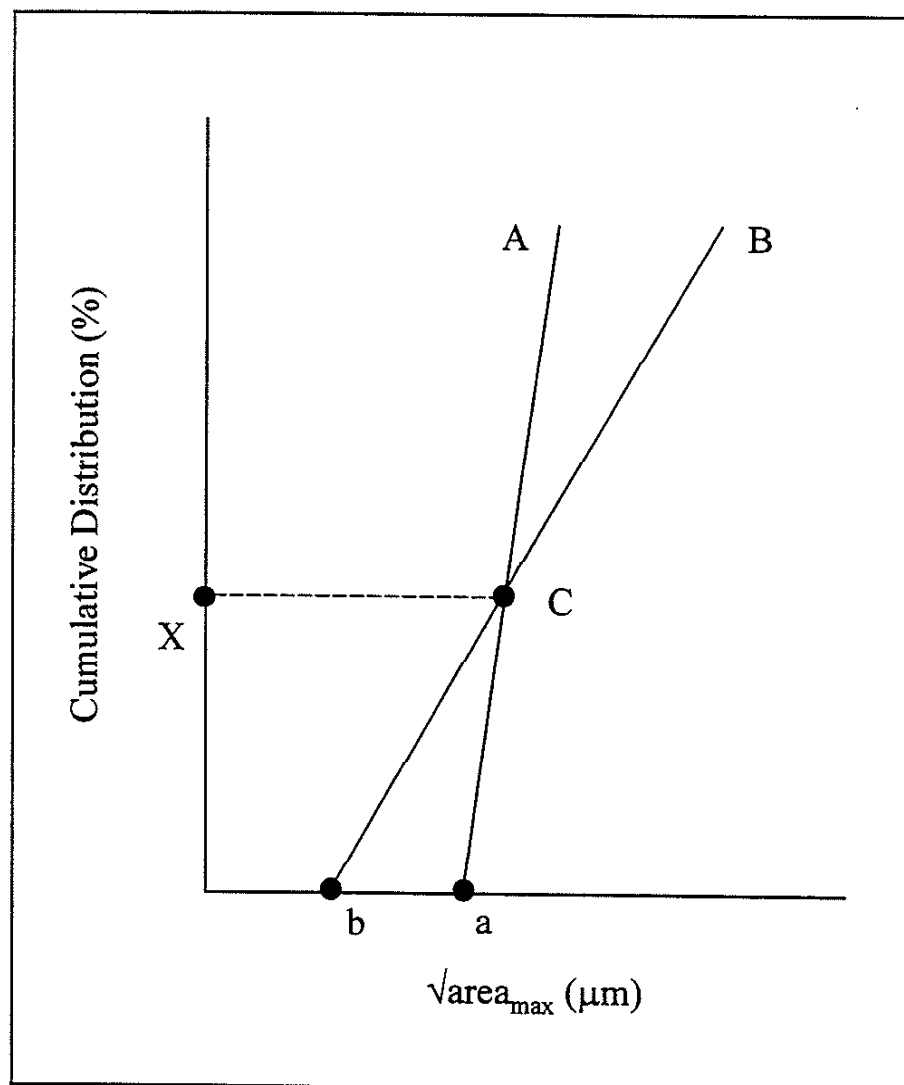


Figure 7.19 Predicting the Percentages of Failed Specimens Associated with Two Competing Flaws

Surface finish is predicted to be the dominant fatigue origin in the M300 and rough ground groups as illustrated by the decreasing fatigue limit predictions associated with the SF measures in figure 7.16. The same qualitative prediction could have been made by observing that both the M300 and rough ground surface flaw distributions indicate that surface flaws in both groups are significantly larger in size than the flaws indicated by the inclusion flaw distribution as illustrated in figure 7.12. Thus, it is not surprising that all cracks were observed to nucleate from surface finish flaws in both the M300 and rough ground groups. An example of a fatigue origin observed in one of the M300 specimens is shown in figures 7.20a and 7.20b. Figure 7.20a provides a macroscopic view of the crack growth as outlined by the white dashed line. A closer view is provided in figure 7.20b where the crack growth direction is indicated by a dashed white line and the actual flaw origin depth is denoted by the white arrows. Notice the shallow depth and large aspect ratio of the surface finish flaw. Predicted and observed flaw depths are in excellent agreement, 7.1-29.1  $\mu\text{m}$  and 10  $\mu\text{m}$  respectively. Examination of the fracture surfaces for the rough ground surface finish group confirm the PV/D predictions in a similar fashion as the M300 group. Overall, the PV/D concept qualitatively and quantitatively explains why and when fatigue cracks will originate from surface or subsurface flaws.

Before moving on to other topics, a brief note regarding scatter and the statistical nature of the fatigue limit follows. Scatter in the observed fatigue limit is mainly attributed to the statistical nature of the flaw size and flaw competition. In order to interpret fatigue data correctly a statistical approach is essential. Generating large

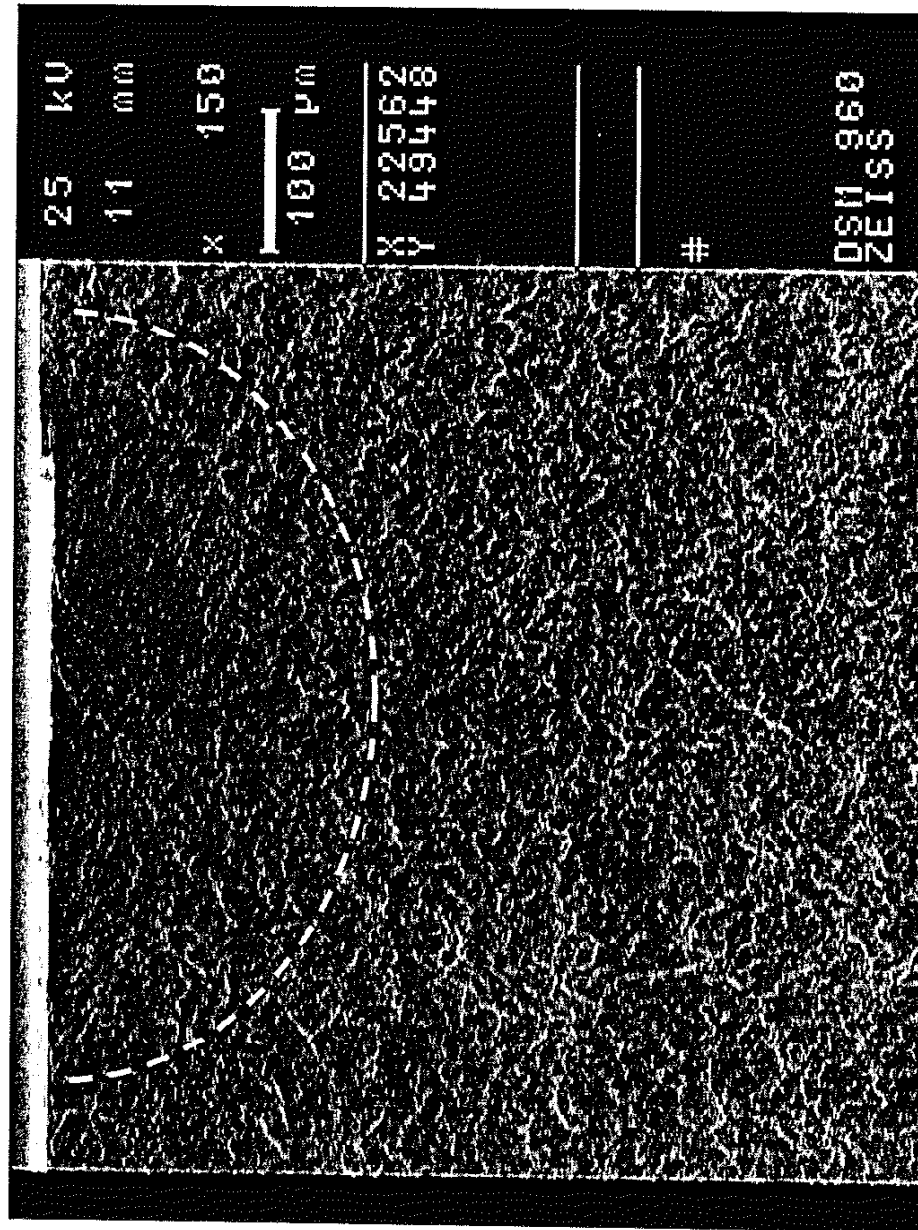


Figure 7.20a Macroscopic View of Surface Finish Nucleated Fatigue Origin in M300 Group

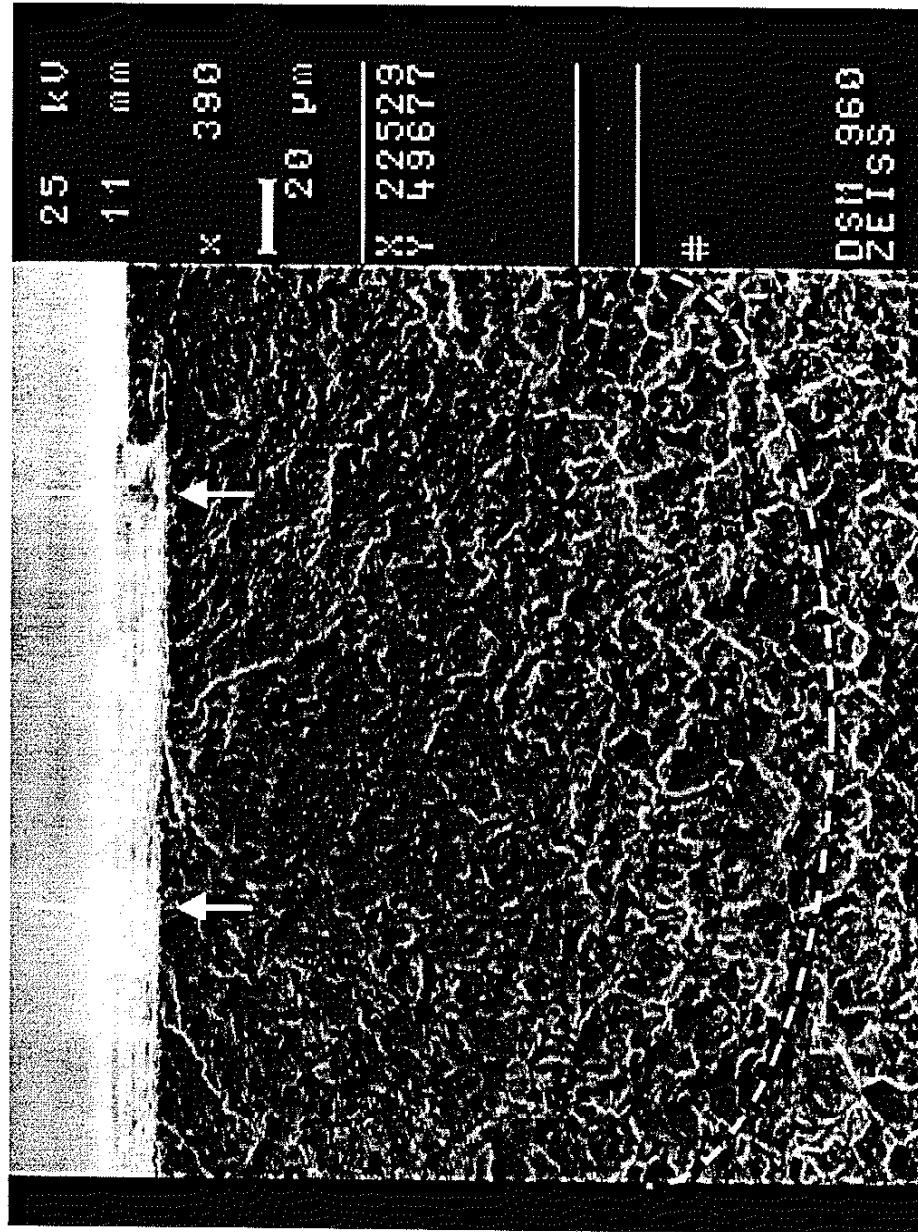


Figure 7.20b Surface Finish Nucleated Fatigue Origin in M300 Group

amounts of fatigue data is not only expensive and time consuming but the results themselves will often fail to reveal any additional insight about the fatigue process. Neither the average or extreme basis is always the correct basis to use. Selection of the basis will depend on the application. For example, in situations where failure of a structural component would result in the loss of life, a severe injury, or a large expensive warranty claim the extreme basis would be appropriate. Some applications exist where the average strength or life of a component, i.e. brake pads, is more important and deviations from the average are acceptable or desired. Use of the extreme basis could likely result in a large waste of resources, time, and/or money; the average basis would be more appropriate. However, for most structural applications the extreme basis will be the more appropriate choice.

## 7.6 Observations of Critical Surface Roughness

Competition of flaws for determining the dominant flaw size in a material explains another important observation. Siebel and Gaier [86] performed a number of push-pull, pull, and torsion fatigue tests on both ferrous and non-ferrous steels with various surface finishes in one of the earliest surface finish studies reported. Their results indicated that a critical roughness depth  $R_o$ , not the root mean square or rms value but the peak-valley depth of the surface finish, exists where smaller surface finish flaws have no effect on the fatigue limit. Several examples of Siebel and Gaier's results are illustrated in figure 7.21. All five materials follow the same general behavior. Fatigue strength

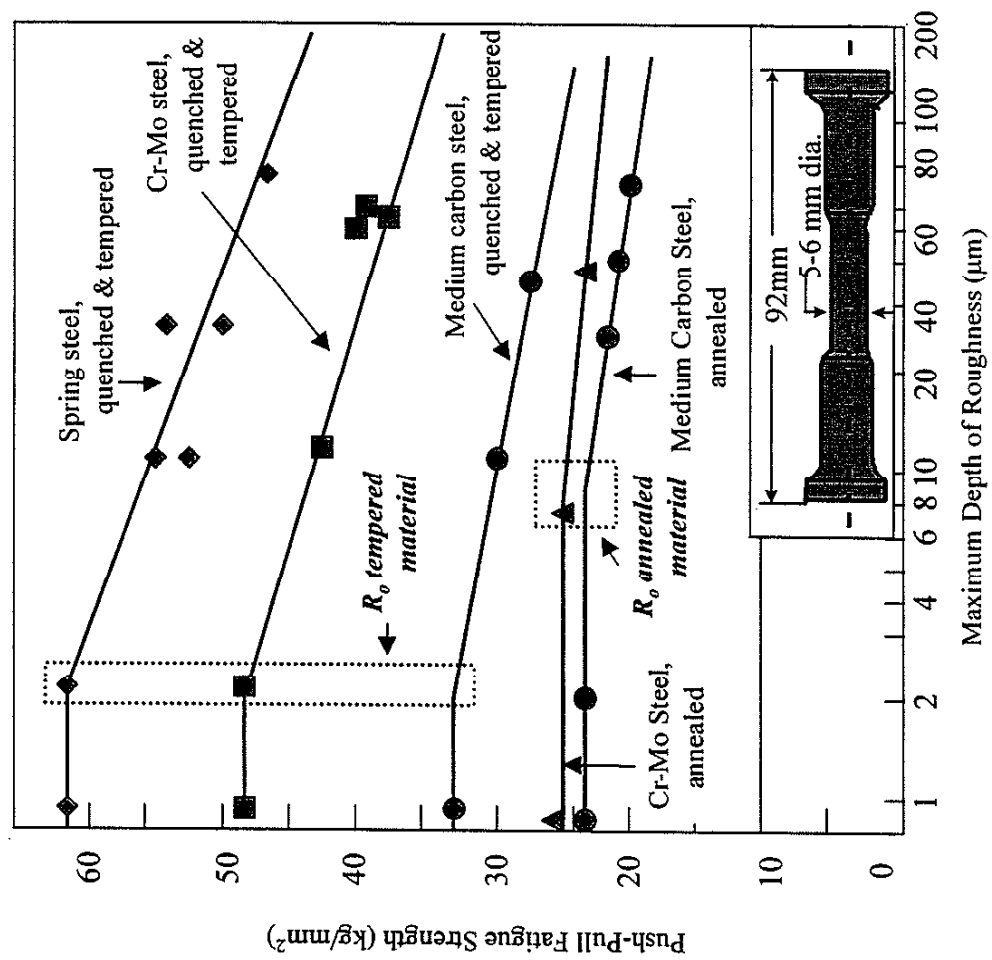


Figure 7.21 Siebel & Gaier's Observations of  $R_0$  in Tempered and Annealed Steels [86]

increases at approximately the same rate with a reduction in surface roughness. Eventually a critical roughness,  $R_o$ , is reached where any further reduction in surface roughness has no effect on the fatigue limit.  $R_o$  is larger for the annealed steels than for tempered steels. Unfortunately, they had no means of quantifying the effects of these flaws at that time. Even so, Siebel and Gaier were the first to indicate that  $R_o$  is a function of the material's microstructure although no relation between  $R_o$  and structure size was formed. Similar observations were reported by Verpoest et al [87]. They discovered that initial polishing increased the fatigue limit of steel wire. However, the benefits were limited due to the presence of inclusions.

The three tempered materials indicated in figure 7.21 all possess fine microstructures, i.e. fine martensite, bainite, or both. Each exhibits a different fatigue limit which can be attributed to differences in hardness assuming that the inherent flaw size (inclusions) in each is approximately equal.  $R_o$  will typically be determined by inclusion content in high strength steels because the inherent flaws are larger than the intrinsic flaws. If the assumption of equal inclusion size in the three tempered materials is valid, it is not surprising to observe that  $R_o$  is approximately equal for each tempered material. Furthermore,  $R_o$  for the two annealed steels are equal but much larger than  $R_o$  for the tempered steels. This observation is expected since annealed materials have significantly larger structures than the quenched and tempered materials. In other words, intrinsic flaws are usually larger than inherent flaws in annealed materials. Thus, the PV/D concept can be applied to intrinsic and processing flaws as well.

The other interesting aspect of the fatigue behavior of the steels investigated by Siebel and Gaier is the fact that the fatigue limit increases at nearly the same rate with a reduction in surface roughness for a wide range of strengths. The lines that indicate the observed changes in fatigue strength with increasing surface roughness all have slopes of approximately  $-1/6^{\text{th}}$ . This is understandable since Murakami has shown that the threshold condition changes at a certain rate with a decrease in flaw size as seen in figure 7.22. The rate is constant for many metals including carbon steels, stainless steels, maraging steels, aluminum, copper, and brass. Furthermore, the rate is equal to the rate predicted by Murakami's  $\sqrt{\text{area}}$  parameter model and the HPM model as indicated by the

exponent of the  $\sqrt{\text{area}}$  term in the fatigue prediction: 
$$\Delta\sigma = \frac{1.43(H_v + 120)}{\sqrt{\text{area}}^{1/6}}.$$



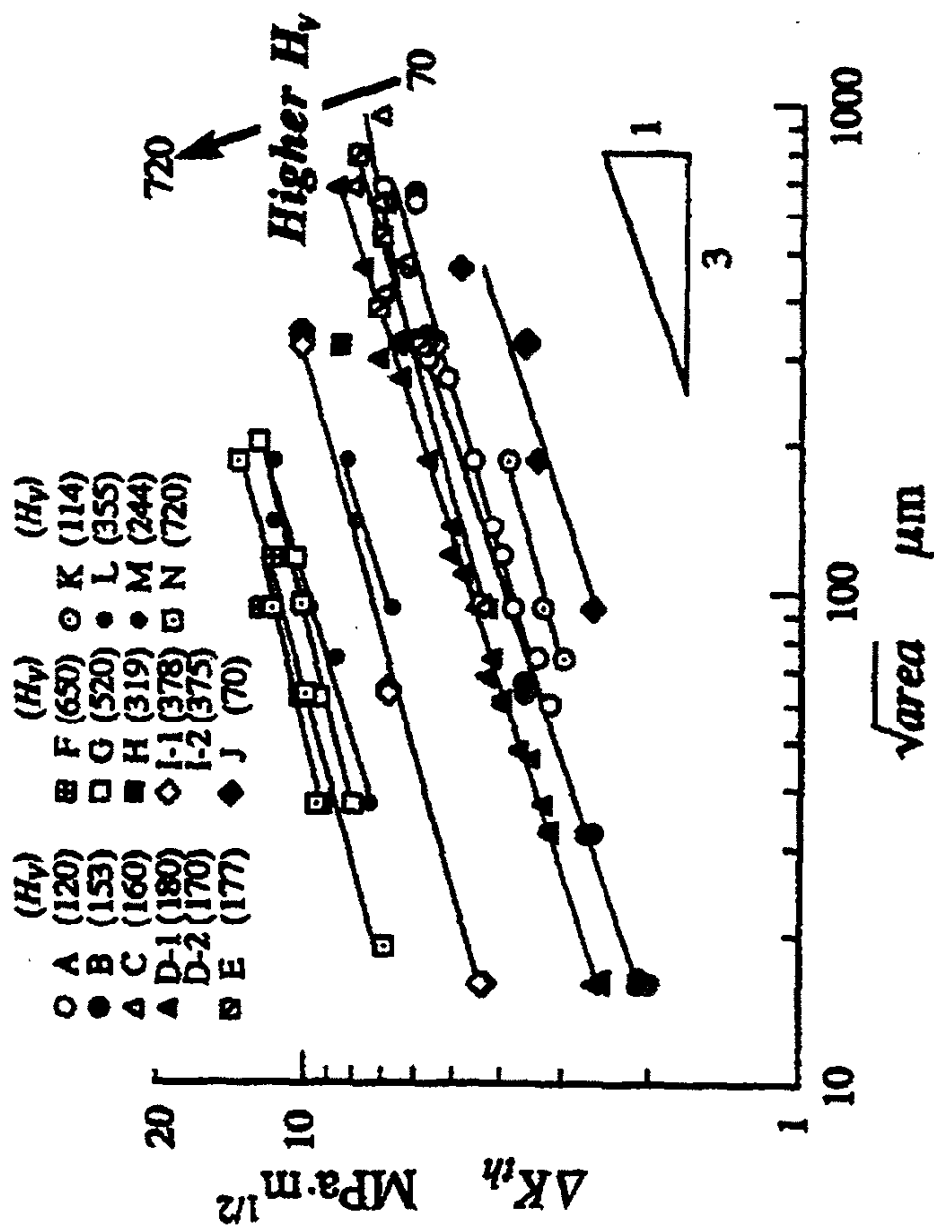


Figure 7.22 Relationship Between Rate of Change of Threshold Stress Intensity Range and Flaw Size for Various Strengths of Materials [8]

## 7.7 Transition from the Inherent Regime to the Intrinsic Regime in Smooth Specimens

The transition from the intrinsically flawed regime to the inherently flawed regime in a polished specimen is determined by the competition of the size of the NPC and the inherent inclusion. Thus, the transition is dependent on the cleanliness and microstructure of the material. The problem is analogous to the decrease in notch sensitivity in high strength steels. In low strength materials the flaws do not affect the notch sensitivity (or fatigue limit) because they are smaller than the microstructure (or NPC size); notch sensitivity (or fatigue limit) is determined solely by the microstructure. Increases in hardness result in an increase in notch sensitivity (or fatigue limit) due to the decrease in microstructure size associated with the increase in hardness. Eventually, flaws become large enough in size relative to the microstructure and the notch sensitivity (or fatigue limit) reaches a maximum which is governed by the inherent flaw size. Any further increase in hardness may cause the material to be less sensitive to notches (no increase in the fatigue limit) if processing type flaws are activated, i.e. the processing flaws act as larger notches (cracks) in the material.

Consider a material whose fatigue strength is currently limited by inherent inclusions. An engineer wishes to use the same material but requires an increase in the fatigue strength. One solution may be to reduce the inclusion size and content of the existing steel. Although a reasonable approach, the microstructure of the material will limit the increase in fatigue strength that is typically assumed to be associated with the

reduction of inclusion content. The HPM model provides both a qualitative and quantitative means of addressing the problem. Two annealed carbon steel investigations found in the literature are considered to illustrate the solution methodology, a 0.10%C and 0.45%C steel [3].

Inherent inclusion sizes for the 0.10%C and 0.45%C steels were reported to have  $\sqrt{a}$  areas of approximately 60  $\mu\text{m}$  and 30  $\mu\text{m}$  respectively. Fatigue limits were determined for specimens that had artificial flaws introduced into the material and for polished specimens. Artificial flaw had  $\sqrt{a}$  areas of approximately 60 and 37  $\mu\text{m}$  for the 0.10%C and 0.45%C steels respectively. Results are plotted in figure 7.23 along with HPM predictions for the artificial flaws and NPC flaw sizes equal to  $d$ ,  $3d$ , and  $10d$ . A fictitious intrinsic flaw size,  $d$ , has been assumed for the purposes of illustrating the concept of the transition from one flaw dominated regime to another. Results agree with the predictions for the artificially flawed specimens as indicated by the proximity of the observed results with the HPM prediction given by the dashed line(s). Similarly, smooth specimen results are consistent with the HPM model if the maximum inclusion size is considered as the dominating flaw.

First, consider the 0.10%C steel. Fatigue limits for the polished and 60  $\mu\text{m}$  artificially flawed specimens are identical which is not surprising since the inherent flaw size is approximately 60  $\mu\text{m}$  as well. Assume that the NPC flaw size associated with the microstructure is equal to  $10d$ , which is about equal to the 60  $\mu\text{m}$  inherent flaw size. So, reduction of the inclusion content would leave a NPC flaw of the same size in the

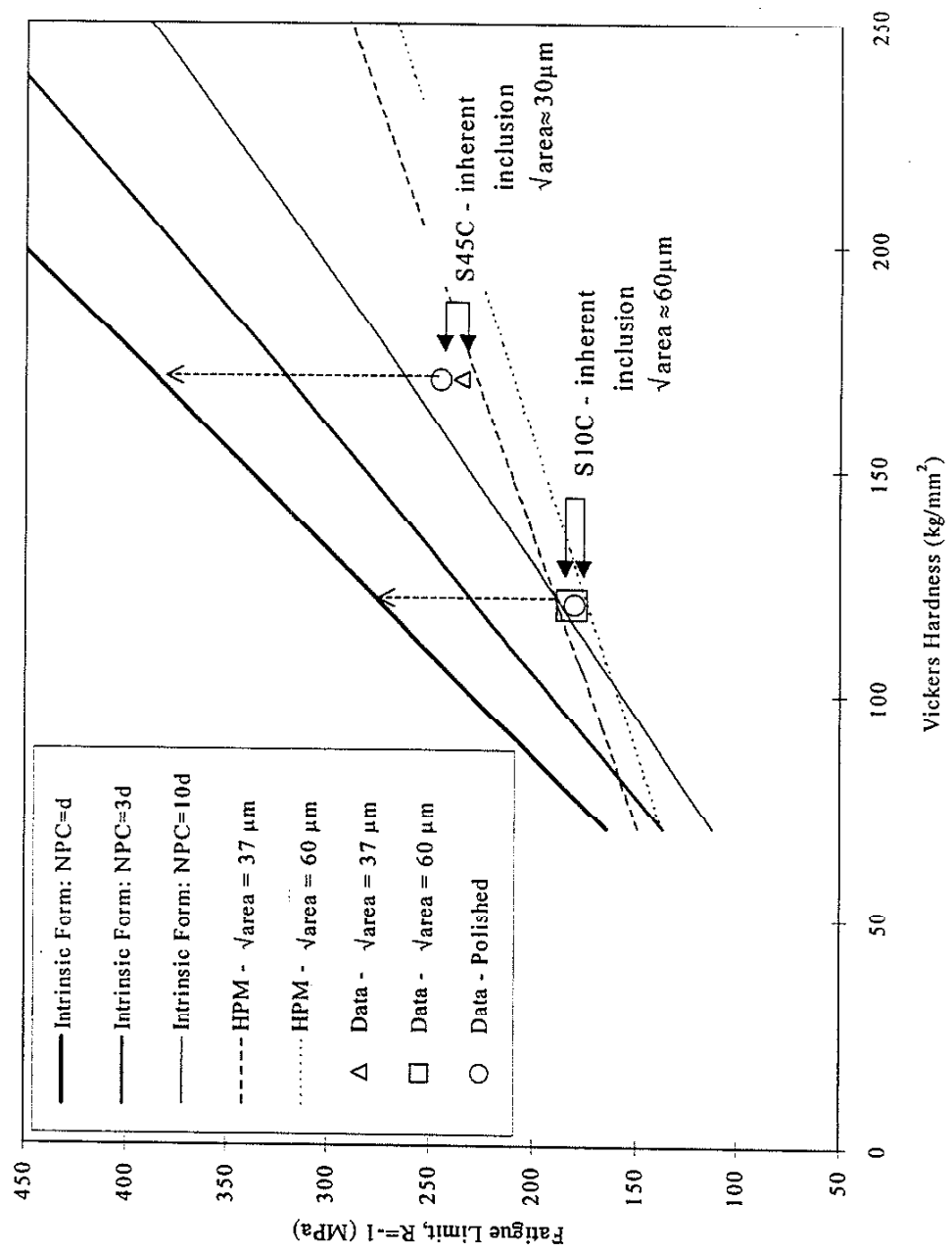


Figure 7.23 Transition from Inherent to Intrinsic Flaw Regime in Two Annealed Carbon Steels

material. No gain should be observed by reducing the inclusion content. However, assume that the microstructure was such that the intrinsic NPC size would be equal to  $d$  rather than  $10d$ . For example, another microstructure may be obtained by using a different heat treating process to obtain a smaller NPC size with the same barrier strength. In this case, an increase in the fatigue limit should be observed if a cleaner steel were used due to the reduction in inherent flaw size as illustrated by the vertical arrow in figure 7.23, i.e. the NPC size is smaller than the initial inclusion flaw size. The same premise can be applied to the S45C steel as indicated in the same figure.

This calls attention to another application. Assume that a material does contain inclusions of a given size, but the inclusions are not detrimental to the fatigue strength of the material. In other words, the fatigue limit is limited by the NPC size associated with the microstructure. Similar to the former problem, an increase in the fatigue strength may be obtained by reducing the NPC size by using a different heat treatment process. A reduction in inclusion size would not be necessary, although the inclusion size will limit the effects of reducing the intrinsic NPC flaw size.

## CHAPTER 8

### CONCLUSIONS AND RECOMMENDATIONS FOR FUTURE WORK

#### 8.1 Summary and Conclusions

This dissertation deals with the threshold conditions of small non-propagating cracks that nucleate naturally or from inherent flaws in metals. Research focused on modeling the physical mechanisms that govern these threshold conditions. Critical parameters that determine threshold conditions were identified. Likewise, the manner by which microstructure and other flaws compete in determining these critical parameters was addressed both qualitatively and quantitatively. Predictions of the proposed model were verified with more than 50 different fatigue limits obtained both by experiments performed in this investigation and numerous results found in the literature. The model has been successfully verified in ferritic, ferritic-pearlitic, martensitic, and martensitic-bainitic steels.

To summarize, comparison of the HPM and empirical predictions with observed results are presented in figure 8.1 for low and intermediate strength materials and figure 8.2 for high strength steels. Empirical predictions in figure 8.1 are inferior to the HPM model predictions. The basis of the empirical model is a correlation of fatigue strength to

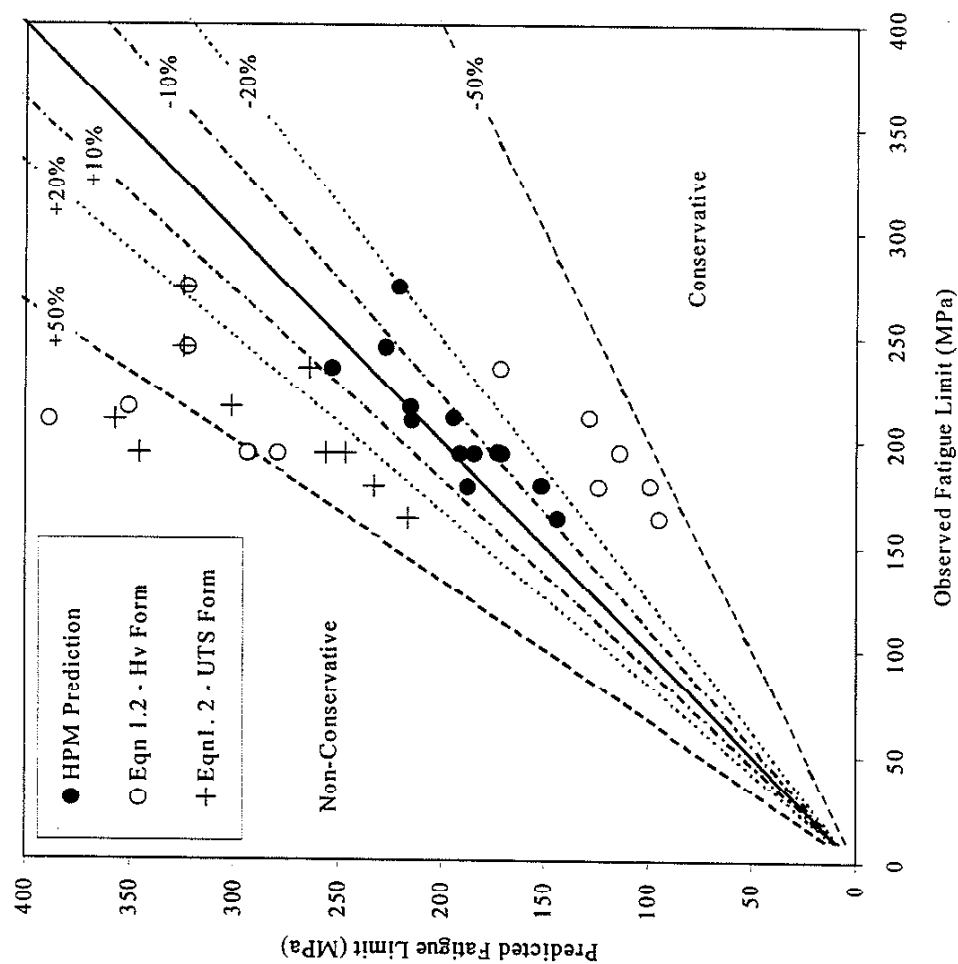


Figure 8.1 Comparison of HPM Model Predictions and Empirical Predictions to Observed Results of Various Low and Intermediate Strength Steels

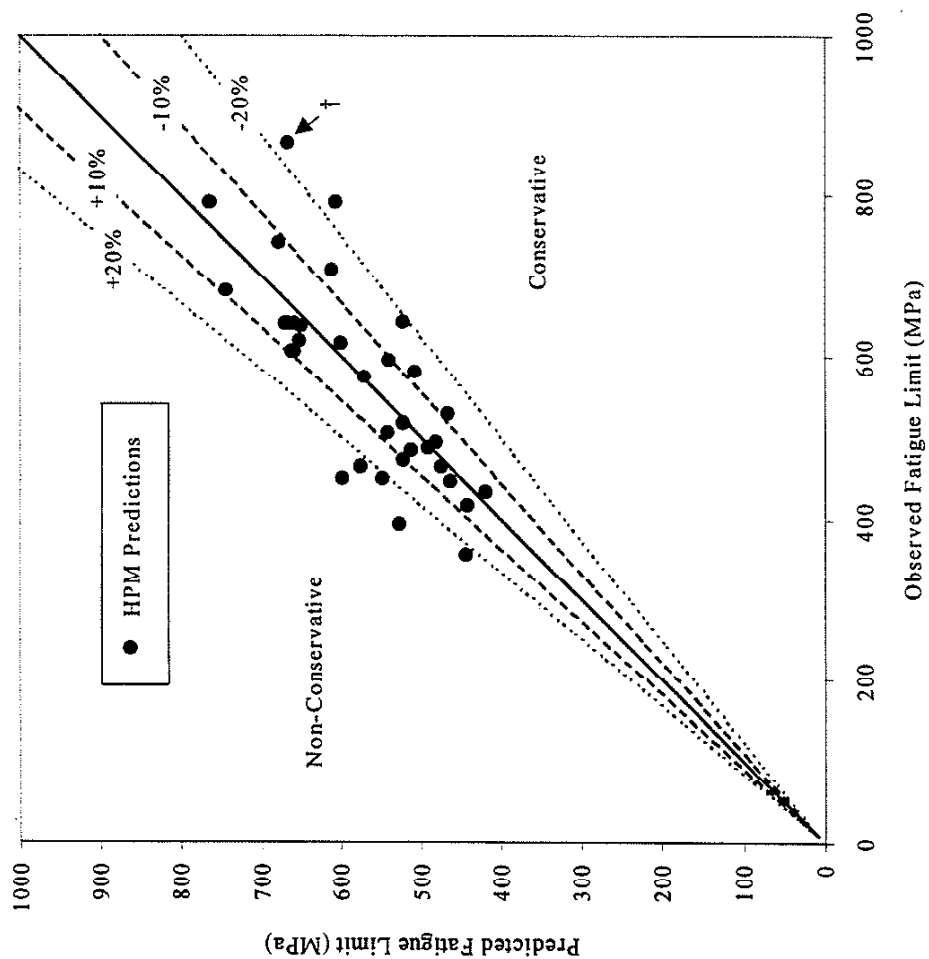


Figure 8.2 Comparison of HPM Model Predictions vs. Observed Fatigue Behavior of Numerous High Strength Steels



bulk strength. However, macroscopic properties and mechanisms are not always representative of the microscopic properties and mechanisms. Hence, variations in the fatigue limits associated with changes in microstructure are captured by the HPM model whereas the empirical model fails.

High strength steels predictions are summarized in figure 8.2. No useful empirical predictions exist for high strength steels, only a broad range of bounds since large amounts of scatter are observed. However, the majority of fatigue limit predictions for the high strength steels shown in figure 8.2 are within 20% of the observed fatigue limits despite the broad range of fatigue strengths considered.

Conclusions of this research are:

- 1) The fatigue limit is determined by the non-propagating flaw size and the crack barrier strength.
- 2) Three types of flaws exist and compete for the dominant non-propagating crack role: intrinsic, inherent, and processing flaws.
- 3) Tempering can alter the active fatigue mechanisms in high strength steels that contain processing flaws and reduce their adverse effects.
- 4) Synergistic effects of surface finish and intergranular cracks are predictable by employing the concept of a notch within a notch.
- 5) The PV/D concept successfully predicts the occurrence and competition of surface and sub-surface fatigue initiated failures;  $R_0$  is defined.

- 6) The importance of selecting the correct basis for estimating flaw size, average vs. extreme, is essential in addressing the statistical nature of the fatigue limit.
- 7) Overall, the HPM model can be used as a simple but robust means of quantifying benefits associated with material screening, selection, and processing and can be implemented as an aid in directing material research and material design.

## 8.2 Future Work

Future work should focus on optimizing hardness and fatigue strength for applications involving both non-contact fatigue (axial, bending, or combinations thereof) and rolling-sliding contact fatigue, e.g. gears. This should include mapping the effects of the steel production route, alloy variations, heat treating process parameters, etc. on the size of and the mechanisms associated with the formation of intergranular flaws. Similarly, the effects of microstructure such as distribution, size, volume fraction, and phase connectivity should be systematically investigated to understand qualitatively and quantitatively how to control the naturally nucleated NPC size and barrier strength in duplex structures. Success in optimizing and enhancing fatigue strength will be determined by how well the manufacturer can control these parameters. Nucleation and growth mechanisms in ferritic-martensitic structures should also be investigated to see if the fatigue limit for these types of steels can be predicted by the HPM model. Also, the

methodology used in the HPM and  $\sqrt{\text{area}}$  models may be applicable to other fatigue modes, i.e. multiaxial loading. Finally, development of statistically based fatigue simulation models could prove extremely valuable in determining both qualitatively and quantitatively what the important fatigue variables are and how sensitive fatigue performance is to each. With these questions answered, manufacturers would have a better idea of how to use their resources to maintain reliability, increase durability, and optimize profit.

## APPENDIX A

### METALLURGICAL DETAILS OF HEAT TREATMENT AND STEELS TESTED

BY GARWOOD ET AL

Specimens were machined to nominal dimension and copper plated prior to austenitizing, quenching, and tempering. Various tempering temperatures were used to achieve the desired range of hardness. Finally, specimens were circumferentially ground and polished to remove the copper plating and any small scale that may have accumulated during heat treatment. Tempering temperatures (35°C – 750°C) certainly induced carbide precipitation at grain boundaries and in the matrix, at least for the extreme tempering temperatures. Grain boundary carbides are now well known to cause tempered martensite embrittlement (TME) in hard steel, a fact which was not well understood until two or three decades after Garwood's study. However, embrittling may still occur without tempering, i.e. "quenched martensite embrittlement" (QME). Quenched martensite embrittlement is analogous to tempered martensite in that cementite forms but does so during the austenitizing process. [88]. Details of the microstructure were not reported. One can surely make qualitatively comparisons between the model and Garwood's results, but quantitative predictions are difficult to make without quantitative knowledge of the microstructure. Therefore, assumptions were made and justified by work found in the literature for estimating the microstructure size in an attempt to make quantitative comparisons.

The material consists of martensite, retained austenite, and carbides after austenitizing and quenching. Since no information is reported regarding tempering times, the typical tempering time of one hour is assumed. Intuitively, the higher tempering temperatures would likely lead to recovery, recrystallization, and grain growth. However, investigations by numerous researchers indicate that medium and high carbon steels do not recrystallize during such tempering. This is attributed to the pinning action of the high-density cementite carbide particles that prevent the migration of high-angle boundaries required for recrystallization [89,90]. Martensite laths/plates transform to acicular ferrite grains and cementite, often called bainite, although slight coarsening may occur. Ferritic grain sizes have been reported to vary from ASTM 12.5-17 (3.2 to 0.56  $\mu\text{m}$  respectively) from prior austenitic grain sizes of ASTM 6-8. Thus, the size of the resulting ferrite structure should not have changed significantly. The carbides do not embrittle the material at low hardness levels since the matrix is fairly ductile. The intrinsic flaw size is governed by the ferritic grain size.

## APPENDIX B

### CLASSICAL EXPERIMENTAL SURFACE FINISH STUDIES

Countless studies have been conducted to ascertain the effects of numerous factors on the fatigue limit of a wide variety of metals, too many for review in this paper. A brief summary is provided in an attempt to illuminate the relevance of the proposed work.

Some of the classical studies of surface finish effects have been summarized in a design handbook by Hanley and Dolan [91]. Following is a summary of several of the important aspects reported along with findings reported in several investigations that are more recent. Brodstein suggested using the rms roughness as a standard for assessing surface finish. However, the physical quality and type of surface irregularities cannot be described with this reading. Studies by Moore & Kommers, Hoger & Neifert, Houdremont & Mailander, and Buchholtz & Schultz all agree that the effect of turning versus superpolish finishes results in an increased reduction of the fatigue limit from 15% to 21% with increasing material strength. Sinclair, Corten, and Dolan [92] reported that the fatigue limit is a weaker function of surface finish than strength with the rate of decrease in fatigue limit decreasing rapidly with surface finish. Noll and Lipson [85] compiled data from the literature (including some of the results mentioned above) for fatigue limit vs. tensile strength for ground, machined, hot-rolled, and as-forged specimens as illustrated in figure 7.1. Note the scatter, extrapolation, and limited number

of data. This data is commonly quoted and is often cited with the prediction of the fatigue limit reduction factor.

Other studies produced more questions and resulted in conflicting results. Among these were studies on the effects of grinding on the fatigue limit. Cledwyn-Davies [93] and Bacon [94] report as much as a 12% reduction. Tarsov and Grover [95] report an increase of 20% for a Rc 59 material but a decrease of 9% for a Rc 45 material. Results obviously point to other effects, i.e. residual stresses, cold-working, inclusions, and microstructure.

One rather fruitful study was conducted which seems to be the first attempt to isolate the synergistic effects of numerous variable to a certain degree, Siebel and Gaier [86]. A series of ferrous and non-ferrous metals were studied in push-pull, pull, and torsion fatigue with various surface finishes. Results indicated that a critical roughness depth,  $R_o$ , not rms but maximum depth of the surface finish grooves, exists where smaller grooves have no effect on the fatigue limit. Siebel and Gaier are the first to indicate that  $R_o$  is a function of the material's microstructure; however, no relation between  $R_o$  and structure size is formed.

More recent studies by Greenfield and Allen [96] and Suhr [97] utilized fracture mechanics to predict surface finish and flaw effects on the fatigue limit with some success. Greenfield and Allen, however, failed to eliminate the residual stresses which rendered their data of a 0.40%C steel difficult to interpret. In addition, they used the rms

or centerline average roughness reading to characterize the effect of surface finish depth, not  $R_o$  or a more meaningful parameter. Suhr didn't report the actual surface finish measurements for his experiments on a 0.30%C steel, but he did eliminate the residual stresses by annealing after machining. Furthermore, Suhr observed that all flaws associated with the fatigue origins were larger than the surface flaws measured with a profilometer. Suhr employed El Haddad's model to predict the fatigue limit as a function of flaw size with some success.

Verpoest et al [87] conducted studies of pearlitic steel wire and pre-existing surface flaws. The influence of polishing to reduce the flaw or surface flaw size was investigated. Reduction of flaw depth was achieved by polishing. Similar to Siebel and Gaier, after removing a certain amount of material additional polishing did not reduce the effect of inherent inclusions. Consequently, the following question is raised: what combination of surface finish and inherent flaws such as intergranular oxides or inclusions will provide the best and most economical fatigue performance? The problem is further complicated when the two types of flaws are opposite in nature, i.e. their aspect ratios differ considerably.



## APPENDIX C

### AUGER ELECTRON SPECTROSCOPY

The presence of a carbide layer at the grain boundary of the modified 8680 steel was investigated with Auger Electron Spectroscopy. Auger fracture specimens were ground from the remaining ligaments of fractured specimens. Fracture specimens were manufactured from the first lot of specimens that were used in the synergistic surface finish and intergranular cracking study and from both the tempered and non-tempered specimens taken from the second lot. Profile measurements were made on several locations of the fracture surface, both grain boundaries and bulk grain surfaces. Segregation of impurity elements such as phosphorous were very difficult to detect and measure with any confidence. Phosphorous signals were either non-existent or were comparable in intensity to the inherent noise of the measuring process. Therefore, attention was focused on the carbon profiles to determine if a carbide layer was present at the grain boundary; and, if a carbide layer was present, its thickness was to be measured.

Results for the first and second lots (both tempered and non-tempered materials in the second lot) were consistent and revealed virtually identical results. A carbide approximately 10 nm thick was present on the grain boundaries of the fracture surfaces. Figure C.1 illustrates typical results from profiles of the fracture surface for the three materials investigated. The carbon derivative peak height is plotted as a function of depth from the fracture surface. High amounts of carbon were concentrated on the grain

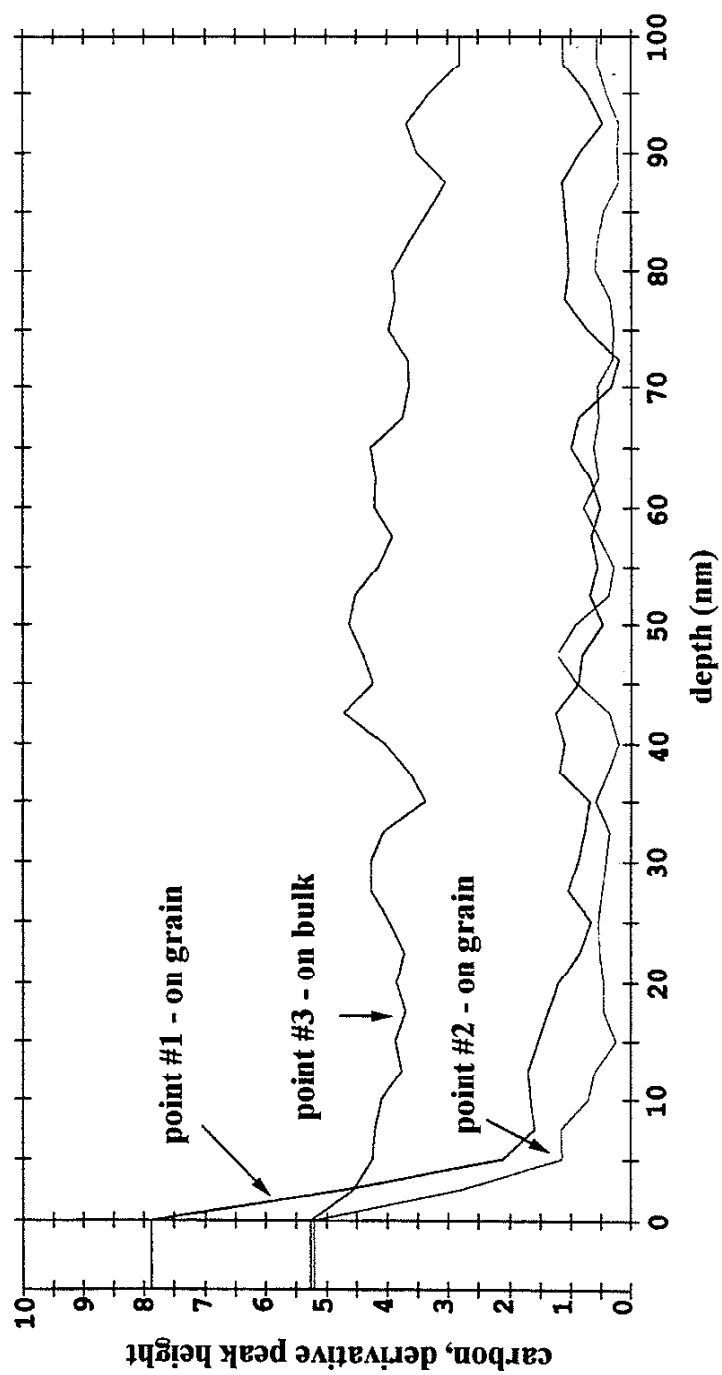


Figure C.1 Derivative Peak Heights for Bulk and Grain Boundary Surfaces

boundary surfaces as indicated by points number 1 and 2 in figure C.1. Carbon levels drop off very quickly for both grain boundary measurements. In contrast, the bulk carbon content did not exhibit a gradient as indicated by point #3.

Figure C.2 indicates the atomic percent of carbon and oxygen measured from the surface of the grain boundary on point #1. Note that the atomic percent of carbon at the surface is around 10 at%. This is much larger than the nominal 3 at% (0.77 wt%) carbon that is soluble in iron prior to cementite formation in the iron-carbon phase diagram. Of course, alloying elements will alter the eutectoid reaction, but only slightly. Thus, a carbide must exist at the grain boundary. Since the atomic percentage of carbon is less than 25 at%, the atomic percentage for pure cementite, the area over which the Auger spectroscopy was conducted is not entirely covered with the carbide. The atomic concentration of carbon at the grain boundaries quickly decreases to about 3 at% (0.77 wt%), which is expected since after a certain depth the bulk of the grain is being measured. Thus, differences in the fatigue limits of the three steels is unlikely to be associated with the presence of the carbide layer, although the carbide layer may have degraded the fatigue limit of all three steels by causing intergranular crack nucleation.

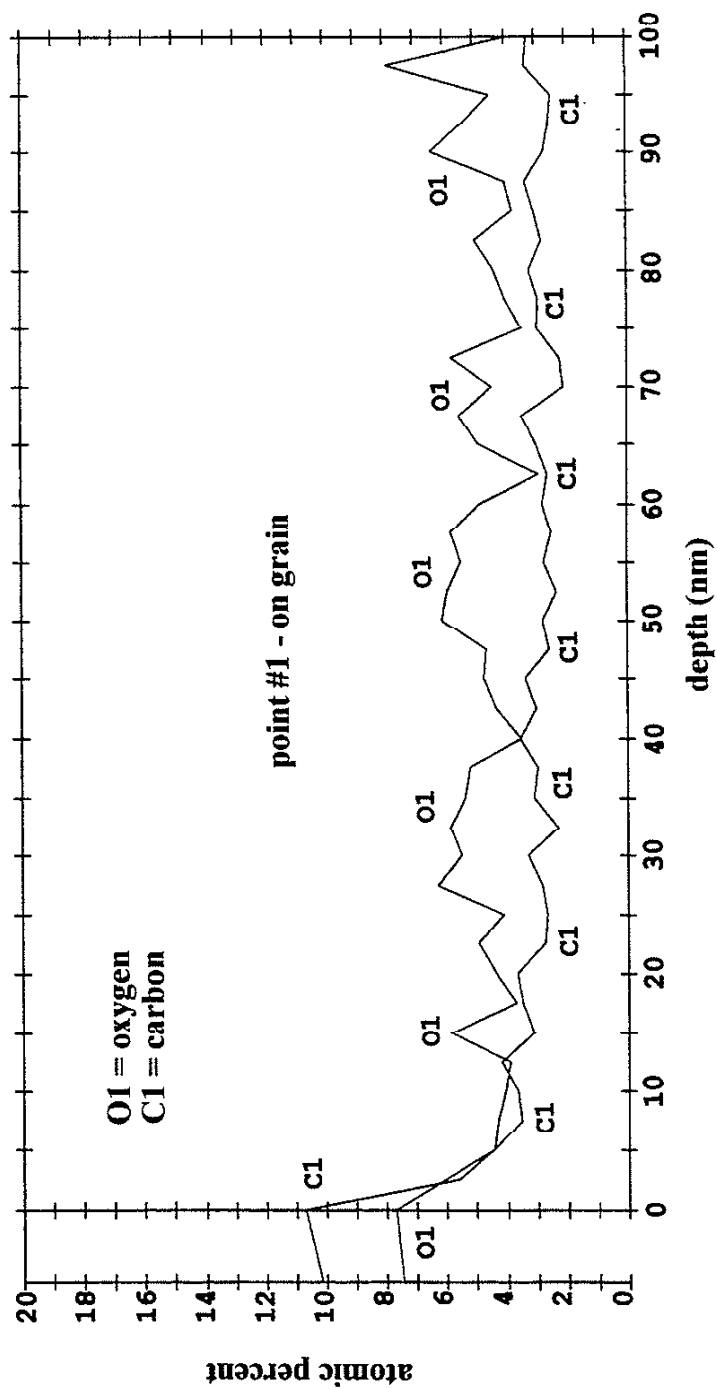


Figure C.2 Carbon Profile for Grain Boundary

## REFERENCES

1. Ewing, J. A. and Humfrey, J. C., "The Fracture of Metals Under Repeated Alterations of Stress", *Phil. Trans. Royal Society*, Vol. 210, pp. 241-253, 1903.
2. Forsyth, P. J. E., "Fatigue Damage and Crack Growth in Aluminum Alloys", *Acta Metallurgica*, Vol. 11, pp. 703-715, July, 1963.
3. Murakami, Y., *Metal Fatigue: Effects Small Defects and Nonmetallic Inclusions*, Yokendo Ltd., Tokyo, 1993.
4. Dowling, Norman E., *Mechanical Behavior of Materials: Engineering Methods for Deformation, Fracture, and Fatigue*, Prentice Hall, 1993.
5. Peterson, R. E., "Notch Sensitivity", *Metal Fatigue*, G. Sines and J. L. Waisman, eds., McGrawHill, New York, 1959, pp. 293-306.
6. Mitchell, R. M., *A Unified Predictive Technique of the Fatigue Resistance of Cast-Ferrous Based Metals and High Hardness Wrought Steels*, Ph. D. Thesis, 1976, University of Illinois Urbana-Champaign.
7. Kitagawa, H. and Takahashi, S., "Applicability of Fracture Mechanics to Very Small Cracks or the Crack in the Early Stage", *Proceedings 2<sup>nd</sup> International Conference on Mechanical Behavior of Materials*, American Society for Metals, Boston, 1976, pp. 627-631.

8. Murakami, Y. and Endo, M., "Effect of Hardness and Crack Geometries on  $\Delta K_{th}$  of Small Cracks Emanating from Small Defects," The Behaviour of Short Fatigue Cracks, EFG Pub. 1 (Edited by K. J. Miller and E.R. de los Rios) 1986, Mechanical Engineering Publications, London, pp. 275-293.
9. Murakami, Y. and Endo, M., "The  $\sqrt{area}$  Parameter Model for Small Defects and Nonmetallic Inclusions in Fatigue Strength: Experimental Evidences and Applications", In *'Proceedings of Theoretical Concepts and Numerical Analysis of Fatigue'* held May 25-27, 1992, Univ. of Birmingham, U.K.
10. Smith, R.A., "On the Short Crack Limitations of Fracture Mechanics", *Int. J. Fract.* 1977, Vol. 13, No. 5, pp. 717-720.
11. El Haddad, M.H., Topper, T.H., and Smith, K.N., "Predictions of NonPropagating Cracks", *Eng. Fract. Mech.* 1979, Vol. 11, No. 3, pp. 573-584.
12. Tanaka, K, Nakai, Y., and Yamashita, M., "Fatigue Growth Threshold of Small Cracks", *Int. J. Fract.* 1981, Vol. 17, No. 5, pp. 519-533.
13. Tanaka, K. and Mura, T., "A Dislocation Model for Fatigue Crack Nucleation", *Journal of Applied Mechanics*, March 1981, Vol. 48, pp. 97-103.
14. Tanaka, K. and Mura, T., "A Theory of Fatigue Crack Initiation at Inclusions", *Metallurgical Transactions A*, Vol. 13A, January 1982, pp. 117-123.
15. Taira, S., Tanaka, K., and Hoshina, M., "Grain Size Effect on Crack Growth Nucleation and Growth in Long-Life Fatigue of Low Carbon Steel", *Fatigue Mechanisms, Proceedings of an ASTM-NBS-NSF Symposium, Kansas City, Mo., May 1978*, J. T. Fong, Ed., ASTM STP 675, American Society for Testing and Materials, 1979, pp. 135-173.

16. Tanaka, K. et al, "Modeling of Small Fatigue Crack Growth Interacting with Grain Boundary", *Engineering Fracture Mechanics*, Vol. 24, No. 6, pp. 803-819, 1986.
17. Navarro, A. and de los Rios, E. R., "A Model for Short Fatigue Crack Propagation with an Interpretation of the Short-Long Crack Transition", *Fatigue Fract. Engng. Mater. Struct.*, 1987, Vol. 10, No. 2, pp. 293-298.
18. Navarro, A. and de los Rios, E. R., "A Microstructurally-Short Fatigue Crack Growth Equation", *Fatigue Fract. Engng Mater. Struct.*, 1988, Vol. 11, No. 5, pp. 383-396.
19. Hussain, K., de los Rios, E. R., and Navarro, A., "A Two-Stage Micromechanics Model for Short Fatigue Cracks", *Fatigue Fract. Engng Mater. Struct.*, 1993, Vol. 44, No. 3, pp. 425-436.
20. Hoshida, T and Socie, D. F., "Crack Nucleation and Growth Modeling in Biaxial Fatigue", *Engineering Fracture Mechanics*, Vol. 29, No. 3, pp. 287-299, 1988.
21. Socie, D. F., "Critical Plane Approaches for Multiaxial Fatigue Damage Assessment", *In Advances in Multiaxial Fatigue, ASTM STP 1191*, ed. D.L. McDowell and R. Ellis. ASTM, Philadelphia, 1993, pp. 7-36.
22. McDowell, D. L., "An Engineering Model for Propagation of Small Cracks in Fatigue", *Engineering Fracture Mechanics*, Vol. 56, No. 3, pp. 357-377, 1997.
23. McDowell, D.L., "Basic Issues in the Mechanics of High Cycle Metal Fatigue", *Int. J. of Fract.*, Vol. 80, No. 2-3, pp. 103-145, 1996.

24. Kunio, T. et al, "Endurance Limit and Threshold Condition for Microcrack in Steels", *Fatigue '84*, A Proceedings of the 2<sup>nd</sup> International Conference on Fatigue and Fatigue Thresholds held at the University of Birmingham, UK, 3-7, September 1984.
25. Yamada, K., Kim, M.G., and Kunio, T., "Tolerant Microflaw Sizes and Non-Propagating Crack Behaviour", *The Behaviour of Short Fatigue Cracks*, EGF Pub. 1 (Edited by K. J. Miller and E. R. de los Rios) 1986, Mechanical Engineering Publications, London, pp. 261-274.
26. Tokaji, K., Ogawa, T., and Harada, Y., "The Growth of Small Fatigue Cracks in a Low Carbon Steel; The Effect of Microstructure and Limitations of Linear Elastic Fracture Mechanics", *Fatigue Fract. Engng. Mater. Struct.*, Vol. 9, No. 3, pp. 205-217, 1986.
27. Murakami, Y. and Nemat-Nasser, "Interacting Dissimilar Semi-Elliptical Surface Flaws Under Tension and Bending", *Engineering Fracture Mechanics*, Vol. 16, No. 3, pp. 373-386, 1982.
28. Murakami, Y. and Nemat-Nasser, S., "Growth and Stability of Interacting Surface Flaws of Arbitrary Shape", *Engng. Fracture Mech.*, Vol. 17, No. 3, 1983, pp. 193-210.
29. Murakami, Y. and Endo, M., "Quantitative Evaluation of Fatigue Strength of Metals Containing Various Small Defects or Cracks", *Engineering Fracture Mechanics*, Vol. 17, No. 1, pp. 1-15, 1983.
30. Murakami, Y., "Analysis of Stress Intensity Factors of Modes I, II, and III for Inclined Surface Cracks of Arbitrary Shape", *Engineering Fracture Mechanics*, Vol. 22, No. 1, pp. 101-114, 1985.



31. Murakami, Y. et al, "Effect of Mean Stress on the Fatigue Strength of High-Strength Steels Containing Small Defects or Nonmetallic Inclusions", *Transactions of JSME (A)*, Vol. 56, No. 525, pp. 1074-1081.
32. Murakami, Y., "Inclusion Rating by Statistics of Extreme Values and Its Application to Fatigue Strength Predictions and Quality Control of Materials", *Journal of Research of the National Institute of Standards and Technology*, Vol. 99, No. 4, 1994, pp. 345-351.
33. Murakami, Y., Toriyama, T., and Coudert, E.M., "Instructions for a New Method of Inclusion Rating and Correlations with the Fatigue Limit", *Journal of Testing and Evaluation*, Vol. 22, No. 4, 1994, pp. 318-326.
34. Ikeda, H. and Murakami, Y., "Fatigue Design and Quality Control of Compressor Flapper Valves for Automobile Airconditioners", *VTT Symposium 155, Fatigue Design 1995*, Vol. 1, pp. 93-104.
35. Kobayashi, M. et al, "Fatigue Strength Prediction of Automobile Suspension Spring Steels: Explicit Analysis of Nonmetallic Inclusions, Shot Peening, Decarburized Layer, Surface Roughness and Corrosion Pits", *MD-Vol. 28, Impact of Improved Material Quality on Properties, Product Performance, and Design*, ASME 1991, pp. 171-183.
36. Toriyama, T. and Murakami, Y., "The  $\sqrt{area}$  Parameter Model for Evaluation of Effects of Various Artificial Small Defects and Mutual Interaction of Small Defects on Fatigue Limit", *Journal Society Material Science., Japan*, Vol. 44, No. 481, pp. 1160-1166, Oct. 1993.

37. Murakami, Y., "Effects of Nonmetallic Inclusions on Fatigue Strength of High Strength Steels: Historical Overview and New Method of Quantitative Evaluation", *MD-Vol. 28, Impact of Improved Material Quality on Properties, Product Performance, and Design*, ASME 1991, pp. 89-103.
38. Murakami, Y. and Usuki, H., "Prediction of Fatigue Strength of High-Strength Steels Based on Statistical Evaluation of Inclusion Size", *Transactions of the Japan Society of Mechanical Engineers*, Vol. 55, No. 510, 1989, pp. 213-221.
39. Kobayashi, M. and Matsui, T., "Prediction of Fatigue Strength of Aluminum Casting Alloys by the  $\sqrt{\text{area}}$  Parameter Model", *Transactions of the Japan Society of Mechanical Engineers*, Vol. 62, No. 594, 1996, pp. 341-346.
40. Takahashi, K. and Murakami, Y., "Quantitative Evaluation of Effect of Surface Roughness on Fatigue Strength", *Engineering Against Fatigue Symposium*, Sheffield, 17-21 March, 1997.
41. Murakami, Y. and Endo, M., "The Effects of Small Defects on the Fatigue Strength of Hard Steels", In *'Proceedings of Fatigue '81'*, Eds. F. Sherrat and J. B. Sturgen, Westburg House, 1981, pp. 431-440.
42. Murakami, Y. and Endo, M., "Effects of Defect, Inclusions and Inhomogeneities on Fatigue Strength", *International Journal of Fatigue*, 1994, Vol. 16, pp. 163-182.
43. Smith, R.A. and Miller, K.J., "Predictions of Fatigue Regimes in Notched Components", *Int. J. Mech. Sci.*, 1978, Vol. 20, No. 4, pp. 201-206.
44. Hammouda, M.M.I. and Miller, K.J., "Elastic-Plastic Fracture Mechanics Analyses of Notches", *ASTM STP 668*, 1979, pp. 703-719.

45. Radhakrishnan, V. M. and Mutoh, Y., "On Fatigue Crack Growth in Stage I", The Behaviour of Short Fatigue Cracks, EFG Pub. 1 (Edited by K. J. Miller and E.R. de los Rios) 1986, Mechanical Engineering Publications, London, pp. 87-99.
46. Hyde, R. S., Krauss, G., and Matlock, D. K., "Phosphorous and Carbon Segregation: Effects on Fatigue and Fracture of Gas Carburized Modified 4320 Steel", *Metallurgical and Materials Transactions A*, Vol. 25A, June 1994, pp. 1229-1240.
47. Hyde, Scott R., "Quench Embrittlement and Intergranular Oxide Embrittlement: Effects on Bending Fatigue Initiation of Gas-Carburized Steel", Ph. D. Thesis, Colorado School of Mines, 1994.
48. Cohen, Rachael E., Krauss, G., and Matlock, David K., "Bending Fatigue Performance of Carburized 4320", SAE Technical Paper Series No. 930963, 1993.
49. Magnusson, L. and Ericsson, T., "Initiation and Propagation of Fatigue Cracks in Carburized Steel", *Proc. Conf. Heat Treatment '79*, Birmingham, Metals Society, pp. 202-208.
50. Hyde, Scott R. et al, "Bending Fatigue Crack Characterization and Fracture Toughness of Gas Carburized SAE 4320 Steel", SAE Technical Paper Series No. 20534, 1994.
51. Pacheco, Jose L. and Krauss, G., "Microstructure and High Bending Fatigue Strength in Carburized Steel", In *Carburizing: Processing and Performance*, ASM International, Metals Park, OH, 1989, pp. 227-237.

52. Preston, S. "Fatigue Crack Initiation and Growth from a Gas Carburized Surface", *Materials Transactions, JIM*, Vol. 34, No. 1 (1993), pp. 27-32.
53. Kristan, Joseph "Effect of Imposed Stress Conditions on the Bending Fatigue Performance of Case Carburized Steels", Ph.D. Thesis, Colorado School of Mines, August, 1997.
54. Garwood, M. F. et al, "Correlation of Laboratory Tests and Service Performance", *Interpretation of Tests and Correlation with Service*, ASM, Cleveland Ohio, 1951, pp. 1-77.
55. Stuhlen, F. B., Cummings, H. N., and Shulte, W. C., "Relation of Inclusions to the Fatigue Properties of High-Strength Steels", In *Proceedings International Conference on Fatigue of Metals*, London, 1956, pp. 439-444.
56. Cummings, H. N., Stuhlen, F. B., and Shulte, W. C., "Tentative Fatigue Strength Reduction Factors for Silicate-Type Inclusions in High-Strength Steels", *ASTM Proc.*, 1958, pp. 505-514.
57. Kung, C. Y., and Fine, M. E., "Fatigue Crack Initiation and Microcrack Growth in 2024-T4 and 2124-T4 Aluminum Alloys", *Metallurgical Transactions A*, 10A, May 1979, pp. 603-610.
58. Castillo, E. et al, "Statistical Model for Fatigue Analysis of Wires, Strands, and Cables", *Report 8002-2, Institut fur Baustatik und Konstruktion, Zurich*, 1983.
59. Forrest, P. G., Fatigue of Metals, Pergamon Press, Oxford, UK, and Addison-Wesley, Reading, Ma., 1962.

60. Sinclair, G. M. and Dolan, T. J., "Effects of Stress Amplitude on Statistical Variability in Fatigue Life of 75S-T6 Aluminum Alloy", *Transactions of the American Society of Mechanical Engineers*, July 1953, pp. 867-872.
61. Prandtl, L., Über die Haerte Plastischer Koerper, Nachr Akad Wiss Goettingen, MathPhysik Kl, 1920.
62. Hill, R., "*The Mathematical Theory of Plasticity*", Clarendon Press, Oxford, 1950.
63. "Nondestructive Inspection and Quality Control", *Metals Handbook*, 8<sup>th</sup> Edition, Vol. 11, American Society for Metals, 1976, pp. 1-20.
64. Petch, N. J., "The Cleavage Strength of Polycrystals", *Journal of Iron and Steel Institute*, May 1953, pp. 25-28.
65. Thompson, A. W., 1975, "Yielding in Nickel as a Function of Grain Size or Cell Size", *Acta Metall.*, Vol. 23, No. 11, pp. 1337-1342.
66. Thompson, A. W., 1977, "Effects of Grain Size on Work Hardening of Nickel", *Acta Metall.*, Vol. 25, No. 1, pp. 83-86.
67. Meyers, Marc A. and Ashworth, E., "A Model for the Effect of Grain Size on the Yield Stress of Metals", *Philosophical Magazine A*, 1982, Vol. 46, No. 5, pp. 737-759.
68. Kuguel, R., "The Highly Stressed Volume of Material as a Fundamental Parameter in the Fatigue Strength of Metal Members", *Theoretical and Applied Mechanics Report No. 169*, Dept. of T&AM, University of Illinois Urbana-Champaign, June 1960.

69. Apple, C. A. and Krauss, G., "Microcracking and Fatigue in a Carburized Steel", *Metallurgical Transactions*, Vol. 4, May 1973, pp. 1195-1200.
70. Krauss, G., "The Microstructure and Fracture of a Carburized Steel", *Metallurgical Transactions A*, Vol. 9A, November 1978, pp. 1527-1535.
71. Ando, T. and Krauss, G., "The Effect of Phosphorus Content on Grain Boundary Cementite Formation in AISI 52100 Steel", *Metallurgical Transactions A*, Vol. 12A, July 1981, pp. 1283-1291.
72. Wu, Ruqian, Freeman, A. J., and Olson, G. B., "On the Electronic Basis of the Phosphorous Intergranular Embrittlement of Iron", *Journal of Materials Research*, Vol. 7, No. 9, Sep. 1992, pp. 2403-2411.
73. Rice, James R. and Wang, Jian-Sheng, "Embrittlement of Interfaces by Solute Segregation", *Materials Science and Engineering*, A107, 1989, pp. 23-40.  
Presented at the *Symposium on Interfacial Phenomena in Composites: Processing, Characterization, and Mechanical Properties*, Newport, RI, June 1-3, 1988.
74. Kunio T. et al, "The Role of Prior Austenite Grains in Fatigue Crack Initiation and Propagation in Low Carbon Martensite", *Fatigue of Engineering Materials and Structures*, Vol. 2, pp. 237-249, 1979.
75. Gladman, T. and Pickering, F. B., "The Effect of Grain Size on the Mechanical Properties of Ferrous Metals", *Yield, Flow and Fracture of Polycrystals*, (Edited by T. N. Baker) 1983, Applied Science Publishers Ltd., pp. 141-198.

76. Murakami, Y., Kodama, S. and Konuma, S., "Quantitative Evaluation of Effect of Non-metallic Inclusions on Fatigue Strength of High Strength Steels. I: Basic Fatigue Mechanisms and Evaluation of Correlation Between the Fatigue Fracture Stress and the Size and Location of Non-metallic Inclusions", *Int. J. Fatigue*, 1989, Vol. 11, No. 5, pp. 291-298.
77. Murakami, Y. and Usuki, H., "Quantitative Evaluation of Effect of Non-metallic Inclusions on Fatigue Strength of High Strength Steels. II: Fatigue Limit Evaluation Based on Statistics for Extreme Values of Inclusion Size", *Int. J. Fatigue*, 1989, Vol. 11, No. 5, pp. 299-307.
78. Murakami, Y. and Shimizu, M., "Effects of Nonmetallic Inclusions, Small Defects and Small Cracks on Fatigue Strength of Metals", *Trans. Jpn Soc. Mech. Eng. Ser. A*, 1988, Vol. 54, 499, pp. 11-16.
79. Murakami, Y., "Fundamental Aspects of Fatigue Threshold of Metals Containing Small Defects, Small Cracks, and Nonmetallic Inclusions – a Unified Quantitative Evaluation and Its Applications", In '*Basic Mechanisms in Fatigue of Metals*' (Ed. P. Lukas and J. Ploak), Materials Science Monographs 46, Elsevier, Amsterdam, 1988, pp. 343-350.
80. Murakami, Y., "Effects of Small Defects and Nonmetallic Inclusions on the Fatigue Strength of Metals, *JSME Int. J. Ser. 1*, 1989, Vol. 32, No. 2, pp. 167-180.
81. Murakami, Y. "Effects of Nonmetallic Inclusions on the Fatigue Strength of Metals", In '*Micromechanics and Inhomogeneity*', The Toshio Mura 65<sup>th</sup> Anniversary Volume' (Ed. G.J. Weng, M. Taya and H. Abe), Springer-Verlag, New York, 1990, pp. 283-295.

82. Natsume, Y., Miyakawa, S., Uemura, Y., and Murakami, Y., "Prediction of the Fatigue Strength of High Speed Steel Based on Estimation of the Maximum Size of Inclusions", In *'Proceedings Fatigue '90'*, Honolulu, Hawaii, USA, H. Kitagawa and T. Tanaka, Eds., Vol. I, 1990, pp. 349-354.
83. Murakami, Y. Kawakami, K. and Saito, M., "Effects of Inclusions on Fatigue Strength of Suspension Spring Steel", *Journal of Spring, Japan Society of Spring*, Vol. 35, 1990, pp. 1-7.
84. Bullens, D. K., *Steel and Its Heat Treatment*, John Wiley and Sons, New York, Vol. 1, 1938, p. 37.
85. Noll, G. C. and Lipson, L., "Allowable Working Stresses", *Proceedings of the Society of Experimental Stress Analysis*, 3(2), 1945.
86. Siebel, E. and Gaier, M., "The Influence of Surface Roughness on the Fatigue Strength of Steels and Non-Ferrous Alloys", *Engineers Digest*, 18, pp 109-112, 1957. (Translation from *VDI Zeitschrift*, Vol. 98, No. 30, pp. 1715-1723, 1956.)
87. Verpoest et al, "The Fatigue Threshold, Surface Condition and Fatigue Limit of Steel Wire", *Int. J. Fatigue*, October, pp. 199-213, 1985.
88. *Martensite*, Edited by G. B. Olson and W. S. Owen, American Society for Materials, 1992.
89. R. N. Caron, G. Krauss, "The Tempering of Fe-C Lath Martensite", *Metallurgical Transactions*, Vol. 3, pp. 2381-2389, 1972.



90. B. S. Lement, B. L. Averbach, Morris Cohen, "Further Study of Microstructural Changes on Tempering Iron-Carbon Alloys", *Transactions of the ASM*, Vol. 47, pp. 291-320, 1954.
91. B. C. Hanley, Thomas J. Dolan, "Surface Finish", *Metals Engineering - Design*, American Society of Mechanical Engineers, pp. 215-225, 1953.
92. G. M. Sinclair, H. T. Corten, and T. J. Dolan, "Effect of Surface Finish on the Fatigue Strength of Titanium Alloys RC 130B and Ti 140A", *Transactions of American Society of Mechanical Engineers*, Vol. 79, pp. 89-96, 1957.
93. D. N. Cledwyn-Davies, "The Effect of Grinding on the Fatigue Strength of Steels", *Proc. Instn. Mech. Engrs.*, 169, pp. 83-92, 1955.
94. F. Bacon, "Fatigue and Corrosion Fatigue with Special Reference to Service Breakages", *Proc. I.Mech.E.*, Vol. 124, p. 685, 1933.
95. L. P. Tarsov, H. J. Grover, "Effects of Grinding and Other Finishing Processes on the Fatigue Strength of Hardened Steel", *Proceedings of the American Society of Testing Materials*, Vol. 50, pp. 668-698, 1950.
96. P. Greenfield, D. H. Allen, "The Effect of Surface Finish on the High Cycle Fatigue Strength of Materials", *GEC Journal of Research*, Vol. 5, No. 3, pp. 129-140, 1987.
97. R. W. Suhr, "The Effect of Surface Finish on a High Cycle Fatigue of a Low Alloy Steel", *The Behavior of Short Fatigue Cracks*, EFT Pub 1 (Edited by K. J. Miller and E. R. de los Rios) 1986, Mechanical Engineering Publications, London, pp. 69-86.

## VITA

Timothy Edward McGreevy was born on March 3, 1969 in Baltimore, Maryland. However, being raised in central Illinois he considers himself a native mid-westerner. After graduating from Chatham Glenwood High School in 1987 he attended Bradley University in Peoria, Illinois where he conducted research in manufacturing technologies for Boeing Commercial Airplanes. He received the CILCO Award for Outstanding Junior Mechanical Engineering Student in 1990 and graduated in 1991 Magna Cum Laude. The following year he worked for Sunnen Products Company in St. Louis, MO in their testing and evaluation laboratory and began graduate studies at Washington University. Returning to Bradley in 1992, he continued his research for Boeing and was co-author in three referred journal articles pertaining to "Fluidized Particulate Bed Fixturing". During this period Tim served as a teaching assistant, university tutor, computer software consultant, math instructor, and worked as a consultant. Prior to receiving his M.S.M.E. degree, Tim also worked for one year at Caterpillar's Advanced Materials Technology Division where he conducted component failure analysis and X-ray measurements of residual stresses. In the fall of 1994, he enrolled as a Ph.D. candidate at the University of Illinois where he has held both teaching and research assistantships. Honors and awards include an Excellent Teaching Award from the University of Illinois (1994), two SME Wayne Kay Graduate Fellowships (1994,1995) and the SAE Fatigue Design & Evaluation H.O. Fuchs Award (1997). He also served as a part-time instructor in the Mechanical Engineering Department at Bradley University in 1996 and is a

member of the American Society for Testing and Materials. Upon graduation he will work for Caterpillar's Advanced Materials Technology Division in Mossville, Illinois and intends to continue teaching part-time at Bradley University.

### **Publications**

"Dynamic Behavior and Creep Characteristics of Flexible Particulate Bed Fixtures", *Journal of Manufacturing Systems* (JMS), Vol. 12, No. 6, 1993, pp. 496-505.

"Experimental Vertical and Torsional Static and Dynamic Behavior of Workpieces in Flexible Fluidized Particulate Bed Fixtures", *Journal of Manufacturing Systems* (JSM), Vol. 13, No. 3, 1994, pp. 177-189.

"Sinkage of Plain and Finned Rod Workpieces in Flexible Particulate Bed Fixtures", *Journal of Manufacturing Systems* (JMS), Vol. 13, No. 5, 1994, pp. 359-369.